Cracow, 2-5 July 2018

ITSRCP18

3rd Conference on Information Technology,
Systems Research and Computational Physics

CompIMAGE18

6th International Symposium CompIMAGE'18
Computational Modeling of Objects Presented in Images
Fundamentals, Methods, and Applications

Faculty of Physics and Applied Computer Science
AGH University of Science and Technology

ITSRCP18
3RD Conference on Information Technology, Systems Research and Computational Physics

CompIMAGE18
6TH International Symposium CompIMAGE'18
Computational Modeling of Objects Presented in Images
Fundamentals, Methods, and Applications

Cracow, Poland, 2-5 July 2018

Contemporary Computational Science

edited by

Piotr Kulczycki
Piotr A. Kowalski
Szymon Łukasik

3rd Conference on Information Technology, Systems Research and Computational Physics

and

6th International Symposium CompIMAGE'18 – Computational Modeling of Objects Presented in Images: Fundamentals, Methods, and Applications

Proceedings of *the International Multi-Conference*
on Computational Science (CS 2018)
2-5 July 2018, Kraków, Poland
http://cs2018.fis.agh.edu.pl/

Kraków 2018

ISBN: 978-83-66016-22-4

AGH University of Science and Technology Press
AGH-UST, 30 Mickiewicza Av., 30-059 Kraków, Poland

Preface

This e-book contains conference material from two concurrent conferences:

- *3rd Conference on Information Technology, Systems Research and Computational Physics (ITSRCP'18)*,
- *6th International Symposium CompIMAGE'18 – Computational Modeling of Objects Presented in Images: Fundamentals, Methods, and Applications (CompIMAGE'18)*,

which has been organized on 2-5 July 2018 by the Faculty of Physics and Applied Computer Science of the AGH University of Science and Technology. The co-organizer is the Systems Research Institute of the Polish Academy of Sciences in Warsaw, Poland. The conferences are being held under auspices of the Committee on Automatic Control and Robotics of the Polish Academy of Sciences. Significant contributions are also being made by the Széchenyi István University (Győr, Hungary), the Slovak University of Technology (Bratislava, Slovakia), and the State University of New York at Fredonia, and the SUNY Buffalo State, both in the USA. Detailed information can be found on the website *http://cs2018.fis.agh.edu.pl/*, and also on the webpages of the particular conferences, *http://itsrcp18.fis.agh.edu.pl/* and *http://isci18.fis.agh.edu.pl/*, respectively.

The intention of holding simultaneous conferences is to combine the two subject areas; the first of which is general, the second presents valuable tools for solving many problems that are highlighted in the former area. The first conference covers all aspects of information technology (in particular, including computational intelligence and data analysis), systems research (especially control engineering and dynamical systems), and computational methods of contemporary applied physics; worthwhile contributions are also made in the related fields of applied mathematics. The second conference includes theoretical and practical aspects of the computational modeling of objects presented in images along with applications in this field.

This publication incorporates short papers and abstracts of regular papers presented at both conferences. For an entire e-book provided as one file, please click here. Full texts of regular papers will be available in the Springer's edited books:

- *Information Technology, Systems Research and Computational Physics*, eds. Kulczycki P., Kacprzyk J., Kóczy L.T., Mesiar R. Wisniewski R., *Advances in Intelligent Systems and Computing* series,
- *Computational Modeling of Objects Presented in Images. Fundamentals, Methods, and Applications*, eds. Barneva R.P., Brimkov V.E., Kulczycki P., Tavares J.M.R.S., *Lecture Notes in Computer Science* series,

respectively for the particular conferences.

In conclusion, we would like to express our heartfelt thanks to the International Program Committee for their input in reviewing the submitted manuscripts. Their scientific contribution and kind help were particularly appreciated in the rapid and reliable management of received subject material, both valuable and varied in theme.

Editors

Piotr Kulczycki

Piotr A. Kowalski

Szymon Łukasik

Table of Contents

Preface iv

Table of Contents v

Section 1

Computational Physics 1

Generative Models for Fast Cluster Simulations in the TPC for the ALICE Experiment (*Kamil Deja, Tomasz Trzciński, and Łukasz Graczykowski*) . . 2

2D-Raman Correlation Spectroscopy Recognizes the Interaction at the Carbon Coating and Albumin Interface (*Anna Kołodziej, Aleksandra Wesełucha-Birczyńska, Paulina Moskal, Ewa Stodolak-Zych, Maria Dużyja, Elżbieta Długoń, Julia Sacharz, and Marta Błażewicz*) 3

Effect of elastic and inelastic scattering on electronic transport in open systems (*Karol Kulinowski, Maciej Wołoszyn, and Bartłomiej J. Spisak*) 4

Phase-space approach to time evolution of quantum states in confined systems. The spectral split-operator method (*Damian Kołaczek, Bartłomiej J. Spisak, and Maciej Wołoszyn*) 5

Section 2

Modeling, Segmentation, Recognition 7

Automatic Segmentation and Quantitative Analysis of Irradiated Zebrafish Embryos (*Melinda Katona, Tüde Tőkés, Emília Rita Szabó, Szilvia Brunner, Imre Zoltán Szabó, Róbert Polanek, Katalin Hideghéty, and László G. Nyúl*) 8

Classification of breast lesions using quantitative dynamic contrast enhanced-MRI (*Mohan Jayatilake, Teresa Gonçalves, and Luís Rato*) 9

Recognizing Emotions with EmotionalDAN (*Ivona Tautkute, Tomasz Trzciński, and Adam Bielski*) 10

Clustering functional MRI Patterns with Fuzzy and Competitive Algorithms (*Alberto Arturo Vergani, Samuele Martinelli, and Elisabetta Binaghi*) . . . 11

Section 3

Information Technology 13

Integer Programming Based Optimization of Optical Node Architectures (*Stanisław Kozdrowski and Sławomir Sujecki*) 14

Two approaches for the computational model for software usability in practice (*Eva Rakovská and Miroslav Hudec*) 21

Content-based recommendations in an e-commerce platform (*Łukasz Dragan and Anna Wróblewska*) 22

Analysis of dispersive part of AC magnetic susceptibility measurement of high-temperature superconductors by means of neural network (*Marcin Kowalik, Waldemar Tokarz, Andrzej Kołodziejczyk, Marek Giebułtowski, Ryszard Zalecki and Wiesław Marek Woch*) 23
A method of Functional Test interval selection with regards to Machinery and Economical aspects (*Jan Piesik and Emilian Piesik*) 31

Section 4

Data Analysis and Systems Research **45**
Using Random Forest Classifier for particle identification in the ALICE Experiment (*Tomasz Trzciński, Łukasz Graczykowski, and Michał Glinka*) 46
Fault Propagation Models Generation in Mobile Telecommunication Networks based on Bayesian Networks with Principal Component Analysis Filtering (*Artur Maździarz*) 47
An efficient model for steady state numerical analysis of erbium doped fluoride glass fiber lasers (*Sławomir Sujecki*) 48
Image enhancement with applications in biomedical processing (*Małgorzata Charytanowicz, Piotr Kulczycki, Szymon Łukasik, and Piotr A. Kowalski*) . . . 54
Efficient Astronomical Data Condensation using Approximate Nearest Neighbors (*Szymon Łukasik, Konrad Lalik, Piotr Sarna, Piotr A. Kowalski, Małgorzata Charytanowicz, and Piotr Kulczycki*) 55
Comparative analysis of segmentation methods and extracting heart features in Cardiovascular MRI (*Joanna Świebocka-Więk*) 56
Similarity-based outlier detection in multiple time series (*Grzegorz Gołaszewski*) 68

Section 5

Tomography **69**
Multimaterial Tomogrpahy: Reconstruction from Decomposed Projection Sets (*László G. Varga*) 70
Sequential Projection Selection Methods for Binary Tomography (*Gábor Lékó and Péter Balázs*) 71
Variants of Simulated Annealing for Strip Constrained Binary Tomography (*Judit Szűcs and Péter Balázs*) 72

Section 6

Computational Intelligence **73**
Optimizing Clustering with Cuttlefish Algorithm (*Piotr A. Kowalski, Szymon Łukasik, Małgorzata Charytanowicz, and Piotr Kulczycki*) 74
A Memetic version of the Bacterial Evolutionary Algorithm for discrete optimization problems (*Boldizsár Túű-Szabó, Peter Földesi, and László T. Kóczy*) 75
A Hybrid Cascade Neural Network with Ensembles of Extended Neo-Fuzzy Neurons and its Deep Learning (*Yevgeniy Bodyanskiy and Oleksii Tyshchenko*) 76

Section 7

Applied Mathematics **77**
Probability Measures and projections on Quantum Logics (*Oľga Nánásiová, Ľubica Valášková, and Viera Čerňanová*) 78
Statistical analysis of models' reliability for punching resistance assessment (*Jana Kalická, Mária Minárová, Jaroslav Halvoník, and Lucia Majtánová*) 79

Statistical test for fractional Brownian motion based on detrending moving average algorithm (*Grzegorz Sikora*) 80
On persistence of convergence of kernel density estimates in particle filtering (*David Coufal*) 91
Multidimensional copula models of dependencies between selected international financial market indexes (*Tomáš Bacigál, Magdaléna Komorníková, and Jozef Komorník*) 92
New Types of Decomposition Integrals and Computational Algorithms (*Adam Šeliga*) 93
Trend analysis and detection of change-points of selected financial and market indices (*Dominika Ballová*) 94
Picturing Order (*Karl Javorszky*) 95

Section 8

Discrete Geometry and Topology **105**
Endpoint-Based Thinning with Designating Safe Skeletal Points (*Kálmán Palágyi and Gábor Németh*) 106
Maximal P-simple Sets on (8,4) Pictures (*Péter Kardos and Kálmán Palágyi*) . 107
An immersed boundary approach for the numerical analysis of objects represented by oriented point clouds (*László Kudela, Stefan Kollmannsberger, and Ernst Rank*) 108
Structuring digital spaces by closure operators associated to n-ary relations (*Josef Slapal*) 109

Section 9

Computer Vision **111**
Graph Cutting in Image Processing handling with Biological Data Analysis (*Mária Ždímalová, Tomáš Bohumel, Katarína Plachá-Gregorovská, Peter Weismann, and Hisham El Falougy*) 112
Comparison of 3D graphics engines for particle track visualization in the ALICE Experiment (*Piotr Nowakowski, Julian Myrcha, Tomasz Trzciński, Łukasz Graczykowski and Przemysław Rokita*) 113
A methodology for trabecular bone microstructure modelling agreed with three-dimensional bone properties (*Jakub Kamiński, Adrian Wit, Krzysztof Janc, and Jacek Tarasiuk*) 124
Human stress detection using non-contact remote photoplethysmography from video stream (*Sergii Nikolaiev, Sergii Telenyk and Yury Tymoshenko*) . . . 125

Section 10

Fuzzy Logic **137**
On wavelet based enhancing possiilities of fuzzy classification of measurement results (*Ferenc Lilik, Levente Solecki, Brigita Sziová, László T. Kóczy, and Szilvia Nagy*) 138
On the Convergence of Fuzzy Grey Cognitive Maps (*István Á Harmati and László T. Kóczy*) 139
Hierarchical fuzzy decision support methodology for packaging system design (*Kata Vörösk̋oi, Gergő Fogarasi, Adrienn Buruzs, Peter Földesi, and László T. Kóczy*) 140

Section 11
Machine Learning **141**
Applicability of Deep Learned vs Traditional Features for Depth Based Classification (*Fabio Bracci, Mo Li, Ingo Kossyk, and Zoltan-Csaba Marton*) . . . 142
Effect of image view for mammogram mass classification (*Sk Md Obaidullah, Sajib Ahmed, and Teresa Gonçalves*) 143
Solving a Combinatorial Multiobjective Optimization Problem by Genetic Algorithm (*Marcin Studniarski, Liudmila Koliechkina and Elena Dvernaya*) . 144

Section 12
Image Analysis **157**
Fast Object Detector based on Convolutional Neural Networks (*Karol Piaskowski, and Dominik Belter*) 158
Applying computational geometry to designing an occlusal splint (*Dariusz Pojda, Agnieszka Anna Tomaka, Leszek Luchowski, Krzysztof Skabek, and Michał Tarnawski*) 159
Assessment of Patients Emotional Status According To iris Movement (*Alhamzawi Hussein and Attila Fazekas*) 160
Computer-aided diagnosis system for lumbar spinal stenosis detection in MRI based on radiological criteria (*Dominik Horwat and Marek Krośnicki*) . . . 177

Section 13
Intelligent Data Analysis **191**
Credibility of Fuzzy Knowledge (*Oleksandr Provotar*) 192
RMID: a novel and efficient image descriptor for mammogram mass classification (*Sk Md Obaidullah, Sajib Ahmed, Teresa Gonçalves, and Luís Rato*) 203
Instrumentals/songs separation for background music removal (*Himadri Mukherjee, Sk Md Obaidullah, K.C. Santosh, Teresa Gonçalves, Santanu Phadikar, and Kaushik Roy*) 204
Modern metaheuristics in physical processes optimization (*Tomasz Rybotycki*) . 205

Section 14
From Theory to Applications **207**
Effect of left ventricular longitudinal axis variation in Pathological hearts using Deep learning (*Yashbir Singh, Deepa, Shi-Yi Wu, João Manuel R. S. Tavares, Michael Friebe and Weichih Hu*) 208
Finding Graph from Retinal Vascular Network for Image Verification (*Nilanjana Dutta Roy and Arindam Biswas*) 213
Pure Hexagonal Context-Free Grammars Generating Hexagonal Patterns (*Pawan Kumar Patnaik, Venkata Padmavati Metta, Jyoti Singh, and D.G. Thomas*) 225
Design of a haptic exoskeleton for the hand with Internet of Things (*Juan Camilo Calvera Duran, Octavio José Salcedo Parra and Carlos Enrique Montenegro Marín*) 226

Section 15
Early Stage Researchers **227**
Crisp vs Fuzzy Decision Support Systems for the Forex Market (*Przemysław Juszczuk and Lech Kruś*) 228

Neural network and dynamic programming for R&D sector development in Poland (*Jacek Chmielewski*) 229
Recurrent Neural Networks with grid data quantization for modeling LHC superconducting magnets behavior (*Maciej Wielgosz and Andrzej Skoczeń*) . 240

Author Index **241**

Section 1
Computational Physics

Generative Models for Fast Cluster Simulations in the TPC for the ALICE Experiment

Kamil Deja[1], Tomasz Trzciński[1], and Łukasz Graczykowski[2]

[1] Institute of Computer Science, Warsaw University of Technology, Poland;
[2] Faculty of Physics, Warsaw University of Technology, Poland;

Abstract. Simulating the possible detector response is a key component of every high-energy physics experiment. The methods used currently for this purpose provide high-fidelity results. However, this precision comes at a price of a high computational cost, which renders those methods infeasible to be used in other applications, e.g. data quality assurance. In this work, we present a proof-of-concept solution for generating the possible responses of detector clusters to particle collisions, using the real-life example of the Time Projection Chamber (TPC) in the ALICE experiment at CERN. We introduce this solution as a first step towards a semi-real-time anomaly detection tool. It's essential component is a generative model that allows to simulate synthetic data points that bear high similarity to the real data. Leveraging recent advancements in machine learning, we propose to use state-of-the-art generative models, namely Variational Autoencoders (VAE) and Generative Adversarial Networks (GAN), that prove their usefulness and efficiency in the context of computer vision and image processing. The main advantage offered by those methods is a significant speedup in the execution time, reaching up to the factor of 10^3 with respect to the GEANT3, a currently used cluster simulation tool. Nevertheless, this computational speedup comes at a price of a lower simulation quality. In this work we show quantitative and qualitative limitations of currently available generative models. We also propose several further steps that will allow to improve the accuracy of the models and lead to the deployment of anomaly detection mechanism based on generative models in a production environment of the TPC detector.

The full text will be available in the edited book “Information Technology, Systems Research and Computational Physics”, eds. Kulczycki P., Kacprzyk J., Kóczy L.T., Mesiar R., Wisniewski R., to be published by Springer in the *Advances in Intelligent Systems and Computing* series soon.

2D-Raman Correlation Spectroscopy Recognizes the Interaction at the Carbon Coating and Albumin Interface

Anna Kołodziej[1], Aleksandra Wesełucha-Birczyńska[1], Paulina Moskal[1], Ewa Stodolak-Zych[2], Maria Dużyja[3], Elżbieta Długoń[2], Julia Sacharz[1], and Marta Błażewicz[2]

[1] Faculty of Chemistry, Jagiellonian University, Krakow, Poland;
[2] Faculty of Materials Science and Ceramics,
AGH-University of Science and Technology, Krakow, Poland;
[3] Technolutions, Łowicz , Poland;

Abstract. Carbon materials open new perspectives in biomedical research, due to their inert nature and interesting properties. For biomaterials the essential attribute is their biocompatibility, which refers to the interaction with host cells and body fluids, respectively. The aim of our work was to analyze two types of carbon layers differing primarily in topography, and modeling their interactions with blood plasma proteins. The first coating was a layer formed of pyrolytic carbon (CVD) and the second was constructed of multi-walled carbon nanotubes obtained by electrophoretic deposition (EPD), both set on a Ti support. The results of the performed complex studies of the two types of model carbon layers exhibit significant dissimilarities regarding their interaction with chosen blood proteins, and the difference is related to the origin of a protein: whether it is animal or human. Wettability data, nano sctatch tests were not sufficient to explain the material properties. In contrast, Raman microspectroscopy thoroughly decodes the phenomena occurring at the carbon structures in contact with the selected blood proteins interface. The 2D correlation method selects the most intense interaction and points out the different mechanism of interactions of proteins with the nanocarbon surfaces and differentiation due to the nature of the protein and its source: animal or human. The 2D- correlation of the Raman spectra of the MWCNT layer+HSA interphase confirms an increase in albumin β-conformation. The presented results explain the unique properties of the C-layers (CVD) in contact with human albumin..

The full text will be available in the edited book “Information Technology, Systems Research and Computational Physics”, eds. Kulczycki P., Kacprzyk J., Kóczy L.T., Mesiar R., Wisniewski R., to be published by Springer in the *Advances in Intelligent Systems and Computing* series soon.

Effect of elastic and inelastic scattering on electronic transport in open systems

Karol Kulinowski, Maciej Wołoszyn, and Bartłomiej J. Spisak

AGH University of Science and Technology, Faculty of Physics and Applied Computer Science,
al. Mickiewicza 30, 30-059 Krakow, Poland;

Abstract. The purpose of this study is to apply the distribution function formalism to the problem of electronic transport in open systems, and numerically solve the kinetic equation with a dissipation term. This term is modeled within the relaxation time approximation, and contains two parts, corresponding to elastic or inelastic processes. The collision operator is approximated as a sum of the semiclassical energy dissipation term, and the momentum relaxation term which randomizes momentum but does not change energy. As a result, the distribution of charge carriers changes due to the dissipation processes, which has a profound impact on the electronic transport through the simulated region discussed in terms of the current–voltage characteristics and their modification caused by the scattering.

The full text will be available in the edited book "Information Technology, Systems Research and Computational Physics", eds. Kulczycki P., Kacprzyk J., Kóczy L.T., Mesiar R., Wisniewski R., to be published by Springer in the *Advances in Intelligent Systems and Computing* series soon.

Phase-space approach to time evolution of quantum states in confined systems. The spectral split-operator method

Damian Kołaczek, Bartłomiej J. Spisak, and Maciej Wołoszyn

AGH University of Science and Technology, Faculty of Physics and Applied Computer Science,
al. Mickiewicza 30, 30-059 Krakow, Poland;

Abstract. Using the phase space approach, we consider the dynamics of a quantum particle in an isolated confined quantum system with three different potential energy profiles. We solve the Moyal equation of motion for the Wigner function with the highly efficient spectral split-operator method. The main aim of this study is to compare the accuracy of the used algorithm by analysis of the total energy expectation value, in terms of the deviation from its exact value. This comparison is performed for the second and fourth order factorizations of the time evolution operator.

The full text will be available in the edited book "Information Technology, Systems Research and Computational Physics", eds. Kulczycki P., Kacprzyk J., Kóczy L.T., Mesiar R., Wisniewski R., to be published by Springer in the *Advances in Intelligent Systems and Computing* series soon.

Section 2
Modeling, Segmentation, Recognition

Automatic Segmentation and Quantitative Analysis of Irradiated Zebrafish Embryos

Melinda Katona[1], Tüde Tőkés[2], Emília Rita Szabó[2], Szilvia Brunner[2],
Imre Zoltán Szabó[2], Róbert Polanek[2], Katalin Hideghéty[2], and László G. Nyúl[1]
[1]Department of Image Processing and Computer Graphics, University of Szeged,
Árpád tér 2, Szeged, H-6720 Hungary;
[2]ELI-HU Non-Profit Ltd., Dugonics tér 13, Szeged, H-6720 Hungary;

Abstract. Radiotherapy is one of the most common methods to treat different cancer cells in clinical application despite having harmful effects on healthy tissues. Radiobiological experiments are very important to determine the irradiation-caused acute and chronic effects to define the exact consequences of different irradiation sources. Photon irradiation has been used on zebrafish embryos, a very new *in vivo* and appropriate model system in radiobiology. After irradiation, dose-dependent morphological changes were observable in the embryos. These morphological deteriorations were measured manually by biologist researchers during three weeks, which was an extremely time demanding process (15 minutes per image). The aim of this project was to automate this evaluating process, to save time for researchers and to keep the consistence and accuracy of the evaluation. Hence, an algorithm was developed and used to detect the abnormal development of zebrafish embryos.

The full text will be available in the edited book “Computational Modeling of Objects Presented in Images. Fundamentals, Methods, and Applications”, eds. Barneva R.P., Brimkov V.E., Kulczycki P., Tavares J.M.R.S., to be published by Springer in the *Lecture Notes in Computer Science* series soon.

Classification of breast lesions using quantitative dynamic contrast enhanced-MRI

Mohan Jayatilake[1], Teresa Gonçalves[2], and Luís Rato[2]

[1]University of Peradeniya, Sri Lanka;

[2]Computer Science Department, University of Évora, Portugal;

Abstract. Imaging biomarkers are becoming important in both research and clinical studies. This study is focused on developing measures of tumour mean, fractal dimension, homogeneity, energy, skewness and kurtosis that reflect the values of the pharmacokinetic (PK) parameters within the breast tumours, evaluate those using clinical data and investigate their feasibility as a biomarker to discriminate malign from benign breast lesions. In total, 75 patients with breast cancer underwent Dynamic Contrast Enhanced-Magnetic Resonance Imaging (DCE-MRI). Axial bilateral images with fat-saturation and full breast coverage were performed at 3T Siemens with a 3D gradient echo-based TWIST sequence. The whole tumour mean, fractal dimension, homogeneity, energy, skewness and kurtosis of K^{trans} and V_e values were calculated. Median of both the mean and fractal dimension of K^{trans} and V_e for benign and malignant show significant discrimination. Further, the median of skewness and kurtosis of V_e between benign and malignant are also significantly varying. In conclusion, mean and fractal dimension of both K^{trans} and V_e and skewness and kurtosis of V_e for typical breast cancer, computed from PK parametric maps, show potential as a biomarker for breast tumour diagnosis either as a benign or malignant.

The full text will be available in the edited book “Computational Modeling of Objects Presented in Images. Fundamentals, Methods, and Applications”, eds. Barneva R.P., Brimkov V.E., Kulczycki P., Tavares J.M.R.S., to be published by Springer in the *Lecture Notes in Computer Science* series soon.

Recognizing Emotions with EmotionalDAN

Ivona Tautkute, Tomasz Trzciński, and Adam Bielski
Polish-Japanese Academy of Information Technology, Warsaw, Poland;
Warsaw University of Technology, Warsaw, Poland;
Tooploox, Poland;

Abstract. Classification of human emotions remains an important and challenging task for many computer vision algorithms, especially in the era of humanoid robots which coexist with humans in their everyday life. Currently proposed methods for emotion recognition solve this task using multi-layered convolutional networks that do not explicitly infer any facial features in the classification phase. In this work, we postulate a fundamentally different approach to solve emotion recognition task that relies on incorporating facial landmarks as a part of the classification loss function. To that end, we extend a recently proposed Deep Alignment Network (DAN), that achieves state-of-the-art results in the recent facial landmark recognition challenge, with a term related to facial features. Thanks to this simple modification, our model called EmotionalDAN is able to outperform state-of-the-art emotion classification methods on two challenging benchmark dataset by up to 5%.

The full text will be available in the edited book "Computational Modeling of Objects Presented in Images. Fundamentals, Methods, and Applications", eds. Barneva R.P., Brimkov V.E., Kulczycki P., Tavares J.M.R.S., to be published by Springer in the *Lecture Notes in Computer Science* series soon.

Clustering functional MRI Patterns with Fuzzy and Competitive Algorithms

Alberto Arturo Vergani, Samuele Martinelli, and Elisabetta Binaghi
University of Insubria, Varese, Italy;

Abstract. We used model free methods to explore the brain's functional properties adopting a partitioning procedure based on cross-clustering: we selected Fuzzy C-Means (FCM) and Neural Gas (NG) algorithms to find spatial patterns with temporal features and temporal patterns with spatial features, applied to a shared fMRI repository of Face Recognition Task. We investigated the partitioning matching the BOLD signal signatures with the classes found and with the results of functional connectivity analysis. We compared the outcomes using the just known model-based knowledge as likely ground truth, confirming the role of Fusiform brain regions. Partitioning results globally show a better spatial clustering than temporal clustering for both algorithms; in the case of temporal clustering, FCM outperforms Neural Gas. The relevance of brain subregions related to Face Recognition were correctly distinguished by algorithms and the results are in agreement with the current neuroscientific literature.

The full text will be available in the edited book "Computational Modeling of Objects Presented in Images. Fundamentals, Methods, and Applications", eds. Barneva R.P., Brimkov V.E., Kulczycki P., Tavares J.M.R.S., to be published by Springer in the *Lecture Notes in Computer Science* series soon.

Section 3
Information Technology

Integer Programming Based Optimization of Optical Node Architectures

Stanisław Kozdrowski[1] and Sławomir Sujecki[2]

[1] Warsaw University of Technology, Warsaw, Poland,
`S.Kozdrowski@tele.pw.edu.pl`,
[2] Wrocław University of Science and Technology,
Wrocław, Poland

Abstract. The main objective of this study is to minimize capex and opex in telco optical networks which use colorless, directionless, contentionless node architecture. In the paper therefore a review of new generation reconfigurable optical add drop multiplexer architectures is presented with a particular focus on optimization of optical node resources. The problem is formulated as an integer linear programming problem. The results of numerical experiments are presented for network topologies of different dimensions and with a large demand set.

Keywords: Network design, ROADM, CDC optical node, Integer Programming, Linear Programming optimization

1 Introduction

New Generation Reconfigurable Optical Add Drop Multiplexers (NG ROADMs) deployed currently in high speed optical telecom networks have colorless, directionless and contentionless (CDC) architectures [1, 2]. Hence, CDC optical node architectures are a subject of an intense research [3, 4] and are of great interest to network operators and equipment suppliers. Additionally, NG ROADMs may also have flex spectrum/flex grid, functionality typically referred to as colorless, directionless and contentionless - flex spectrum/flex grid (CDC-F) architecture [5, 6].

NG ROADMs enable operators to offer a flexible service and provide potentially significant savings in Operational Expenditure (OpEx) and Capital Expenditure (CapEx). OpEx reductions are delivered primarily by means of touchless provisioning and activation of network bandwidth (Figure 1). Concerning CapEx, network operators do not need to pay high capital expense by replacing at once all traditional transponders and nodal elements with those compliant with CDC-F technology but can implement instead an investment strategy of “pay as you grow” with a goal of eventually replacing all elements [7, 8]. Additionally, having colorless functionality one can use different wavelengths for different sections in the optical path to avoid congestion in the network.

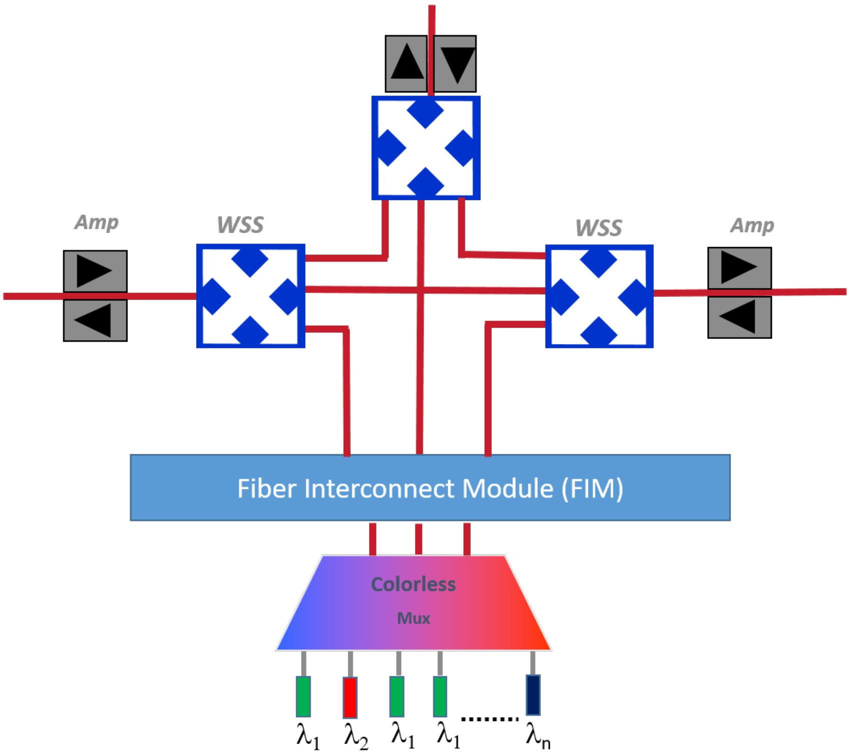

Fig. 1: CDC ROADM

During the last decade attention of the telecommunication community have been concentrated on Routing and Wavelength Assignment (RWA) and Routing and Spectrum Allocation (RSA) problems. Consequently, numerous exact and heuristic approaches are now available to solve RWA and RSA problems [5, 9]. However, with the advent of CDC-F technology there is a need to develop more accurate modes of an optical node. In this study we concentrate therefore on optical node resources optimization and compare various types of ROADMs both classical and CDC-F. We formulate the problem as Integer Programming (IP) both for classical ROADM node network and colorless ROADM one. Traffic demands range from 1 Gb to 1 Tb, between each pair of nodes, and are represented via traffic matrix, which is changing in each time period, which in turn depends on the duration of the service.

In the paper we concentrate on optimization of optical node resources (i.e. vatious types of transponders). In the paper the problem is formulated as Integer Programming [10] and solved using CPLEX software package. Linear Programming (LP) is also applied to obtain to evaluate the distance to the global optimum. Several alternative Integer Programming and Mixed Integer Programming (MIP) formulations of the RSA problem can be found in the literature [11, 12].

The rest of the paper is organized as follows. In Section 2 the problem and the constraints are presented. In the next Section the numerical results are showed and in the last Section concluding remarks are provided.

2 Problem Description

First, let us consider an optical network conecting a set of nodes $n \in \mathcal{N}$ with number of transponders t installed in the node - $i(t, n)$. Second, consider a set of transponders $t \in \mathcal{T}$, each transponder type t is characterized by number of outputs - $o(t)$, bitrate of one output - $b(t)$ and cost of using transponder - $\xi(t)$.

Next, let us consider a set of Time Period $\mathcal{P}$, with volume $h(n, n', p)$ from node n to node n' (the values $h(\cdot)$ constitute the traffic matrix for each period $p \in \mathcal{P}$). Additionally, $\xi(n)$ denotes cost of intervention in node n with binary variable w_{np} equal 1 - if intervention is needed in node n in period p and 0 - otherwise. Detailed sets, constants and variables description is presented in the table bellow.

Sets		Constants		Variables	
$\mathcal{N}$	nodes	$o(t)$	number of outputs of transponder t	x_{tnp}	number of transponder t installed in node n in period p
$\mathcal{T}$	transponders	$b(t)$	bitrate of one output of transponder t	$y_{tp}^{(n,n')}$	number of outputs of transponder t installed in relation (n, n') in period p
$\mathcal{P}$	time period	$\xi(t)$	cost of using transponder t in one period	$z_{n''p}^{(n,n')}$	bitrate in relation (n, n') with node n'' being the final destination in period p
		$h(n, n', p)$	volume from node n to node n' in period p	w_{np}	binary; if intervention is needed in node n in period p
		$i(t, n)$	number of transponders t installed in node n		
		$\xi(n)$	cost of intervention in node n		
		$p(p)$	period before period p; p is the first period if $p(p) = \emptyset$		
		M	a large number		

We define the objective function as the sum of intervention cost and transponder cost, representing opex and capex cost of the considered networks.

$$\mathcal{F} = \min \sum_{p \in \mathcal{P}} \sum_{n \in \mathcal{N}} (w_{np}\xi(n) + \sum_{t \in \mathcal{T}} x_{tnp}\xi(t)) \tag{1a}$$

Additionally, we have the following constraints.

$$\sum_{n' \in \mathcal{N}} z_{n''p}^{(n,n')} = \sum_{n' \in \mathcal{N}} z_{n''p}^{(n',n)} + h(n,n'',p) \quad \forall n, n'' \in \mathcal{N} : n \neq n'', \forall p \in \mathcal{P} \tag{2a}$$

$$\sum_{t \in \mathcal{T}} y_{tp}^{(n,n')} b(t) \geq \sum_{n'' \in \mathcal{N}} z_{n''p}^{(n,n')} \quad \forall n, n' \in \mathcal{N}, \forall p \in \mathcal{P} \tag{2b}$$

$$x_{tnp} o(t) \geq \sum_{n' \in \mathcal{N}} (y_{tp}^{(n,n')} + y_{tp}^{(n',n)}) \quad \forall t \in \mathcal{T}, \forall n \in \mathcal{N}, \forall p \in \mathcal{P} \tag{2c}$$

$$w_{np} M \geq x_{tnp} - x_{tnp(p)} \quad \forall n \in \mathcal{N}, \forall p \in \mathcal{P} : p(p) \neq \emptyset, \forall t \in \mathcal{T} \tag{2d}$$

$$w_{np} M \geq x_{tnp(p)} - x_{tnp} \quad \forall n \in \mathcal{N}, \forall p \in \mathcal{P} : p(p) \neq \emptyset, \forall t \in \mathcal{T} \tag{2e}$$

$$w_{np} M \geq x_{tnp} - i(t,n) \quad \forall n \in \mathcal{N}, \forall p \in \mathcal{P} : p(p) = \emptyset, \forall t \in \mathcal{T} \tag{2f}$$

$$w_{np} M \geq i(t,n) - x_{tnp} \quad \forall n \in \mathcal{N}, \forall p \in \mathcal{P} : p(p) = \emptyset, \forall t \in \mathcal{T} \tag{2g}$$

$$w_{np} \in \{0,1\} \quad \forall n \in \mathcal{N}, \forall p \in \mathcal{P} \tag{2h}$$

where the first three sets of constraints guarantee that each transponder t has a sufficient bitrate and number of outputs. The latter sets of constraints are associated with interventions on sites. Finaly, (2h) assures that variables are binary.

3 Numerical Experiments

We have considered optimization problem presented in Section 2 with objective function given by equation (1a) and constraints (2a)–(2h). We have choosen 3 types of transponders, whose parameters are presented in Table 1a. For each transponder t there are different parameter settings (i.e., number of outputs $o(t)$, bitrate $b(t)$ and cost $\xi(t)$).

transponder type - t	1	2	3
$o(t)$	1	4	1
$b(t)$	10	10	100
$\xi(t)$	1	3	5

(a) Transponder parameters

Case	A	B	C	D
number of nodes	5	12	5	12
$\xi(n)$	2	2	5	5

(b) Network parameters

Table 1: Network model parameters

We have taken various problem instances into the consideration for 4 cases A, B, C and D. These cases concern the size of the network and intervention cost $\xi(n)$, presented in Table 1b .

Cases A and C consider the network topology encompassing 5 nodes and 7 links, presented in Figure 2a with intervention cost $\xi(t)$ equal 2 and 5, respectively. Cases B and D consider the network topology with 12 nodes and 20 links presented in Figure 2b, with intervention cost $\xi(t)$ equal 2 and 5, respectively. The network of Figure 2b is taken from [7].

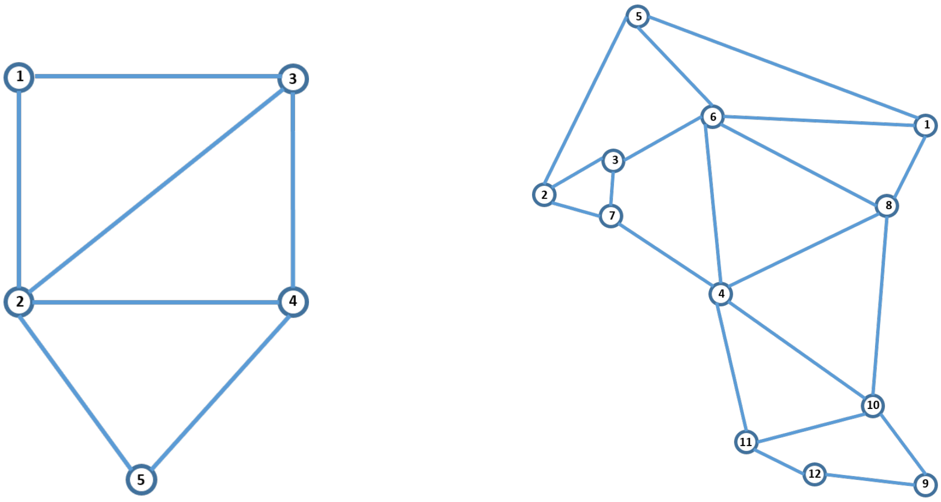

(a) net_5 (b) net_12

Fig. 2: Network topologies

We have analyzed both networks - net_5 and net_12 for 3 Time Periods. Each Time Period $p \in \mathcal{P}$ contains a demand matrix. Demands are expressed in Gb. For the network net_5 demands were generated artificially, while for the network net_12 demands were taken from a real network [13].

Case	Time Period	$\mathcal{F}$ LP	$\mathcal{F}$ IP	Time (Gap)
A	1	59,6	64	1
	2	139,7	140	3
	3	226,1	228	14
B	1	263,7	267	72000 (1,7%)
	2	509,3	557	72000 (8,5%)
	3	815,7	861	72000 (12,4%)

Table 2: Computational results for cases A and B

To solve all problem instances we have used CPLEX 12.6.1, running 8 parallel threads with a runtime limit of 20 hours under a 64-bit Windows OS with 64 GB of RAM. Table 2 presents the results for case A and B. Column "$\mathcal{F}$" presents both LP and IP best volume and column "Time (Gap)" presents the running time volume (in seconds) whilst the final percentage gap of the best found solution is presented in brackets, whenever the runtime limit was reached.

Table 3 presents the results for cases C and D. Cases A and C, which coresponds to the smal networks were solved to optimality. The results for large network (cases B and D) show that the optimal solution has not been found and all final gaps were significantly large.

Case	Time Period	$\mathcal{F}$		Time (Gap)
		LP	IP	
C	1	65,4	74	1
	2	149,7	154	4
	3	238,9	241	80
D	1	281,7	290	72000 (1,9%)
	2	554,5	608	72000 (9,5%)
	3	822,7	975	72000 (17,4%)

Table 3: Computational results for cases C and D

Table 3 presents results with an increased value of the intervention cost $\xi(n) = 5$ when compared with the results presented in the table 2, where $\xi(n) = 2$. The results from Table 3 show that the change of $\xi(n)$ has practically no influence on the calculation time for Time Period 1 and 2. For Time Period 3 significant different is observed. Also the calculation time strongly depends on the size of the network and the number of Time Periods considered.

The results obtained for cases B and D (larger network, Tables 2 and 3) show that the minima attained are suboptimal and there is a need to improve the method by using, for example, metaheuristics (i.e., evolutionary algorithms).

4 Concluding Remarks

A novel CDC ROADM architecture is presented and compared with the traditional one. LP and IP methods were applied to optimize the node resources. IP problem for CDC architecture with objective function taking into account opex and capex indicator was formulated. It has been shown that for small networks, in all cases, an optimal solution can be reached using IP method. However, the performance of an optimization algorithm for larger networks might be further improved by implementing relaxation, parallel processing and heuristics. The presented research is supposed to be continued with a goal to further examin Integer Programming and Mixed Integer Programming as well as various metaheuristics.

References

1. R. Jensen, A. Lord, N. Persons, Colourless, directionless, contentionless roadm architectures using low-loss optical matrix switches, European Conference and Exhibition on Optical Communication (ECOC), 2010,doi:10.1109/ECOC.2010.5621248.
2. P. Ji, Y. Aono, Colorless and directionless multi-degree reconfigurable optical add/drop multiplexers, Wireless and Optical Communication Conference (WOCC), 2010,doi:10.1109/WOCC.2010.5510664.
3. R. Jensen, A. Lord, N. Persons, Highly scalable oxc-based contentionless roadm architectures with reduced network implementation costs, Optical Fiber Communication Conference and Exposition (OFC/NFOEC), 2012,.
4. J. Pedro, S. Pato, Towards fully flexible optical node architectures: Inpact on blocking performance od dwdm transport networks, Transparent Optical Networks (ICTON), 2011,doi:10.1109/ICTON.2011.5970863.
5. M. Klinkowski, K. Walkowiak, Routing and spectrum assignment in spectrum sliced elastic optical networks, IEEE Communications Letters 15 (2011) 884–886. doi:10.1109/LCOMM.2011.060811.110281.
6. S. Kozdrowski, S. Sujecki, Optical node architectures in the context of the quality of service in optical networks, IARIA 2018 The Tenth International Conference on Advanced Service Computing (Brarcelona 2018) 57–60. doi:ISBN: 978-61208-606-4.
7. A. de Sousa, A. Tomaszewski, M. Pióro, Bin-packing based optimization of eon networks with s-bvts, Optical Network Design and Modeling International Conference, 2016 24. doi:10.1109/ONDM.2016.7494082.
8. M. Klinkowski, M. Żotkiewicz, K. Walkowiak, M. Pióro, M. Ruiz, L. Valasco, Solving large instances of the rsa problem in flexgrid elastic optical networks, IEEE/OSA Journal of Optical Communications and Networking, 8 (2016) 320–330. doi:10.1364/JOCN.8.000320.
9. A. Cai, G. Shen, L. Peng, M. Zukerman, Novel node-arc model and multiiteration heuristics for static routing and spectrum assignment in elastic optical networks, Journal of Lightwave Technology 31 (2013) 3402–3413. doi:10.1.1.718.3148.
10. B. Korte, J. Vygen, Combinatorial optimization. theory and algorithms,, Springer-Verlag 5 ed.
11. K. Christodoulopoulos, I. Tomkos, E. A. Varvarigos, Elastic bandwidth allocaton in flexible ofdm-based optical networks, IEEE Journal of Lightwave Technology 29 (2011) 1354–1366. doi:10.1109/JLT.2011.2125777.
12. Y. Wang, X. Cao, Q. Hu, Y. Pan, Towards elastic and fine-granular bandwidth allocation in spectrum-sliced optical networks, IEEE/OSA Journal of Optical Communications and Networking 4 (2012) 906–917. doi:10.1364/JOCN.4.000906.
13. http://sndlib.zib.de/home.action.

Two approaches for the computational model for software usability in practice

Eva Rakovská and Miroslav Hudec
Faculty of Economic Informatics, University of Economics in Bratislava;

Abstract. Rapid software development and its massive deployment into practice brings a lot of problems and challenges. How to evaluate and manage the existing software in an enterprise is not an easy task. Despite different methodologies in IT management, we encounter problems with how to measure usability of software. Software usability is based on user experience and it is strongly subjective. Every IT user is unique, so the measurement of IT usability has often qualitative character. The main tool for such measurement is survey, which maps her or his needs of daily work. The article comes from experimental study in the medium-sized company. It was based on the idea of using rule-based expert system for measurement of software usability in enterprises. Experimental study gave a more detailed view into the problem; how to design the fuzzy-rules and how to compute them. The article points to problems in designing a computational model of software usability measurement. Thus, it suggests a computational model, which is able to avoid the main problems arising from experimental study and to deal with uncertainty and vagueness of IT user experience, different number of questions for each users group, different ranges of categorical answers among groups, and variations in number of answered questionnaires. This model is based on the three hierarchical levels of aggregation with the support of fuzzy logic.

The full text will be available in the edited book “Information Technology, Systems Research and Computational Physics”, eds. Kulczycki P., Kacprzyk J., Kóczy L.T., Mesiar R., Wisniewski R., to be published by Springer in the *Advances in Intelligent Systems and Computing* series soon.

Content-based recommendations in an e-commerce platform

Łukasz Dragan and Anna Wróblewska
Faculty of Mathematics and Information Science,
Warsaw University of Technology, ul. Koszykowa 75, 00-662 Warsaw, Poland;

Abstract. Recommendation systems play an important role in modern e-commerce services. The more relevant items are presented to the user, the more likely s/he is to stay on a website and eventually make a transaction. In this paper, we adapt some state-of-the-art methods for determining similarities between text documents to content-based recommendations problem. The goal is to investigate variety of recommendation methods using semantic text analysis techniques and compare them to querying search engine index of documents. As a conclusion we show, that there is no significant difference between examined methods. However using query based recommendations we need more precise meta-data prepared by content creators. We compare these algorithms on a database of product articles of the biggest e-commerce marketplace platform in Eastern Europe - Allegro.

The full text will be available in the edited book “Information Technology, Systems Research and Computational Physics”, eds. Kulczycki P., Kacprzyk J., Kóczy L.T., Mesiar R., Wisniewski R., to be published by Springer in the *Advances in Intelligent Systems and Computing* series soon.

Analysis of dispersive part of AC magnetic susceptibility measurement of high-temperature superconductors by means of neural network

Marcin Kowalik, Waldemar Tokarz, Andrzej Kołodziejczyk, Marek Giebułtowski,
Ryszard Zalecki, Wiesław Marek Woch

AGH University of Science and Technology, al. Mickiewicza 30, 30-059 Kraków, Poland
`mkowalik@agh.edu.pl`

Abstract. This paper demonstrates the results of neural network application for analysis of temperature dependent, dispersive part of dynamic susceptibility for the granular, polycrystalline high-temperature superconductors. The goal of neural network is to classify a small section of single measurement and to find out if in this particular section a beginning of superconducting transition is present, from which the value of critical temperature T_c could be estimated.

Keywords: High-temperature superconductors, critical temperature, neural networks applications

1 Introduction

A superconductor is a material, which cooled below certain temperature, called critical temperature T_c, has exactly zero electrical resistance. Below T_c also expulsion of external magnetic field from inside of superconductor material is observed which is called a Meissner effect. The critical temperature T_c is the most basic characteristic of the superconducting material [Tinkham 1996]. In 1986 Bednorz and Müller discovered that cuprate-perovskite ceramic material Ba-La-Cu-O is superconducting near 30 K. [Bednorz 1986]. Year later superconductivity transition between 80 K and 93 K was observed in the Y-Ba-Cu-O system at ambient pressure by American scientists [Wu 1987]. Research in the follow 30 years has led to the discovery of numerous cuprate superconductors that belong to several families with T_c up to 134 K for $HgBa_2Ca_2Cu_3O_9$ at ambient pressure [Schilling 1993] and 164 K under 30 GPa [Gao 1994]. These ceramic materials with high value of T_c became known as High Temperature Superconductors (HTS).

In the last several years the neural networks (NN) demonstrated the ability to classify with a very high degree of accuracy sets of labeled data [Rosenblatt 1958, Nielsen 2017]. The neural network with ease can properly recognize and classify handwritten digits or letters [LeCun 2018], classify phases in condensed matter physics [Ch'ng 2017] or even classify stars light curves in searching for Exoplanets [Pearson 2017].

In this paper, we study how well the neural network will perform in classification task of a small section (subpart) of single AC magnetic susceptibility measurement of HTS. The goal of neural network is to find out if in this particular section a beginning of superconducting transition is present, from which the value of critical temperature T_c could be estimated.

2 Experiment and computation

2.1 The AC magnetic susceptibility measurements

The AC magnetic susceptibility can be written as a complex number by the formula:

$$\chi = \chi' + i\chi'' \tag{1}$$

where χ' is the dispersion and χ'' is the absorption part of the dynamic susceptibility. The value of dispersion part corresponds to the diamagnetic nature - a negative magnetization of the HTS sample, when external magnetic field is applied. The value of absorption part corresponds to the energy converted into heat during one cycle of the external, AC magnetic field H_{ac}. For the bulk HTS samples this energy loss is connected with the magnetic field penetration into the intra and inter-granular regions [Gömöry 1997].

The values of χ' and χ'' for HTS change with temperature. Above certain temperature, called the critical temperature T_c, the values of both parts of AC susceptibility are equal to zero. On the other hand, below critical temperature T_c the χ' part has negative values, χ'' is positive or equal to zero. The absolute value of χ' will decreases if temperature raises and increases if temperature lowers, which can be used to define the critical temperature T_c of HTS[Kowalik 2017]. The shapes of χ' and χ'' parts as a function of temperature and the value of T_c are strongly correlated with crystal structure and microstructure of specific HTS material. The AC magnetic susceptibility, next to resistance measurements, is the most important method for characterization the physical properties of HTS materials. Selected examples of AC measurement results and technique of T_c determination are shown in Fig. 1.

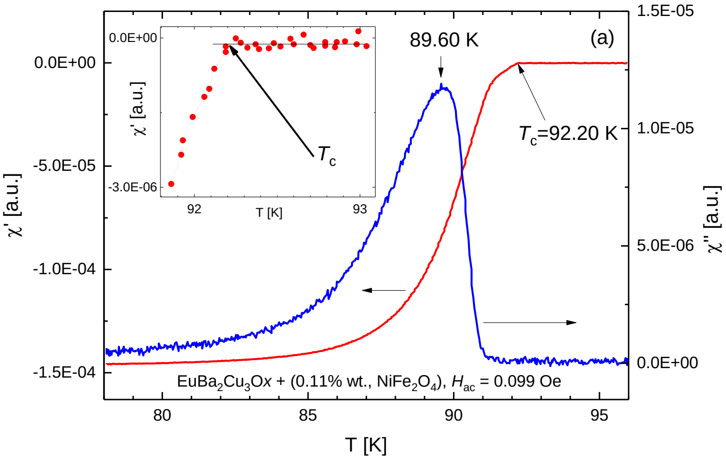

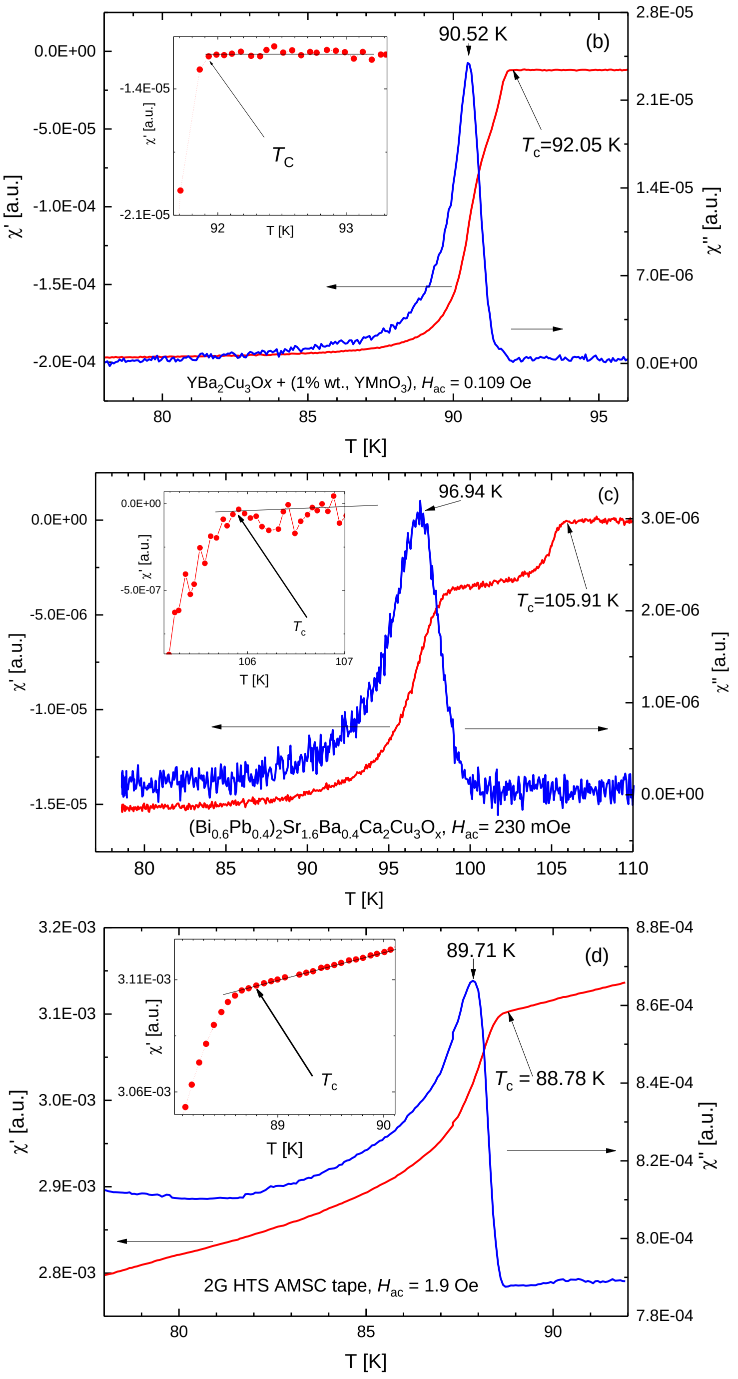

Fig. 1. The selected examples of AC susceptibility measurement results for a) nanocomposite $EuBa_2Cu_3O_x$ + 0.11% wt. nanoparticles of $NiFe_2O_4$, b) mixture of $YBa_2Cu_3O_x$ and 1% wt. $YMnO_3$, c) $(Bi_{0.6}Pb_{0.4})_2Sr_{1.6}Ba_{0.4}Ca_2Cu_3O_x$ and d) 2G (second generation) HTS tape manufactured by AMSC. The tape has multilayer structure and one layer has ferromagnetic properties. The insets shows the estimation of T_c values. The Figs. a), b) and c) shows results for bulk polycrystalline samples, which were prepared by solid state reaction.

Measurements of dynamic magnetic susceptibility as a function of temperature and intensity of the AC magnetic field, ranging up to 10.9 Oe, were made using an inductance bridge consisting of a transmission coil and two detector coils setup in the helium cryostat [Chmist 1991]. A SRS830 DSP Lock-In amplifier was used as a detector and the AC current source at 189 Hz. The temperature was monitored by the Lake Shore Model 330 autotuning temperature controller employing chromel-gold – 0.07% Fe thermocouple with the accuracy of about 0.3 K and resolution of about 0.05 K. The control of the measurements and data acquisition was performed with a computer. The direction of an applied magnetic H_{AC} field was parallel to the longest side of the parallelepipedal HTS sample.

2.2 Dataset

The dataset contains results of AC magnetic susceptibility measurements for HTS like: $YBa_2Cu_3O_x$, $EuBa_2Cu_3O_x$ (REBCO-123, where RE is rare earth element) and $Bi_2Sr_2Ca_2Cu_3O_x$ (BISCO-2223). The measurements were performed as a function of temperature and AC magnetic field H_{ac}. Temperature range for REBCO samples was 77-100K and 77-125K for BISCO. More than 400 measurements were considered. Part of these measurements were analyzed and published in the paper[Peczkowski 2017]. Single measurement had 459 data points on average (median 431) and there were 22 points/K on average (median 21). Every data point had assigned three values: sample temperature, value of χ' and value of χ".

In order to prepare dataset for feeding into neural network for every single result following steps were done: a) the lowest value of χ' was normalized to -1, b) all values of χ" were drop out, c) result with m experimental points was divided into n sections (subparts) of size 10, 20 or 30 data points, according to the formula:

$$n = m - s + 1 \tag{2}$$

where m is number of data points in measurement and s is number of data points in section. Section n_{i+1} included 10, 20 or 30 succeeding data points, starting from i data point. Next, d) every section was classified into one of three classes: class 1 - all data points in section had temperatures below critical temperature T_c, class 2 - all data points in section had temperatures above T_c, class 3 - there were data points in section, which had temperatures below and above T_c and e) temperatures were drop out.

Finally, the dataset, prepared for neural network feeding, consisted of about 200,000 labeled sections. Random set of sections is show on Fig 2.

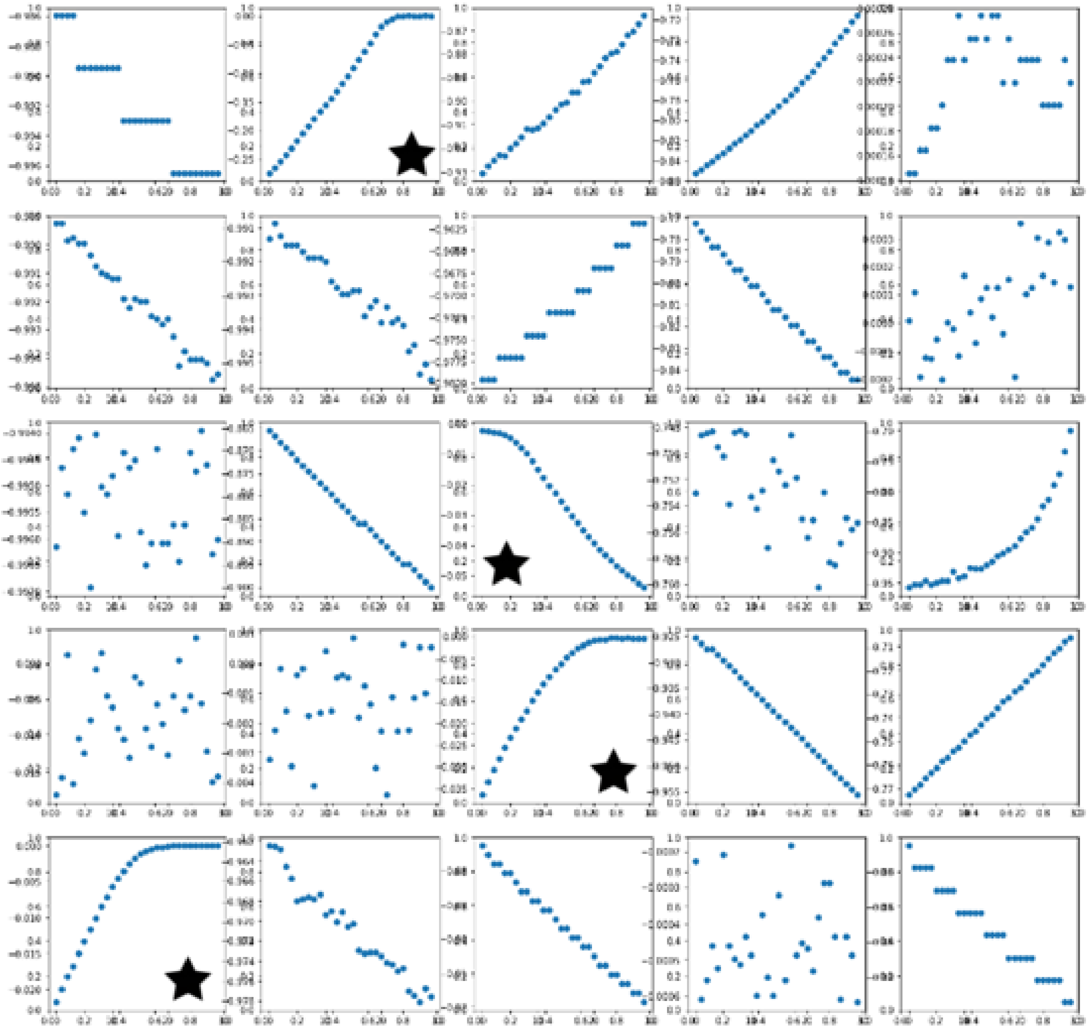

Fig. 2. A random sample of training data with visible differences between sections for the section size of 30 data points. The graphs of sections in which the beginning of superconducting transitions is visible were marked with a star.

2.3 Neural Network Architecture

The deep, feedforward, fully connected neural network architecture was chosen (Fig. 3). The size of input layer was equal to size of section, which is equivalent to number of experimental points in section. We considered sections of sizes of 10, 20 and 30 points. The neural network had two hidden layers marked as $n^{(2)}$ and $n^{(3)}$. Both hidden layers used the tanh activation function. The number of neurons in hidden layers was dependent on size of the section. The layer $n^{(2)}$ had 20 neurons for section size of 10 points, 40 neurons for section size of 20 points and 60 neurons for section size of 30 points. In case of layer $n^{(3)}$ it was 50, 100 or 150 neurons respectively. The last, output layer had three neurons with softmax activation function.

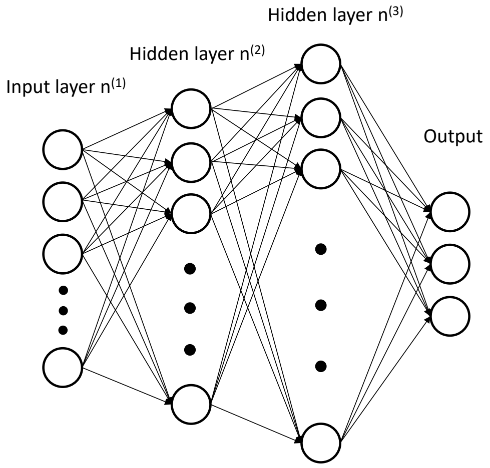

Fig. 3. Architecture of deep, feedforward neural network used to classify a section of χ -dispersion part of AC magnetic susceptibility measurement.

2.4 Training of Neural Network

We employed the TensorFlow package [Abadi 2015] with Keras API [Chollet 2015]. Optimization of the weights of neural network was done by minimizing the loss function, the cross-entropy. The weights in each layer were optimized using a backward propagation scheme. The Adam optimization algorithm was chosen [Kingma 2014]. The parameters of optimizer were set at default values. The dataset was not divided into batches. The training set consisted of 80% sections and the validation set 20%. The neural network was trained by several dozen epochs. Performance for a dozen or so neural networks with different number of neurons in layers n$^{(2)}$ and n$^{(3)}$ were evaluated. Some of the tested NN used two dropout layers, which were placed between layers n$^{(2)}$ and n$^{(3)}$, and between layer n$^{(3)}$ and output layer. The dropout rate was also varied. The details of neural networks architecture and their performance on validation set are shown in Table 1.

Table 1. Selected architectures and performances of tested neural networks

Optimizer	Number of inputs n$^{(1)}$	Number of neurons: n$^{(2)}$, n$^{(3)}$	Activation function for n$^{(2)}$, n$^{(3)}$	Dropout rate: n$^{(2)}$ - n$^{(3)}$, n$^{(3)}$-output	Number of epochs	Value loss	Value accuracy
Adam	10	20, 50	tanh	0, 50	20	0.1542	0.9470
Adam	10	20, 50	tanh	50, 50	20	0.1781	0.9358
Adam	10	20, 50	tanh	0, 0	20	0.1045	0.9702
Adam	10	20, 50	tanh	0.1, 0.1	20	0.109	0.9693
Adam	10	20, 50	tanh	0.05, 0.05	20	0.109	0.9702
SGD	10	20, 50	tanh	0, 0	30	0.1694	0.9389
SGD	10	20, 50	tanh	0, 0	40	0.1704	0.9391
SGD	10	20, 50	tanh	0.2, 0.2	80	0.1789	0.9377
Adam	10	20, 50	sigmoid	0, 0	120	0.0969	0.9719
Adam	20	40, 100	tanh	0, 0	40	0.0958	0.9715
Adam	30	60, 150	tanh	0, 0	40	0.1022	0.9671
Adam	30	60, 150	tanh	30, 30	40	0.1118	0.9645
Adam	30	60, 100	tanh	0, 0	40	0.096	0.9702
Adam	30	50, 100	tanh	0, 0	40	0.1	0.9671
Adam	30	50, 100	tanh	30, 30	40	0.1	0.9671

2.5 Results

We find out that all studied neural network architectures were able to recognize if in small series of data points the beginning of superconducting transition is present. In classification task the best versions of neural networks (see Table 1) achieved an accuracy slightly above 97% for all three section sizes. The section size of 30 data points is sufficient for handmade classification and most important for proper evaluation of T_c of HTS sample. The choice of using the Adam optimization algorithm, which was based on our earlier experiences in training of NN, was a very good one. The performance of Adam was 3% better in comparison with standard method using stochastic gradient descent (SGD). The Adam optimizer also provided the fastest convergence time. The use of two dropout layers decreased accuracy, especially when dropout rate was in range 30-50%, which are a typical values used for deep neural networks learning. This suggests that chosen network architectures was near the optimal one for this classification task. We also tried to use sigmoid activation function instead tanh function. The resulting neural network performed as well as former one (tanh NN), but the convergence time was several times slower.

3 Conclusions

We use an artificial neural network to learn the features of χ' - dispersion part of AC magnetic susceptibility *vs* temperature and applied magnetic field H_{ac} of HTS samples. We found out that our neural network was able to recognize whether the beginning of superconducting transition was present for small series of experimental points. In this classification task an accuracy of about 97% (see Table 1) was achieved. This result allows for extraction just only significant experimental points for determination of real value of critical temperature T_c.

Acknowledgments. This work was supported by the Polish Ministry of Science and Higher Education and its grants for Scientific Research.

References

[Abadi 2015] Abadi, M. et al., TensorFlow: Large-Scale Machine Learning on Heterogeneous Systems (2015), https://www.tensorflow.org/, last accessed 2018/05/15.

[Bednorz 1986] Bednorz, J., G., Müller, K. A.: Possible high T_c superconductivity in the Ba−La−Cu−O system. Z. Phys. B. 64 (1), 189–193 (1986).

[Ch’ng 2017] Ch’ng, K., Carrasquilla, J., Melko, R. G., Khatami, E.: Machine Learning Phases of Strongly Correlated Fermions, Phys Rev X 7, 031038-1–031038-9 (2017).

[Chmist 1991] Chmist, J.: Wpływ technologii na podstawowe właściwości wysokotemperaturowych nadprzewodników typu Y-Ba-Cu-O, Zakład Fizyki Ciała Stałego Instytutu Metalurgii, Akademia Górniczo-Hutnicza im. Stanisława Staszica w Krakowie (1991).

[Chollet 2015] Chollet, F. et al., Keras Homepage, https://keras.io/, last accessed 2018/05/15.

[Gao 1994] Gao, L., Xue, Y. Y., Chen, F., Xiong, Q., Meng, R. L., Ramirez, D., Chu, C. W., Eggert, J. H., Mao, H. K.: Superconductivity up to 164 K in $HgBa_2Ca_{m-1}Cu_mO_{2m+2+\delta}$ (m=1, 2, and 3) under quasihydrostatic pressures. Phys. Rev. B 50(6), 4260-4263 (1994).

[Gömöry 1997] Gömöry, F.: Characterization of high-temperature superconductors by AC susceptibility measurements. Supercond. Sci. Technol. 10, 523–542 (1997).

[Kingma 2014] Kingma, D., P., Ba, J.: Adam: A Method for Stochastic Optimization. CoRR abs/1412.6980, (2014).

[Kowalik 2017] - Kowalik, M., Zalecki, R., Woch, W.M., Tokarz, W., Niewolski, J., Gondek, Ł.: Critical Currents of $(Bi_{1-x}Pb_x)_2Sr_2Ca_2Cu_3O_y$ (x=0.2 and 0.4) Films Deposited on Silver Substrate by Sedimentation. J Supercond Nov Magn 30(9), 2387–2391 (2017).

[LeCun 2018] LeCun, Y., Cortes, C., Burgers, C. J. C., THE MNIST DATABASE of handwritten digits, http://yann.lecun.com/exdb/mnist/, last accessed 2018/05/15.

[Nielsen 2015] Nielsen, M.A.: Neural Networks and Deep Learning. Determination Press, (2015).

[Pearson 2017] Pearson, K. A., Palafox, L.: Searching for Exoplanets using Artificial Intelligence, Workshop on Deep Learning for Physical Sciences (DLPS 2017), NIPS 2017, Long Beach, CA, USA.

[Peczkowski 2017] Pęczkowski, P., Szterner, P., Jaegermann, Z., Kowalik, M., Zalecki, R., Woch, W.,M.: Effects of Forming Pressure on Physicochemical Properties of YBCO Ceramics. J Supercond Nov Magn, (2018).

[Rosenblatt 1958] Rosenblatt, F.: The Perceptron: A probabilistic model for information storage and organization in the brain. Psychological Review 65(6), 386-408 (1958).

[Schilling 1993] Schilling, A., Cantoni, M., Guo, J. D., Ott, H. R.: Superconductivity above 130K in the Hg-Ba-Ca-Cu-O system. Nature 363, 56-58 (1993).

[Tinkham 1996] Tinkham, M., McKay, G.: Introduction to superconductivity. 2nd edn. McGraw-Hill, Inc., New York (1996).

[Wu 1987] Wu, M. K., Ashburn, J. R., Torng, C. J., Hor, P. H., Meng, R. L., Gao, L., Huang, Z. J., Wang, Y. Q., Chu, C. W.: Superconductivity at 93 K in a New Mixed-Phase Y-Ba-Cu-O Compound System at Ambient Pressure. Phys. Rev. let. 58, 908-910 (1987).

A method of Functional Test interval selection with regards to Machinery and Economical aspects

Jan Piesik[1][0000-0002-0883-4830] and Emilian Piesik[2][0000-0002-1618-847X]
and Marcin Sliwinski[3][0000-0001-7577-0526]

[1] Michelin Polska S.A., Leonharda str. 9, 10-454 Olsztyn, Poland
[2, 3] Gdansk University of Technology, G. Narutowicza str.11/12,80-233 Gdansk, Poland
`jan.piesik@michelin.com`

Abstract. This paper discusses the problem of choosing the optimal frequency of functional test, including the reliability calculations and production efficiency, but also the effect of company risk management. The proof test as a part of the functional test interval is well described for the process industry. Unfortunately, this situation is not the case for the machinery safety functions with low demand mode. Afterwards, it is presented current approach of companies, which to pursuing industrial excellence monitor their activity through appropriately selected key performance indicators, which enable, among other things, to increase productivity. In addition, companies are increasingly exploring potential risks in the face of new challenges as a part of sophisticated risk management, including the perception of the enterprise plants as a safe place for work, by customers and business partners. In the elimination of potential risks, the influence of human and its interaction with machines is increasingly taken into account. To illustrate the issue a tire cord twisting machines are used in the case study. In this article, the authors propose a solution in the selection of the functional test interval of safety function and complementary protective measures of machinery as a compromise to obtain satisfactory results regarding safety requirements, productivity indicators and risk management issues.

Keywords: Efficiency enhancement, maintenance engineering, parameter optimization, safety analysis, time-schedule control, tires.

1 Introduction

At present, there is a sharp increase in the requirements and scope that every enterprise manages. Year after year, business requirements set by companies are increasing. Those results in finding further areas which can be better managed to get tangible benefits for the company. One of such areas is planned stoppages for maintenance.

Planned maintenance consists of: functional test, inspection, cleaning, lubrication, planned replacement of elements, e.g. batteries, condition monitoring.

A comprehensive approach to maintenance and effective optimisation is implemented in companies through the implementation of Total Productive

Maintenance (TPM) [1] and the implementation of the Reliability Centered Maintenance (RCM) [17].

At this paper authors concerns on proof tests and functional test optimisation. In the literature, the optimisation of the preventive maintenance stops is widely described. Their optimization is analyzed for cost incurred [20], in short-term cost optimization and long cost optimization [3] as well as time-dependent inspection frequency models [19]. Most of the current articles has focused on the narrow scope of particular cost optimization. At industry, in addition to compliance with the costs, law, safety standards, workplace requirements, increasingly essential interactions between them, and other business-related risks (e.g. brand receipt by customers) are becoming increasingly important. This is something that has been seen in more and more companies. The approach for company management also changes rapidly in recent years. It can be observed in many changes over the years in the standards, e.g. quality management standard, which last version ISO 9001:2015 [8] implement new, additional requirements of interested parties. The certification of this standard become now the basis for business management. However, it still doesn't cover all scope of activities. For that reason, standards ISO 31000 [12], and ISO 22301 [11] was created and covers risk management and business continuity management. The reason for this is that the management process becomes more complex than at the end of the twentieth century and new risks affecting companies are identified. Actual methods presented in the literature does not cover that issues. For the response, the new policy has to be implemented, and approach has to be modified and adapted. The authors in this article present a new integrated approach to this subject, based on well-known methodology presented in international standards [4],[6],[9] and impact of environment and humans aspects to the functional test interval selection. Due to the new risk areas managed by companies, counting the stoppage connected to the functional test interval has also taken into consideration other factors, in addition to the direct costs of stoppages, or the costs of potential defects. Taking into account the wide range of risks in accordance with ISO 31000. It can be stated that the brand good image loss, costs a company (e.g. an accident at work) much more than the cost of additional machine stops associated with the proof test or functional test. Direct costs and efficiency of planned maintenance can be evaluated through Key Performance Indicators (KPIs). The KPIs can be defined according to international standard ISO 22400 [10].

2 Background

The following tests and fault detection help to detect and remove hidden faults in the safety system. We have three possibilities for failure detection [18]:

- failure detection by automatic (diagnostic) self-tests (including operator observation),
- failure detection by functional test (manual test), e.g. proof test,
- failure detection during process requests/shutdowns.

2.1 Proof test

The term proof test is sometimes used interchangeably with the function test, while some authors consider them to be identical, others see them as different and even use other terms such as functional proof test. As it was mentioned the elaborate description about proof test is given in process industry literature and on this basis. The definition of proof test given is a ‘‘periodic test performed to detect failures in safety-related systems so that the system can be restored to an ‘‘as new’’ condition or as close as practical to this condition’’[15]. The need for routine maintenance action to detect unrevealed failures is established by the standard, and the proof test is one of these activities. Those tests should be made in conditions as close as it is possible to normal operating conditions of Safety Requirement Specification (SRS). The test has to include all elements of SRS starting from sensors, by logic controllers up to output devices. The proof test has to be complex what means all elements have to be tested at the same time. The term functional testing as used in IEC-61508 [4] part 7 means to "reveal failures during the specification and design phases to avoid failures during implementation and integration of software and hardware". This consequently means that proof test and functional tests have different meanings. Sometimes because of production specificity, there are made tests only of few elements, what is called partial tests. However, also with rare frequency entire tests has to be done. Differences between them arrive in three most important aspects: frequency of tests, percent of failure detection and need to stop complete installation or made during normal work. The partial tests (e.g. visual inspections) can detect only some system failures. The full tests done mainly during overhauls granted restore the system to full operating condition. According to IEC61508-2 [4], the frequency of proof test will be dependent upon the target failure measure associated with the Safety Integrity Level (SIL), the architecture, the automatic diagnostic coverage and the expected demand rate.

2.2 Functional test

In the article, it is assumed that proof test is one of the functional tests. Functional testing shall include, but not be limited to, verifying the following:

- the operation of all input devices including primary sensors and Safety-Related Electrical Control System (SRECS) input modules;
- logic associated with each input device;
- logic associated with combined inputs;
- trip initiating values (set-points) of all inputs;
- release of alarms functions;
- the speed of response of the SRECS when necessary;
- operating sequence of the logic program;
- the function of all final control elements and SRECS output modules;
- computational functions performed by the SRECS;
- timing and speed of output devices;
- the function of the manual trip to bring the system to its safe state;

- the function of user-initiated diagnostics;
- complete system functionality;
- the SRECS is operational after testing.

For those applications where partial functional testing is applied, the procedure shall also be written to include [15].:

- describing the partial testing on the input and logic solver during operation;
- testing the final element during unit shut down;
- executing the output(s).

There are two ways to minimalise the percentage of planned stops. First is a reduction of the time spent for planned stops what means optimisation and increase the efficiency of works done during those stops. The second way is to maximalist the frequency of planned stops. Finding the root cause of failure mentioned in the previous point can result in the elimination of some checking and planned jobs. The most critical to optimise is the time spent for actions required by the law and other regulations. The fact which cannot be neglected is a key role of maintenance in maintaining the safety at the appropriate level in operation [21], maintenance and repair stage of overall safety lifecycle [4]. After machine commissioning the maintenance department take care of safety aspects [13] as well as cost criteria what has to be done choosing correct maintenance strategy [14].

2.3 Testing methods

There exist three general types of systems testing methods:

- Shutdown testing. Cons of this type of test are that demands stop of the whole installation to perform the test. This inconvenience is much more severe in the process industry, but it also affects in other branches of industry. The second disadvantage is the need to perform the test manually and to record it also manually.
- Bypass testing. On the other hand, for this type of testing, the inconvenience lies in need to disable the safety function during the test and manual testing and to record it manually. The manual test also involves the risk of human error. Moreover, the last item is additional costs for bypass elements.
- Partial stroke testing (PST). Pros for this type of test is that it can be done automatically and registered automatically. Cons is that it does not give absolute certainty about the operation of tested elements.

In the machinery, the most common type of testing is shutdown testing.

2.4 Frequency of test

At start-up, the operation of the safety function is validated but the safety function must be maintained by periodic proof testing. The full proof test performing a safety function is treated as the undesired stopping of the production process which reduces production effectiveness. According to the general safety standard 61508 stated that the proof test interval could be determined based on Average Probability of Failure on Demand (PFD_{avg}) value [4]. According to standard PN-EN ISO 12100:2011 product manufacturer should provide information for end user about the nature and frequency of inspections for safety functions [6]. Unfortunately, in safety manuals frequently can be found no information about proof test frequency or there is a statement that proof test is recommended to be performed at least once per year. The frequently encountered rule is also that Proof Test Interval should not be more than 50% of demand rate. The standards assume that lifetime of the machinery as twenty years. It is based on the assumption that only a few modern systems last more than twenty years without being replaced or rebuilt. It is also assumed that machine controls get at least one proof test during the lifetime.

The proof test is performed as a test of a complete subsystem and not some separate components (subsystem elements) unless the subsystem contains only one element.

Subsystem could include the following elements:

- complex electronic devices, e.g. PLCs,
- electronic devices with the predefined behaviour are, e.g. IO modules,
- electromechanical elements, e.g. relays, contactors.

The obligation for end-user touch three main domain:

- follow the law and regulations,
- follow the safety manuals of the manufacturer of the machines,
- follow the PFD_{avg} and Probability of Failure per hour (PFH) calculations.

The first obligation can be fulfilled partially by applying the rules contained in the Recommendation of Use CNB / M / 11.050 published by European co-ordination of Notified Bodies for Machinery concerning dual-channel safety-related systems with two channels with electromechanical outputs:

- If the safety integrity requirement for safety function is SIL 3 (Hardware Fault Tolerance (HFT) =1) or Performance Level (PL) e (Cat.3 or Cat. 4) then the proof test of this function shall be performed at least every month;
- If the safety integrity requirement for safety function is SIL2 (HFT=1) or PL d (Cat.3) then the proof test of this function shall be performed at least every twelve months.

The excellent example of this recommendation is contactor relays, safety relays, emergency stop buttons, switches which are typically safety devices with electromechanical outputs. Second obligation to perform periodic inspections is given by Directive 2009/104/EC of the European Parliament and of the Council of 16 September 2009 concerning the minimum safety and health requirements for the use of work equipment by workers at work. It is implementation done by national law regulations.

Following the second obligation only in the standard PN-EN ISO 14119 covering interlocks, we can find direct values of test proof interval. For applications using interlocking devices with automatic monitoring, it is stated that for PL e with Category 3 or

Category 4 or SIL 3 with HFT equal one functional test should be performed every month. Moreover, for PL d with category 3 or SIL 2 with HFT=1 functional test should be carried out at least every twelve months [7]. In safety manuals of safety equipment, it can often be found that the producer advises or recommend to make a proof test of the device at least once per year or IEC 61511-1:2016 for the process industry states in clause 16.3.1.3:„ The schedule for the proof tests shall be according to the SRS. The frequency of proof tests for a SIF shall be determined through PFD_{avg} or PFH calculation in accordance with 11.9 for the SIS as installed in the operating environment." [5]. Also, in IEC EN 61508, it is stated that the proof test interval should be based on the PFD calculations [4]. IEC/EN 62061 states that a proof test interval of twenty years is preferred (but not mandatory) [10]. Recently in many safety manuals, manufacturers write that maximum proof test interval in a high demand mode of operation is twenty years.

The third obligation is assuming those written above, generally consider PL ≤ c or SIL 1. Determination of the optimal frequency of testing poses difficulties in many companies. The mathematical approach is not very common and demands a high level of technical knowledge and familiarity with the norms and safety aspects. Determining the level of safety after the modification of equipment and adapt it to the requirements put technical departments in the face of new requirements and problems [16]. It was assumed that the hardware component with the smallest value for the proof test interval determines the proof test time for the subsystem.

Simplified calculation of PFD with perfect proof-test can be obtained as shown below.

$$PFD(t) \approx \lambda_D t \tag{1}$$

where:

λ_D – dangerous failure rate,

t – time.

Assuming that the system is using non-repairable elements in configuration 1oo1, equation receives following form equal :

$$PFD_{avg1oo1} \approx \frac{1}{2}\lambda_{DU}T_I \tag{2}$$

where:

λ_{DU} – dangerous undetected failure rate,

T_I- proof test interval.

Values of the failure probability requirements are required for the whole safety function, including different systems or subsystems. The average probability of failure on demand of a safety function is determined by calculation of PFD_{avg} for all subsystems, which as a whole create safety function.

The end user of the safety-related system has to make an analysis of PFD_{avg} based on the data received from the producer of each part of the safety-related system.

2.5 Key Performance Indicators for production management

The efficiency of production plant can be evaluated through KPIs. This method is widely utilized in many companies. Recently definition of KPIs was defined by international standards, e.g. ISO 22400 [10]. KPIs in manufacturing facilities are ranked according to many categories. Indicators are reflected in the objectives of the plant. They play the role of a performance measure of plant operations. Typically, they are different at different levels of business management. Their right choice often determines the success of the company. KPIs can be implemented in all types of industries, including machinery, continuous and batch processes. Proper selection of indicators allows for quick identification of losses. The key maintenance indicators set out in standard ISO 22301 allow for increased dynamics in maintenance operations.

2.6 Risk Management

As has been presented previously, from year to year can be seen increasing role of quality management in improving business performance. That is due to the fact of strong market competition and similar technical solutions used in machines and processes. In many cases, companies buy machines from external companies, which causes competitors to have the same machine park. Consequently, to be competitive companies are working to improve management efficiency that will increase revenue and hence profits. Analysed by the author's aspects of the management to be effective, must represent all the emerging opportunities and threats. That is a significant change in the analysis approach proposed by ISO 9001: 2015[8]. Due to the changes, the presented in the past management models have been recently enriched by internal and external risk identification. Risk management can be implemented at every level and type of business activity. Risk identification process is the task of finding, identifying, classifying risk sources and dangerous events, taking into account their causes and consequences. Risk identification process can be based on different information sources such as historical expert knowledge, theoretical analysis and emerging risks taking into account stakeholder's needs [2]. As a part of Risk management can also be treated Business Continuity Management described at standard ISO 22301 [11]. In this article, the solution proposed by the authors take into account the results of the analysis of the Risk Management process. This is because many procedural imperatives have their origins in the results of risk analysis. As an example, the instructions which oblige departments to perform a monthly functional test. The frequency of these tests is not based due to risk analysis of safety functions, but rather on risks minimalisation of an accident at work.

3 Proposed solution

As it was presented in previous chapters, a test of machinery issue is not precisely defined taking into consideration three crucial factors:

- law and standards requirements,
- new aspects of risk analysis,
- the increase of productivity.

The proof test objective is to discover critical errors not found by the diagnostics. Definition of proof test frequency is stated as diagnostics of components, sub-systems and whole control systems. Is intended to determine their state in the formulation of the assessment of the willingness to perform safety functions. The proposition consists of two elements:

1. The proposition of test interval for machinery;
2. Method of estimation additional risk influences into proof test frequency for low demand mode.

The first part of proposition helps to increase the productivity of the machines by standardisation of test frequency. The second part takes into account the risks defined by a broader approach to company risk management.

3.1 Estimation of test intervals for machinery

A variety of installation in many industry branches required periodic proof testing and functional tests. In the law and standards, there is a gap in clarifying the frequency of functional, proof tests and shutdowns used for failure detection. It mainly concerns functions with SIL 1. As it is stated in the literature, user defining the functional test has to base on the data delivered by the manufacturer of the machine.

Table 1. Summarised proposition for test intervals of machinery

SIL (EN 62061)	HFT (EN 62061)	Preconized test interval	Source
1	1	1/year	Authors
2	1	1/year	CNB / M / 11.050
3	1	1/month	CNB / M / 11.050

Frequently proof test interval is estimated by the manufacturer to twenty years. The second source of information can be historical data about the frequency of demands for the safety-related action of the Safety Related Part of the Control System. On the basis of those data, the interval can be changed. The first in the order is the authors' proposal presented in Table 1.

3.2 Estimation of identified risks influences into proof test frequency for low demand mode

For some machines equipped with safety function and complementary protective measures working in low demand mode because of construction, the specification of production, ergonomics, lack of space happens that safety functions or complementary protective measures can be activated incidentally, e.g. forklift attacked safety mate, product fall and activate safety line. This provokes that machine stops because of function activation. The more dangerous is the situation, where this function was not activated, and only some mechanical parts were defected. That in future can result in incorrect operation of the safety function. Usually, operators should alert maintenance stuff, and after verification, the machine can be given back for production. This situation has taken place in general but taking into consideration human errors (e.g. damage could not be seen from forklift operator), based on author's analysis quarter of such incidents are not reported. To assure that safety function or complementary protective measures are still able to fulfil its function authors propose to made additional estimation shown in Fig. 1.

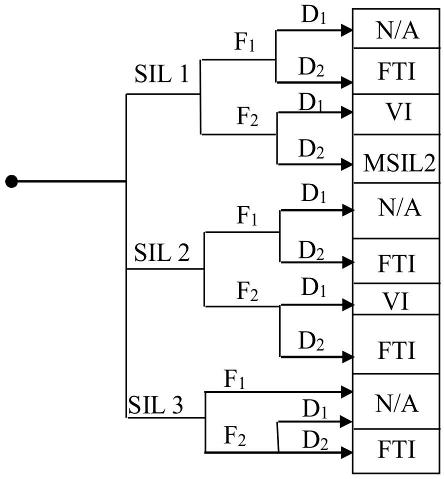

Fig. 1. Graph of additional action estimation for machines working in low demand mode.

where:

Safety Integrity Level: *SIL1, SIL2, SIL3.*

The frequency of unplanned activation of the function: F_1 *- seldom to less often;* F_2 *– frequent;*

The possibility of detection eventual damages without stopping machines/production line: D_1 *- possible;* D_2 *- practically impossible;*

Action: *N/A – No action necessary, VI – Visual inspection, FTI – More Frequent Time interval; MSIL2 – Modification to SIL2;*

Presented analysis took into account three categories: SIL of the system and dived it into three scopes. First for SIL1, the second one for the SIL2, and the third one for SIL3.

The second category is the frequency of such unintended safety function activation. It is divided into seldom and frequent. The third category is the possibility of eventual damages detection without stopping the production line or machine. This category is divided into possible to detect cases and impossible to detect without stop events.

As a result, it can be obtained four possible scenarios. First with lowest risk finish with no actions. The second result is adding into maintenance preventive plan additional visual verification of safety function elements, or complementary protective measures elements state. The term complementary safety measures are used in ISO 12100 standard and are used to avoid or to limit the harm [6]. Example of this can be emergency stop systems. The frequency of that inspection should be not less than twice as often as the period between two proof or functional tests. The third action is requested to modify the elements to fulfil the requirements of SIL2. The last scenario is an increase in the frequency of proof or functional test interval. The frequency of the test should be not less than twice the period between two known accidental activation.

4 Case Study- Production of Semi-Finished Products for tire

For case study was chosen Tire Cord Twisting Machines. After risk analysis (Failure Modes, Effects and Criticality Analysis) were identified one safety function and two complementary protective measures. Safety function protects by restricting access to the cabinet, with rotating elements. The first complementary protective measures function is to secure the hand or forearm by the thread of the textile cord by installing the cable pull safety switch on both sides of the machine. Second is a typical emergency stop button. All functions have estimated SIL1. Based on the manufacturer's data, it can be calculated that each of the given safety function and complementary protective measures has achieved SIL1.

During analysis of productivity looses, one of them - Preventive maintenance time causing the downtime, was identified as one of the leading productivity loss. This indicator shows that every month the company loses one hour of production per month for the machine. In total for all machines of this type, it gives 132 hours yearly lost only for functional tests. In order to improve this result, it was decided to analyse the indicated machines according to the presented above model.

The first complementary measure which secures the hand or forearm by the thread of the textile cord based on a reliability data of elements of this function has functional test equal to service life and equal to twenty years what means that there is no need to perform a proof test of this function. Taking into consideration the facts about risk management was made analysis proposed by the authors.

At the analysis was adopted – SIL1. The analysis of the entries to the Computerized Maintenance Management Application and interviews with both production operators and maintenance workers shows that the unintended activation of the complementary protective measures function by the operator or the product takes place on average once per twelve months. So, it can be qualified to F_1 group. The last criterion of analysis, which is the possibility of defect detection, has been evaluated as practically impossible detection.

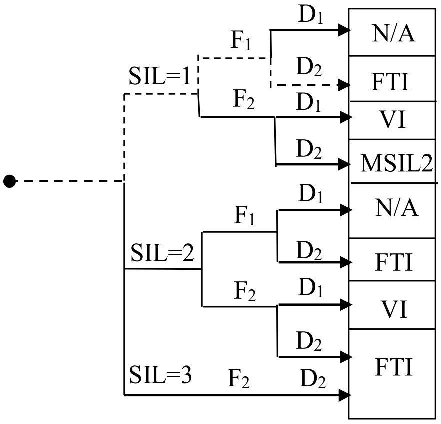

Fig. 2. Graph of additional action estimation for a first complementary measure of cord twisting machines working in low demand mode.

From the estimation of additional action estimation (Fig. 2) can be stated that it is necessary to change time interval of functional test. Taking into account the function activation and damage frequency, at average once every year, the proposition is to double the frequency of the occurrence of activation – what equal six months. In summary, the result of the analysis is the change in interval of functional test time to six months. Profit for the company can be estimated as an additional 110 hours of machines work per year and minimisation of risks identified in risk analyse.

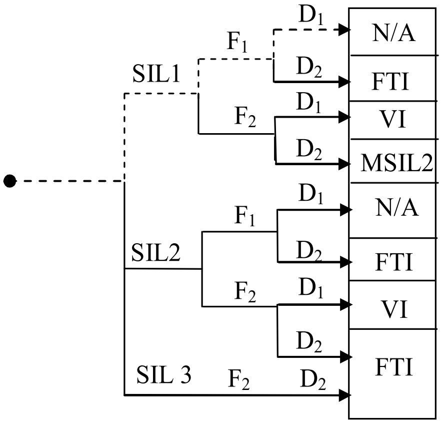

Fig. 3. Graph of additional action estimation for a second complementary measure of cord twisting machines working in low demand mode.

Second complementary measure – emergency stop. The frequency of use is rare, and detection was quantified as possible. For this reason, no additional action is necessary (Fig. 3). Also in this case producer gave T1 value as twenty years. Concluding there is no proof test necessary during lifetime of this function. According to authors proposition (every year test for SIL1) time the functional test of that complementary measure is done in the double frequency as the first one.

Safety function which protects by restricting access to the cabinet has estimated SIL1 based on SIL assignment matrix proposed in the EN 62061 standard. The severity of the injury was estimated as level 3. Frequency and duration with note 3, the probability of hazard event as possible and note 3, avoidance as possible with note 3. Cl=Fr+Pr+Av=3+3+3=9 (Fig. 4).

Severity (Se)	Class (Cl)				
	3-4	5-7	8-10	11-13	14-15
4	SIL2	SIL2	SIL2	SIL3	SIL3
3			SIL1	SIL2	SIL3
2				SIL1	SIL2
1					SIL1

Fig. 4. SIL assignment matrix for the analysed safety function.

Safety function with value SIL1. Analyzing available data was assumed that frequency of unplanned activation is frequent and detection of possible damages is possible without stopping the machine. Following proposed method can be estimated that additional action, in this case, is additional visual inspection (Fig. 5). As the average frequency of unplanned activation or damage was estimated to six months, visual inspection of that element was planned for three months. Manufactures data presents the T_1 value for proof test interval as 20 years. So there is no need to plan an additional test for this element. According to authors proposal, functional test is completed with the frequency of twelve months.

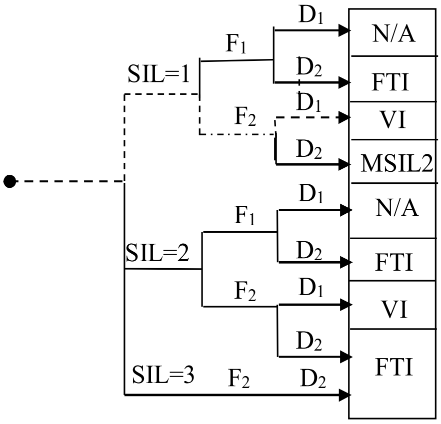

Fig. 5. Graph of additional action estimation for defined safety function of cord twisting machine.

Summarizing achieved results can be stated that by the use of proposed method were achieved two goals.

First, the rules of functional test frequency become clear from a user point of view. Based on risk analysis and manufacturer data, level can be stated required SIL and SIL achieved by the installation. With this information based on Tab. 1 user can stated recommended frequency. This influence into minimalisation of time spends into preventive maintenance. What in consequence increase productivity KPIs.

Second, a graph of additional action estimation helps the user to minimalise additional risks not covered before. The tool is easy in use and can be easily utilised by maintenance or responsible for safety personnel. Implementation of actions defined in proposed graph influence on results of risk analysis made at the different level of company management according to ISO 31000 [12].

5 Discussion

The proposed solution allows providing the required SIL, taking into account aspects of company risk management that are not taken into account when calculating SIL according to the standard IEC 62061 [9]. The method takes into account the UE recommendations and standard regulations. Additional verification or shorter frequency of proof test help minimalise the risk of decreasing in time performance level value. The third important thing is that frequency of different tests is joined to minimalise the stoppages of machines and as a result, minimalise loose of production. Presented above tools is a new approach taking in the account author's experience.

At the same time, it is recommended to perform the analysis of the causes of unintended activation of SIF, in order to eliminate the primary cause of the increased risk. A compelling analysis and subsequent action plan can eliminate the cause, which will result in a return to the regular interval.

6 Conclusions

Management through KPIs is a useful tool for identifying sources of loss of various types as well as monitoring progress in eliminating identified risks. In turn, the tool presented by the authors serves to improve the above-defined productivity KPIs, helps to optimise the functional and proof test interval taking into account specific aspects of risk management. An important issue which has to be underlined is that many manufacturers of safety-related systems assume a lifetime of machinery as the twenty-year mission time. This fact has to be taken into consideration by the user on machines which have already at about twenty years, as they have to prepare for the wear-out stage of systems. Other conditions that could be included with the new versions of the risk management or quality management standards may force changes in the proposed method. The tool has so far been used several times; further tests are needed to confirm its effectiveness in different cases.

References

1. Carannante, T.: The introduction and implementation of TPM using a conceptual model developed in-house – phase I. Maintenance & Asset Management. vol. 18, No 5/6 (2003).
2. Golebiewski, D., Kosmowski, K.T.: Towards a process based management system for oil port infrastructure in context of insurance. Journal of Polish Safety and Reliability Association, Summer Safety and Reliability Seminars, vol. 8, No. 1, 23-38 (2017).

3. Guo, H., Szidarovsky F.,Gerokostopoulos A.,Niu P. On Determining Optimal Inspection Interval for Minimizing Maintenance Cost, Reliability and Maintainability Symposium (RAMS), 2015 Annual. IEEE. Palm Harbour (2015).
4. IEC 61508 1-7:2010: Functional safety of electrical/ electronic/programmable electronic safety-related systems. International Electrotechnical Commission (2010).
5. IEC 61511 1-3:2016: Functional safety – Safety instrumented systems for the process industry sector. International Electrotechnical Commission (2016).
6. ISO 12100-2:2010: Safety of machinery - Basic concepts, general principles for design - Part 2: Technical principles. International Organization for Standardization. Geneva (2010).
7. EN ISO 14119:2013: Safety of machinery - interlocking devices associated with guards - Principles for design and selection, International Organization for Standardization. Geneva (2013).
8. ISO 9001:2015: Quality Management System – Requirements. International Organization for Standardization. Geneva (2015).
9. EN 62061:2005: Safety of machinery – Functional safety of safety-related electrical, electronic and programmable electronic control system. International Electrotechnical Commission. Geneva (2005).
10. ISO 22400: Automation Systems and integration - Key performance Indicators for Manufacturing Operations Management, International Organization for Standardization. Geneva (2014).
11. ISO 22301: Societal security – Business continuity management - Requirements, International Organization for Standardization. Geneva (2012).
12. ISO 31000: Risk management- Principles and guidelines. International Organization for Standardization. Geneva (2009).
13. Kelly, T.P., McDermid, J.A.: A systematic approach to safety case maintenance. Reliability Engineering & System Safety, 71, 271–284 (2001).
14. Lu, L., Jiang, J.: Analysis of on-line maintenance strategies for k-out-of-n standby safety systems. Reliability Engineering and System Safety*,* 92, 144–155 (2007).
15. Norwegian oil and gas. 070 - Norwegian oil and gas application of IEC61508 and IEC 61511 in the Norwegian Petroleum Industry (2004).
16. Piesik, J., Kosmowski, K.T.: Aktualne problemy zarządzania niezawodnością i bezpieczeństwem linii produkcyjnej. Application of computers in Science and Technology 2016. The Scientific Papers of Faculty of Electrical and Control Engineering Gdansk University of Technology. 51. 155-158 (2016).
17. Rausand, M.: Reliability centered maintenance. Reliability Engineering and System Safety, 60, 121–132 (1998).
18. Sintef: Reliability Prediction Method for Safety Instrumented Systems PDS Method Handbook, 2010 Edition. Trondheim (2010).
19. Subhash, M.: Optimal inspection frequency. A tool for maintenance planning/forecasting. International Journal of Quality & Reliability Management. vol. 21, No.7, 763-771. (2004).
20. Vaurio, J.K.: A note of optimal inspection intervals, International Journal of Quality and Reliability Management, 11, 65-68 (1994).
21. Zio, E., Compare, M.: Evaluating maintenance policies by quantitative modeling and analysis. Reliability Engineering and System Safety 109, 53–65 (2013).

Section 4
Data Analysis and Systems Research

Using Random Forest Classifier for particle identification in the ALICE Experiment

Tomasz Trzciński[1], Łukasz Graczykowski[2], and Michał Glinka[1]

[1] Institute of Computer Science, Warsaw University of Technology;
[2] Faculty of Physics, Warsaw University of Technology, Poland;

Abstract. Particle identification is very often crucial for providing high quality results in high-energy physics experiments. A proper selection of an accurate subset of particle tracks containing particles of interest for a given analysis requires filtering out the data using appropriate threshold parameters. Those parameters are typically chosen sub-optimally by using the so-called “cuts" – sets of simple linear classifiers that are based on well-known physical parameters of registered tracks. Those classifiers are fast, but they are not robust to various conditions which can often result in lower accuracy, efficiency, or purity in identifying the appropriate particles. Our results show that by using more track parameters than in the standard way, we can create classifiers based on machine learning algorithms that are able to discriminate much more particles correctly while reducing traditional method’s error rates. More precisely, we see that by using a standard Random Forest method our approach can already surpass classical methods of cutting tracks.

The full text will be available in the edited book “Information Technology, Systems Research and Computational Physics”, eds. Kulczycki P., Kacprzyk J., Kóczy L.T., Mesiar R., Wisniewski R., to be published by Springer in the *Advances in Intelligent Systems and Computing* series soon.

Fault Propagation Models Generation in Mobile Telecommunication Networks based on Bayesian Networks with Principal Component Analysis Filtering

Artur Maździarz

Systems Research Institute Polish Academy of Science, Warsaw, Poland

Abstract. The mobile telecommunication area has been experiencing huge changes recently. Introduction of new technologies and services (2G, 3G, 4G(LTE)) as well as multivendor environment distributed across the same geographical area bring a lot of challenges in network operation. This explains why effective yet simple tools and methods delivering essential information about network problems to network operators are strongly needed. The paper presents the methodology of generating the so-called fault propagation model which discovers relations between alarm events in mobile telecommunication networks based on Bayesian Networks with Primary Component Analysis pre-filtering. Bayesian Network (BN) is a very popular FPM which also enables graphical interpretation of the analysis. Due to performance issues related to BN generation algorithms, it is advised to use pre-processing phase in this process. Thanks to high processing efficiency for big data sets, the PCA can play the filtering role for generating FPMs based on the BN.

The full text will be available in the edited book "Information Technology, Systems Research and Computational Physics", eds. Kulczycki P., Kacprzyk J., Kóczy L.T., Mesiar R., Wisniewski R., to be published by Springer in the *Advances in Intelligent Systems and Computing* series soon.

An efficient model for steady state numerical analysis of erbium doped fluoride glass fiber lasers

Slawomir Sujecki

Department of Telecommunications and Teleinformatics, Faculty of Electronics, Wroclaw University of Science and Technology, Wyb. Wyspianskiego 27, 50-370 Wroclaw, Poland

slawomir.sujecki@pwr.edu.pl

Abstract. The paper presents an efficient model for steady state numerical analysis of erbium doped fluoride glass fiber lasers operating within the near infrared wavelength range. The problem of calculation of photon flux density and populations of electronic state levels within the fiber laser cavity is reduced to a solution of a set of coupled ordinary differential equations. The boundary conditions imposed at the cavity facets result in a two point boundary value which is solved using a relaxation method. A Newton-Raphson method is used to calculate the populations of the energetic levels. The modelling parameters are taken from the literature. A simplified five level model is used for the description of the erbium ion electronic levels, which participate in interactions with pump and signal light. Pump wavelength is set to 980 nm. The results obtained show that the applied numerical technique is stable, efficient and can be readily applied on a standard personal computer.

Keywords: Fiber Laser, Numerical Modelling, Ordinary Differential Equations.

1 Introduction

Fiber lasers due to their superior quality in terms of the output beam brightness and output beam delivery are a preferred choice of a light source for many applications. Therefore large effort is invested into the development of new fiber laser sources. In recent years a particular focus has been given to fiber lasers operating at wavelengths exceeding 2000 nm. These fiber lasers are based on fluoride glass since silica glass has an unacceptable level of light propagation loss for wavelengths larger than 2000 nm. Of particular interest due to the ease of pumping are lanthanide ion doped fluoride fiber lasers. Erbium ion doped fluoride glass fiber laser (EIDFFL) or instance can be pumped with a standard 980 nm laser diode, which has been developed for applications in long distance fiber optic telecom applications. This fact made EIDFFL a subject of intensive research, which resulted in a large number of remarkable achievements. Up until now EIDFFLs with output power as high as 24 W [1] have been realized, peak pulsed power oover 10 kW under Q-switched pulse operation was achieved [2] while the longest operating wavelength for any lanthanide ion doped fluoride glass fiber laser has also been achieved using EIDFFL and is 3680 nm [3]. All these achievements were accompanied by a noticeable design and modelling effort, which was mainly accomplished using time domain models, e.g. [4-11].

In this contribution a model that relies on solving the rate equations and ordinary differential equations describing an evolution of pump and signal power within the laser cavity is presented. The results show a stable operation of the proposed algorithm and also very good computational efficiency.

2 Numerical Model

The energy level diagram for EIDFFL pumped at 976 nm is shown in Fig.1. The pump laser promotes the ions to level 2 via the ground state absorption process and to level 4 from level 2 via excited stated absorption process. The lasing takes place between levels 2 and 1 at the wavelength of 2800 nm. The rate equations can be derived consistently with the energy diagram from Fig.1, [4,6]:

$$\begin{aligned}
&W_{22}N_2^2-\frac{N_4}{\tau_4}+R_{ESA}=0\\
&\frac{\beta_{43}N_4}{\tau_4}-\frac{N_3}{\tau_3}=0\\
&R_{GSA}-R_{SE}-R_{ESA}+\sum_{i=3}^{4}\frac{\beta_{i2}N_i}{\tau_i}-\frac{N_2}{\tau_2}-2W_{22}N_2^2+W_{11}N_1^2=0\\
&R_{SE}+\sum_{i=2}^{4}\frac{\beta_{i1}N_i}{\tau_i}-\frac{N_1}{\tau_1}-2W_{11}N_1^2=0\\
&-R_{GSA}+\sum_{i=1}^{4}\frac{\beta_{i0}N_i}{\tau_i}+W_{22}N_2^2+W_{11}N_1^2=0
\end{aligned}\tag{1}$$

whereby the sum of level populations N_0, N_1, N_2, N_3, N_4, respectively for levels 0, 1, 2, 3 and 4 (Fig.1) is equal to the total doping concentration N. τ_1, τ_2, τ_3, τ_4 give the life times of levels 1, 2, 3 and 4 respectively while β_{xx} give the branching ratios. W11 and W22 are the cooperative up-conversion coefficients for levels 1 and 2, respectively. R_{GSA} gives the ground state absorption rate, R_{SE} gives the rate of stimulated emission between levels 1 and 2 while R_{ESA} gives the rate of the excited state absorption from level 2. The equations (1) are complemented by a set of four ordinary differential equations, which describe the evolution of pump and signal waves. Aligning the fiber with the z axis of the coordinate system allows to write the four differential equations in the following form:

$$
\begin{aligned}
&\frac{d}{dz}P_p^+ = \left(g_p - \alpha_p\right)P_p^+ \\
&-\frac{d}{dz}P_p^- = \left(g_p - \alpha_p\right)P_p^- \\
&\frac{d}{dz}P_s^+ = \left(g_s - \alpha_s\right)P_s^+ \\
&-\frac{d}{dz}P_s^- = \left(g_s - \alpha_s\right)P_s^-
\end{aligned}
\tag{2}
$$

where P_s and P_p are powers for signal and pump, respectively. The superscripts '+' and '-' denote the forward and backward propagating wave respectively. In (2) g_p and g_s denote the gain for pump and signal respectively while α_x gives the value of loss.

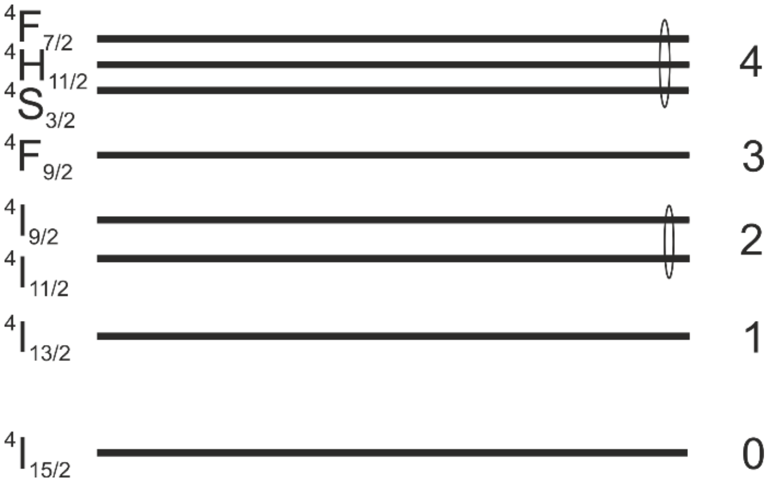

Fig. 1. A schematic diagram of energy levels for erbium ion doped into fluoride glass.

Figure 2 shows a schematic diagram for the considered laser cavity. A beam splitter separates pump and signal waves at the left side of the fiber.

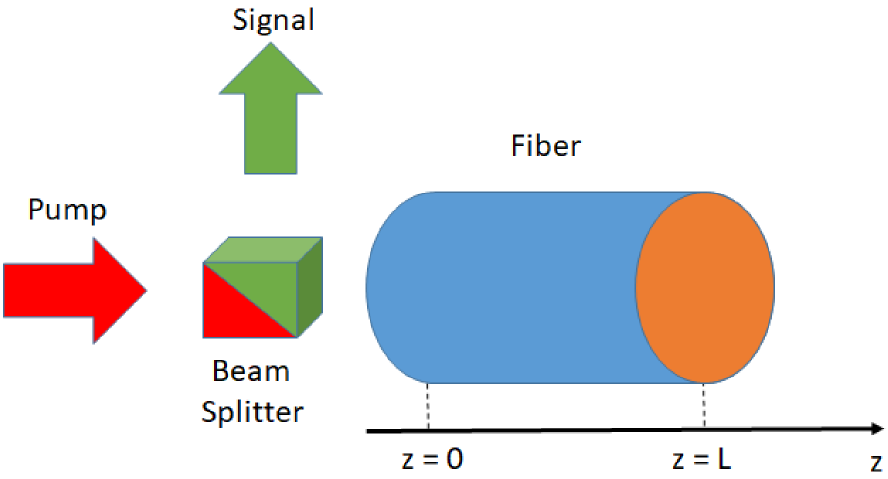

Fig. 2. A schematic diagram of energy levels for erbium ion doped into fluoride glass.

For fiber cavity shown in Fig.2 the set of boundary conditions is:

$$\begin{aligned}
&P_p^+\left(z=0\right)=R_p\left(z=0\right)P_p^-\left(z=0\right)+\left(1-R_p\left(z=0\right)\right)P_{pump}\\
&P_p^-\left(z=L\right)=R_p\left(z=L\right)P_p^+\left(z=L\right)\\
&P_s^+\left(z=0\right)=R_s\left(z=0\right)P_s^-\left(z=0\right)\\
&P_s^-\left(z=L\right)=R_s\left(z=L\right)P_s^+\left(z=L\right)
\end{aligned} \tag{3}$$

where R_s and R_p are the reflectivity for signal and pump, respectively. powers for signal and pump, respectively. The set of ordinary differential equations (2) is solved subject to boundary conditions (3) using a relaxation method and Runge-Kutta 4-5 algorithm. The consistent calculation of the level populations subject to known distribution of pump and signal power is obtained by solving equations (1). As these equations are nonlinear a Newton-Raphson method is applied to solve them. As an initial solution a simplified energy level model neglecting the up-conversion and excited state absorption processes is used. Such approximation reduces the equations (1) to a set of 3 linear algebraic equations, which can be solved analytically, whilst the populations of levels 3 and 4 are equal to zero implicitly.

3 Numerical Results

The modelling parameters are presented in tables 1 and 2. Figs. 3 and 4 show the calculated dependence of the CPU time and output power on the iteration number for typical values of the pump power. The simulations were performed within MATLAB computational environment, in Windows 10 operating system at 64-bit Intel Core i7-6700 processor with CPU clock at 3.4 GHz.

Table 1. Numerical modelling parameters used in simulations.

Quantity	Unit	value
W_{11}	m^3/s	$1x10^{-24}$
W_{22}	m^3/s	$0.3x10^{-24}$
Pump wavelength	nm	976
Pump wavelength	nm	2800
N	$1/m^3$	$9.6x10^{26}$
L	m	1
α_p	1/m	$23x10^{-3}$
α_s	1/m	$3x10^{-3}$
$R_p(z=0)$		0
$R_p(z=L)$		0.96
$R_s(z=0)$		0.04
$R_s(z=L)$		0.96

Table 2. Branching ratios and level lifetimes.

Quantity	Unit	value
τ_1	ms	9
τ_2	ms	6.9
τ_3	ms	0.12
τ_4	ms	0.57
β_{21}, β_{20}		0.37, 0.63
β_{32}, β_{31}, β_{30}		0.856, 0.004, 0.014
β_{43}, β_{42}, β_{41}, β_{40}		0.34, 0.04, 0.18, 0.44

separates pump and signal waves at the left side of the fiber.

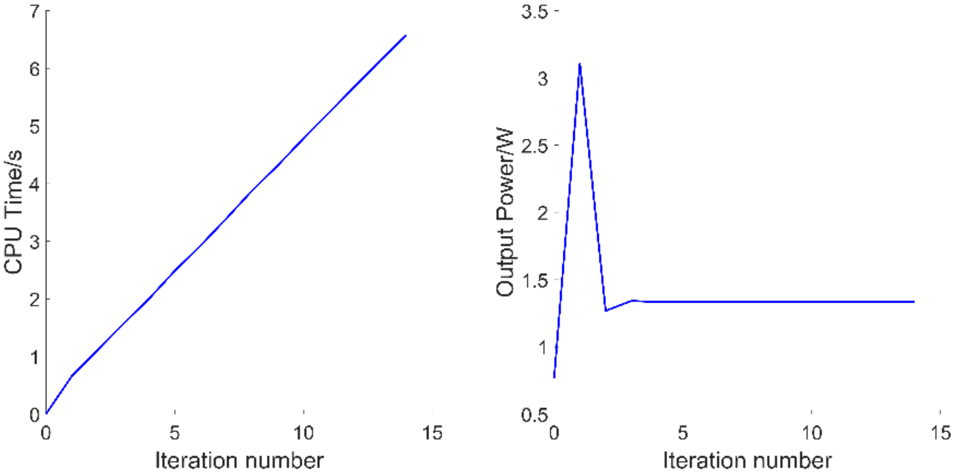

Fig. 3. The dependence of CPU time and Output power on the iteration number at pump power of 5 W.

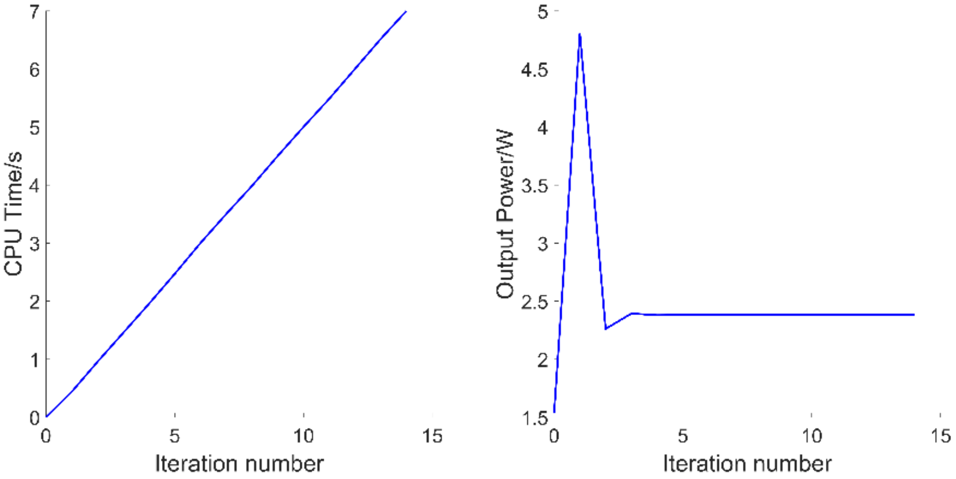

Fig. 4. The dependence of CPU time and Output power on the iteration number at pump power of 10 W.

The results shown in Fig.3 and Fig.4 confirm that using the proposed algorithm results can be obtained at a standard personal computer within several seconds per one bias point. The algorithm behaves in a stable manner and converges to a solution within a couple of iteration steps. These results also confirm that the proposed algorithm is relatively tolerant to an initial guess.

Acknowledgements

The author wishes to thank Wrocław University of Science and Technology (statutory activity) for financial support.

References

1. Tokita, S., Murakami, M., Shimizu, S., Hashida, M. and Sakabe, S.: Liquid-cooled 24 W mid-infrared Er:ZBLAN fiber laser, Optics Letters 34(20), 3062-3064 (2009).
2. Lamrini, S., Scholle,,K., Schäfer, M., Fuhrberg, P., Ward, J., Francis, M., Sujecki, S., Oladeji, A., Napier, B., Seddon, A., Farries, M., and Benson, T.: High-Energy Q-switched Er:ZBLAN Fibre Laser at 2.79 μm, CLEO/Europe-EQEC 2015, Mid-IR fibre laser systems II CJ_7_2, OSA, Munich, 2015.
3. Qin, Z., Xie, G., Ma, J., Juan, P. and Qian, L.: Mid-infrared Er:ZBLAN fiber laser reaching 3.68 μm wavelength,Chinese optics Letters 15(11), 111402 (2017).
4. G. Zhu, X. Zhu, R. A. Norwood, and N. Peyghambarian, Experimental and Numerical Investigations on Q-Switched Laser-Seeded Fiber MOPA at 2.8 mu m, Journal of Lightwave Technology 32(23), 3951-3955 (2014).
5. Sujecki, S. : Simple and efficient Method of Lines based algorithm for modelling of erbium doped Q-switched ZBLAN fibre lasers, J. Opt. Soc. Am. B 33(11), 2288-2295 (2016)
6. J. Li and S. D. Jackson: Numerical Modeling and Optimization of Diode Pumped Heavily-Erbium-Doped Fluoride Fiber Lasers, IEEE Journal of Quantum Electronics 48(4), 454-464 (2012).
7. J. Li, L. Gomes and S. D. Jackson: Numerical Modeling and Optimization of Diode Pumped Heavily-Erbium-Doped Fluoride Fiber Lasers, IEEE Journal of Quantum Electronics 48(5), 596-607 (2012).
8. J. Li, H. Luo, Y. Liu, L. Zhang, and S. D. Jackson: Modeling and Optimization of Cascaded Erbium and Holmium Doped Fluoride Fiber Lasers, IEEE Journal of Selected Topics in Quantum Electronics 20(5),1-14 (2014)
9. M. Gorjan, M. Marincek, and M. Copic, Role of Interionic Processes in the Efficiency and Operation of Erbium-Doped Fluoride Fiber Lasers, IEEE Journal of Quantum Electronics 47(2), 262-273 (2011).
10. M. Pollnau, The route toward a diode-pumped 1-W erbium 3-mu m fiber laser, IEEE Journal of Quantum Electronics 33(11), 1982-1990 (1997)
11. M. Eichhorn, Numerical modelling of Tm-doped double-clad fluoride fiber amplifiers, IEEE Journal of Quantum Electronics 41(12), 1574-1581 (2005)

Image enhancement with applications in biomedical processing

Małgorzata Charytanowicz[1,2], Piotr Kulczycki[1,3], Szymon Łukasik[1,3], and
Piotr A. Kowalski[1,3]

[1] Polish Academy of Sciences, Systems Research Institute,
Centre of Information Technology for Data Analysis Methods;
[2] Catholic University of Lublin, Institute of Mathematics and Computer Science;
[3] AGH University of Science and Technology,
Faculty of Physics and Applied Computer Science, Kraków, Poland;

Abstract. The images obtained by X-Ray or computed tomography (CT) may be contaminated with different kinds of noise or show lack of sharpness, too low or high intensity and poor contrast. Such image deficiencies can be induced by adverse physical conditions and by the transmission properties of imaging devices. A number of enhancement techniques in image processing may improve the quality of the image. These include: point arithmetic operations, smoothing and sharpening filters and histogram modifications. The choice of the technique, however, depends on the type of image deficiency.

In this paper, the primary aim is to propose an efficient image enhancement method based on nonparametric estimation so as to enable medical images to have better contrast. To evaluate the method performance, X-Ray and CT images have been studied. Experimental results verify that applying this approach can engender good image enhancement performance when compared with classical techniques.

The full text will be available in the edited book "Information Technology, Systems Research and Computational Physics", eds. Kulczycki P., Kacprzyk J., Kóczy L.T., Mesiar R., Wisniewski R., to be published by Springer in the *Advances in Intelligent Systems and Computing* series soon.

Efficient Astronomical Data Condensation using Approximate Nearest Neighbors

Szymon Łukasik[1,2], Konrad Lalik[1], Piotr Sarna[1], Piotr A. Kowalski[1,2],
Małgorzata Charytanowicz[2,3], and Piotr Kulczycki[1,2]
[1] AGH University of Science and Technology,
Faculty of Physics and Applied Computer Science, Kraków, Poland;
[2] Polish Academy of Sciences, Systems Research Institute,
Centre of Information Technology for Data Analysis Methods;
[3] Catholic University of Lublin, Institute of Mathematics and Computer Science;

Abstract. Analyzing astronomical observations represents one of the most challenging tasks of data exploration. It is largely due to the volume of the data acquired using advanced observational tools. While other challenges typical for the class of Big Data problems - like data variety - are also present, datasets size represents the most significant obstacle in visualization and subsequent analysis.

The paper studies efficient data condensation algorithm aimed at providing its compact representation. It is based on approximate nearest neighbor calculation using parallel processing. The properties of the proposed approach are studied on astronomical datasets related to the GAIA mission. It is concluded that introduced technique might serve as a scalable method of alleviating the problem of data sets size.

The full text will be available in the edited book “Information Technology, Systems Research and Computational Physics”, eds. Kulczycki P., Kacprzyk J., Kóczy L.T., Mesiar R., Wisniewski R., to be published by Springer in the *Advances in Intelligent Systems and Computing* series soon.

Comparative analysis of segmentation methods and extracting heart features in Cardiovascular MRI

Joanna Świebocka-Więk[1]

AGH University of Science and Technology, Cracov 30-059, PL,
Faculty of Physics and Applied Computer Science
`jsw@agh.edu.pl`,
WWW home page: `http://home.agh.edu.pl/jsw`

Abstract. The aim of the paper is to propose new method of cardiac magnetic resonance (CMR) image segmentation and compare its efficiency with the available methods used for segmentation and feature extraction. The addition goal is to identify defects and benefits of proposed methodology, to check how the algorithm copes with photos captured with the various projections and quality and to verify whether they could be used routinely in medical centers. Following segmentation methods were compared: global thresholding (with manulally selected threshold and mean value threshold), local thresholding, grain growth, area division, area growth and division and deformable models.

Keywords: image segmentation, MRI, medical imaging, cardiology

1 Introduction

Image segmentation is the process of extracting the object (or the region) of interest from the background. Unlike the computer vision systems, the human perception system allows to distinguish and recognize the patterns, shapes and objects in a fully automatic and involuntary way. However modern technology is still and fast developing and results in such a large amount of data that it is not possible for a man to process all captured images and signals in a manually way. Therefore newer and more advanced algorithms for automatic or semi-automatic image segmentation are created and used in computer vision systems in biometrics, face recognition and smile at cameras photographic, motion video games and many others.

Medical imaging is an unique area where the best image segmentation application is extremely needed. Diagnosis and therapy are the huge source of images and data, which require further processing and analysis. Imaging systems such as MRI (Magnetic Resonance Imaging) are used routinely in the study of thousands of patients each year. A single study is a collection of hundreds or even thousands of scans. In addition, the accuracy of segmentation process affects the diagnostic value of the image obtained and the evaluation of the patient's health as well.

Although the physician is able to recognize the individual structures in the image, without their isolation it is not possible to proceed the geometric measurements, which might be crucial process in case of pathological tissues size assessment. It is worth to highlight that any kind on manual segmentation is time-consuming, and time is one of the most critical factors in a patient treatment. The challenge becomes even more complicated when we realize the results of tests using various methods differ, and additionally illustrates the various parts of the body of patients and therefore there is no universal segmentation methods used in medical imaging. Taking this arguments into consideration, it is highly recommended to look for the best and most effective methods of automatic and semi-automatic segmentation methods to support the doctors in their work.

The aim of the paper is to propose new method of cardiac magnetic resonance (CMR) images segmentation and compare its efficiency with the available methods used for segmentation and feature extraction. The addition goal is to identify defects and benefits of proposed methodology, to check how the algorithm copes with photos captured with the various projections and quality and to verify whether they could be used routinely in medical centers. Following segmentation methods were compared: global thresholding (with manulally selected threshold and mean value threshold), local thresholding, grain growth, area division, area growth and division and deformable models.

2 Cardiovascular Magnetic Resonance (CMR)

Imaging of the heart and blood vessels MRI is so popular and common technique that it is isolated from the MRI and Cardiovascular Magnetic Resonance (CMR) imaging. The reason why MRI is so often used in medical practice, is its safety (lack of ionizing radiation), high-resolution images and many options in selecting the best projection. [1]
There are two basic types of sequences giving different output images:

- Gradient Echo Sequence (GE) - blood and fat are white (this technique is often called *white blood imaging*). It has greater use in the functional imaging, for example in the examination of blood flow;
- Spin Echo Sequence (SE) - fat is white, but the blood is black. The sequence is very useful in anatomical imaging techniques

CMR is very useful in diagnosis of a huge amount of diseases, like coronary heart disease (which leads to heart attack), heart failure, cardiomyopathy, the diagnosis of pathological structures within the heart, as well as myocarditis, or pericardial diseases.
The CMR method allows for the selection of any projection during the image acquisition. The radiographer can proceed the heart-section in any direction, but mostly four projections, which have the greatest diagnostic value are in common use: 4-chamber views, 3-chamber views, 2-chamber views, and short axis. . Comparison of these projections were shown in 1. Projections names are

similar to those used in echocardiography. The most common examinations in CMR are performed in all these projections, regardless of the imaging reason The body of the patient can also be imaged on any depth, which allows the cross-sectional views of heart throughout its volume.

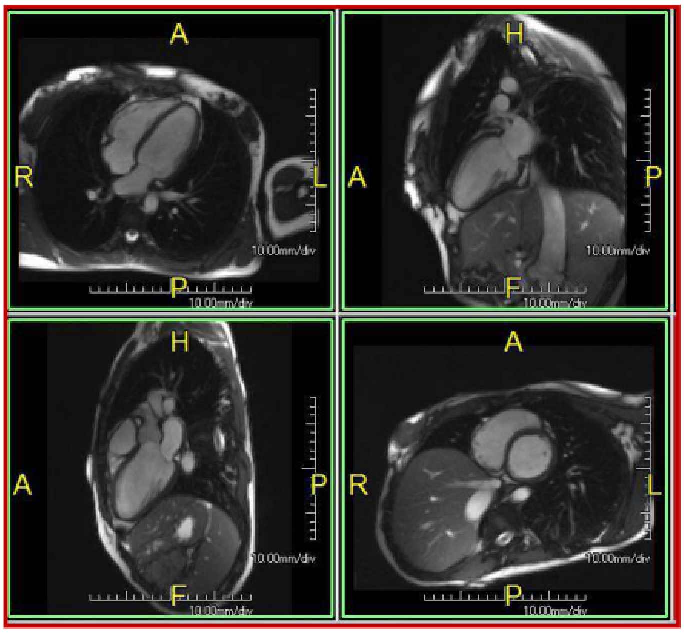

Fig. 1. Cross-section of the heart in four projections: a) four-chamber b) two-chamber c) three-chamber d) short axis [2]

3 Cardiovascular image segmentation

As it was already mentioned, CMR is a type of examination which allows to diagnose a tremendous amount of heart and vascular diseases. In every case the diagnosis is a results of the analysis of different image areas in different projections. That is why it is needed to propose segmentation algorithms, dedicated to extract specific portions of images, depending on the purpose of the study and projection. This observation leads to conclusion that it is not possible to design one, fully universal, generic methods for heart segmentation of the heart, which could be implemented in all medical cases. According to the *American Heart Association*, in CMR images analysis it is possible to distinguish 9 segments within the left ventricle itself for diagnostic purposes, while even 400 for research purposes. However, literature studies proved the optimal number of left ventricular parts, which provides diagnostic capabilities is 17.
This scheme of segmentation, which is widely used is shown in Figure 2. Fully automatic and universal algorithm should be able not only to isolate the interior cavity of the heart and the wall, but also to divide cardiac muscle depending on the depth of the section to the indicated segments.

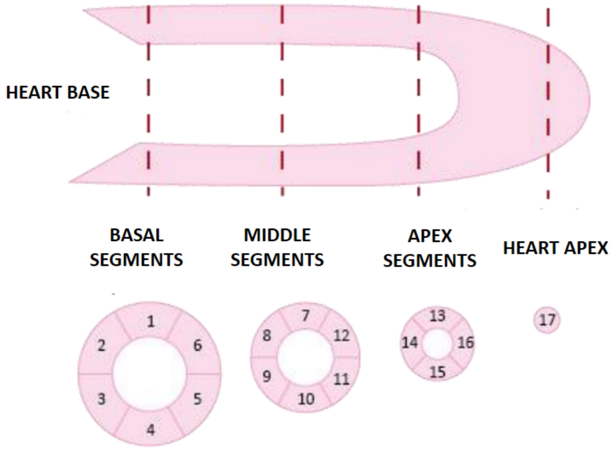

Fig. 2. 17-segment scheme of the segments distribution of left ventricle in cardiac muscle (recommended by the American Heart Association, based on [1][3])

4 Implementation

Following the generally accepted trend of software development and cross-platform solutions, all algorithms were implemented in JavaScript (compliant with the ECMA Script 5 standard), and as the core of different algorithms the application *DWV* was used [5]. It is mainly used for parsing and displaying images in DICOM format. Additionally, the application provides the basic tools of analysis and image processing, such as zoom in, zoom out; manipulation of contrast and brightness. he code is written in JavaScript, allowing it to run in most web browsers, both desktop and mobile devices, and applications on the desktop (using web-view). To view the content HTML5 (rendering elements, composition) and CSS3 (styling) was used. In application, the external libraries were also applied (jQuery with jQuery Mobile, KineticJS, magic-wand-js).

5 Comparison of different segmentation methods

Images All methods were tested on 2 images shown in Figure 3. Selected projection (4-chamber) was chosen, and for this projection 2 images, related with the heart phase were taken into consideration: end-diastolic and end-systolic. Both projections have significant diagnostic value. This choice allows to confront compared methods with some difficulties related with cardiac images segmentation:

- various projections are characterized by the different, very specific heart shapes,
- in each projection, size, shape, and the location of anatomical structures in heart is changing,
- research images have often low diagnostic value.

The purpose of each method to extract the left ventricle from the image. That is why in Figure 3, the specific region of extraction were marked. The contours were determined manually using the tool *live wire*, available in the software DWV [5]. This tool allows to create an active contour selecting consecutive, belonging points (user is pointing to the points, while the contour between them is dynamically created by the program). In case of each image, contours correctness has been verified and approved by the medical physicist with experience in segmentation of medical heart images (expert knowledge).

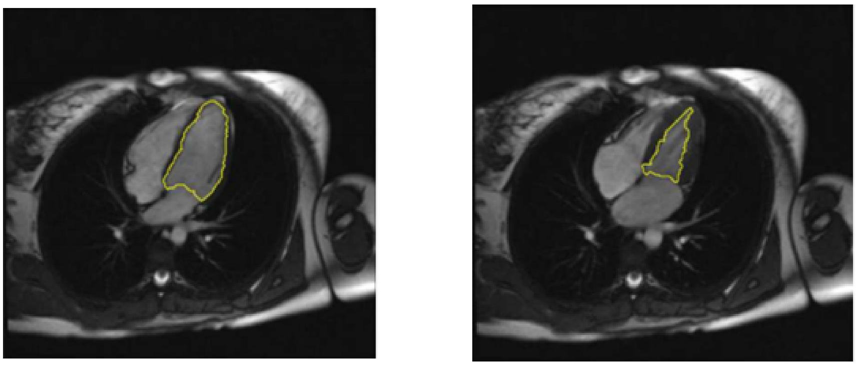

Fig. 3. Images of the heart used to compare methods of segmentation with marked reference areas: 4-chamber diastolic (left), 4-chamber systolic (right) (based on [4]

6 Results

For each of the contour marked in Figure 3 the field was calculated. These fields will be treated as a reference to compare with contours and field calculated after using proposed segmentation algorithms. Two other metrics which be helpful in algorithms evaluation ant their comparison is the percentage of pixels redundant pixels and undersized (not marked). The application of these two parameters is essential because during the comparison between reference image and image after segmentation it might occur that in both cases area limited by contour are similar yet offset related to each other or have slightly different shapes. This problem was illustrated in Figure 4

Therefore, comparison of algorithms is a sum of two kinds of evaluation: a qualitative assessment (visual) proceed by a high qualified and experienced in image segmentation person and quantitative one, implemented according to the following procedure with the following procedure:

- For each image (n) we determined a reference field (in pixels) limited by contour (Pn), based on Figure 3
- For each of the algorithms (x), and selected image (n), we extracted an area after segmentation and calculated its filed (P_{nx}). Next we verify its

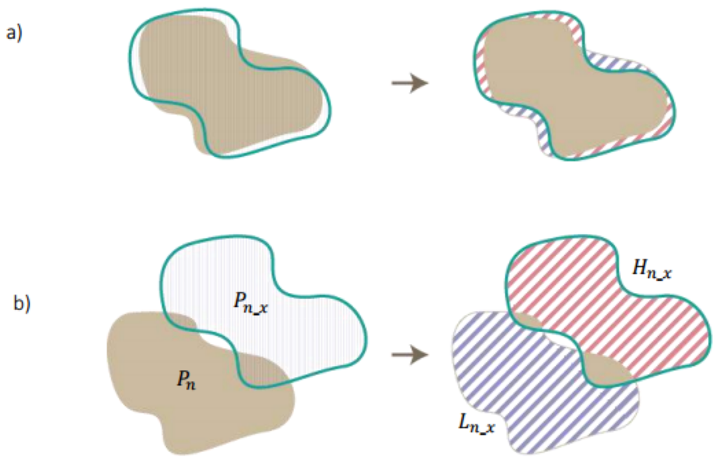

Fig. 4. The ratio of the fields and the percentage of coverage. Brown shape of a reference area, a green outline of the designated area. The red lines indicate redundantly marked pixels, blue pixels lines not covered by the designated area (undersized) a) both areas have similar field, while a small number of pixels differing in both areas; b) contours are shaped like a painting), so their fields are very similar, while the percentage of coverage is negligible - there is a very large number of redundant pixels and unselected. On this basis, not only qualitatively but also quantitatively determine the contour in the case of a) is closer to the reference

correlation to the corresponding area in the reference image (if the algorithm has identified a few areas, only the largest one is taken into consideration as the one who assures maximum possible correlation).

- We set the number of pixels selected redundantly (H_{nx}) and undersized (L_{nx}),
- Based on this parameters we proposed the similarity coefficient, which allows for quantitative assessment of compliance of designated areas. Individual members should be as small as possible (ideally 0), so the whole metric - the closer to 0, the better the result:

$$S_X = \frac{|P_{nx} - P_n|}{Pn} + \frac{H_{nx}}{P_n} + \frac{L_{nx}}{P_n} \tag{1}$$

- It was assumed that the uncertainty of the reference field is equal to 0, while the uncertainty of other variables are based on the uncertainty of a measuring instrument (graphic program). Each pixel in DICOM format results in 26 pixels screenshot displayed in a graphics program and on the basis of this the uncertainty is calculated as:

$$u(P_{nx}) = u(L_{nx}) = u(S_{nx}) = \frac{26px}{\sqrt{3}} \tag{2}$$

According to the right of uncertainty transfer:

$$u(S_{nx}) = \sqrt{\left(\frac{\delta S_{nx}}{\delta P_{nx}} u(P_{nx})\right)^2 \left(\frac{\delta S_{nx}}{\delta H_{nx}} u(H_{nx})\right)^2 \left(\frac{\delta S_{nx}}{\delta L_{nx}} u(L_{nx})\right)^2} \tag{3}$$

This metric is not resistant to rotation or scaling areas, however it is not relevant: both contours are determined on the basis of the same image, in the same scale, and the image was not subject to any rotation. All fields (measured as a number of pixels) were calculated using a graphics program for the output of DWV application). In a consequence their size and the resolution was much larger than the size of DICOM images (256 x 256 pixels). However, the proportions are retained, and so the use of metrics relative to the reference field and contour allows to receive the absolute value independent form the resolution in the final image.

6.1 Global thresholding (manually selected threshold)

In Figure 5 the images obtained after of global thresholding were shown. There is no clear border between the atrium and ventricle. Thus, the left ventricle and left atrium was extracted as a one final structure.

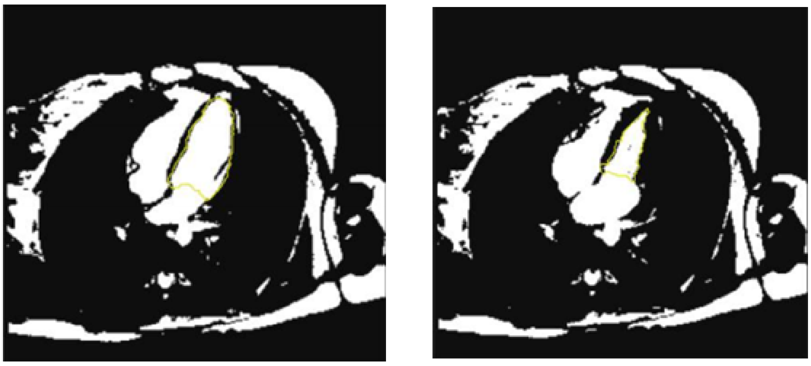

Fig. 5. The resulting 4-chamber images after the application of a global thresholding imposed predetermined threshold the image selected individually. Yellow marked for reference contour of the left ventricle. The applied thresholds: 110 Diastolic (left) and systolic (right)

6.2 Global thresholding (mean value as threshold)

In Figure 6 the results of images global thresholding with mean value as threshold were shown. The algorithm handled with all images registered in short axis projection (left ventricle is surrounded by much darker myocardium). In other case large areas were extracted without detailed structures.

6.3 Local thresholding

Local thresholding (threshold for a given pixel was the mean of the surrounding pixels) gave unsatisfactory results, therefore the calculation of metrics for

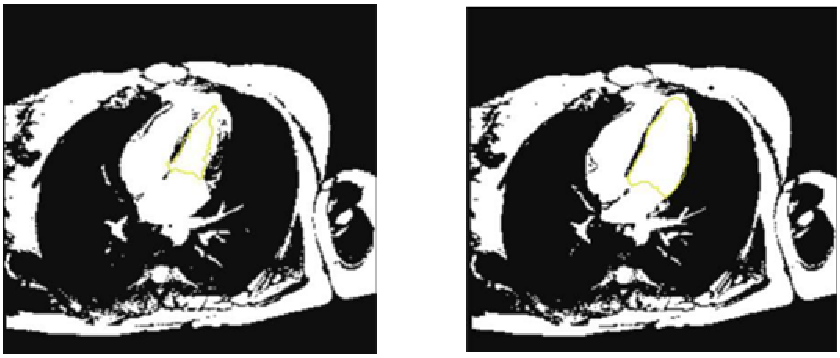

Fig. 6. The resulting 4-chamber images after applying thresholding global threshold for being average with pixel intensity values. Yellow marked for reference contour of the left ventricle.Diastolic (left) and systolic (right)

comparison was pointless. The tremendous effect of oversegmentation and inappropriately large amount of small areas caused blurring the information about the objects in the image. Some of characteristic results were shown in Figure 7

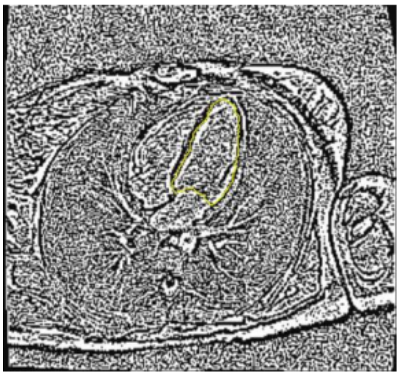

Fig. 7. The resulting images for the local thresholding - you can see the oversegmentation effect. The pictures of the yellow reference contours. 4-chamber diastolic.

6.4 Grain growth

In Figure 8 the results of grain growth method were shown. The precised choosing of a starting point and selecting a proper threshold (for homogeneity test) required generation of many images. The algorithm gave satisfactory results in case of short axis projection (the contour of the left ventricle is clear, and the contrast relative to the surrounding myocardium is high). In all three cases, extracted area did not exceed the reference contour. In case of 4-chamber projection once again we had a problem of separation of the left ventricle and left atrium (there is no clear border between). For lower quality images there were significant fluctuations in intensity levels within the structure of the heart. The grain growth algorithm is a sensitive method what manifested in very strong oversegmentation effect.

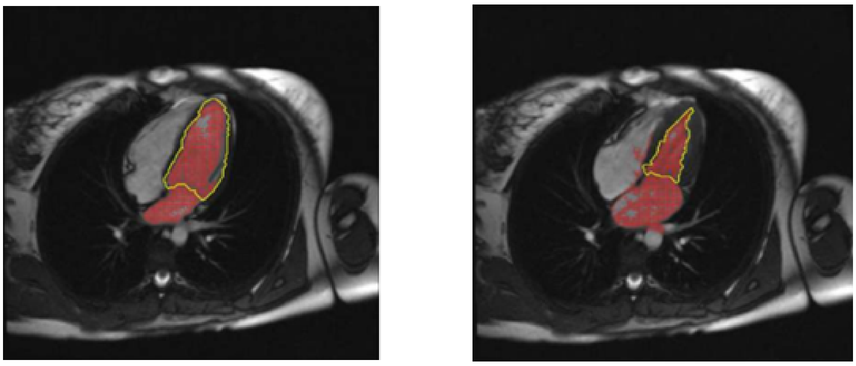

Fig. 8. The effects of grain growth algorithm for the left ventricle (the homogenous test). It was assumed that the absolute value of the intensity difference with respect to the initial pixel does not exceed a certain threshold. It has been arbitrarily chosen (as starting point equals to 45), 4-chamber diastolic (left) and systolic (right)

6.5 Area division

The area division method is not resistant for oversegmentation effect and has low resolution. Figure 9 shows the results; in each case the imperfection of the method can be seen. In left ventricle, there are several major areas extracted (lack of one major area). The algorithm assigns separate color for each found areas. For each image, the homogeneity test was proceed. It was based on a comparison of pixel intensity to the mean intensity of the area - if more than 10% of the pixels has exceeded the tolerance threshold (set individually for the each area), then it was divided in the next iteration. It allows to detect one of the drawbacks of the method - if the searched object (or tissue) is not entirely placed in one of the image parts after division in the 1st iteration, it is a small chance that it will be extracted correctly (in the first iteration it is cut by the areas border).

6.6 Area growth and division

In the case of growth and dividing algorithm the results are similar to the division method. Influence of the "growth" step is particularly visible in the case of large, homogenous areas, such as background. Inhomogeneity in left ventricle and its small size caused denser, separable segments. The homogeneity was proceed (as in the case of division method). The resulting images with the applied reference contour was presented in Figure 10.

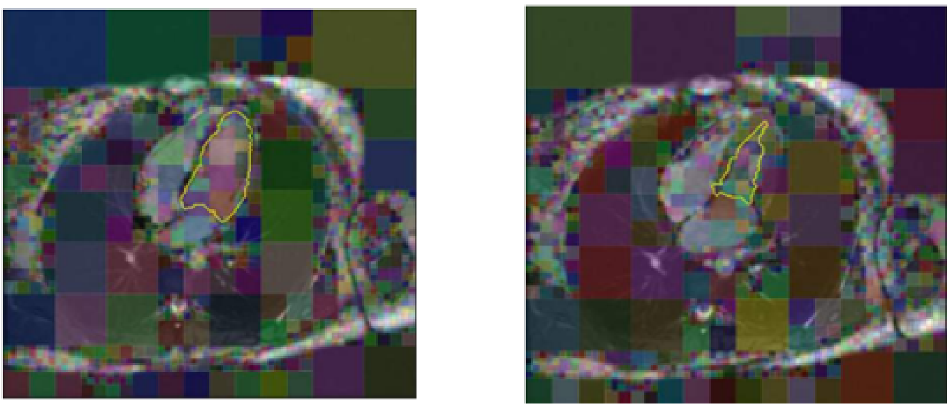

Fig. 9. The resulting images for the method of dividing the area; it shows a strong over-segmentation effect. For each image the individual threshold was used for homogeneous test, thresholds=60 (4-chamber diastolic (left) and systolic (right))

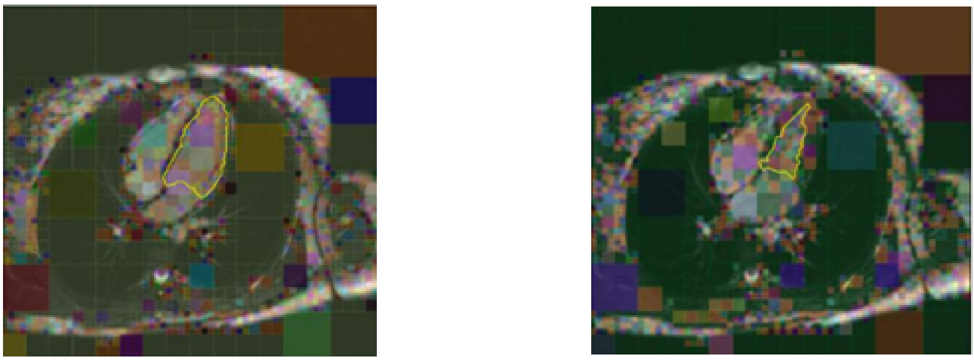

Fig. 10. The results of the growth and division of the area algorithm. Background is homogenous, and within the left ventricle in each case we can see a large number of small surfaces (heterogonous structure). Threshold=30, 4-chamber diastolic (left) and systolic (right)

6.7 Deformable models method

For all examined methods, the deformable model algorithm gave the best results (showed in Figure 11). All input images were preprocessed (Gaussian blurring). There is strong correlation between calculated and reference field (contours are covered). Some disadvantage of this method might be the fact that starting point is needed as one of the input parameters to contour evolution. What is more threshold is individual for each image. Time computational and algorithm complexity is also higher.

7 Conclusions

The expert rating of the resulting images showed that the best and most effective algorithm is deformable model. The main reason is its ability to adapt to

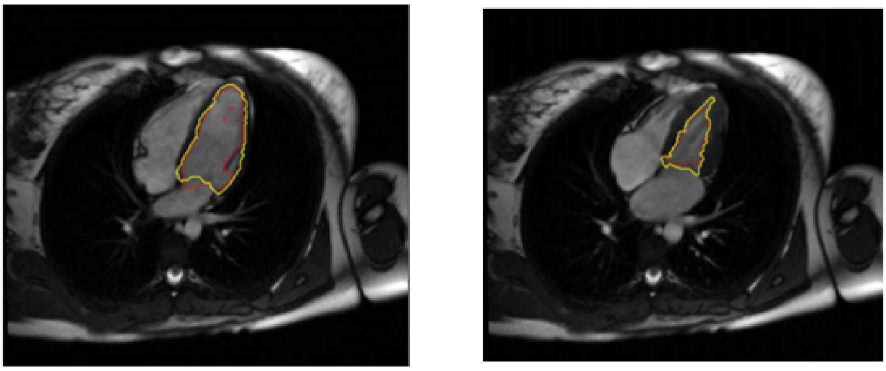

Fig. 11. The results of deformable model algorithm- a red outline with yellow contour reference. In all cases, the two areas are very close to each other. 4-chamber diastolic (left) and systolic (right)

the image content, and resistance to oversegmentation process, which was major drawback. However it needs a starting point as an initial condition what might be considered as some disadvantage.

Little worse, but still acceptable results were given by the grain growth method. This method is more simple than the previous one and it takes similar actions, however it is less resistant to image structure and content . The applied homogeneity test was checking only the difference between the initial and processed pixel intensities. As a result, some heterogeneous of the segmented structures were omitted. In this method, the structure edges are also more sharpened and there are some losses inside the structures which may be seen in the image as partial filling of the left ventricle (the round shape of the segmented structures was not forced like in case of deformable model application). Choosing the initial point is also part of the procedure.

Global thresholding with manually selected threshold was also effective; after segmentation of left ventricle, left atrium was also extracted.

Unfortunately, applying a threshold counted as a mean pixel intensity gave unsatisfactory results. In both cases, the both ventricles and atria area of the heart was marked. It is worth to highlight that the algorithm would be very effective, if the goal whole heart segmentation . The other algorithms (local thresholding, division of the area, growth and the division of the area) resulted in unwanted, oversegmentation effect which disqualified them from the further analysis and comparison.

In conclusion, it was noted that the most advanced method (deformable model) gave the best results, but it was also the most expensive (computing power, time complexity). On the other hand even the simplest method, such as thresholding with appropriate threshold could give only slightly worse results. The result of segmentation was strongly influenced by the image acquisition conditions and projection.

References

1. Roberts A.,: Human anatomy, Dorling Kindersley, 2014
2. Bogeart J., Dymarkowski S, Taylor A ,: Clinical cardiac MRI, 2nd Edition, Springer, 2012
3. Materials in kindly permission of John Paul, the 2nd Hospital in Cracov and Karol Manijak
4. Cerqueira M. D. et al.,: Standarized Myocardial Segmentation and Nomenclature for Tomographic Imaging of the Heart: A statement for Healthcare Professionals From the Cardiac Imaging Commitee of the Council on Clinical Cardiology of the American Heart Association, Circulation, 2002.
5. https://github.com/ivmartel/dwv (access: 17.05.2018)
6. https://github.com/pmneila/morphsnakes (access 03.05.2018).

Similarity-based outlier detection in multiple time series

Grzegorz Gołaszewski

Division for Information Technology and Systems Research, Department of Applied Informatics and Computational Physics Faculty of Physics and Applied Computer Science, AGH University of Science and Technology;

Abstract. Outlier analysis is very often the first step in data pre-processing. Since it is performed on mostly raw data, it is crucial that algorithms used are fast and reliable. These factors are hard to achieve when the data analysed is highly dimensional, such is the case with multiple time series data sets. In this article, various outlier detection methods (distance distribution-based methods, angle-based methods, k-nearest neighbour, local density analysis) for numerical data are presented and adapted to multiple time series data. The study also addresses the problem of choosing an appropriate similarity measure (L-p norms, Dynamic Time Warping, Edit Distance, Threshold Queries based Similarity) and its impact on efficiency in further analysis. Work has also been put into determining the impact of an approach to apply these measures to multivariate time series data. To compare the different approaches, a set of tests were performed on synthetic and real data.

The full text will be available in the edited book "Information Technology, Systems Research and Computational Physics", eds. Kulczycki P., Kacprzyk J., Kóczy L.T., Mesiar R., Wisniewski R., to be published by Springer in the *Advances in Intelligent Systems and Computing* series soon.

Section 5
Tomography

Multimaterial Tomogrpahy: Reconstruction from Decomposed Projection Sets

László G. Varga
University of Szeged,
Department of Image Processing and Computer Graphics H-6720, Szeged, Árpád tér 2;

Abstract. We propose a reconstruction method for a theoretic projection acquisition technique, where we assume, that the object of study consists of a finite number of material, and we can separately measure the amount of materials along the paths of projection beams. The measurement decomposes the projections for separating materials, i.e., we get a separate projection set for each material (called decomposed projections), and each projection set holds information on one material only. We describe a mathematical formulation where the newly proposed reconstruction problem is formalised by an equation system and show that the model can be solved by equation system-based reconstruction techniques like the SIRT method while maintaining convergence. We test the theoretic setup on simulated data by reconstructing phantom images from simulated projections and compare the results to reconstructions from classical X-ray projections. We show that using decomposed projections can lead to better results from 20 times less projections than classical X-Ray tomography.

The full text will be available in the edited book “Computational Modeling of Objects Presented in Images. Fundamentals, Methods, and Applications”, eds. Barneva R.P., Brimkov V.E., Kulczycki P., Tavares J.M.R.S., to be published by Springer in the *Lecture Notes in Computer Science* series soon.

Sequential Projection Selection Methods for Binary Tomography

Gábor Lékó and Péter Balázs
Department of Image Processing and Computer Graphics, University of Szeged,
Árpád tér 2, H-6720 Szeged, Hungary;

Abstract. Binary tomography reconstructs binary images from a low number of their projections. Often, there is a freedom how these projections can be chosen which can significantly affect the quality of reconstructions. We apply sequential feature selection methods to find the 'most informative' projection set based on a blueprint image. Using various software phantom images, we show that these methods outperform the previously published projection selection algorithms.

The full text will be available in the edited book "Computational Modeling of Objects Presented in Images. Fundamentals, Methods, and Applications", eds. Barneva R.P., Brimkov V.E., Kulczycki P., Tavares J.M.R.S., to be published by Springer in the *Lecture Notes in Computer Science* series soon.

Variants of Simulated Annealing for Strip Constrained Binary Tomography

Judit Szűcs and Péter Balázs
Department of Image Processing and Computer Graphics, University of Szeged,
Árpád tér 2. H-6720, Szeged, Hungary;

Abstract. We consider the problem of reconstructing binary images from their row and column sums with prescribed number of strips in each row and column. In a previous paper we compared an exact deterministic and an approximate stochastic method (Simulated Annealing – SA) to solve the problem. We found that the latter one is much more suitable for practical purposes. Since SA is sensitive to the choice of the initial state, in this paper we present different strategies for choosing a starting image, and thus we develop variants of the SA method for strip constrained binary tomography. We evaluate the different approaches on images with varying densities of object pixels.

The full text will be available in the edited book “Computational Modeling of Objects Presented in Images. Fundamentals, Methods, and Applications”, eds. Barneva R.P., Brimkov V.E., Kulczycki P., Tavares J.M.R.S., to be published by Springer in the *Lecture Notes in Computer Science* series soon.

Section 6
Computational Intelligence

Optimizing Clustering with Cuttlefish Algorithm

Piotr A. Kowalski[1,2], Szymon Łukasik[1,2], Małgorzata Charytanowicz[2,3], and
Piotr Kulczycki[1,2]

[1] AGH University of Science and Technology,
Faculty of Physics and Applied Computer Science, Kraków, Poland;
[2] Polish Academy of Sciences, Systems Research Institute,
Centre of Information Technology for Data Analysis Methods;
[3] Catholic University of Lublin, Institute of Mathematics and Computer Science;

Abstract. The aim of the article is to outline the Cuttlefish Algorithm - a modern metaheuristic procedure - and to demonstrate its usability in data mining problems. Cuttlefish Algorithm is a very recent solution to a broad-range of optimization tasks. In this paper, we utilized this metaheuristic procedure for the clustering problem with Calinski-Harabasz index used as a measure of solution quality. To examine the algorithm performance selected datasets from UCI Machine Learning Repository were used. Furthermore, the well-known and commonly utilized k-means procedure was applied to the same data sets - to obtain broader and independent comparison. The quality of generated results were assessed via the use of the Rand Index.

The full text will be available in the edited book "Information Technology, Systems Research and Computational Physics", eds. Kulczycki P., Kacprzyk J., Kóczy L.T., Mesiar R., Wisniewski R., to be published by Springer in the *Advances in Intelligent Systems and Computing* series soon.

A Memetic version of the Bacterial Evolutionary Algorithm for discrete optimization problems

Boldizsár Túű-Szabó[1], Peter Földesi[2], and László T. Kóczy[1,3]

[1] Department of Information Technology, Széchenyi István University, Győr, Hungary;
[2] Department of Logistics, Széchenyi István University, Győr, Hungary;
[3] Department of Telecommunications and Media Informatics,
Budapest University of Technology and Economics, Budapest, Hungary.

Abstract. In this paper we present our test results with our memetic algorithm, the Discrete Bacterial Memetic Evolutionary Algorithm (DBMEA). The algorithm combines the Bacterial Evolutionary Algorithm with discrete local search techniques (2-opt and 3-opt).

The algorithm has been tested on four discrete NP-hard optimization problems so far, on the Traveling Salesman Problem, and on its three variants (the Traveling Salesman Problem with Time Windows, the Traveling Repairman Problem, and the Time Dependent Traveling Salesman Problem). The DBMEA proved to be efficient for all problems: it found optimal or close-optimal solutions. For the Traveling Repairman Problem the DBMEA outperformed even the state-of-the-art methods.

The full text will be available in the edited book "Information Technology, Systems Research and Computational Physics", eds. Kulczycki P., Kacprzyk J., Kóczy L.T., Mesiar R., Wisniewski R., to be published by Springer in the *Advances in Intelligent Systems and Computing* series soon.

A Hybrid Cascade Neural Network with Ensembles of Extended Neo-Fuzzy Neurons and its Deep Learning

Yevgeniy Bodyanskiy[1] and Oleksii Tyshchenko[2]

[1] Control Systems Research Laboratory at Kharkiv National University of Radio Electronics;
[2] Institute for Research and Applications of Fuzzy Modeling,
CE IT4Innovations, University of Ostrava;

Abstract. This research contribution instantiates a framework of a hybrid cascade neural network rest on application of a specific sort of neo-fuzzy elements and a new peculiar adaptive training rule. The main trait of the offered system is its competence to continue intensifying its cascades until the required accuracy is gained. A distinctive rapid training procedure is also covered for this case that gives possibility to operate with nonstationary data streams in an attempt to provide online training of multiple parametric variables. A new training criterion is examined which suits for handling nonstationary objects. Added to everything else, thereâĂŹs always an occasion to set up (increase) an inference order and a quantity of membership relations inside the extended neo-fuzzy neuron.

The full text will be available in the edited book “Information Technology, Systems Research and Computational Physics”, eds. Kulczycki P., Kacprzyk J., Kóczy L.T., Mesiar R., Wisniewski R., to be published by Springer in the *Advances in Intelligent Systems and Computing* series soon.

Section 7
Applied Mathematics

Probability Measures and projections on Quantum Logics

Oľga Nánásiová[1], Ľubica Valášková[2], and Viera Čerňanová[3]

[1] Slovak University of Technology, Institute of Computer Science and Mathematics,
Ilkovičova 3, 812 19 Bratislava, Slovakia;
[2] Slovak University of Technology, Department of Mathematics and Descriptive Geometry,
Radlinského 11, 810 05 Bratislava, Slovakia;
[3] Department of Mathematics and Computer Science, Faculty of Education,
Trnava University, Priemyselná 4, 918 43 Trnava, Slovakia;

Abstract. The present paper deals with modelling of a probability measure of logical connectives on a quantum logic. We follow the work in which the probability of logical conjunction, disjunction and symmetric difference and their negations for noncompatible propositions are studied.

We study a special map (G-map) on a quantum logic, which represents a probability measure of a projection and and implication show, that unlike classical (Boolean) logic, probability measure of projections on a quantum logic are not necessarilly pure projections.

In the end, we compare properties of a G-map with properties of a probability measure related to logical connectives on a Boolean algebra.

The full text will be available in the edited book "Information Technology, Systems Research and Computational Physics", eds. Kulczycki P., Kacprzyk J., Kóczy L.T., Mesiar R., Wisniewski R., to be published by Springer in the *Advances in Intelligent Systems and Computing* series soon.

Statistical analysis of models' reliability for punching resistance assessment

Jana Kalická, Mária Minárová, Jaroslav Halvoník, and Lucia Majtánová
Slovak University of Technology, Bratislava, Slovakia

Abstract. The paper deals with statistical analysis of engineering data set. The purpose of analysis is to stipulate suitability of formulas that compete for being involved in prepared EuroCode that will be valid from 2020. Authors dispose with a sufficient numbers of lab tests. Having input geometrical and physical parameters of each experiment at hand, the corresponding theoretical value is computed by using three formulas provided by three models. Case by case, the ratio between measured and theoretical value reveal the safety immediately: greater then one means safety, less then one means failure. This ratio stands as the one parametric dimensionless statistical variable which is analysed afterwards.

The full text will be available in the edited book "Information Technology, Systems Research and Computational Physics", eds. Kulczycki P., Kacprzyk J., Kóczy L.T., Mesiar R., Wisniewski R., to be published by Springer in the *Advances in Intelligent Systems and Computing* series soon.

Statistical test for fractional Brownian motion based on detrending moving average algorithm

Grzegorz Sikora[a]

[a]*Faculty of Pure and Applied Mathematics, Hugo Steinhaus Center*
Wroclaw University of Science and Technology, Janiszewskiego 14a, 50-370 Wrocław, Poland

---

Abstract

Motivated by contemporary and rich applications of anomalous diffusion processes we propose a new statistical test for fractional Brownian motion, which is one of the most popular models for anomalous diffusion systems. The test is based on detrending moving average statistic and its probability distribution. Using the theory of Gaussian quadratic forms we determined it as a generalized chi-squared distribution. The proposed test could be generalized for statistical testing of any centered non-degenerate Gaussian process. Finally, we examine the test via Monte Carlo simulations for two exemplary scenarios of subdiffusive and superdiffusive dynamics.

Keywords: detrending moving average algorithm, statistical test, fractional Brownian motion

---

1. Introduction

The theory of stochastic processes is currently an important and developed branch of mathematics [10, 22, 25]. The key issue from the point of view of the application of stochastic processes is statistical inference for such random objects [41, 53, 62, 64]. This field consists of statistical methods for the reliable estimation, identification, and validation of stochastic models. Such a part of the theory of stochastic processes and the statistics developed for them are used to model phenomena studied by other fields such as physics [28, 60, 75], chemistry [28, 66, 75], biology [11, 14, 28, 32, 65, 66], engineering [7, 67], among others.

This work is motivated by growing interest and applications of the special class of stochastic processes, namely anomalous diffusion processes, which largely depart from the classical Brownian diffusion theory [50, 63]. Such processes are characterized by a nonlinear power-law growth of the mean squared displacement (MSD) in the course of time. Their anomalous diffusion behavior manifested by nonlinear MSD is intimately connected with the breakdown of the central limit theorem, caused by either broad distributions or long-range correlations. Today, the list of systems displaying anomalous dynamics is quite extensive [26, 31, 35, 44, 56, 59]. Therefore in recent years, there has been great progress in the understanding of the different mathematical models that can lead to anomalous diffusion [36, 37, 51]. One of the most popular of them is the fractional Brownian motion (FBM) [29, 33, 35, 42, 51, 73, 78]. Introduced by Kolmogorov [38] and studied by Mandelbrot in a series of papers [46, 47], it is now well-researched stochastic process. FBM is still constantly developed by mathematicians in different aspects [5, 23, 55, 57, 77].

The main subject considered in this work is the issue of rigorous and valid identification of the FBM model. The problem of FBM identification has been described in the mathematical literature for a long time [8, 18]. However, most of the works mainly concern various methods of estimating the parameters of the FBM model. They are based, among others, on p-variation [45], discrete variation [19], sample quantiles [20] and other methods [9, 12, 21, 27, 43, 52, 74, 81]. A certain gap in this theory is the lack of tools such as rigorous statistical tests to identify the FBM model in empirical data. Some approaches to FBM identification are known, e.g., application of empirical quantiles [13], distinguishing FBM from pure Brownian motion [40]. According to the author's current knowledge, the only statistical test for the FBM model is the test based on the distribution of the time average MSD [71]. Due to the lack of statistical tests specially designed for the FBM model, in this work, we propose such a statistical testing procedure.

Email address: `grzegorz.sikora@pwr.edu.pl` (Grzegorz Sikora)

Preprint submitted to Elsevier

The proposed test has a test statistic which is the detrending moving average (DMA) statistic introduced in the paper [2]. For more than a decade, the DMA algorithm has become an important and promising tool for the analysis of stochastic signals. It is constantly developed and improved [4, 16, 17, 69], its multifractal version was created and used [15, 30, 34, 80] and it is applied for different empirical datasets [39, 58, 61, 68]. As one of the important method for fluctuation analysis, the DMA algorithm was often compared with other methods [6, 79, 82]

In section 2 we show that the distribution of the DMA statistics follows the generalized chi-squared distribution. The main section 3 demonstrates the statistical testing procedure based on computing the DMA statistic for empirical data. In section 4 the results of Monte Carlo simulations of the proposed test are presented and discussed. Section 5 contains conclusions and final remarks. In the last section 6, the Matlab code of the proposed test is presented.

2. Probability distribution of DMA statistic

The DMA algorithm was introduced in [2]. For a finite trajectory $\{X(1), X(2), \ldots, X(N)\}$ of a stochastic process the DMA statistic has the following form

$$\sigma^2(n) = \frac{1}{N-n}\sum_{j=n}^{N}(X(j) - \tilde{X}_n(j))^2, \quad n = 2, 3, \ldots, N-1, \tag{1}$$

where $\tilde{X}_n(j)$ is a moving average of n observations $X(j), \ldots, X(j-n+1)$, i.e.

$$\tilde{X}_n(j) = \frac{1}{n}\sum_{k=0}^{n-1} X(j-k).$$

The statistic $\sigma^2(n)$ is a random variable which computes the mean squared distance between the process $X(j)$ and its moving average $\tilde{X}_n(j)$ of the window size n. It has scaling law behavior $\sigma^2(n) \sim C_H n^{2H}$, where H is a self–similarity parameter of the signal [2, 4]. The constant C_H has explicit expression computed in the case of fractional Brownian motion [4]. As a byproduct of this scaling law one can estimate the self–similarity parameter H from linear fitting on double logarithmic scale [6, 17, 70].

In this work, we leave the issue of DMA algorithm as an estimation method and concentrate on the probability characteristics of this random statistic. Throughout the paper, we assume that the stochastic process $X(j)$ is a centered Gaussian process. Therefore a finite trajectory $\mathbb{X} = \{X(1), X(2), \ldots, X(N)\}$ is a centered Gaussian vector with covariance matrix $\Sigma = \{E[X(j)X(k)] : j, k = 1, 2, \ldots, N\}$. Let introduce the process $Y(j) := X(j+n-1) - \tilde{X}_n(j+n-1)$, which is still a centered Gaussian process. We calculate the covariance matrix of the vector $\mathbb{Y} = \{Y(1), Y(2), \ldots, Y(N-n+1)\}$

$$\begin{aligned} E[Y(j)Y(k)] &= E[X(j+n-1)X(k+n-1)] - E\left[X(j+n-1)\tilde{X}_n(k+n-1)\right] - E\left[\tilde{X}_n(j+n-1)X(k+n-1)\right] \\ &+ E\left[\tilde{X}_n(j+n-1)\tilde{X}_n(k+n-1)\right] = E[X(j+n-1)X(k+n-1)] - \frac{1}{n}\sum_{m=k}^{k+n-1} E[X(j+n-1)X(m)] \\ &- \frac{1}{n}\sum_{l=j}^{j+n-1} E[X(k+n-1)X(l)] + \frac{1}{n^2}\sum_{j\le l\le j+n-1}\ \sum_{k\le m\le k+n-1} E[X(l)X(m)]. \end{aligned} \tag{2}$$

That matrix we denote by $\tilde{\Sigma} = \{E[Y(j)Y(k)] : j, k = 1, 2, \ldots, N-n+1\}$. We see that the dependence structure of the process $Y(i)$ is fully determined by the covariance of the process $X(i)$. Moreover the covariance $E[X(k)X(m)]$ in formula (2) has a prefactor

$$\begin{array}{rll} \left(1-\frac{1}{n}\right)^2, & \text{for} & l = j+n-1 \wedge m = k+n-1, \\ \frac{1}{n^2} - \frac{1}{n}, & \text{for} & (l = j+n-1 \wedge m \neq k+n-1) \vee (l \neq j+n-1 \wedge m = k+n-1), \\ \frac{1}{n^2}, & \text{for} & l \neq j+n-1 \wedge m \neq k+n-1. \end{array}$$

Therefore we can rewrite the formula (2) in the equivalent form

$$
\begin{aligned}
E\left[Y(j)Y(k)\right] &= \left(1-\frac{1}{n}\right)^2 E\left[X(j+n-1)X(k+n-1)\right] + \left(\frac{1}{n^2}-\frac{1}{n}\right)\left[\sum_{m=k}^{k+n-2} E\left[X(j+n-1)X(m)\right]\right. \\
&+ \left.\sum_{l=j}^{j+n-2} E\left[X(l)X(k+n-1)\right]\right] + \frac{1}{n^2}\sum_{j\le l\le j+n-2}\ \sum_{k\le m\le k+n-2} E\left[X(l)X(m)\right]. \qquad (3)
\end{aligned}
$$

The average value of random variable $\sigma^2(n)$ we can now express based on (2) and (3) by covariance structure of the process $X(j)$

$$
\begin{aligned}
E\left[\sigma^2(n)\right] &= \frac{1}{N-n}\sum_{j=n}^{N} E\left[\left(X(j)-\tilde{X}_n(j)\right)^2\right] = \frac{1}{N-n}\sum_{j=n}^{N} E\left[Y^2(j-n+1)\right] \\
&= \frac{1}{N-n}\sum_{j=n}^{N}\left\{\left(1-\frac{1}{n}\right)^2 E[X^2(j)] + 2\left(\frac{1}{n^2}-\frac{1}{n}\right)\sum_{m=j-n+1}^{i-1} E[X(j)X(m)] + \frac{1}{n^2}\sum_{j-n+1}^{j-1} E[X^2(m)] + \frac{2}{n^2}\sum_{j-n+1\le k<m\le j-1} E[X(m)X(l)]\right\}. \quad (4)
\end{aligned}
$$

We can also express the variance of the random variable $\sigma^2(n)$

$$
\begin{aligned}
Var\left[\sigma^2(n)\right] &= \frac{1}{(N-n)^2} Var\left[\sum_{j=n}^{N} Y^2(j-n+1)\right] = \frac{1}{(N-n)^2}\sum_{l,m=n}^{N} Cov\left(Y^2(l-n+1), Y^2(m-n+1)\right) \\
&= \frac{1}{(N-n)^2}\sum_{l,m=n}^{N} E\left[Y^2(l-n+1)Y^2(m-n+1)\right] - E\left[Y^2(l-n+1)\right]E\left[Y^2(m-n+1)\right]. \qquad (5)
\end{aligned}
$$

The terms $E\left[Y^2(l-n+1)\right]$ and $E\left[Y^2(m-n+1)\right]$ one can compute from covariance of the process $Y(j)$ according to (3). The 4th–order moment $E\left[Y^2(l-n+1)Y^2(m-n+1)\right]$ can be expressed by covariance structure of process $Y(j)$ according to Isserlis' theorem [72]:

$$
E\left[Y^2(l-n+1)Y^2(m-n+1)\right] = E\left[Y^2(l-n+1)\right]E\left[Y^2(m-n+1)\right] + 2E\left[Y(l-n+1)Y(m-n+1)\right]^2.
$$

Therefore applying above to (5) we get

$$
Var\left[\sigma^2(n)\right] = \frac{2}{(N-n)^2}\sum_{l,m=n}^{N} E\left[Y(l-n+1)Y(m-n+1)\right]^2. \qquad (6)
$$

Using (3) one can present formula (6) for variance in terms of covariance structure of the underlying process $X(i)$.

In order to describe more probabilistic properties of the random variable $\sigma^2(n)$ we notice the quadratic form representation

$$
\sigma^2(n) = \frac{1}{N-n}\sum_{j=n}^{N} Y^2(j-n+1) = \frac{1}{N-n}\mathbb{Y}\mathbb{Y}^T,
$$

where $\mathbb{Y}^T$ is a vertical vector which is a transpose of the vector $\mathbb{Y}$. The random object $\mathbb{Y}\mathbb{Y}^T$ is a quadratic form of a Gaussian vector $\mathbb{Y}$. Therefore we apply the theory of Gaussian quadratic forms to study random variable $(N-n)\sigma^2(n)$. The theory of Gaussian quadratic forms [49] provides us with the following representation

$$
(N-n)\sigma^2(n) \overset{d}{=} \sum_{j=1}^{N-n+1} \lambda_j(n)U_j, \qquad (7)
$$

where $\overset{d}{=}$ means equality in distribution. The probability distribution in (7) is the generalized chi-squared distribution [24]. The random variables U_j's form an i.i.d. sequence of chi-squared distribution with one degree of freedom. The coefficients $\lambda_j(n)$ are the eigenvalues of covariance matrix $\tilde{\Sigma}$ of the vector $\mathbb{Y}$. They depend on n and the parameters of the process $Y(j)$. The distribution in (7) one can interpret as a sum of independent gamma distributions with constant shape parameter $1/2$ and different scale parameters, i.e. $\lambda_j(n)U_j \overset{d}{=} G(1/2, 2\lambda_j(n))$. By $G(\alpha,\beta)$ we denote the gamma distribution with the shape parameter α and scale parameter β. It has a PDF of the form

$$f_{(\alpha,\beta)}(x) = \frac{x^{\alpha-1}\exp(-x/\beta)}{\Gamma(\alpha)\beta^{\alpha}} \quad (x > 0)$$

and CDF

$$F_{(\alpha,\beta)}(x) = \frac{1}{\Gamma(\alpha)}\gamma(\alpha, x/\beta),$$

where Γ function and lower incomplete gamma function γ are defined respectively $\Gamma(z) = \int_0^\infty x^{z-1}e^{-x}dx$ and $\gamma(s,x) = \int_0^x t^{s-1}e^{-t}dt$. The characteristic function of random variable $(N-n)\sigma^2(n)$ is a product of characteristic functions of gamma distributions

$$\phi_{(N-n)\sigma^2(n)}(t) = \prod_{j=1}^{N-n+1} \frac{1}{\left[1 - 2\lambda_j(n)it\right]^{1/2}}.$$

Therefore based on representation (7) we get the average value for $\sigma^2(n)$

$$E\left[\sigma^2(n)\right] = \frac{1}{N-n}\sum_{j=1}^{N-n+1}\lambda_j(n) = \frac{1}{N-n}tr\left(\tilde{\Sigma}\right),$$

where $tr(A)$ is a trace of the matrix A. That gives the same result for the mean of $\sigma^2(n)$ as in (4) and connects eigenvalues $\lambda_j(n)$ with a dependence structure of the observed process $X(j)$. Representation (7) provides also the variance formula

$$Var\left[\sigma^2(n)\right] = \frac{1}{(N-n)^2}\sum_{j=1}^{N-n+1}\lambda_j^2(n)Var\left[U_j\right] = \frac{2}{(N-n)^2}\sum_{j=1}^{N-n+1}\lambda_j^2(n) = \frac{2}{(N-n)^2}tr\left(\tilde{\Sigma}^2\right),$$

which is the same as in (6).

The generalized chi-squared distribution in (7) was intensively studied. In the literature, there are many different representations for PDF or CDF of such distribution f.e. in terms of zonal polynomials and confluent hypergeometric functions [48], single gamma-series [54], Lauricella multivariate hypergeometric functions [1], extended Foxs functions [3] and others [76]. Here we present the formulas for PDF and CDF according to [54]. The PDF of $\sigma^2(n)$ has a form for $x > 0$

$$f_n(x) = C\sum_{k=0}^{\infty}\frac{\delta_k x^{\frac{N-n}{2}+k-1}\exp\left(-\frac{x(N-n)}{2\lambda_1(n)}\right)}{\Gamma\left(\frac{N-n}{2}+k\right)\left(\frac{2\lambda_1(n)}{N-n}\right)^{\frac{N-n}{2}+k}}, \tag{8}$$

where $\lambda_1(n)$ is the smallest eigenvalue of the matrix $\tilde{\Sigma}$ and

$$C = \prod_{j=1}^{N-n+1}\left(\frac{\lambda_1(n)}{\lambda_j(n)}\right)^{1/2}, \quad \gamma_k = \sum_{j=1}^{N-n+1}\frac{(1-\lambda_1(n)/\lambda_j(n))^k}{2k}, \quad \delta_{k+1} = \frac{1}{k+1}\sum_{j=1}^{k+1}j\gamma_j\delta_{k+1-j}, \quad \delta_0 = 1. \tag{9}$$

The PDF in (8) can be understood as a series of densities of gamma distributions $G((N-n)/2+k, 2\lambda_1(n)/(N-n))$:

$$f_n(x) = C\sum_{k=0}^{\infty}\delta_k f_{\left(\frac{N-n}{2}+k, \frac{2\lambda_1(n)}{(N-n)}\right)}(x), \; (x > 0).$$

Moreover justified term-by-term integration leads to the CDF formula of $\sigma^2(n)$:

$$F_n(x) = P\left(\sigma^2(n) \le x\right) = C\sum_{k=0}^{\infty}\delta_k\int_0^x f_{\left(\frac{N-\tau}{2}+k, \frac{2\lambda_1(\tau)}{(N-\tau)}\right)}(y)dy = C\sum_{k=0}^{\infty}\delta_k F_{\left(\frac{N-\tau}{2}+k, \frac{2\lambda_1(\tau)}{(N-\tau)}\right)}(x). \tag{10}$$

We have also the formula for the tail of random variable $\sigma^2(n)$:

$$P\left(\sigma^2(n) > x\right) = 1 - F_n(x) = 1 - C\sum_{k=0}^{\infty} \delta_k F_{\left(\frac{N-\tau}{2}+k, \frac{2\lambda_1(\tau)}{(N-\tau)}\right)}(x). \tag{11}$$

Therefore we obtain:

$$P\left(\sigma^2(n) > x\right) = C\sum_{k=0}^{\infty} \delta_k \Gamma\left(\frac{N-\tau}{2} + k, \frac{x(N-\tau)}{2\lambda_1(\tau)}\right),$$

where $\Gamma(s,x)$ is upper incomplete gamma function defined as $\Gamma(s,x) = \int_x^\infty t^{s-1}e^{-t}dt$.

3. Statistical test based on DMA

Knowing the exact probability distribution of the random variable $\sigma^2(n)$ we can propose the statistical test. Because of the generality of this distribution the test is general for any centered Gaussian process. In this paper, we concentrate on the FBM denoted by $B_H(j)$, defined by its covariance function

$$E\left(B_H(j), B_H(k)\right) = D\left(j^{2H} + k^{2H} - |j-k|^{2H}\right),$$

where D is a scale parameter called diffusion constant and H is a self-similarity parameter also called Hurst index. The null hypothesis of proposed statistical test is

$$\mathcal{H}_0 : \{B_H(1), B_H(2), \ldots, B_H(N)\} \text{ is a trajectory of FBM with parameters } D \text{ and } H,$$

while alternative hypothesis is

$$\mathcal{H}_1 : \{B_H(1), B_H(2), \ldots, B_H(N)\} \text{ is not a trajectory of FBM with parameters } D \text{ and } H.$$

The test statistic is the random variable $\sigma^2(n)$ distributed according to the CDF of the form (10). Therefore we define the p-value of the test as the double-tailed event probability

$$p = 2\min\{P(\sigma^2(n) < t), P(\sigma^2(n) > t)\} = 2C\min\left\{\sum_{k=0}^{\infty} \delta_k \Gamma\left(\frac{N-\tau}{2} + k, \frac{t(N-\tau)}{2\lambda_1(\tau)}\right), \sum_{k=0}^{\infty} \delta_k \frac{\gamma\left(\frac{N-\tau}{2} + k, \frac{t(N-\tau)}{2\lambda_1(\tau)}\right)}{\Gamma\left(\frac{N-\tau}{2} + k\right)},\right\} \tag{12}$$

where t is the value of DMA statistics $\sigma^2(n)$ calculated for empirical trajectory of data. Because p-value in (12) has infinite series representation one has to truncate the sum and compute it as finite truncated sum, where M is the truncation parameter. The error of such approximation was studied in details in [54]. From our perspective it is enough to apply Monte Carlo simulations and compute p-value as an empirical quantile from sample of generalized chi-squared random variables of the form $1/(N-n)\sum_{j=1}^{N-n+1} \lambda_j(n) U_j$.

Summarizing the procedure for testing hypothesis

$$\mathcal{H}_0 : \{B_H(1), B_H(2), \ldots, B_H(N)\} \text{ is a trajectory of FBM with parameters } D \text{ and } H,$$

is the following:

Step 1) For empirical trajectory $\{B_H(1), B_H(2), \ldots, B_H(N)\}$ compute DMA statistic

$$\sigma^2(n) = \frac{1}{N-n}\sum_{j=n}^{N}(X(j) - \tilde{X}_n(j))^2 := t.$$

Step 2) Compute the matrix $\tilde{\Sigma} = \{E\left[Y(j)Y(k)\right] : j,k = 1,2,\ldots,N-n+1\}$ and its eigenvalues $\{\lambda_j(n) : j = 1,2,\ldots,N-n+1\}$.

Step 3) L times generate a sample $\mathbf{U}^l = \{U_1^l, U_2^l, \ldots, U_{N-n+1}^l\}$ from chi-squared distribution with one degree of freedom, $l = 1, 2, \ldots, L$.

Step 4) L times compute the value of generalized chi-squared random variable

$$\sigma_l^2(n) = \frac{1}{N-n} \sum_{j=1}^{N-n+1} \lambda_j(n) U_j^l, \qquad l = 1, 2, \ldots, L.$$

Step 5) Compute double-tailed event p-value as

$$p = \frac{2 \min\left\{\#\{\sigma_l^2(n) > t\}, \#\{\sigma_l^2(n) < t\}\right\}}{L}.$$

If $p < \alpha$ reject the null hypothesis $\mathcal{H}_0$, where α is a significant level. In other case there is no significant statistical proof for rejection of $\mathcal{H}_0$.

We propose the test based on the distribution of DMA statistic $\sigma^2(10)$ for argument $n = 10$, because random variable $\sigma^2(10)$ has different domains for different values of Hurst index H in the case of fixed scale parameter D. However two issues need further studies. The first open problem is the optimization of the proposed test according to the argument n. Natural questions arise about the optimal choice of n and the most effective performance of the test. The crucial point is the dependence of the domain of DMA test statistic on the different values of Hurst exponent H. The second issue is the problem of the testing procedure in the case of unknown scale parameter D. The essence of this problem is that the DMA test statistic can have not disjoint domains for different pairs of parameters (D, H). These problems need continuing research and will be developed by the author.

In the simulation examination of the proposed statistical test, we consider the case of standard FBM model with fixed $D = 1$.

4. Monte Carlo simulations

In order to examine the proposed test, we perform Monte Carlo simulations. First we present results for the case of the Hurst index $H_{real} = 0.25$, which corresponds exemplary subdiffusion case. We generate $T = 1000$ independent trajectories of FBM process with fixed $D = 1$ and length $N = 1000$. For each trajectory we test the null hypothesis

$$\mathcal{H}_0 : \{B_H(1), B_H(2), \ldots, B_H(N)\} \text{ is a trajectory of FBM with } H_{test},$$

where $H_{test} \in \{0.05, 0.1, \ldots, 0.95\}$. Therefore for each case of H_{test} we test $\mathcal{H}_0$ 1000 times and obtain 1000 corresponding p-values. On the Figure 1 we present boxplots of obtained p-values for all cases of H_{test}. The results for $H_{test} < 0.2$ and $H_{test} > 0.3$ are almost all $p < 0.05$ and that is the strong statistical evidence to reject incorrect $\mathcal{H}_0$. For $H_{test} = 0.2$ and $H_{test} = 0.3$ we obtained 767 and 751 results with $p < 0.05$ respectively. That means more than 75% of correct rejections of incorrect $\mathcal{H}_0$. In the case when $H_{test} = 0.25$ and $\mathcal{H}_0$ is true we obtained 76 results with $p < 0.05$. In other words we made a type I error (incorrect rejection of true $\mathcal{H}_0$) 7.6% of $T = 1000$ tests. The detailed numbers of accepting of $\mathcal{H}_0$ or $\mathcal{H}_1$ for the case with $H_{real} = 0.25$ we present in Table 1.

H_{test}	0.05	0.1	0.15	0.2	0.25	0.3	0.35	0.4	0.45	0.5
$\mathcal{H}_0$	0	0	0	233	924	249	2	0	0	0
$\mathcal{H}_1$	1000	1000	1000	767	76	751	998	1000	1000	1000

H_{test}	0.55	0.6	0.65	0.7	0.75	0.8	0.85	0.9	0.95
$\mathcal{H}_0$	0	0	0	0	0	0	0	0	0
$\mathcal{H}_1$	1000	1000	1000	1000	1000	1000	1000	1000	1000

Table 1: Numbers of accepting of $\mathcal{H}_0$ or $\mathcal{H}_1$ at the significant level $\alpha = 0.05$ for the case with $H_{real} = 0.25$ obtained from $T = 1000$ Monte Carlo simulations.

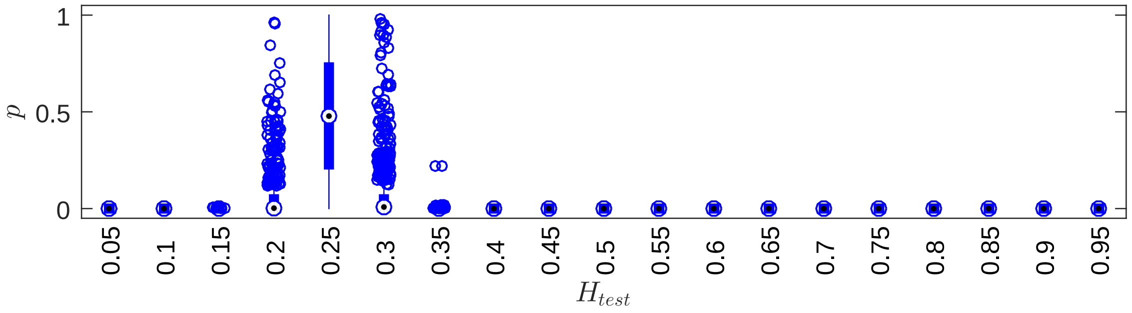

Figure 1: p-values obtained from $T = 1000$ Monte Carlo simulations from testing $\mathcal{H}_0$ for any $H_{test} \in \{0.05, 0.1, \ldots, 0.95\}$. The significant level was $\alpha = 0.05$ and the $H_{real} = 0.25$.

The next case is a validation of the proposed test for exemplary superdiffusion case with $H_{real} = 0.75$. Analogous simulations produced 19 sets of p-values corresponding $H_{test} \in \{0.05, 0.1, \ldots, 0.95\}$. The each set contains 1000 p-values presented as a boxplot on the Figure 2. The results for $H_{test} < 0.65$ are almost all $p < 0.05$ and that is the strong statistical evidence to reject incorrect $\mathcal{H}_0$. For cases with $H_{test} = 0.7$ and $H_{test} > 0.75$ the test works not so good as for previous subdiffusion scenario. It incorrectly accepts $\mathcal{H}_1$ more than 80% times for $H_{test} = 0.7$ and $H_{test} = 0.8$ and around 60% times for $H_{test} > 0.8$. So for those cases the type II error is committed very often and the power of the test is weak. On the other hand in the case when $H_{test} = 0.75$ and $\mathcal{H}_0$ is true we obtained 63 results with $p < 0.05$. In other words we made a type I error 6.3% of $T = 1000$ tests. The detailed numbers of accepting of $\mathcal{H}_0$ or $\mathcal{H}_1$ for the case with $H_{real} = 0.75$ we present in Table 2.

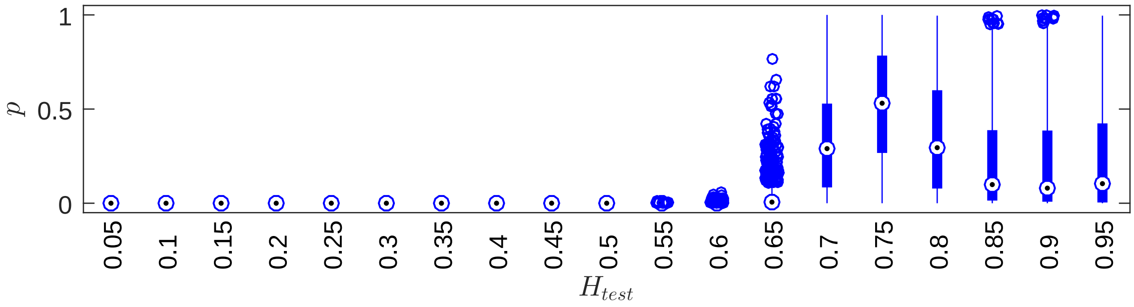

Figure 2: p-values obtained from $T = 1000$ Monte Carlo simulations from testing $\mathcal{H}_0$ for any $H_{test} \in \{0.05, 0.1, \ldots, 0.95\}$. The significant level was $\alpha = 0.05$ and $H_{real} = 0.75$.

H_{test}	0.05	0.1	0.15	0.2	0.25	0.3	0.35	0.4	0.45	0.5
$\mathcal{H}_0$	0	0	0	0	0	0	0	0	0	0
$\mathcal{H}_1$	1000	1000	1000	1000	1000	1000	1000	1000	1000	1000

H_{test}	0.55	0.6	0.65	0.7	0.75	0.8	0.85	0.9	0.95
$\mathcal{H}_0$	0	1	233	844	937	835	611	568	582
$\mathcal{H}_1$	1000	999	767	156	63	165	389	432	420

Table 2: Numbers of accepting of $\mathcal{H}_0$ or $\mathcal{H}_1$ at the significant level $\alpha = 0.05$ for the case with $H_{real} = 0.75$ obtained from $T = 1000$ Monte Carlo simulations.

5. Conclusion

In this work, we proposed a new statistical test to identify the FBM model in empirical data. This tool is based on the exact probability distribution of the DMA test statistic $\sigma^2(n)$, which is very sensitive due to the Hurst index H. The proposed procedure is a new original result in the theory of statistical inference of Gaussian processes.

Conducted Monte Carlo simulations indicate that the constructed test works worse in the case of the superdiffusion when $H > 1/2$. In such a scenario, the type II error is very often committed and the power of the test seems to be weaker than for the subdiffusion. This is due to the fact that for the superdiffusion, the domains of the test statistic $\sigma^2(n)$ are close to each other and have joint parts to differing H parameters. This is not the case for subdiffusion where the test works much better. However, it should be strongly emphasized that for both sub and superdiffusion the type I error occurs very rarely and the test correctly accepts the null hypothesis when it is true. In connection with such a test performance and the type II errors, it is possible to modify and optimize the proposed procedure. Namely, a better test performance can be obtained by selecting the argument n of the test statistic $\sigma^2(n)$. It is an interesting issue, worth attention and further research.

Another direction of research on the constructed test is its generalized version due to the unknown parameter of the scale parameter D. In this paper, we assumed a standard FBM with $D = 1$. In the general case with the unknown D, the proposed test should be combined with the pre-estimation of the parameter D by other known methods. However, by applying the theory of the ratios of quadratic Gaussian forms [49], it is possible to generalize the described test to the situation of the unknown and non-estimated parameter D. In this case, the probability distribution of the ratios of quadratic forms will not depend on D at all and this parameter will be irrelevant.

The described test procedure can be applied in a sequential manner according to the grid of the values of the parameter H. This will allow to reject the hypotheses with false H values and accept the FBM hypothesis with the true H. Such performance of the proposed test will also be a method for estimating the Hurst exponent as well as a reliable test procedure.

Finally, we want to point out that the statistical test proposed for FBM can be generalized (due to the theory of Gaussian quadratic forms) for each non-degenerated Gaussian process.

6. Appendix

Here we present the Matlab code for the proposed statistical test.

```
function [h,p,t]=DMAtest(x,n,H,D,alpha,L)
%
% This function performs the statistical test for FBM (Fractional Brownian
% Motion) with known scale parameter D and unknown suggested Hurst index H.
% The test statistics is a DMA (Detrended Moving Average) statistic
% computed for empirical vector data x. The test is
% proposed by Grzegorz Sikora.
%
% Input:
% x <- vector of empirical data
% n <- argument of DMA statistic
% H <- Hurst index
% D <- known scale parameter of FBM
% alpha <- significant level
% L <- number of Monte Carlo simulations
%
% Output:
% h <- accepted hypothesis: h=0 null hypothesis, h=1 alternative hypothesis
% p <- p-value
% t <- value of DMA statistic for empirical data x
%
```

```
% Written by Grzegorz Sikora 13.02.2018, grzegorz.sikora@pwr.edu.pl

% Step 1)
N=length(x);
xmean=sum(x(repmat([1:n]',1,N-n+1)+repmat(0:N-n,n,1)))/n;
t=sum((x(n:N)-xmean).^2)/(N-n);

%Step 2)
%Covariance matrix of FBM:
R=repmat([1:N]',1,N);
C=R';
X=D*(R.^(2*H)+C.^(2*H)-abs(R-C).^(2*H));

%Covariance matrix of process Y(i):
Y1=zeros(N-n+1,N-n+1);
Y2=Y1;
Y3=Y1;
Y=Y1;
for i=1:N-n+1
    for j=1:N-n+1
        Y1(i,j)=(1-1/n)^2*X(i+n-1,j+n-1);
        Y2(i,j)=(1/(n^2)-1/n)*(sum(X(i+n-1,j:j+n-2))+sum(X(i:i+n-2,j+n-1)));
        Y3(i,j)=1/(n^2)*sum(sum(X(i:i+n-2,j:j+n-2)));
    end
end
Y=Y1+Y2+Y3;
lambda=eig(Y)';

%Step 3)
U_j=chi2rnd(1,N-n+1,L);

%Step 4)
sigma_j=1/(N-n)*lambda*U_j;

%Step 5)
p=2*min(sum(sigma_j>t)/L,sum(sigma_j<t)/L);
if p<alpha
    h=1;
else
    h=0;
end
```

Acknowledgements

The author would like to acknowledge the support of NCN Maestro Grant No. 2012/06/A/ST1/00258.

[1] Aalo, V.A., Piboongungon, T., Efthymoglou, G.P., 2005. Another look at the performance of MRC schemes in Nakagami-m fading channels with arbitrary parameters. IEEE Trans. Commun. 53, 20022005.

[2] Alessio, E., Carbone, A., Castelli, G., Frappietro, V., 2002. Second-order moving average and scaling of stochastic time series. Eur. J. Phys. B 27 197.

[3] Ansari, I.S., Yilmaz, F., Alouini, M.S., Kucur, O., 2014. New results on the sum of Gamma random variates with application to the performance of wireless communication systems over Nakagami-m fading channels. Trans. Emerging Tel. Tech. 28 (1), e2912.

[4] Arianos, S., Carbone, A., 2017. De trending moving average algorithm: A closed-form approximation of the scaling law. Physica A 382, 9-15.

[5] Bahamonde, N., Torres, S., Tudor, C.A., 2018. ARCH model and fractional Brownian motion. Stat. Probabil. Lett. 134, 70-78.

[6] Bashan, A., Bartsch, R., Kantelhardt, J.W., Havlin, S., 2008. Comparison of detrending methods for fluctuation analysis. Physica A, 387, 5080-5090.

[7] Beichelt, F., 2006. Stochastic Processes in Science, Engineering and Finance. C hapman & Hall/CRC.

[8] Beran, J., 1994. Statistics for long memory processes. Chapman and Hall, London.

[9] Bondarenko, V.V., 2012. An iterative algorithm of estimating the parameters of the fractal Brownian motion. J. Automat. Inf. Sci. 44 (7), 62-68.

[10] Borodin, A.N., 2017. Stochastic Processes. Series: Probability and Its Applications, Birkhäuser Basel.

[11] Bressloff, P.C., 2014. Stochastic Processes in Cell Biology. Series: Interdisciplinary Applied Mathematics 41, Springer International Publishing.

[12] Breton, J.C., Coeurjolly, J.F., 2012. Confidence intervals for the Hurst parameter of a fractional Brownian motion based on finite sample size. Statistical inference for stochastic processes 15 (1), 1-26.

[13] Burnecki, K., Kepten, E., Janczura, J., Bronshtein, I., Garini, Y., Weron, A., 2012. Universal Algorithm for Identification of Fractional Brownian Motion. A Case of Telomere Subdiffusion. Biophysical Journal 103, 18391847.

[14] Capasso, V., Bakstein, D., 2015. An Introduction to Continuous-Time Stochastic Processes: Theory, Models, and Applications to Finance, Biology, and Medicine. Series: Modeling and Simulation in Science, Engineering and Technology, Birkhäuser Basel.

[15] Carbone, A., 2007. Algorithm to estimate the Hurst exponent of high-dimensional fractals. Phys. Rev. E 76, 056703.

[16] Carbone, A., 2009. Detrending Moving Average algorithm: a brief review. Science and Technology for Humanity (TIC-STH), IEEE Toronto International Conference.

[17] Carbone, A., Kiyono, K., 2016. Detrending moving average algorithm: Frequency response and scaling performances. Phys. Rev. E 93, 063309.

[18] Coeurjolly, J.F., 2000. Simulation and identification of the fractional Brownian motion: a bibliographical and comparative study. Journal of Statistical Software 5 (7).

[19] Coeurjolly, J.F., 2001. Estimating the parameters of a fractional Brownian motion by discrete variations of its sample paths. Statistical Inference for stochastic processes 4 (2), 199-227.

[20] Coeurjolly, J.F., 2008. Hurst exponent estimation of locally self-similar Gaussian processes using sample quantiles. Ann. Statist. 36 (3), 1404-1434.

[21] Coeurjolly, J.F., Kortas, H., 2012. Expectiles for subordinated Gaussian processes with applications. Electron. J. Statist. 6, 303-322.

[22] Cox D.R., Miller, H.D., 2017. The Theory of Stochastic Processes. Chapman & Hall/CRC.

[23] Davidson, J., Hashimzade, N., 2009 Type I and type II fractional Brownian motions: A reconsideration. Comput. Stat. Data Anal. 53 (6), 2089-2106.

[24] Davies, R.B., 1980. The distribution of a linear combination of x2 random variables. Applied Statistics 29, 323-333.

[25] Durrett, R., 2016. Essentials of Stochastic Processes. Springer Texts in Statistics, Springer.

[26] Efros, A.L., Nesbitt, D.J., 2016. Origin and control of blinking in quantum dots. Nat. Nanotechnol. 11, 661-671.

[27] El Hajjar, S.T., 2015. A Statistical Study to Provide Estimators of Hurst Parameter for a Fractional Brownian Motion Through Unbalanced Sampling Time. Analysis and Applications 2 (1), 1-8.

[28] Freund, J.A., Pöschel, T., 2010. Stochastic Processes in Physics, Chemistry and Biology. Series: Lecture Notes in Physics. Springer.

[29] Fuliński, A., 2017. Fractional Brownian motions: memory, diffusion velocity, and correlation functions. J. Phys. A: Math. Theor. 50, 054002.

[30] Gu, G.F., Zhou, W.X., 2010. Detrending moving average algorithm for multifractals. Phys. Rev. E 82, 011136.

[31] Gudowska-Nowak, E., Dybiec, B., 2010. Subordinated diffusion and continuous time random walk asymptotics. Chaos 20, 043129.

[32] Holcman, D., 2017. Stochastic Processes, Multiscale Modeling, and Numerical Methods for Computational Cellular Biology. Springer International Publishing.

[33] Jeon, J.H., Metzler, R., 2010. Fractional Brownian motion and motion governed by the fractional Langevin equation in confined geometries. Phys. Rev. E 81, 021103.

[34] Jiang, Z.Q., Zhou, W.X., 2011. Multifractal detrending moving-average cross-correlation analysis. Phys. Rev. E 84, 016106.

[35] Kepten, E., Bronshtein, I., Garini, Y., 2011. Ergodicity convergence test suggests telomere motion obeys fractional dynamics Phys. Rev. E 83, 041919.

[36] Klafter, J., Lim, S.C., Metzler, R., 2012. Fractional Dynamics. Recent Advances, World Scientific, New Jersey.

[37] Klafter, J., Sokolov, I.M., 2011. First Steps in Random Walks. From Tools to Applications. Oxford University Press, Oxford.

[38] Kolmogorow, A. , 1940. Wienersche Spiralen und einige andere interessante Kurven in Hilbertschen Raum. C.R. (Doklady) Acad. Sci. URSS (N.S.), 26, 115-118.

[39] Li, Q., Cao, G., Xu, W., 2018. Relationship research between meteorological disasters and stock markets based on a multifractal detrending moving average algorithm. Int. J. Mod. Phys. B 32, 1750267.

[40] Li, M., Genay, R., Xue, Y., 2016. Is it Brownian or fractional Brownian motion? Economics Letters 145, 52-55.

[41] Lindsey, J.K., 2004. Statistical analysis of stochastic processes in time. Series: Cambridge series in statistical and probabilistic mathematics 14, Cambridge University Press, 2004.

[42] Lisy, V., Tothova, J., 2018. NMR signals within the generalized Langevin model for fractional Brownian motion. Physica A 494, 200-208.

[43] Liu, Y., Liu, Y., Wang, K., Jiang, T., Yang, L., 2009. Modified periodogram method for estimating the Hurst exponent of fractional Gaussian noise. Phys. Rev. E 80, 066207.

[44] Magdziarz, M., Klafter, J., 2010. Detecting origins of subdiffusion. P-variation test for confined systems. Phys. Rev. E 82, 011129.

[45] Magdziarz, M., Wójcik, J., Ślezak, J., 2013. Estimation and testing of Hurst parameter using p-variation. J. Phys. A: Math. Theor., 46, 325003.

[46] Mandelbrot, B.B., 1983. The Fractal Geometry of Nature, Freeman, New York.

[47] Mandelbrot, B.B., Van Ness, J.W., 1968. Fractional Brownian motions, fractional noises and applications. SIAM Rev. 10, 422-437.

[48] Mathai, A.M., 1982. Storage capacity of a dam with gamma type inputs. Ann. Inst. Stat. Math. 34, 591597.

[49] Mathai, A.M., Provost, S.B., 1992. Quadratic Forms in Random Variables: Theory and Applications. Marcel Dekker, New York.

[50] Metzler, R., Klafter, J., 2000. The random walks guide to anomalous diffusion: a fractional dynamics approach. Phys. Rep. 339, 1-77.

[51] Meroz, Y., Sokolov, I.M., 2015. A toolbox for determining subdiffusive mechanisms. Phys. Rep. 573, 1-29.

[52] Mielniczuk, J., Wojdyłło, P., 2007. Estimation of Hurst exponent revisited. Comput. Stat. Data Anal. 51 (9), 4510-4525.

[53] Mishura, Y., Shevchenko, G., 2017. Theory and Statistical Applications of Stochastic Processes. Series: Mathematics and Statistics, Wiley-ISTE.

[54] Moschopoulos, P.G., 1985. The distribution of the sum of independent gamma random variables. Ann. Inst. Stat. Math. 37, 541544.

[55] Mukeru, S., 2017. Representation of local times of fractional Brownian motion, Stat. Probabil. Lett. 131, 1-12.

[56] Negro, L., Inampudi, S., 2017. Fractional Transport of Photons in Deterministic Aperiodic Structures. Sci. Rep. 7, 2259.

[57] Nourdin, I., 2012. Selected aspects of fractional Brownian motion. Series: Bocconi & Springer series 4, Springer.

[58] Pal, M., Rao, P.M., Manimaran, P., 2014. Multifractal detrended cross-correlation analysis on gold, crude oil and foreign exchange rate time series. Physica A 416, 452-460.

[59] Palombo, M., Gabrielli, A., De Santis, S., Cametti, C., Ruocco, G., Capuani, S., 2011. Spatio-temporal anomalous diffusion in heterogeneous media by nuclear magnetic resonance. J. Chem. Phys. 135, 034504.

[60] Paul, W., Baschnagel, J., 2013. Stochastic Processes: From Physics to Finance. Springer International Publishing.

[61] Ponta, L., Carbone, A., Cincotti, S., 2017. Detrending Moving Average Algorithm: Quantifying Heterogeneity in Financial Data. Computer Software and Applications Conference (COMPSAC), IEEE 41st Annual.

[62] Rajarshi, M.B., 2013. Statistical Inference for Discrete Time Stochastic Processes. Series: Springer Briefs in Statistics, Springer India.

[63] Rakotonasy, S.H., Néel, M.C., Joelson, M., 2014. Characterizing anomalous diffusion by studying displacements. Commun. Nonlinear Sci. Numer. Simul. 19, 2284-2293.

[64] Rao, M.M., 2014. Stochastic Processes - Inference Theory. Series: Springer Monographs in Mathematics, Springer International Publishing.

[65] Schinazi, R.B., 2014. Classical and Spatial Stochastic Processes: With Applications to Biology. Birkhäuser.

[66] Schuster, P., 2016. Stochasticity in Processes: Fundamentals and Applications to Chemistry and Biology. Series: Springer Series in Synergetics, Springer International Publishing.

[67] Scott M., 2012. Applied stochastic processes in science and engineering. U. Waterloo.

[68] Serinaldi, F., 2010. Use and misuse of some Hurst parameter estimators applied to stationary and non-stationary financial time series. Physica A 389 (14), 2770-2781.

[69] Shao, Y.H., Gu, G.F., Jiang, Z.Q., Zhou, W.X., 2015. Effects of polynomial trends on detrending moving average analysis. Fractals 23 (3), 1550034.

[70] Shao, Y.H., Gu, G.F., Jiang, Z.Q., Zhou, W.X., Sornette, D., 2012. Comparing the performance of FA, DFA and DMA using different synthetic long-range correlated time series. Sci. Rep. 2, 835.

[71] Sikora, G., Burnecki, K., Wyłomańska, A., 2017. Mean-squared-displacement statistical test for fractional Brownian motion. Phys. Rev. E 95, 032110.

[72] Song, I., Lee, S., 2015. Explicit formulae for product moments of multivariate Gaussian random variables. Stat. Probabil. Lett. 100, 27-34.

[73] Szymanski, J., Weiss, M., 2009. Elucidating the Origin of Anomalous Diffusion in Crowded Fluids. Phys. Rev. Lett. 103, 038102.

[74] Taqqu M., Teverovsky V., 1995. Estimators for long-range dependence: an empirical study. Fractals 3 (4), 785-798.

[75] Van Kampen, N.G., 2007. Stochastic Processes in Physics and Chemistry. Series: North-Holland personal library, Elsevier.

[76] Vellaisamy P., Upadhye, N.S., 2009. On the sums of compound negative binomial and gamma random variables. J. Appl. Probab. 46, 272-283.

[77] Wang, W., Chen, Z., 2018. Large deviations for subordinated fractional Brownian motion and applications, J. Math. Anal. Appl. 458 (2), 1678-1692.

[78] Weiss, M., 2013. Single-particle tracking data reveal anticorrelated fractional Brownian motion in crowded fluids. Phys. Rev. E 88, 010101(R).

[79] Xi, C., Zhang, S., Xiong, G., Zhao, H., 2016. A comparative study of two-dimensional multifractal detrended fluctuation analysis and two-dimensional multifractal detrended moving average algorithm to estimate the multifractal spectrum. Physica A 454, 34-50.

[80] Xiong, G., Zhang, S., Zhao, H., 2014. Multifractal spectrum distribution based on detrending moving average. Chaos, Solitons & Fractals 65, 97-110.

[81] Yerlikaya-Özkurt, F., Vardar-Acar, C., Yolcu-Okur, Y., Weber, G.W., 2014. Estimation of the Hurst parameter for fractional Brownian motion using the CMARS method. Journal of Computational and Applied Mathematics 259, 843-850.

[82] Zhang, Q., Zhou, Y., Singh, V.P., Chen, Y.D., 2011. Comparison of detrending methods for fluctuation analysis in hydrology. Journal of Hydrology 400 (12), 121-132.

On persistence of convergence of kernel density estimates in particle filtering

David Coufal[1,2]

[1]The Czech Academy of Sciences, Institute of Computer Science,
Pod Vodárenskou věží 2, 182 07 Praha 8, Czech Republic;
[2]Charles University, Faculty of Mathematics and Physics,
Department of Probability and Mathematical Statistics,
Sokolovská 83, 186 75 Praha 8, Czech Republic;

Abstract. A sufficient condition is provided for keeping the character of the filtering density in the filtering task. This is done for the Sobolev class of filtering densities. As a consequence, estimating the filtering density in particle filtering persists its convergence at any time of filtering. Specifying the condition complements previous results on using the kernel density estimates in particle filtering.

The full text will be available in the edited book “Information Technology, Systems Research and Computational Physics”, eds. Kulczycki P., Kacprzyk J., Kóczy L.T., Mesiar R., Wisniewski R., to be published by Springer in the *Advances in Intelligent Systems and Computing* series soon.

Multidimensional copula models of dependencies between selected international financial market indexes

Tomáš Bacigál[1], Magdaléna Komorníková[1], and Jozef Komorník[2]

[1] Slovak University of Technology, 810 05 Bratislava, Slovakia;
[2] Comenius University, 820 05 Bratislava, Slovakia;

Abstract. In this paper we focus our attention on multi–dimensional copula models of returns of the indexes of selected prominent international financial markets. Our modeling results, based on elliptic copulas, 7-dimensional vine copulas and hierarchical Archimedean copulas demonstrate a dominant role of the SPX index among the considered major stock indexes (mainly at the first tree of the optimal vine copulas). Some interesting weaker conditional dependencies can be detected at it's highest trees. Interestingly, while global optimal model (for the whole period of 277 months) belong to the Student class, the optimal local models can be found (with very minor differences in the values of GoF test statistic) in the classes of vine and hierarchical Archimedean copulas. The dominance of these models is most striking over the interval of the financial market crisis, where the quality of the best Student class model was providing a substantially poorer fit.

The full text will be available in the edited book "Information Technology, Systems Research and Computational Physics", eds. Kulczycki P., Kacprzyk J., Kóczy L.T., Mesiar R., Wisniewski R., to be published by Springer in the *Advances in Intelligent Systems and Computing* series soon.

New Types of Decomposition Integrals and Computational Algorithms

Adam Šeliga

Slovak University of Technology, Faculty of Civil Engineering,
Radlinského 11, 810 05 Bratislava, Slovakia;

Abstract. In this paper we define two new types of decomposition integrals, namely the chain and the min-max integral and prove some of their properties. Their superdecomposition duals are also mentioned. Based on the wide applicability of decomposition integrals, some computational algorithms and their complexity are discussed.

The full text will be available in the edited book "Information Technology, Systems Research and Computational Physics", eds. Kulczycki P., Kacprzyk J., Kóczy L.T., Mesiar R., Wisniewski R., to be published by Springer in the *Advances in Intelligent Systems and Computing* series soon.

Trend analysis and detection of change-points of selected financial and market indices

Dominika Ballová

Slovak University of Technology, Bratislava 81005, Slovakia;

Abstract. From the macroeconomic point of view, the stock index is the best indicator of the behavior of the stock market. Stock indices fulfill different functions. One of heir most important function is to observe developments of the stock market situation. Therefore, it is crucial to describe the long-term development of indices and also to find moments of abrupt changes. Another interesting aspect is to find those indices that have evolved in a similar way over time. In this article, using trend analysis, we will uncover the long-term evolution of selected indices. Other goal is to detect the moments in which this development suddenly changed using the change point analysis. By means of cluster analysis, we find those indices that are most similar in long-term development. In each analysis, we select the most appropriate methods and compare their results.

The full text will be available in the edited book "Information Technology, Systems Research and Computational Physics", eds. Kulczycki P., Kacprzyk J., Kóczy L.T., Mesiar R., Wisniewski R., to be published by Springer in the *Advances in Intelligent Systems and Computing* series soon.

Picturing Order

Karl Javorszky[1]

[1] Institut für Angewandte Statistik, 1090 Wien, Austria
karl.javorszky@gmail.com

Abstract. Some of the implications of simple numeric facts had been, for lack of computers, not available for research in previous generations. We present numeric interdependencies regarding differing linear positions of an element of a set, built of instances of sequences of natural numbers, which are not visible to the naked eye, as the relevant tables consist of several thousands of rows and hundreds of columns. Two linear positions of an element create a coordinate on a plane. If there exist three planes that possess common axes, a rectangular space can be constructed. The position of the element then reflects the innate differences that constitute the deviating linear positions. The logical conflicts arising from differing linear positions, of the same element in differing sorting orders, are of arithmetic nature, as the tables we construct contain nothing but linear positions derived by simple sorting operations, conducted on natural numbers. The tools known as *cyclic permutations* are used to build up a model, that predicts properties of a multi-dimensional assembly, based on the linear position of a logical marker, and the other way around. The cycles that connect instances of place-amount coincidences with each other, create in their standard form logical statements that are triplets, where each element of the triplet can have one of four forms. The interdependences are in need of professional visualization.

Keywords: DNA, Cycles, Logical First Section

1 Constructing the Model

We present an arithmetic tool. It is built on simple readings of values of $a+b=c$, which we sequence (sort, order) according to some aspects of the expression. One finds surprisingly complex interdependences resulting from simple sorting operations. The subject opens up a door to a new approach to information processing. Research has progressed to a stage, where visualization is necessary to proceed. The present paper is an invitation to professional artists of visualization of complex interdependencies.

1.1 Sizes and Extents.

The model to demonstrate, and define, in a deictic fashion, terms connected to the idea of *order* is built on natural numbers. The principles remain the same as we order a collection, irrespective of the cardinality n of the set, as long as n remains within some bounds $(\sim 6 < n < \sim 140)$. The main property of the collection is d, the number of different categories of (a,b). The number n of objects (rows in the table) is given by

$$n = d\,(d+1)/2 \qquad (1)$$

These are the triangular numbers. [1] That the triangular numbers give the possible sizes of models is an artefact of the generating algorithm, which is as follows:

1.2 Generating Algorithm

```
$\#d=16$
begin outer loop, $i:1,d$
        begin inner loop, $j:i,d$
                append new record
                write
                $a=i,\ b=j,\ c=a+b,\ k=b-2a,$
                $u=b-a,\ t=2b-3a,$
                $q=a-2b,\quad s=(d+1)-(a+b),$
                $w=2a-3b$
        end inner loop
end outer loop
```

There exists an optimal size for a set to utilize the accounting-translational relations among natural numbers to the maximum. If all circumstances are ideal, there exist surjective relations in both directions sequenced ↔ commutative, in dependence of the logical fragmentation of the collection into sub-collections that are sequential, commutative, or both. The fragmentation can be utilized to point out properties of multi-dimensional, commutative assemblies as implications of linear positions of elements with specific logical properties; the implications work of course both ways: the existence of specific properties of multi-dimensional commutative assemblies severely restricts possible properties of elements occupying specific linear places in the related, accounting-translationally equivalent sequence. The relation is shown in [2]. The numeric relations shown there are the reason we use 16 different versions of (a,b), and also the reason for not using more than 9 describing aspects of $a+b=c$, as $log(OEIS/A000041) \sim 13$ at the relevant value of $n \sim 67$.

The collection created such will now be sequenced, and the linear position of each of the elements registered, in each of the sorting (sequencing) orders. Not more than ~ 13 independent describing aspects can be used to describe commutative arrangements of symbols on a collection of ~ 67 elements, therefore combinations of 2 of 9 describing aspects as sorting keys will leave no non-redundant sequences undiscovered. We create *72 catalogued sorting orders* by using each of the 9 describing aspects once as the *first*, and once as the *second* sorting criterium. The table has now 136 rows and 9+72 columns.

1.3 Consolidating Logical Contradictions

The last of the preparatory steps to set up the model has to do with the logical contradictions arising from the differing linear positions assigned to the same element, in dependence of *which* of the sorting orders is in the present moment *relevant.* (If we line up the students once on their first name, and once on their family name, there will be in all probability differing linear positions in the two sorting orders for several of the students.) We extend the Wittgenstein set of logical sentences by allowing sentences describing such states of the world which are *not the case*. By knowing that *position(set S, element i, sorting order [α,β]) = j,* we can conclude that *sorting order [γ,δ]* is not the case. That, what is not the case, is the background to that, what is the case.

The numeric facts in the tables show, how the logical background can be consolidated with the classical foreground: into tautologies, compromises and discontinuities. The logical compromise between the contradicting statements: *pos()=i* ↔ *pos()=j* is accessible to imagination, if we see the element to be in transit, *en route*, under way. We cannot have explicit logical contradictions in a Wittgenstein system. The solution is to find a diplomatic compromise: if belligerent A states, that the right position of harbor for ship *e(a,b)* is in port Nr. *i,* while belligerent B states, hat the right harbor for that ship is port Nr. *j,* then a diplomatic compromise would propose that the ship is perpetually under way between ports Nr. *i,j.* This can be done by reading off the *cycles* that are the mechanism of a transition between *sorting order [α,β]* → *sorting order [γ,δ].* We generate the *Table of Movements* which is a step-by-step record of each movement *(from_linear_place, to_linear_place)* that is done by an element during a *reorder* from any of the *72 catalogued orders* into any of the other *71 catalogued orders.* The cycles have a literature in mathematics, their deictic definition is [3]. The table of movements has 347.616 rows. These we consolidate in a Table of Cycles, which is the actual tool we use.

We have to count in terms of cycles, because the traditional ways of enumerating logical objects have a slight bias. The improved method makes counting to be a three-step process: identifying the commutative symbols the elements carry, identifying the positions the elements occupy, match this occurrence to a natural number, somewhat more precise than the present method of identifying *how many* positions the elements occupy (and determining the *position* of an element from the *number* of identical units that make up the element). Without computers, there is no chance to milk out this last drop of information about an occurrence: tabulating the results is not possible with paper and pencil methods; for the drawing of the relevant Figures, professional capacities are needed.

1.4 Associations, Ideal and Actual Circumstances

Each element is a data depository, which registers, with which other elements it is associated. To be associated with other elements goes beyond being a member in the corpus of a specific cycle. The extent of the association of a new element added to a collection of elements among which associations already exist, is the extent in improvement of predictions caused by adding the new element as an additional search criterium. The manifold ways of the elements to be associated with each other, by rules provided by the natural numbers, appear to be the set of directing meta-principles that can be understood to be the grammar of logical sentences.

There are cycles that can co-exist. Then there are some, that cannot exist concurrently. The interplay is governed by symbols that are *concurrently sequential and commutative*. What we look for is collections of cycles that can coexist in specific slices of time in specific segments of space. That would constitute the ideal case, when all circumstances are permissive, where we observe combinatorial variants of one and the same tautology.

The symbols which denote the membership in a cycle are *concurrently sequential and commutative*. Elements with such symbols are needed to explain the correspondence between *sequentially ordered* logical symbols, like the codons of the DNA, and properties of *multi-dimensional commutative assemblies*, like the biochemical constituents of the organism. The symbols are commutative with respect to their property of pointing out a subset of the elements, for which the membership in a specific corpus is true, and they are sequential, as the members of the corpus of a cycle are sequenced among each other. The total number of distinct cycles is of no primary relevance, because many of the cycles are mutually exclusive.

The ideal case is then a local biotope, like a happy valley surrounded by uninhabitable wildernesses of many kinds. We shall discuss first the functioning of the model under ideal circumstances: this allows picturing theoretical genetics, information transmission, learning and the development of intelligence.

The numbers show clearly, that some of the compromises made by pushing explicit contradictions into the future, somewhere else, will not be sustainable, and a breakdown occurs. The last chapter deals with the circumstances being not of the ideal, but of the most probable types.

2 Ideal Circumstances

The memory functions, like genetics, only under optimal, ideal circumstances. A few drinks are sufficient to wreck the intellect, as are minimal influences sufficient to disturb fertility. The match between the packed-up, compressed, stored form of information, and its realization in the form of a multidimensional arrangement of symbols, is apparently subject to a stable constellation of circumstances, which provide the screen for a movie, in which sequences and mixtures interact [4] [5] [6]. If there are no stable walls of a cave, no shadows can be observed while they metamorphose into each other.

Main requirements of the idealized environment are:

- Standard reorders,
- Two, exact, Euclid-type rectangular spaces,
- One, inexact, Newton-like space,
- The existence of logical shadows,
- The existence of ties,
- The predictability of subsequent members of a cycle, based on previous members of the cycle.

These preconditions allow picturing logical processes that resemble rules assumed to be at work behind genetics and learning.

2.1 Standard Reorders and Spaces

Among the catalogued reorders, we find 10 that are lending themselves to be *standard reorders.* They move the elements of the set in 45 cycles of 3 elements each, and one cycle with one, stationary element, which we propose to call the *central element.* The standard cycles move each: $\sum a = 18, \sum b = 33$. Relative to these, the other cycles are {long, thick, fast, …}.

The standard reorders have furthermore the advantage of common axes, which allow creating *rectangular spaces* with 3-D coordinates of objects. There appear 2 such spaces, of which the axes are perpendicular and the planes of which are fixated by readings of $a+b=c$ according to some of their aspects. We call these the a-, and b-versions of Euclid spaces. Their axes are: $\{(a: a+b, a; b-2a, a; a-2b, b-2a), (b: a+b, b; b-2a, a-2b; a-2b, a)\}$. The position of an element in two sorting orders is given by its coordinates on a plane, the axes of which are the two sorting orders. The planar coordinates of an element mirror the two linear positions of the element *exactly.*

The two Euclid type spaces can be merged into one common, Newton type space, of which the axes are $\{a+b, b-2a, a-2b\}$. On each of the 3 planes of the Newton space, both of the axes are an inexact summary of two Euclid axes: so, every element can have *four* logically equivalent positions. (E.g. $a+b$ is an inexact summary of $\{a+b,a; a+b,b\}$, $b-2a$ is an inexact summary of $\{b-2a,a; b-2a,a-2b\}$, so the position of an element on the plane x: $a+b$, y: $b-2a$ can be any of $\{(x_1;y_1): (a+b,a;b-2a,a), (x_1;y_2): (a+b,a;b-2a,a-2b), (x_2;y_1): (a+b,b;b-2a,a), (x_2;y_2): (a+b,b;b-2a,a-2b)\}$.)

It appears that theoretical genetics is based on arithmetic rules of sequenced collections, where 3 standard reorders connect 3 planes, on each of which one of 4 possible positions can be pointed out by the position of elements in two linear sequences. In a strict logical sense, one spatial moment is a sequenced succession of three planes, because the commutative moment of “now” is a plane across the temporal sequence, which the numbers show to be a numeric sequence connecting three planes in two spaces; of these, our neurology and psychology create the impression of one common space, of which we believe the constituents to be sub-spaces, although, in fact, the common, encapsulating Newton space is less organically rooted in the complex inner associations of $a+b=c$, than the two two-thirds-spaces, in which the planar positions of the elements are tautologic implications of their respective linear positions. We live in two two-thirds-spaces, although we may believe, and have reason to believe, that we live in one common space, which splits up into two almost-exactly-half-spaces.

2.2 Learning

The background to that, what is the case, is the medium to register and carry information. Those elements of a cycle, that have already been or have not yet been, are not the case, but predictions can be made about them. We can conclude, based on occurrences of *{elements, places, temporal sequence},* which of any reorganizations can be happening presently, which are excluded and which remain possible.

Those cycles, the existence of which is explicitly excluded by the facts of elements $\{e_i\}$ being on places $\{p_i\}$ are called the *shadow* of what is the case. Neighbors of the shadow are then also associated, in their own way, with that, what is the case.

It is possible to register a new, identifying symbol that describes the present state by using the unordered state of elements that are in a *tie.* (The members of the rowing team stand all on step 1 of the podium. If they stand there internally sorted, according to their ranks in discus-throwing, we will conclude that a competition, in discus-throwing, had taken place in the not so distant past.) Elements of the background are presently not *relevant*, and this common, commutative symbol makes them all to be a part of a tie. Under ideal circumstances, to one state of the world belongs one shadow of it, and the potential neighborhoods among elements that are not the case keep their neighborhood relations after repetitions. Then, it is possible to retrieve experiences relating to a previous occurrence of this state of the world, as remembered by the content of the neighbors of its shadow.

To learn is to improve the accuracy of predictions about what will happen next. Our neurology obviously reckons with logical processes that have predictable continuations. Biologic processes are cyclic, periodic, rhythmic; a period is a cycle that includes other cycles, the rhythm is the interference pattern caused by cycles within periods. The ability to conclude from the rhythm of smaller changes (e.g. day/night) within larger changes (e.g. lunar phases) to the predictable appearance of specific occurrences is a very basic aptitude of organisms. The nervous system makes predictions based on cycles, rhythms and periods. The succession of elements according to the rules of succession that constitute a cycle is a prediction about the elements that follow.

The ideal case deals with predictions in a stable spatial structure. In that case, both the *where* and the *when* are a given, the *what* is the content of the message. The actual case is less accommodating than the ideal case, and there appear less or more than one contestants for one and the same place.

3 Actual Circumstances

In its present, introductory phase, the tool may evoke associations in some to a Rorschach plate. It is one's own phantasy, creativity and intuition, that determine the ways of reading and interpreting the numbers. Presenting the relations, by graphical means, among natural numbers to be dependent of sorting and ordering, can be a great help while building up an inner order among the concepts in the user's brain. The following points need professional attention:

- Spatial fixation
- Concept of mass
- Two transcendent planes
- Tolerance intervals

3.1 Agglomeration in Space : Mass

Those triplets of elements $\{e_1, e_2, e_3\}$, that are a standard cycle in a standard, spatial reorder, may also appear embedded in other, longer cycles. The spatial effect is identical, whether this happens within 1, or rather in 2, or even 3 independent cycles that run concurrently, but independently of each other. In these cases, the spatial fixation appears as an independent property of the individual cycles, which – without the occurrence of specific other elements being their neighbors – would otherwise not have specific spatial properties.

The occurrence of space-generating standard triplets of elements $\{e_1, e_2, e_3\}$ being but a small portion of all occurrences, one can visualize a general inevitability of traffic jams, pile-ups at specific coordinates in space. Cycles running, as they are, at differing speeds, there appears necessarily a deceleration at coordinates that have to be cleared by differing cycles. We state, that the pile-ups, agglomerations, have properties that allow recognizing similarities and differences among them.

The general property of all spatial agglomerations is that there is an additive load to the congregation of cycles that agglomerate at spatial coordinates. The expressions $\sum a$, $\sum b$ over each cycle can be used as an allegory of the concept of a "mass" of a cycle. Actual, measurable appearances will exist at points of deceleration, where material mass appears to come into existence, and at points of acceleration, where material mass appears to disappear from existence.

3.2 Logical Archetypes : Chemical Elements

The unavoidable agglomerations in space can be classified, typified, categorized on their differing properties, e.g. on their genesis or morphology. The aggregated loads can be distinguished, As the granularity they cause is an implication of $a+b=c$, they can be called *logical archetypes*. The logical archetypes can well serve as an allegory of the concepts of *chemical elements.*

3.3 Two Planes More

The standard reorders have 10 different types. Of these, twice 3 have been mentioned: these create the rectangular spaces we are familiar with. These are connected to the following aspects of *a+b=c: {(a+b), (b-2a), (a-2b)}*. There remain 4 more standard reorders, of which 2 planes with common axes can be constructed. These are: *{(a), (b-a)}*. The two planes transcend the orthogonal spaces; they also have the effect of assigning places within the rectangular spaces, but these places are only two-dimensionally fixated. Whether the places, which the two extra planes assign to elements, are an allegory for "the elements should/could also be here" or can serve as allegories for the concepts of magnetism and electricity, can be discussed, as soon as professionally constructed illustrations are available of the paths convoys (strings, chains, filaments, cycles) occupy in space.

3.4 Overall Target Values and Tolerance Ranges

It appears that a concept of a Grand Total of dislocations can be an arguable idea. If the tool stands still, each element has an *expected linear place* in each of the orders imposed by two of the aspects of *a+b=c*, and an *observed linear place* in each of the orders imposed by two different aspects of *a+b=c*.

Having an overall, general value, established on a dimension (which may be related to χ^2), that can be interpreted as conformity, consistency, inner truth, potential foreground, or the like, allows support for ideas as:

- Nature maintains an order,
- The strictness of order can range from rigid to appearing chaotic,
- There is a natural tendency to continuity and stability,
- There is a range of tolerance before a threshold is hit.

One can use the inner numeric inexactitudes of the classical counting system to establish tolerance ranges around target – transformation – levels. The proposition is to use as the basis of counting the differing maximal numbers of logical relations possible on *n* objects, when these are commutative or sequential, and to count back to properties of objects: to deduct the number of objects from the basis of a given, fixed number of logical relations. The translational equivalences that appear as we reckon back from logical relations to properties of elements can appear in various forms regarding the number, position, sequence of elements.

May the questions raised in this paper, fundamental and technical, appear inviting for further research.

References

1. OEIS A000217. Available online: www.oeis.org/A000217 (accessed on 25 May 2018).
2. OEIS A242615. Available online: www.oeis.org/A242615 (accessed on 25 May 2018).
3. OEIS A235647. Available online: www.oeis.org/A235647 (accessed on 25 May 2018).
4. Javorszky, K. Learn to Count in Twelve Easy Steps: Webinar in FIS: listas.unizar.es/pipermail/fis/, (2013) available online: www.tautomat.com (accessed on 25 May 2018)
5. Javorszky, K. Transfer of Genetic Information: An Innovative Model, available online: http://www.mdpi.com/2504-3900/1/3/222 (2017) (accessed on 25 May 2018)
6. Javorszky, K. Natural Orders, De Ordinibus Naturalibus; Morawa: Vienna, Austria, ISBN 978-3-99057-139-2. (2016)
7. Javorszky, K. Biocybernetics : A Mathematical Model of the Memory; Wien: Eigenverlag; Oesterr. Nationalbibliothek: http://data.onb.ac.at/rec/AC01018124 (1985)
8. Javorszky, K. Summary of lectures held about granularity algebra at Grupo Bioinformatica at Centro Politecnico Superior de la Universidad de Zaragoza; Bergheim : Mackinger; ISBN: 3900676070, Oesterr. Nationalbibliothek: http://data.onb.ac.at/rec/AC01333418 (1995)
9. Javorszky, K. Principia philosophiae naturalis : (draft); Bergheim : Mackinger; ISBN: 3900676062, Oesterr. Nationalbibliothek: http://data.onb.ac.at/rec/AC01116989 (1995)
10. Javorszky, K. A Rational Model In Theoretical Genetics. tripleC, ISSN: 1726-670X, Vol 2 No 1; https://doi.org/10.31269/triplec.v2i1.13 (2004)
11. Javorszky, K. Essay On Order; International Journal “Information Theories and Applications”, Vol. 21, Number 1, p76-84 (2014) (accessed on 25 May 2018)
12. Javorszky, K. Accounting in Theoretical Genetics; International Journal “Information Theories and Applications”, Vol. 19, Number 1, 100. p86-98, www.foibg.com/ijita/vol19/ijita19-01-toc.pdf (2012) (accessed on 25 May 2018)
13. Javorszky, K. Information Processing in Auto-regulated Systems, Entropy, 5, p161-192. https://doi.org/10.3390/e5020161 (2003) (accessed on 25 May 2018)
14. Javorszky, K. Logical Structure Of Chromosomes; International Journal “Information Theories and Applications”, Vol. 18, Number 1, p69-81 www.foibg.com/ijita/vol18/ijita18-1-p06.pdf (2011) (accessed on 25 May 2018)
15. Javorszky, K. Unique Identification of States of Sets, In: 6th International Conference on Applied Informatics, Eger, Hungary, January 27–31, 2004; icai.ektf.hu/pdf/ICAI2004-vol1-pp229-234.pdf (2004) (accessed on 25 May 2018)
16. Javorszky, K. Explaining Bio-coding: The Concept of Stability; In: Petitjean, M (Ed.) http://www.mdpi.org/fis2005/proceedings.html. (2005) (accessed on 25 May 2018)
17. Javorszky, K. Minisymposium: Approaches to Autoregulation; In: SMB Convention, Ann Arbor, July 2004; http://www.math.lsa.umich.edu/SMB2004/SMBindex.html (2004) (accessed on 25 May 2018)
18. Javorszky, K. A Rational Model of the Information Processing in Theoretical Genetics, Session 7.1; In: CASYS 03: Sixth International Conference on Computing Anticipatory Systems, Liège, Belgium, August 11-16, 2003 (2003) (accessed on 25 May 2018)
19. Javorszky, K. The Logic of Self-sustaining Sampling Systems; In: http://ipcat95.csc.liv.ac.uk/IPlinks.html (1995) (accessed on 25 May 2018)

Section 8
Discrete Geometry and Topology

Endpoint-Based Thinning with Designating Safe Skeletal Points

Kálmán Palágyi and Gábor Németh
Department of Image Processing and Computer Graphics,
University of Szeged, Szeged, Hungary;

Abstract. Thinning is an iterative object reduction: border points that satisfy some topological and geometric constraints are deleted until stability is reached. If a border point is not deleted in an iteration, conventional implementations take it into consideration again in the next step. With the help of the concepts of a 2D-simplifier point and a weak-3D-simplifier point, rechecking of some 'survival' points is not needed. In this work an implementation scheme is reported for sequential thinning algorithms, and it is shown that the proposed method can be twice as fast as the conventional approach in the 2D case.

The full text will be available in the edited book "Computational Modeling of Objects Presented in Images. Fundamentals, Methods, and Applications", eds. Barneva R.P., Brimkov V.E., Kulczycki P., Tavares J.M.R.S., to be published by Springer in the *Lecture Notes in Computer Science* series soon.

Maximal P-simple Sets on (8,4) Pictures

Péter Kardos and Kálmán Palágyi
University of Szeged, Szeged, Hungary

Abstract. Bertrand proposed the notion of a P-simple set for constructing topology-preserving reductions. In this paper, we define the maximalness of a P-simple set, give a new sufficient condition for topology-preserving reductions acting on (8,4) pictures on the square grid, and it is proved that this condition designates a maximal P-simple set.

The full text will be available in the edited book "Computational Modeling of Objects Presented in Images. Fundamentals, Methods, and Applications", eds. Barneva R.P., Brimkov V.E., Kulczycki P., Tavares J.M.R.S., to be published by Springer in the *Lecture Notes in Computer Science* series soon.

An immersed boundary approach for the numerical analysis of objects represented by oriented point clouds

László Kudela[1], Stefan Kollmannsberger[1], and Ernst Rank[1,2]
[1] Chair for Computation in Engineering, Technische Universität München,
Arcisstr. 21, 80333 München, Germany;
[2] Institute for Advanced Study, Technische Universität München, Germany;

Abstract. This contribution presents a method aiming at the numerical analysis of solids whose boundaries are represented by oriented point clouds. In contrast to standard finite elements that require a boundary-conforming discretization of the domain of interest, our approach works directly on the point cloud representation of the geometry. This is achieved by combining the inside-outside information that is inferred from the members of the point cloud with a high order immersed boundary technique. This allows for avoiding the challenging task of surface fitting and mesh generation, simplifying the image-based analysis pipeline drastically. We demonstrate by a numerical example how the proposed method can be applied in the context of linear elastostatic analysis of solids.

The full text will be available in the edited book "Computational Modeling of Objects Presented in Images. Fundamentals, Methods, and Applications", eds. Barneva R.P., Brimkov V.E., Kulczycki P., Tavares J.M.R.S., to be published by Springer in the *Lecture Notes in Computer Science* series soon.

Structuring digital spaces by closure operators associated to n-ary relations

Josef Slapal

Brno University of Technology, 616 69 Brno, Czech Republic;

Abstract. We introduce an isotone Galois connection between n-ary relations and closure operators on a set for every integer $n > 1$. We focus on certain n-ary relations on the digital line $\mathbb{Z}$ and study the closure operators on the digital plane $\mathbb{Z}^2$ that are associated, in the Galois connection introduced, to special products of pairs of the relations. These closure operators, which include the Khalimsky topology, are shown to provide well behaved connectedness, so that they may be used as background structures on the digital plane for the study of digital images.

The full text will be available in the edited book "Computational Modeling of Objects Presented in Images. Fundamentals, Methods, and Applications", eds. Barneva R.P., Brimkov V.E., Kulczycki P., Tavares J.M.R.S., to be published by Springer in the *Lecture Notes in Computer Science* series soon.

Section 9
Computer Vision

Graph Cutting in Image Processing handling with Biological Data Analysis

Mária Ždímalová[1], Tomáš Bohumel[1], Katarína Plachá-Gregorovská[2], Peter Weismann[3],
and Hisham El Falougy[3]

[1] Slovak University of Technology in Bratislava;
[2] Institute of Experimental Pharmacology and Toxicology Slovak Academy of Science;
[3] Institute of Anatomy, Faculty of Medicine, Comenius University of Bratislava;

Abstract. In this contribution we present graph theoretical approach to image processing focus on biological data. We use the graph cut algorithms and extend them for obtaining segmentation of biological cells.We introduce completely new algorithm for analysis of the resulting data and sorting them into three main categories, which correspond to the certain type of biological death of cells, based on the mathematical properties of segmented elements.

The full text will be available in the edited book "Information Technology, Systems Research and Computational Physics", eds. Kulczycki P., Kacprzyk J., Kóczy L.T., Mesiar R., Wisniewski R., to be published by Springer in the *Advances in Intelligent Systems and Computing* series soon.

Comparison of 3D graphics engines for particle track visualization in the ALICE Experiment

Piotr Nowakowski[1], Julian Myrcha[1], Tomasz Trzciński[1], Łukasz Graczykowski[2]
and Przemyslaw Rokita[1] for the ALICE Collaboration

[1]Institute of Computer Science, [2]Faculty of Physics
Warsaw University of Technology, Poland,
pnowakow@mion.elka.pw.edu.pl, jmy@ii.pw.edu.pl, t.trzcinski@ii.pw.edu.pl,
lukasz.graczykowski@pw.edu.pl, p.rokita@ii.pw.edu.pl

Abstract. In this paper, we examine possible ways of upgrading the 3D graphics module in the Event Display, a standalone application used to visualize the processes occurring in the ALICE experiment at CERN. This application displays a graphical representation of tracks of elementary particles as measured with the detector and recorded during proton-proton, lead-lead or proton-lead collisions. These visualizations are crucial for monitoring the condition of data acquisition and event reconstruction processes for which they heavily rely on an outdated version of the OpenGL graphics engine. In this work, we analyze the advantages and disadvantages associated with upgrading the graphics engine to a new framework, be it a new version of the OpenGL engine or Vulkan. To that end, we present an extensive comparative evaluation between the new OpenGL and Vulkan graphics libraries and draw conclusions regarding their implementation within the frames of the Event Display application.

1 Introduction

ALICE (*A Large Ion Collider Experiment*) [1] is one of the four main experiments of the LHC (*Large Hadron Collider*) [2]. Its primary goal is to study the physics of ultra-relativistic heavy-ion collisions (lead–lead (Pb–Pb) in the case of LHC) in order to measure the properties of the Quark-Gluon Plasma [3,4]. ALICE is a complex detector consisting of 18 different sub-detectors which register signals left by traversing particles. Tracking (detection of particle trajectories, also referred to as "tracks") in ALICE is performed by three sub-systems, that is the Inner Tracking System (ITS) [5], the Time Projection Chamber (TPC) [6], and the Transition Radiation Detector (TRD) [7]. The TPC, a gaseous detector extending in azimuthal plane from 0.8 m to 2.5 m from the interaction point, is the main tracking device of the experiment.

In this work, we focus on one of the most crucial software applications used in the ALICE Experiment, the Event Display. This software is capable of rendering reconstructed particle tracks on a screen (see Figure 1). These tracks are computed from measurements done by the TPC alone or both the ITS and the

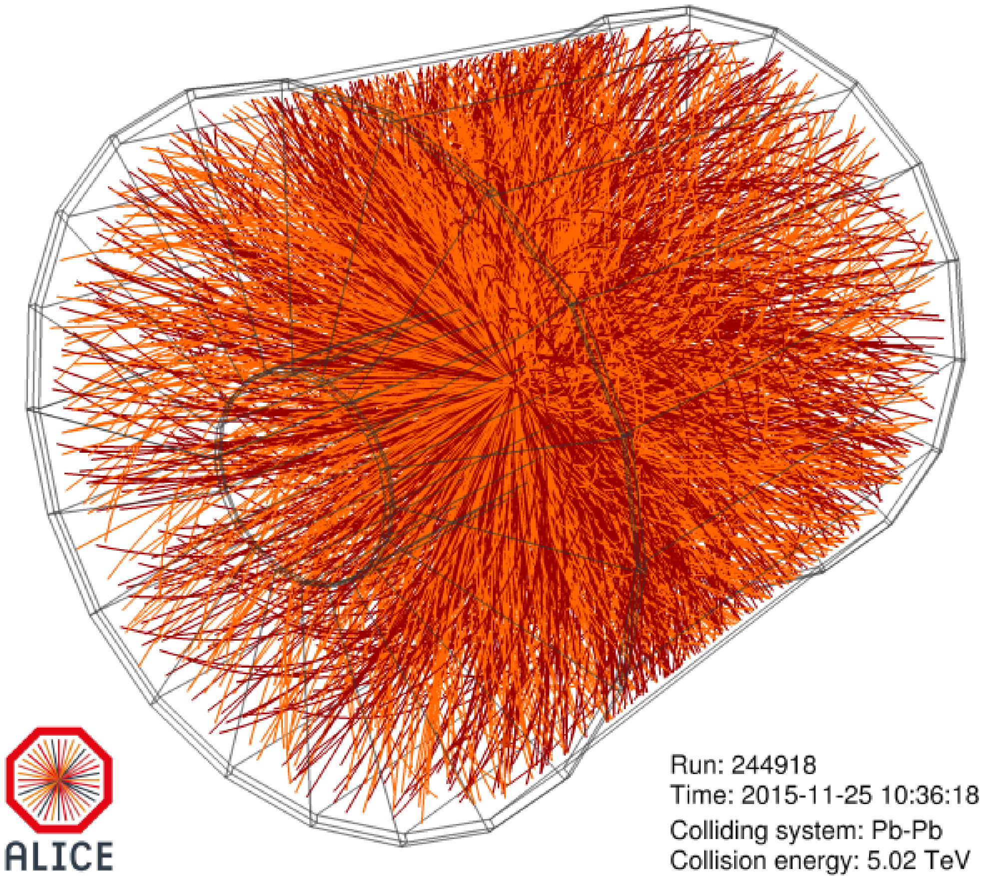

Fig. 1: Visualization of charged particle tracks in the ALICE TPC detector from the Pb–Pb collision at $\sqrt{s_{\mathrm{NN}}} = 5.02$ TeV [8].

TPC. Data for visualization can be sourced either from a database (past collisions) or from a "live" measurement. In this case data are gathered as soon as a partial reconstruction of the tracks collected during data taking is available. The second application is more important, because any hardware or software faults in the detector can lead to wrong, *i.e.* physically impossible, reconstruction results, which can easily be spotted by the monitoring team. Instantaneous error detection is crucial for the functioning of the entire system as, in case of any problems, the data collection process can be restarted thereby avoiding unnecessary corruption of the data. In this case, instead of loosing the data of an entire run of up to 38 hours, only a small portion of the corrupted data is lost.

The current implementation of the Event Display's 3D rendering module uses OpenGL 1.x API (*application programming interface*) which was released more than a decade ago and it is no longer supported by many of the recent visualization libraries. For this very reason an upgrade of the existing implementation to a new graphic engine is planned. In this paper, we investigate possible approaches of performing this upgrade. More precisely, we analyze the performances of the two most prevalent graphical APIs currently available on the market: OpenGL

4.x and Vulkan. Although alternative solutions exist *e.g.* DirectX or Metal, they are vendor specific, meaning that they offer support for a limited number of hardware configurations and we therefore do not consider them in this work. To evaluate the performances of the tested APIs, we developed a set of sample applications using both OpenGL and Vulkan, and compared their results in terms of efficiency and computational cost.

The remainder of this paper is organized in the following way. In the next section, we outline the graphics interfaces that we used in this work, highlighting their advantages and disadvantages. Next, we describe the sample applications we developed for performing experiments. Finally, we present our evaluation testbed and the results of the performed experiments. In the last section, we conclude this work by recommending one of the tested interfaces.

2 Description of Graphics Interfaces

2.1 OpenGL

OpenGL was created in 1992 by Silicon Graphics, Incorporated and is maintained to this day (in 2017 version 4.6 of the specification was released) by OpenGL ARB (*Architecture Review Board*), consisting of the biggest IT companies. In 2006 ARB was made part of a bigger organization called Khronos Group.

OpenGL [9] is based on a state machine called a *context* — global for the application list of settings which affects the way objects are displayed on screen. Ownership of the context is exclusive for a single thread of the application. This ownership can be passed on to other threads, but the context can not be accessed by two threads simultaneously. Because of that it is not possible to use capabilities of current multicore processors to speed up the object drawing itself. Additionally OpenGL functions are blocking, holding the thread execution until their task is completed — this thread will not be able to do any other computing in the meantime, while communication with the GPU is ongoing.

2.2 Vulkan

Vulkan [10] is a new graphic API released in 2016 by the Khronos Group. Vulkan is a low-level API, which provides more control of the graphics card to the programmer, but also requires from him to implement more code — he has to handle some tasks that are taken care of by the driver in OpenGL, such as memory management of the graphics card, synchronization or swapping display buffers for the operating system. Although this makes the application itself more complicated, it significantly simplifies the driver, which in turn can be more aggressively optimized by the graphics card manufacturer.

Vulkan was designed with multi-threading in mind, as it lacks a global context. Configuration is instead split into many Vulkan objects, which can be safely modified in different threads.

Rendering in Vulkan is realized by creating and filling (”recording”) command buffers. Its contents are then placed in the task queue of the graphic card.

Command buffers can be rerecorded in every frame (similarly to how OpenGL operates). However, if it is not necessary (description of a particular object has not changed between frames) they can be reused (queued again), saving a lot of CPU time. Queueing of command buffers has to be performed on a single (usually main) thread, but the recording can be realized on multiple threads simultaneously. This design allows for participation of all processor cores in the drawing task, improving the overall performance.

3 Implementation

Graphics APIs provide a couple of ways that can be used to render an identical image on the screen, but varying in efficiency of GPU utilization, resulting in different performances.

Four graphics interface versions have been developed, starting from a naive implementation (for gauging performance when the code is not optimized) and ending with the most efficient implementation that we could come up with.

3.1 OpenGL

Version A treats reconstructed tracks as separate objects, thus allocating separate set of graphic card resources (vertex buffer, index buffer, color variable) for each one. Additionally, every track is drawn by a separate command. This implementation requires multiple OpenGL context alterations (mainly buffer binding) during rendering a single frame, which is costly — this should be reflected in poor performance.

Main feature of version B is a reduction of the amount of buffer binding while keeping separate drawing calls for each track. All vertex data are aggregated into a single buffer. Additionally, tracks are sorted according to the particle type, which allows configuration of the line color exactly once per group of tracks instead of for every individual track.

In previous two versions each track is drawn via an individual function call. Because a single collision is usually made of thousands of tracks, this adds up to a lot of avoidable, repetitive work for the graphic driver performed every frame. In version C a different drawing function was used, which can visualize the whole collision in a single call. It operates on an array of parameters (where every set of parameters represents a single drawing operation, like in previous versions).

Version C has reduced the number of drawing calls per frame to one, but only from the programmer's perspective — the driver still has to traverse the parameter array and dispatch drawing commands to GPU one by one. It is possible to store the parameters directly in memory buffer of the GPU and then just refer to it, avoiding most of the data transfer when a draw command is enqueued. This way of drawing is called *indirect*, which is a main feature of version D.

3.2 Vulkan

Vulkan sample programs allow to choose a track drawing strategy — with command buffers cleared and recorded for every frame (the *dynamic* version) or recorded only once (the *static* version). The *static* version takes full advantage of command buffering available in Vulkan, while the *dynamic* version tries to simulate rendering in the way of OpenGL in order to compare the two interfaces on a more equal basis.

Versions A, B and D use the same rendering techniques as their OpenGL counterparts, but implemented using the Vulkan API. Since there is no Vulkan equivalent of the drawing call used in OpenGL version C, an approach unique to Vulkan was tested here.

Version C is testing multithreading capabilities of Vulkan by utilizing *secondary* command buffers. *Secondary* command buffers can not be directly placed in the rendering queue of the graphics card, but can be executed as a part of a normal command buffer (which is called *primary*) and inherit some of the pipeline settings of its parent. Although a single command buffer (of any of the two types) can not be written to by more than one thread simultaneously, a piece of rendering work (*e.g.* an object in the virtual world) can be split into multiple secondary command buffers, recorded on multiple threads and then referenced in a single primary command buffer.

3.3 Track visualization

A single trajectory (in the ALICE track reconstruction system) is represented via a list of points describing positions in space where a particle was at a given moment. We use these data to construct composite Bézier curves that are displayed on the screen.

To calculate control points for the curves we have used two different algorithms, one created by Rob Spencer [11] (referred to as *Algorithm #1*) and the other created by John Hobby [12] (referred to as *Algorithm #2*). Curves produced by these algorithms on the same input data have a slightly different shape as shown in Figure 2.

Additionally, control points can be calculated beforehand via the main processor and supplied to the graphic card or calculated on the graphic card directly. These options are labeled as *CPU* and *GPU* in the experimental results, respectively.

Taking both features mentioned above into account, there are four possible configurations of a single implementation variant. Experimental results have been grouped accordingly (see next section).

4 Experiments

4.1 Hardware

Sample programs were tested on Windows 10 with a NVIDIA 388.71 driver on two machines:

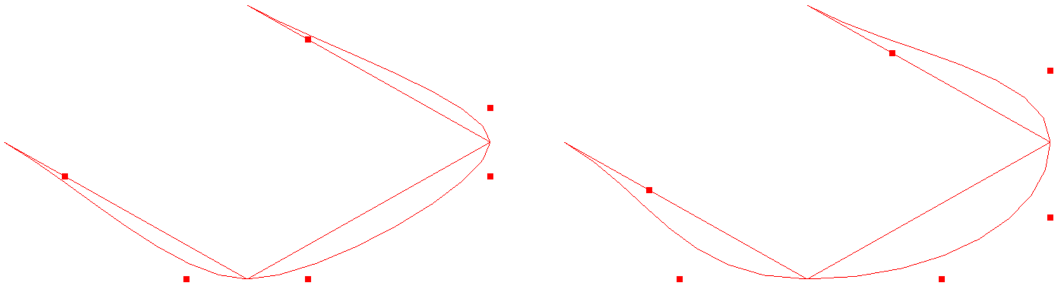

(a) Algorithm #1

(b) Algorithm #2

Fig. 2

- desktop computer — with quad-core Intel i7-4771 processor with 3.50 GHz clock, NVIDIA GeForce 780 GTX graphics card and 32 GB of RAM,
- notebook — with quad-core Intel i7-3610QM processor with 2.40 GHz clock, NVIDIA GeForce GTX 660M graphics card and 8 GB of RAM.

4.2 Performance tests

Performance of every implementation was measured by counting the number of frames rendered by the graphics card in a 10 seconds time period, determined by high-precision clock routines provided by the Windows operating system. In order to reduce the randomness of the results, each test was repeated 10 times and then averaged.

	Alg.#1, CPU	Alg.#2, CPU	Alg.#1, GPU	Alg.#2, GPU	**Average**
Variant A	63.26	64.85	64.96	61.23	**63.58**
Variant B	746.83	734.75	738.00	734.21	**738.45**
Variant C	1078.75	1059.32	1079.91	873.36	**1022.84**
Variant D	1251.56	1253.13	1233.05	997.00	**1183.69**

Table 1: Performance of OpenGL implementations on desktop computer in FPS (frames per second). “Alg. #1” is Algorithm #1, “Alg. #2” is Algorithm #2.

Table 1 presents OpenGL performance measurements gathered on the desktop computer. The biggest gain in performance (around twelve times increase in achieved frames per second) occurs between versions A and B, where the simplest optimization attempt was made (reduction of OpenGL context changes). In subsequent implementations the performance has also increased, although on a smaller scale — around 38% and 15% (if compared to the preceding version), respectively.

	Alg.#1, CPU	Alg.#2, CPU	Alg.#1, GPU	Alg.#2, GPU	**Average**
Variant A	29.21	28.95	28.36	27.88	**28.60**
Variant B	200.60	198.89	198.26	192.57	**197.58**
Variant C	224.82	226.04	225.33	213.49	**222.42**
Variant D	226.40	224.52	223.16	214.45	**222.13**

Table 2: Performance of OpenGL implementations on notebook computer in FPS (frames per second). “Alg. #1” is Algorithm #1, “Alg. #2” is Algorithm #2.

Table 2 presents OpenGL performance measurements gathered on the notebook computer. Like in the previous case, the biggest gain is achieved between implementation A and B (six fold increase). Subsequent implementations in this case, however, have not improved the performance very much — there is a small 12% increase between version B and C, while C and D are in a practical sense equal.

	Alg.#1, CPU	Alg.#2, CPU	Alg.#1, GPU	Alg.#2, GPU	**Average**
	dynamic				
Variant A	532.77	543.18	503.27	442.28	**505.38**
Variant B	1124.86	1116.07	1113.59	1108.65	**1115.79**
Variant C	1103.75	1131.22	1109.88	1101.32	**1111.54**
Variant D	1193.32	1169.59	1201.92	1182.03	**1186.72**
	static				
Variant A	1162.79	1196.17	1201.92	1204.82	**1191.43**
Variant B	1203.37	1203.37	1196.17	1184.83	**1196.94**
Variant C	1173.71	1203.37	1194.74	1191.90	**1190.93**
Variant D	1206.27	1209.19	1219.51	1197.60	**1208.15**

Table 3: Performance of Vulkan implementations on desktop computer in FPS (frames per second). “Alg. #1” is Algorithm #1, “Alg. #2” is Algorithm #2.

Table 3 presents Vulkan performance measurements gathered on the desktop computer.

Usage of the API in a style similar to OpenGL (the *dynamic* version) suffers from a similar bottleneck, as seen in the difference in performance between version A and B. However, the sample programs are running faster overall, especially the less optimized versions. As in OpenGL, a variant that uses the indirect rendering technique is the fastest. Surprisingly, the variant that uses multithreading achieve worse results than variant B.

When command buffers are not recorded for every frame (the *static* version), sample programs perform almost equally as well (with the exception of variant C, which also in this case runs slower).

Vulkan implementation, in the best case, is a little (around 2%) faster than the best implementation of OpenGL on the desktop computer.

	Alg.#1, CPU	Alg.#2, CPU	Alg.#1, GPU	Alg.#2, GPU	**Average**
	dynamic				
Variant A	157.80	158.86	156.08	156.42	**157.29**
Variant B	193.12	193.20	189.29	188.537	**191.04**
Variant C	193.65	193.46	189.00	188.75	**191.22**
Variant D	200.40	200.20	194.74	196.31	**197.91**
	static				
Variant A	201.33	201.65	196.81	196.19	**199.00**
Variant B	200.44	199.64	196.04	197.32	**198.36**
Variant C	201.94	201.41	196.81	196.58	**199.18**
Variant D	199.28	199.16	195.20	196.77	**197.60**

Table 4: Performance of Vulkan implementations on notebook computer in FPS (frames per second). "Alg. #1" is Algorithm #1, "Alg. #2" is Algorithm #2.

Table 4 presents Vulkan performance measurements gathered on the notebook computer. The results are similar to those found in Table 3. However, the difference in speed between variant A and B in the *dynamic* version is significantly smaller (on desktop machine performance gain is around 121%, while here it is only 21%) and the best implementation is not as fast as the best OpenGL implementation on the same machine.

Figure 3 presents the gathered data in a form of a graph. As can be seen, implementations that depend on repeated submission of drawing commands (*dynamic* Vulkan and all of OpenGL) achieve better performance at each optimization step. However, in the case of *static* Vulkan implementations the performance is almost constant, no matter if the code is optimized or not.

Additionally, the computer with a better GPU benefits from the optimization far more than the computer with an inferior version — every implementation with the latter (excluding "naive" version A) is running at around 180 frames per second, while with the former version the performance varies from around 60 frames per second to over 1200 frames per second.

4.3 Difficulty of usage

Difficulty of usage as a trait of programming interface is a subjective matter and as such is hard to measure, but it has an influence on the speed of application development. We tried to estimate this by counting the number of lines of code used in our implementations.

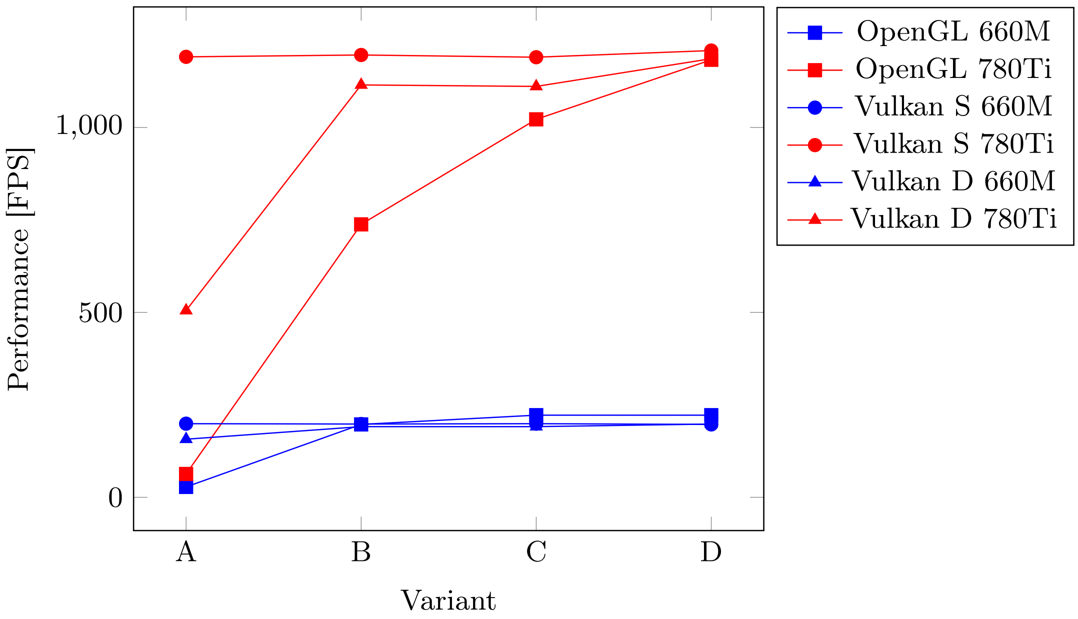

Fig. 3: Measured performance in FPS (frames per second). "Vulkan S" stands for *static* (*i.e.* command buffers recorded only once) while "Vulkan D" represents *dynamic* (*i.e.* command buffers recorded every frame).

Table 5 presents the gathered data. Only A, B and D variants are taken into account, because they use equivalent rendering techniques in both OpenGL and Vulkan. The biggest difference in length occurs in a piece of code that is shared between implementations using the same interface (which handles proper 3D initialization, shader loading, memory management, framebuffer swapping etc.). Sections containing only drawing code (labeled *RendererX*) are longer as well, but not nearly as much (around 40%). Taking everything into account, Vulkan implementation is 80% longer than OpenGL.

Module	OpenGL	Vulkan
Track loading	565	565
Common code	828	2272
RendererA	265	377
RendererB	301	441
RendererD	316	432
Sum	2275	4087

Table 5: Number of code lines.

5 Conclusion

According to the experimental results the application performance is affected mainly by the way it was implemented and not by the chosen graphics API. The most advanced implementation (implementation D) in both OpenGL and Vulkan version on both computers achieves similar rendering speeds (difference is about 10%). Additionally neither API was found to be faster (OpenGL was faster on notebook while Vulkan on desktop). This means that there is a slight variance on how good the graphics driver performs on different hardware configurations. Therefore a simpler API should be selected, as this would reduce development time. OpenGL is in this case considered to be superior.

We have measured FPS in a scenario where only track data are displayed. If this was the only task of the Event Display, almost all compared implementations would be accepted, as rendering speeds are 3 times faster than the required 60 FPS. This is however not the case — the program has other data to display which also consumes time. Track rendering optimization provides more time for other computations.

Acknowledgements

The authors acknowledge the support from the Polish National Science Centre grant no. UMO-2016/21/D/ST6/01946.

References

1. K. Aamodt *et al.*, “The ALICE experiment at the CERN LHC,” *JINST*, vol. 3, p. S08002, 2008.
2. L. Evans and P. Bryant, “LHC Machine,” *JINST*, vol. 3, p. S08001, 2008.
3. E. V. Shuryak, “Quark-Gluon Plasma and Hadronic Production of Leptons, Photons and Psions,” *Phys. Lett.*, vol. 78B, p. 150, 1978. [Yad. Fiz.28,796(1978)].
4. J. Adams *et al.*, “Experimental and theoretical challenges in the search for the quark gluon plasma: The STAR Collaboration’s critical assessment of the evidence from RHIC collisions,” *Nucl. Phys.*, vol. A757, pp. 102–183, 2005.
5. G. Dellacasa *et al.*, “ALICE: Technical Design Report of the Inner Tracking System (ITS),” 1999.
6. G. Dellacasa *et al.*, “ALICE: Technical Design Report of the Time Projection Chamber,” *CERN-OPEN-2000-183, CERN-LHCC-2000-001*, 2000.
7. P. Cortese, “ALICE: Technical Design Report of the Transition Radiation Detector,” 2001.
8. A. Collaboration, “ALICE event display of a Pb-Pb collision at 2.76A TeV.” https://cds.cern.ch/record/2032743?ln=en, 2015.
9. G. Sellers, R. Wright, and N. Haemel, *OpenGL Superbible: Comprehensive Tutorial and Reference.* Addison-Wesley Professional, 7th ed., 2015.
10. G. Sellers and J. Kessenich, *Vulkan Programming Guide: The Official Guide to Learning Vulkan.* Always learning, Addison Wesley, 2016.
11. R. Spencer, “Spline Interpolation.” http://scaledinnovation.com/analytics/splines/aboutSplines.html, 2010.

12. J. Hobby, “Smooth, Easy to Compute Interpolating Splines,” *Discrete & Computational Geometry*, pp. 123–140, June 1986.

A methodology for trabecular bone microstructure modelling agreed with three-dimensional bone properties

Jakub Kamiński, Adrian Wit, Krzysztof Janc, and Jacek Tarasiuk
Faculty of Physics and Applied Computer Science (WFiIS),
AGH âĂŞ University of Science and Technology, al.Mickiewicza 30, 30-059 KrakÃşw, Poland;

Abstract. Bone tissue is a structure with a high level of geometrical complexity as a result of mutual distribution of a large number of pores and bone scaffolds. For the study of the mechanical properties of the bone, there is a demand to generated microstructures comparable to trabecular bone with similar characteristics. Internal structure of the trabecular and compact bone has a high impact of their mechanical and biological character. The novel methodology for the deïňĄnition of three-dimensional geometries with the properties similar to natural bone is presented. An algorithm uses a set of parameters to characterize ellipsoids computed based on Finite Element Method (FEM). A comparative analysis of real trabecular bone samples and the corresponding generated models is presented. Additional validation schemas are proposed. It is concluded that computer-aided modelling appears to be an important tool in the study of the mechanical behavior of bone microstructure.

The full text will be available in the edited book “Information Technology, Systems Research and Computational Physics”, eds. Kulczycki P., Kacprzyk J., Kóczy L.T., Mesiar R., Wisniewski R., to be published by Springer in the *Advances in Intelligent Systems and Computing* series soon.

Human stress detection using non-contact remote photoplethysmography from video stream

S. Nikolaiev[1][0000-0002-2025-8469], S. Telenyk[2][0000-0001-9202-9406],

Y. Tymoshenko[3] [0000-0001-7812-6437]

[1,3.] National Technical University of Ukraine ‘Igor Sikorsky Kyiv Polytechnic Institute’ (Ukraine)
[2] Cracow University of Technology (Poland)

Abstract. This paper presents the experimental results for stress index calculation using developed by the authors information technology for non-contact remote human heart rate variability (HRV) retrieval in various conditions from video stream using common wide spread web cameras. The developed system architecture based on remote photoplethysmography (r-PPG) technology is briefly overviewed. Use-cases of measuring stress index are presented and analyzed in details. The results of the experiments have shown that the r-PPG system is capable of retrieving stress level that is in accordance with the feelings of experiments’ participants.

Keywords: video processing; web cameras; stress index; remote photoplethysmography; rPPG; heart rate; heart rate variability; Predictive, Preventive, Personalized and Participatory Medicine.

1 Introduction

At present, the formation of the XXI century medicine requires a new philosophy and the platforms for more effective person’s treatments to advance current healthcare systems. There are several needs that the modern and innovative healthcare systems across the planet should respond to. Among them are: the rising costs of medical care and the emerging need to reduce such costs; the grand challenges facing the healthcare and biomedical industry in order to utilize many of the novel technologies; the necessity of radical improvement in wellness and disease prevention; the developing shortage of healthcare professionals; the strong desire of the individual persons to participate more in every aspects of their healthcare.

These tasks to be solved need a new paradigm of advanced healthcare in terms of predictive, preventive, personalized, and participatory (P4) medicine [1]. The core elements of that vision are widely accepted now providing physicians and patients with personalized information about each individual’s health on different system levels. During the development of P4 medicine, many rapidly developing technologies such as artificial intelligence, telemedicine, smart clothes with wearable sensors, mobile apps and beyond will result in treating the causes rather than the symptoms of disease, more efficient patient management and hence a better quality of life.

The healthcare industry is on the cusp of substantial changes in the coming decade as new technologies are being developed. In this paper, the authors follow the paradigm of P4M, which is a global trend in the 21st century and it involves continuous monitoring of the humans' condition even before any signs of negative changes [2].

The authors have developed robust contactless remote photoplethysmography information technology that uses video stream processing in real time. The developed system is able to obtain biological indicators like HRV through the use of widely distributed web and other video cameras. Mass adoption of such IT will allow people to provide an appropriate level of heart health through continuous contactless monitoring of HRV without changing their life styles and could make our medicine preventive.

Taking into account that the relationship between stress, heart disease and sudden death has been recognized since antiquity the main focus of this paper will be dedicated to stress. The choice of studying stress is dictated by the following facts:

According to statistics, annual costs to employers because of stress related health care issues and missed work are estimated in $300 Billion.[3] Moreover 77 % of respondents of the research marked that they regularly experience physical symptoms caused by stress. And 73 % of people experience psychological symptoms because of stress. 33% feel that they are living with extreme stress. So detecting and measuring stress may not only help to make lives better, but also to reduce other diseases like heart disease.

In this paper the results of measuring stress index of humans in different conditions with the help of developed system are presented.

2 Heart rate variability

"Heart Rate Variability" (HRV) has become the conventionally accepted term to describe variations of both instantaneous heart rate and the series of times between consequential pairs of heart contractions (so called RR-intervals). The analysis of HRV has been widely used as a non-invasive and reliable tool to evaluate cardiovascular autonomic control in health and disease. In order to describe oscillation in consecutive cardiac cycles, other terms have also been used in the literature: for e.g. cycle length/ heart period variability or RR interval tachogram, and they more appropriately emphasize the fact that it is the interval between consecutive beats that is being analyzed rather than the heart rate per se [4]. In this work the term HRV will be used throughout the article.

Usually for the accurate diagnosis of cardiovascular diseases the Holter device is used as the medical standard for heart activity measuring. It requires a patient to visit a doctor, install the device for couple of days, and then follow doctor's examining of obtained electrocardiograms (ECGs) manually. But many heart diseases do not require the entire ECG to be examined, and for diagnostics it is enough to have only beat-to-beat time intervals, so-called RR intervals. The phenomenon to focus on is the oscillation in the intervals between consecutive heart beats as well as the oscillations between consecutive instantaneous heart rates. Patterns in these oscillations contain enough information for unveiling not only heart pathologies but also dysfunctions of the whole organism.

The modern development of information technology (IT) infinitely extends the possibility of tracking various biological signals of a person with further computer processing of digital data. In recent years, there have been various alternatives to the Holter device, namely: personal pulse meters, "smart" clocks, fitness trackers that allow you to record HR, continuous monitoring of the cardiovascular system and reduce the risk of CVD. Modern markets of mobile soft- and hardware are filled with a different kind of applications for health monitoring and pulsometer-like gadgets that may read, store and process our biological signals.

But the only problem remains that all these approaches are contact and in some types of applications it is impossible to make contact measurement and remote technology is needed to estimate HR and heart rate variability.

3 Contactless remote photoplethysmography

In recent years, the possibility to extract the heart rate (HR) with the help of a remote photo detector has been established, so called remote photoplethysmography (rPPG) [5 - 9]. The new technique offers a heart rate (HR) measurement that does not need to have contact with the studied object, a valuable feature for both medical and surveillance purposes [8]. rPPG contactless monitors of human heart activity by detecting subtle human skin color variations induced by heart contractions and blood flow using observed by the camera reflected light from skin [10].

Lately, several new rPPG algorithms have been developed for pulse-signal extraction from the face with RGB-cameras as photo detectors [6, 7]. These include: (a) Blind Source Separation (e.g., PCA-based [11] and ICA-based [12]), which use different criteria to separate temporal RGB traces into uncorrelated or independent signal sources to retrieve the pulse; (b) CHROM [13], which linearly combines the chrominance signals by assuming a standardized skin-color to white-balance the camera; (c) PBV [14], which uses the signature of blood volume changes in different wavelengths to explicitly distinguish the pulse-induced color changes from motion noise in RGB measurements; and (d) 2SR [15], which measures the temporal rotation between spatial subspaces of skin-pixels for pulse extraction. The essential difference between these rPPG algorithms is in the way of combining RGB-signals into a pulse-signal. The use of three color channels with multiple wavelengths gives the methods the possibility to be robust to motion of the subject. A better understanding of the core rPPG algorithms could benefit many systems/applications for video health monitoring, such as the monitoring of heart-rate [16 – 20], respiration [17], SpO2 [21], blood pressure [22], neonates [23], [24], and the detection of atrial fibrillation [25] and mental stress [26].

4 Remote PPG system’s architecture description

The developed by the authors of this work rPPG technology is based on the one-pixel camera mathematical model and has the following modules structure:

1) Face detection module;
2) Images spatial filtering module;
3) Module for skin tints time series frequencies filtration;
4) Heart beats’ time detection module

Video processing begins with sequential analysis of each video frame applying face detector, and spatial filters like: skin-detector to find skin pixels on the frames; transformations of color tint signal spaces to compensate energy of luminance of skin; aggregating skin pixel colors to reduce camera’s sensor’s pixel noise; and temporal filters including frequency finite impulse response pass-band filter with frequencies of heart rate to remove all temporal noises except heart signal. Heart beats’ time detection module returns sequence of heart contraction moments in time that allow to calculate time deltas between each pair of R-peaks resulting in series of RR-intervals.

The system using normal web camera with frame resolution of 640x480 pixels and average speed of 25 frames per second, detects 99.3% of heart contractions. The experiments have shown that standard deviation of delta time between heart beat contractions’ time detected by the system and Holter monitor is 0.046 seconds.

As the output – the system returns time series of RR intervals and as result Heart Rate Variability (HRV) can be calculated, same as spectrograms of retrieved cardiointervalogramms. [27-29]

5 Stress index calculation

Having series of RR-intervals it is possible to apply variational pulsometry that is used for stress calculation. The essence of variational pulsometry consists in learning the distribution law of cardiointervals. The distributions of cardiointervals are also called histograms. A traditional manner of grouping cardiointervals in the range from 400 to 1300 ms with the buckets’ intervals of 50 ms. was constituted in perennial practice. Thus, 20 fixed ranges of cardio-intervals' length are considered that allow to compare pulsograms received by different researchers. The timing capacity of pulsograms is set to 5-minute standard.

Cardiointerval histogram is a bar plot with buckets' width of 50 ms. Cardio RR-intervals are distributed among these buckets and form columns. The higher the column, the more cardiointervals it includes with duration within the beginning and end time of the bucket. A healthy person with a normal energy potential has symmetrical histogram of pyramidal shape with its central column containing between 30%-50% of all cardiointervals.

According to [30] variational pulsometry is widely practiced in Russia and post-soviet countries and is called "index of regulatory systems tension" or stress index (SI).

The core idea of the stress index proposed by R. Baevskiy is to capture the factors that are caused by stress into one single formula. The formula for calculating the Stress Index is presented below:

$$SI = \frac{AMo}{2 * Mo * MxDMn} \tag{1}$$

where Mo (the mode) — is the most frequently occurring value of cardiointervals in milliseconds. Mo differs a little from mathematic expectation (M) in the case of normal allocation and high stationarity;

Amo (the mode amplitude) — is the proportion of the most common cardiointervals, from which the central column of the histogram was formed, of all cardiointervals.

$MxDMn$ (the RR-intervals variation range) — the difference between cardiointervals of the minimum and maximum duration.

SI Calculation - it is only one of approaches to interpretation and estimation of the histogram (variational pulsogram).

In norm SI varies within the limits of 80-150. This parameter is very sensitive to amplification of sympathetic tone. Small load (physical or emotional) increase SI 1,5-2 times. At significant loads it increases 5-10 times. By illness with constant tension of regulatory systems, SI in rest can be equal to 400-600. By coronary heart disease and with myocardial infarction, SI in rest reaches 1000-1500.

6 Stress index measurement using developed remote rPPG system

Several experiments were conducted to measure stress level of people in different situations with the help of developed rPPG system including car and tractor drivers before and after day shifts and students before and during exams.

6.1 Drivers' stress

The rPPG system was used to track HRV and stress of drivers during many hours' drives in summer 2017. The camera was mounted in the car's interior on the celling to have clear view on the drivers' face. The drivers were 5-6 hours in the road covering intercity distances and measurement of SI before and immediately after the journey were compared. Also the drivers were asked to fill in small survey with questions about their level of tiredness. The results of comparisons have shown that stress index that was in range 14-32 before the journey was almost twice higher in the end of the route.

Fig. 1. – Stress index of the driver after 5 hour intercity journey is twice higher compared to measurement before the journey.

The system was also tested on several drivers in the field using various models of tractors. The camera was mounted near the steering wheel or on the ceiling depending on the tractor model. It was shown that drivers who were working in more comfortable models of tractors and have been fewer hours on their shift by the moment of experiment conduction had less stress index values.

Fig. 2. – The system testing also involved several tractor-drivers in field conditions on tractors of different models.

6.2 Students stress

Another experiment was conducted at IASA NTUU “Igor Sikorsky KPI” involving group of 23 students. The purpose of this experiment was to detect a change in the student's internal state directly before and during the exam at session. The null hypothesis to test was that students would feel calm two days before the exam as they still have two days to prepare. On the exam, everyone will be little worried. Those who fail to pass the exam will be very worried and experience severe stress.

The experiment consisted of two phases: on the first phase students’ stress index was measured in calm conditions. At this stage no coming events for the next 2 days have been planned that could have been treated by students as alert factor and also students have not performed any active physical exercises that could have affected the experiment. During this stage experimental measurements of SI with the rPPG system have shown average SI to be in the range 12-37 and heart rate to be in range 61-73 bpm.

The second phase of the experiment was conducted during exam. It appeared that students were extremely stressed out. SI was in range 75-261 and the lowest average heart rate per student was 83 while the highest was 145 bpm.

Each experiment entry lasted from four to seven minutes. The goal was to collect at least 300 heartbeats in each of the experiments in order to be able to calculate the stress index by Baevsky's method.

After processing the results, it turned out that the null hypothesis was confirmed but not for all students. On average, the stress index level during the exam has been greater than two days before the exam. But there were also students who had normal stress index level during both phases and who were also stressed all the time.

For example, let’s look at the obtained data of the student whose heart rate was within the normal range during both phases of experiment (approximately 67 beats per minute).

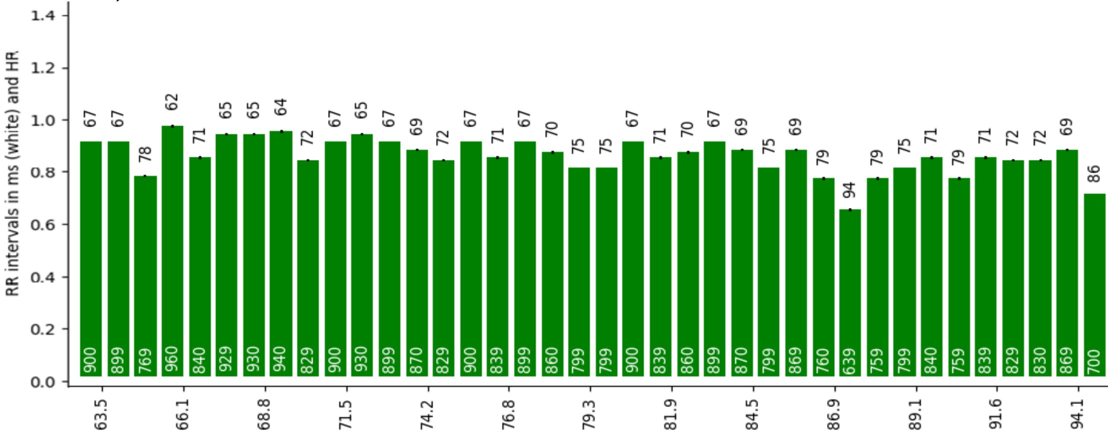

Fig. 3. – Example of RR-intervals of the student in time (sec). Signatures over the bars show the instantaneous pulse (beats/minute).

The figure 3 shows his RR intervals obtained during the experiment on the exam. They are in range from 630 to 1017 milliseconds. The bar height shows the duration of each of the RR intervals in milliseconds (at the bottom of the bar durations in milliseconds are presented in white). Numbers above the bars indicate the instantaneous pulse (beats per minute). Labels under the abscise axis indicate the time of each RR interval occurrence given in seconds from the beginning of the experiment recording.

Judging from the figure above, one can assert that the student is in normal condition and has little stress. After calculating the stress index, we get the figure 4, which shows that the student's stress was in the range of 20 to 40 conventional units. To calculate the stress formula, the duration of RR-intervals series was taken equal to 150 seconds.

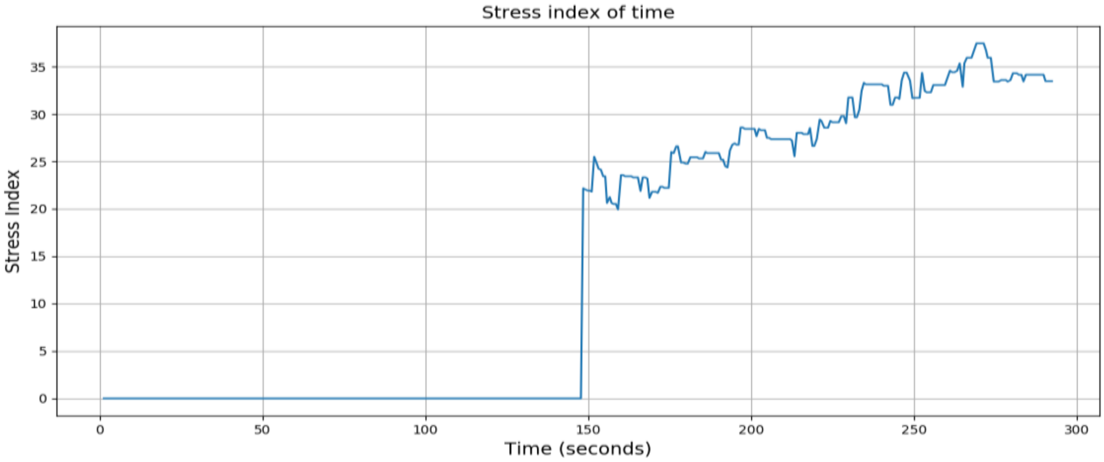

Fig. 4. – Stress index from time plot of calm student (conditional units)

Although most of the students had “poker faces” during this experiment and showed no external signs of their emotions and neither the lecturer nor the stuff conducting the experiment noticed any difference from other students, the rPPG system has detected very high heart rate and big SI values from some of the students. For example the figure 5 shows RR-intervals of an extremely worried student.

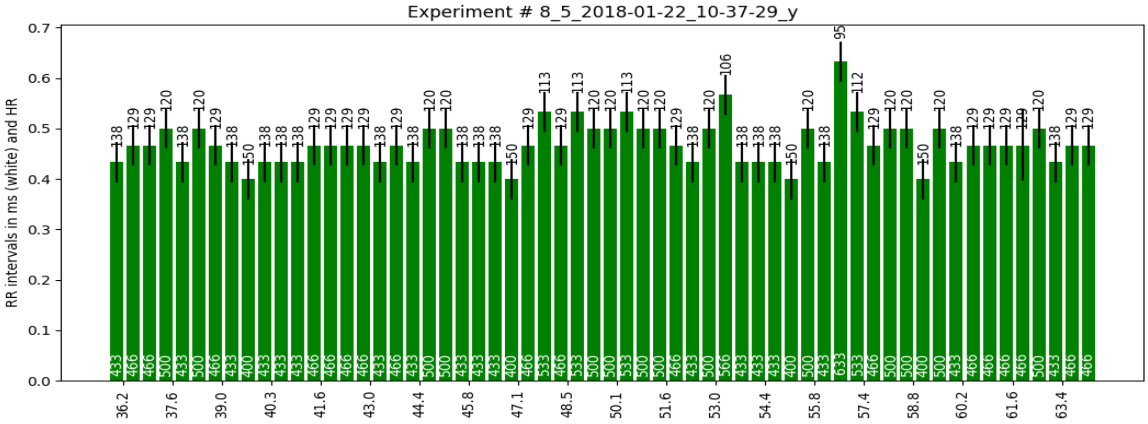

Fig. 5. – Example of obtained RR-intervals from experiment during exam

Her pulse was in the range of 110 to 140 beats per minute and averaged 127 beats per minute, indicating high level of adrenaline in the blood and, accordingly, a high level of stress.

At the same time, two days before the exam, she was calm and her average pulse rate was 65 beats per minute.

The figure below shows the student's photoplethysmogram signal (yellow) and after frequency filtration (violet) obtained using the developed IT. Yellow vertical lines represent heart contraction moments. A good noise to signal ratio of raw signal can be noticed because the amplitude of the signal is much bigger than the amplitude of noise. This testifies to the high quality and reliability of the obtained PPG and RR-intervals, respectively.

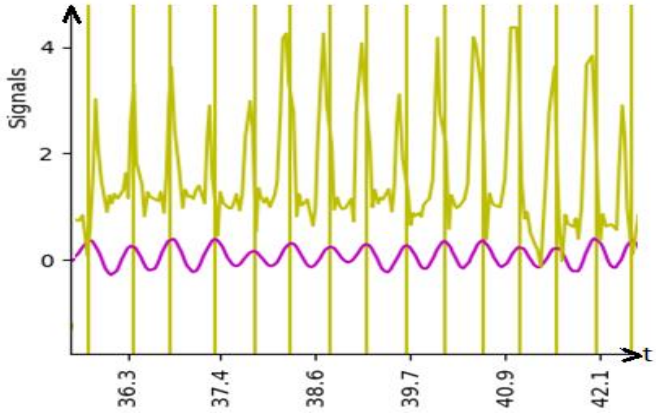

Fig. 6. – Student's rPPG heartbeat signal before (yellow) and after filtering (violet) in time (sec)

After calculating the stress index, we get the following figure 7, from which it can be seen that the student's stress was in the range of 125 to 132 conventional units.

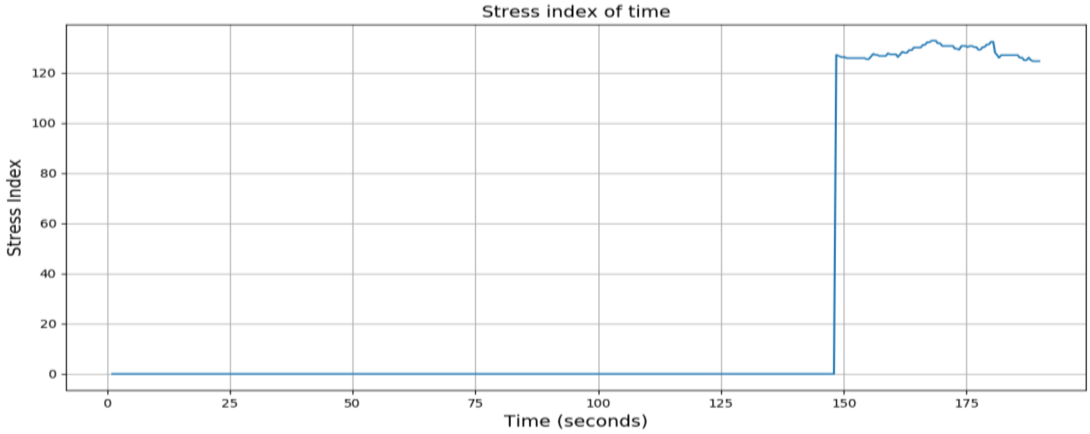

Fig. 7. – Stress index from time plot of the stressed student (conditional units)

The obtained students' levels of stress during the exam were surprising even for the professor with many years of experience who was conducting this exam.

It was shown that the system determined the pulse and stress levels of the students without any problems and the rPPG system measurements results were in accordance with students' answers from questionnaires about their feelings. Also, after a detailed analysis of the rPPG signals retrieved by the system, their quality confirmed as high and conclusions about the reliability of the results of the experiments themselves were marked as reliable.

7 Conclusions

The need of the new non-contact widely available sensors for human bio-signals constant monitoring was described within the framework of predictive, preventive, personalized, and participatory (P4) medicine. It was shown that the heart rate variability can be a good indicator for estimating internal states of the human including heart rate, stress levels and heart diseases that cause decrease in productivity and financial loses for the enterprises and to the whole economy.

Overview of recent papers and approached was made to show how using widely spread web cameras it is possible to build remote non-contact information technology that can extract precise timings of heart beats from video stream based on remote photoplethysmography. Also the architecture and main modules of the developed by the authors contactless rPPG system were presented.

Several experiments were described for human stress index calculation in different conditions including car and tractor drivers.

It was shown that despite the absence of visual signs perceivable by other humans, the rPPG system was able to differentiate and measure internal states of the people who were participating in the experiments. The obtained measurements were in accordance with the feelings of participants and the quality of the obtained results was confirmed by in-depth examining of all stages of signal processing within the rPPG system.

In the summary, it can be stated that the developed personal non-contact automatic remote photoplethysmography system for heart beats time moments' contraction (so called RR-intervals) retrieval, can be used in different applications like:

- Person's functional and emotional states detection;
- Person's Identification & Authentication via remote detection of vital signs presence;
- Contactless remote HRV and stress tracking.

Developed rPPG method has shown good performance using ordinary web cameras for online R-peaks detection. The technology misses heart beats at rate 0.69%, and detects false positives heart beats at rate 1.16%. Root mean square time deviation between correctly classified heart beats is 0.046 seconds. Using cameras filming at higher frame rates one can greatly decrease this errors.

References

1. Golubnitschaja O, Kinkorova J, Costigliola V: Predictive, preventive and personalized medicine as the hardcore of 'Horizon 2020': EPMA position paper. EPMA J, 5(1):6 (2014)
2. S. Nikolaiev, Y. Tymoshenko, "The Reinvention of the Cardiovascular Diseases Prevention and Prediction Due to Ubiquitous Convergence of Mobile Apps and Machine Learning", Proc. of the 2nd Int. Sci. and Pr. Conf. ITIB 2015, Oct 7-9, pp. 23-26 (2015)
3. Transforming stress through awareness, education and collaboration. Homepage https://www.stress.org/stress-and-heart-disease/, last accessed 2018/03/31
4. Heart rate variability. Standards of measurement, physiological interpretation, and clinical use. Task Force of the European Society of Cardiology and The North American Society of Pacing and Electrophysiology. European Heart Journal (1996) 17, pp.354–381

5. X. Li et al. “Remote Heart Rate Measurement from Face Videos under Realistic Situations”. In: Computer Vision and Pattern Recognition (CVPR), IEEE Conference on. June 2014, pp. 4264–4271. doi: 10.1109/CVPR.2014. 543 (2014).
6. W. Verkruysse, L. Svaasand, and J. Nelson. “Remote plethysmographic imaging using ambient light”. English. In: Optics Express 16.26, pp. 21434–21445 (2008).
7. M. Poh, D. McDuff, and R. Picard. “Non-contact, automated cardiac pulse measurements using video imaging and blind source separation”. English. In: Optics express 18.10, p. 10762 (2010).
8. M. van Gastel, S. Stuijk, and G. de Haan. “Motion Robust Remote-PPG in Infrared”. English. In: IEEE Transactions on Biomedical Engineering 62.5, pp. 1425–1433 (2015).
9. K. Humphreys. “A CMOS camera-based system for clinical photoplethysmographic applications”. In: Proceedings of SPIE. Vol. 5823, pp. 88–95 (2005).
10. W. Verkruysse, L. O. Svaasand, and J. S. Nelson, “Remote plethysmographic imaging using ambient light,” Opt. Express, vol. 16, no. 26, pp. 21 434–21 445, (Dec. 2008).
11. M. Lewandowska, J. Ruminski, T. Kocejko, and J. Nowak, “Measuring pulse rate with a webcam - a non-contact method for evaluating cardiac activity,” in Computer Science and Information Systems (FedCSIS), 2011 Federated Conference on, pp. 405–410 (Sept. 2011).
12. M.-Z. Poh, D. McDuff, and R. Picard, “Advancements in noncontact, multiparameter physiological measurements using a webcam,” Biomedical Engineering, IEEE Trans. on, vol. 58, no. 1, pp. 7–11, (Jan. 2011).
13. G. de Haan and V. Jeanne, “Robust pulse rate from chrominance-based rPPG,” Biomedical Engineering, IEEE Trans. on, vol. 60, no. 10, pp. 2878–2886, (Oct. 2013).
14. G. de Haan and A. van Leest, “Improved motion robustness of remote-PPG by using the blood volume pulse signature,” Physiological Measurement, vol. 35, no. 9, pp. 1913–1922, (Oct. 2014).
15. W. Wang, S. Stuijk, and G. de Haan, “A novel algorithm for remote photoplethysmography: Spatial subspace rotation,” Biomedical Engineering, IEEE Transactions on, vol. PP, no. 99 , (2015).
16. X. Li, J. Chen, G. Zhao, and M. Pietikainen, “Remote heart rate measurement from face videos under realistic situations,” in The IEEE Conference on Computer Vision and Pattern Recognition (CVPR), pp. 4264–4271 (June 2014).
17. L. Tarassenko, M. Villarroel, A. Guazzi, J. Jorge, D. Clifton, and C. Pugh, “Non-contact video-based vital sign monitoring using ambient light and auto-regressive models,” Physiological measurement, vol. 35, no. 5, p. 807, (May 2014).
18. W. Wang, S. Stuijk, and G. de Haan, “Exploiting spatial redundancy of image sensor for motion robust rPPG,” Biomedical Engineering, IEEE Trans. on, vol. 62, no. 2, pp. 415–425, (Feb. 2015).
19. M. Kumar, A. Veeraraghavan, and A. Sabharwal, “Distance PPG: Robust non-contact vital signs monitoring using a camera,” Biomed. Opt. Express, vol. 6, no. 5, pp. 1565–1588, (May 2015).

20. S. Tulyakov, X. Alameda-Pineda, E. Ricci, L. Yin, J. F. Cohn, and N. Sebe, “Self-adaptive matrix completion for heart rate estimation from face videos under realistic conditions,” in The IEEE Conference on Computer Vision and Pattern Recognition (CVPR), pp. 2396–2404 (June 2016).
21. A. R. Guazzi, M. Villarroel, J. ao Jorge, J. Daly, M. C. Frise, P. A. Robbins, and L. Tarassenko, “Non-contact measurement of oxygen saturation with an RGB camera,” Biomed. Opt. Express, vol. 6, no. 9, pp. 3320–3338, (Sep. 2015).
22. I. C. Jeong and J. Finkelstein, “Introducing contactless blood pressure assessment using a high speed video camera,” Journal of Medical Systems, vol. 40, no. 4, pp. 1–10, (2016).
23. L. K. Mestha, S. Kyal, B. Xu, L. E. Lewis, and V. Kumar, “Towards continuous monitoring of pulse rate in neonatal intensive care unit with a webcam,” in 36th Annual International Conference of the IEEE Engineering in Medicine and Biology Society, pp. 3817–3820 (Aug. 2014).
24. S. Fernando, W. Wang, I. Kirenko, G. de Haan, S. Bambang Oetomo, H. Corporaal, and J. van Dalfsen, “Feasibility of contactless pulse rate monitoring of neonates using google glass,” in Wireless Mobile Communication and Healthcare (Mobihealth), 2015 EAI 5th International Conference on, pp. 198–201 (Oct. 2015).
25. J.-P. Couderc, S. Kyal, L. K. Mestha, B. Xu, D. R. Peterson, X. Xia, and B. Hall, “Detection of atrial fibrillation using contactless facial video monitoring,” Heart Rhythm, vol. 12, no. 1, pp. 195–201, (2015).
26. B. Kaur, S. Moses, M. Luthra, and V. N. Ikonomidou, “Remote stress detection using a visible spectrum camera,” pp. 949 602–949 602–13, (May 2015).
27. Sergii Nikolaiev, Yurii Tymoshenko, Kateryna Matviiv, Haar Cascade Face Detector Quality Dependence on Training Dataset Variability, Naukovi Visti NTUU KPI, №6, pp. 38-46 (2017).
28. Sergii Nikolaiev, Hryhorii Chereda, Sampling Rate Independent Filtration Approach For Automatic ECG Delineation, International Scientific Journal “Internauka” . Available: http://www.inter-nauka.com/issues/2017/5/2394
29. S. Nikolaiev, Metric And Algorithm For Similarity Between Two Temporal Event Sequences Calculation, System research and information technologies, № 3, pp. 127-135 (2017).
30. Baevskiy R.M, Ivanov G.G. Heart Rate Variability: theoretical aspects and possibilities of clinical application [in Russian]. Ultrazvukovaya i funktsionalnaya diagnostika.. Vol 3:pp. 106-127 (2001).

Section 10
Fuzzy Logic

On wavelet based enhancing possiilities of fuzzy classification of measurement results

Ferenc Lilik[1], Levente Solecki[1], Brigita Sziová[1], László T. Kóczy[1,2], and Szilvia Nagy[1]
[1] Széchenyi István University, H-9026 Győr, Egyetem tér 1, Hungary;
[2] Budapest University of Technology and Economics,
H-1117 Budapest, Magyar tudósok krt. 2, Hungary;

Abstract. In fuzzy classification methods if the antecedents arise as the result of a measurement, the antecedent can have too many dimensions to handle. In order to base a classification scheme on such data, a careful selection, a sampling or re-sampling is necessary. It is also possible to use functions or transformations that reduce the long, high dimensional measurement data vector or matrix into a single point or to a low number of points. Wavelet analysis can be useful in such cases in two ways.

First, the measurement data can be compressed by wavelet analysis, thus reducing the dimensionality of the measured signal. We demonstrate the applicability of this scheme by a telecommunication line evaluation problem with fuzzy rule interpolation to overcome the issue of sparse rulebase

Second, if other functions, such as entropies, are used for extraction of the information from the measured data, and this information is not sufficient for performing the classification well enough, the use the same method of acquiring information on the wavelet analysed version of the signal can increase the dimensionality, thus bringing back some of the information that has been lost during the application of the function. The applicability of this scheme is demonstrated on a combustion engine cylinder surface classification problem (new and worn) using Rényi entropies.

The full text will be available in the edited book “Information Technology, Systems Research and Computational Physics”, eds. Kulczycki P., Kacprzyk J., Kóczy L.T., Mesiar R., Wisniewski R., to be published by Springer in the *Advances in Intelligent Systems and Computing* series soon.

On the Convergence of Fuzzy Grey Cognitive Maps

István Á Harmati[1] and László T. Kóczy[2,3]

[1] Department of Mathematics and Computational Sciences, Széchenyi István University, Győr, Hungary;
[2] Department of Information Technology, Széchenyi István University, Győr, Hungary;
[3] Department of Telecommunications and Media Informatics,
Budapest University of Technology and Economics, Budapest, Hungary;

Abstract. Fuzzy grey cognitive maps (FGCMs) are extensions of fuzzy cognitive maps (FCMs), applying uncertain weights between the concepts. This uncertainty is expressed by so-called grey numbers. Similarly to FCMs, the inference is determined by an iteration process, which may converge to an equilibrium point, but limit cycles or chaotic behaviour may also turn up.

In this paper, based on the grey weighted connections between the concepts and the parameter of the sigmoid threshold function, we give sufficient conditions for the existence and uniqueness of fixed points for sigmoid FGCMs.

The full text will be available in the edited book “Information Technology, Systems Research and Computational Physics”, eds. Kulczycki P., Kacprzyk J., Kóczy L.T., Mesiar R., Wisniewski R., to be published by Springer in the *Advances in Intelligent Systems and Computing* series soon.

Hierarchical fuzzy decision support methodology for packaging system design

Kata Vöröskői, Gergő Fogarasi, Adrienn Buruzs, Peter Földesi, and László T. Kóczy
Széchenyi István University, H-9026 Győr, Egyetem tér 1, Hungary;

Abstract. In the field of logistics packaging (industrial-, or even customer packaging), companies have to take decisions on determining the optimal packaging solutions and expenses. The decisions often involve a choice between one-way (disposable) and reusable (returnable) packaging solutions. Even nowadays, in most cases the decisions are made based on traditions and mainly consider the material and investment costs. Although cost is an important factor, it might not be sufficient for finding the optimal solution. Traditional (two-valued) logic is not suitable for modelling this problem, so here the application of a fuzzy approach, because of the metrical aspects, a fuzzy signature approach is considered. In this paper a fuzzy signature modelling the packaging decision is suggested, based on logistics expert opinions, in order to support the decision making process of choosing the right packaging system. Two real life examples are also given, one in the field of customer packaging and one in industrial packaging.

The full text will be available in the edited book "Information Technology, Systems Research and Computational Physics", eds. Kulczycki P., Kacprzyk J., Kóczy L.T., Mesiar R., Wisniewski R., to be published by Springer in the *Advances in Intelligent Systems and Computing* series soon.

Section 11

Machine Learning

Applicability of Deep Learned vs Traditional Features for Depth Based Classification

Fabio Bracci, Mo Li, Ingo Kossyk, and Zoltan-Csaba Marton
Institute of Robotics and Mechatronics, German Aerospace Center (DLR), Weßling, Germany;

Abstract. In robotic applications often highly specific objects need to be recognized, e.g. industrial parts, for which methods can't rely on the online availability of large labeled training data sets or pre-trained models. This is especially valid for depth data, thus making it challenging for deep learning (DL) approaches. Therefore, this work analyzes the performance of various traditional (global or part-based) and DL features on a restricted depth data set, depending on the tasks complexity. While the sample size is small, we can conclude that pre-trained DL descriptors are the most descriptive but not by a statistically significant margin and therefore part-based descriptors are still a viable option for small but difficult 3D data sets.

The full text will be available in the edited book "Computational Modeling of Objects Presented in Images. Fundamentals, Methods, and Applications", eds. Barneva R.P., Brimkov V.E., Kulczycki P., Tavares J.M.R.S., to be published by Springer in the *Lecture Notes in Computer Science* series soon.

Effect of image view for mammogram mass classification

Sk Md Obaidullah, Sajib Ahmed, and Teresa Gonçalves
Dept. of Informatics, University of Évora, Portugal;

Abstract. Mammogram images are broadly categorized into two types: carniocaudal (CC) view and mediolateral oblique (MLO) view. In this paper, we study the effect of different image views for mammogram mass classification. For the experiments, we consider a dataset of 328 CC view images and 334 MLO view images (almost equal ratio) from a publicly available film mammogram image dataset [3]. First, features are extracted using a novel radon-wavelet based image descriptor. Then an extreme learning machine (ELM) based classification technique is applied and the performance of five different ELM kernels are compared: sigmoidal, sine, triangular basis, hard limiter and radial basis function. Performances are reported in terms of three important statistical measures namely, sensitivity or true positive rate (TPR), specificity or false negative rate (SPC) and recognition accuracy (ACC). Our experimental outcome for the present setup is two-fold: (i) CC view performs better then MLO for mammogram mass classification, (ii) hard limiter is the best ELM kernel for this problem.

The full text will be available in the edited book "Computational Modeling of Objects Presented in Images. Fundamentals, Methods, and Applications", eds. Barneva R.P., Brimkov V.E., Kulczycki P., Tavares J.M.R.S., to be published by Springer in the *Lecture Notes in Computer Science* series soon.

Solving a Combinatorial Multiobjective Optimization Problem by Genetic Algorithm

Marcin Studniarski[1], Liudmila Koliechkina[1], and Elena Dvernaya[2]

[1] Faculty of Mathematics and Computer Science, University of Łódź, Banacha 22,
90-238 Łódź, Poland
{marstud,lkoliechkina}@math.uni.lodz.pl
[2] Chair of Document Management and Information Activities in Economic Systems,
Poltava University of Economics and Trade, Poltava, Ukraine

Abstract. We develop a new method of generating Pareto-optimal solutions of a discrete multiobjective programming problem. This is achieved by using a specially designed genetic algorithm which includes some probabilistic stopping criterion. This approach enables us to find all minimal solutions of the problem with a prescribed probability. Our method is a combination of two algorithms: the RHS (Random Heuristic Search) and the base VV (Van Veldhuizen) algorithm. The RHS starts from a fixed initial population and applies some transition rule to obtain the next population. The VV algorithm collects the best solutions generated by subsequent iterations of the RHS. The proposed method can applied to a combinatorial set of permutations without repetitions or with repetitions, as well as to other combinatorial objects. As a crossover operator, three types of crossover are used.

Keywords: Combinatorial optimization · Genetic algorithm · Stopping criterion.

1 Introduction

The research of many scientists is devoted to the study of multiobjective optimization problems [3, 6, 10, 15–17, 20, 24, 25], in particular, discrete problems [10, 24, 25].

The interest in studying multiobjective models on discrete sets is due to their wide application to solving various problems of the economy, the design of complex systems, decision-making under ambiguity and others. Recently, significant results have been obtained in the areas of study of different classes of combinatorial models and the development of new discrete optimization methods [10, 11]. But developing existing methods and constructing new ones for this class of problems are still important tasks for today.

As is known, the majority of combinatorial optimization problems can be reduced to integer programming problems, but this is not always justified since it is not possible to take into account the combinatorial properties of the problem.

In monographs [5, 23] it is shown that the convex hull of the set of permutations has a common permutable polyhedron, whose vertex set is equal to the set of permutations, which makes it possible to consider the problem as a problem on graphs. In order to solve this problem, a genetic algorithm is proposed in the articles [12, 22]. It should be noted that genetic algorithms have demonstrated their effectiveness for solving problems that cannot be solved by traditional methods; see [1, 7–9, 13, 18, 21, 26]. In addition, the computational time of genetic algorithms for most problems is practically linearly dependent on the size of the problem and the number of optimized parameters [9, 13, 18, 21, 26]. An important stage in the genetic algorithm is the stopping criterion, which is determined by the number of iterations. Genetic algorithms, like heuristic search algorithms, never guarantee that an optimal solution will be obtained, but such solutions could be obtained after a fixed number of iterations. There is always a possibility that we cannot get optimal solutions. However, as in [7], we can consider some convergence in probability. Having given a fixed probability δ ($0 < \delta < 1$), we can determine the smallest number of iterations $t(\delta)$ which will guarantee us to obtain an optimal solution with this probability δ.

Genetic algorithms have been described by many researchers in relation to various applied problems. In [14], Nix and Vose characterize genetic algorithms as Markov chains. Aytug and Koehler [2] use the Markov chain formulation to find an upper bound for $t(\delta)$. In [24], Studniarski applies a general Markov chain model of a genetic algorithm (see [27]) to multiple-criteria optimization problems. He sets an upper bound for the number of iterations that must be performed in order to obtain, with a certain probability, a population consisting entirely of minimal solutions. However, since the population can contain multiple copies of the same element, we can only guarantee that at least one minimal solution is found. The results of [24] have an obvious drawback, because they do not provide the generation of the complete Pareto set, even if it is finite and of low cardinality. In [25], Studniarski improves the previous stopping rules, so that they allow us to find, with a given probability, all the minimal solutions in a finite problem of multiobjective optimization.

The aim of this work is to develop a method for generating Pareto-optimal solutions of a discrete multiobjective problem. This will be achieved by using a genetic algorithm according to the scheme described in [25], with some modifications. In dealing with discrete multiobjective optimization problems, it is necessary to take into account the finiteness of the discrete set of admissible points. At present there are very few developed methods for solving such problems. Since the heuristic genetic algorithm has proved very effective in practical applications, it was chosen to solve the problem in question.

The paper is organized as follows. In Sections 2–4 we review the main results of [25] with necessary modifications taking into account the fact that now only one half of each population undergoes mutation. Section 5 contains the formulation of a combinatorial discrete multiobjective optimization problem. A new algorithm designed for solving this combinatorial problem is described in Section 6. Finally, some computational examples illustrating the theory are presented in Section 7.

2 The RHS algorithm

The RHS (Random Heuristic Search), which is presented in [27], is a general algorithm model providing a unified framework for the description of various evolutionary algorithms, including the classical genetic algorithm. The RHS consists of finding an *initial population* $P^{(0)}$ and a *transition rule* τ which, for a given population $P^{(i)}$, determines a new population $P^{(i+1)}$. Iterating τ, we obtain a sequence of populations:

$$P^{(0)} \xrightarrow{\tau} P^{(1)} \xrightarrow{\tau} P^{(2)} \xrightarrow{\tau} ... \tag{1}$$

Each population is a finite collection of *individuals* which are elements of a given finite set Ω called the *search space*. Populations are *multisets*, which means that the same individual may appear more than once in a given population.

We may assume that Ω is a subset of integers: $\Omega = \{0, 1, ..., l-1\}$. The number l is called the *size of search space*. Then a population can be represented as an *incidence vector* (see [19, p. 141]):

$$v = (v_0, v_1, ..., v_{l-1})^T, \tag{2}$$

where v_i is the number of copies of individual $i \in \Omega$ in the population ($v_i = 0$ if individual i does not appear in the population). The *size of population* v is the number

$$r = \sum_{i=0}^{l-1} v_i. \tag{3}$$

We assume that all the populations appearing in sequence (1) have the same size r. Dividing each component of incidence vector (2) by r, we obtain the *population vector*

$$p = (p_0, p_1, ..., p_{l-1})^T, \tag{4}$$

where $p_i = v_i/r$ is the proportion of individual $i \in \Omega$ in the population. We can observe that representation (4) is independent of population size. Each vector p of this type belongs to the set

$$\Lambda := \left\{ x \in \mathbb{R}^l : x_i \geq 0 \ (\forall i), \ \sum_{i=0}^{l-1} x_i = 1 \right\}. \tag{5}$$

However, not all points of Λ correspond to finite populations. For a fixed $r \in \mathbb{N}$, the following subset of Λ consists of all populations of size r (see [27, p. 7]):

$$\Lambda_r := \frac{1}{r} \left\{ x \in \mathbb{R}^l : x_i \in \mathbb{N} \cup \{0\} \ (\forall i), \ \sum_{i=0}^{l-1} x_i = r \right\}. \tag{6}$$

We now define the mapping

$$\mathcal{G} : \Lambda \longrightarrow \Lambda,$$

called *heuristic* [27, p. 9] or *generational operator* [19, p. 144], in the following way: for a vector $p \in \Lambda$ representing the current population, $\mathcal{G}(p)$ is the probability distribution that is sampled independently r times (with replacement) to produce the next population after p. For each of these r choices, the probability of selecting an individual $i \in \Omega$ is equal to $\mathcal{G}(p)_i$, the i-th component of $\mathcal{G}(p)$.

A transition rule τ is called *admissible* if it is a composition of a heuristic $\mathcal{G}$ with drawing a sample in the way described above. Symbolically,

$$\tau(p) = \text{sample}(\mathcal{G}(p)), \quad \forall p \in \Lambda. \tag{7}$$

A transition rule defined this way is nondeterministic, i.e., by applying it repeatedly to the same vector p, we can obtain different results. It should also be noted that, although $\mathcal{G}(p)$ may not belong to Λ_r, the result of drawing an r-element sample is always a population of size r; therefore, it follows from (7) that $\tau(p) \in \Lambda_r$.

The RHS generates a sequence of populations (in the form of population vectors, see (4))

$$\hat{p},\ \tau(\hat{p}),\ \tau^2(\hat{p}), \dots\ , \tag{8}$$

where $\hat{p}$ is a fixed initial population. The RHS can be regarded as a Markov chain where the state space is Λ_r and the values of successive random vectors X_0, X_1, X_2,... are populations (8). Since $\hat{p}$ is fixed, we may assume that X_0 is a random vector taking on the single value $\hat{p}$ with probability 1.

In this paper we consider a special genetic algorithm as a particular case of the RHS. We assume that a single iteration of the genetic algorithm produces the next population form the current population in the way described below (this will be an abstract model for the more specific algorithm described in Section 6). Contrary to [25], we now construct separately three different parts of the next population.

The first part is formed by the “best” elements from the current population, which may be defined arbitrarily, but in Section 6 it will be the set of all nondominated points in the current population. We assume that there are r_0 different “best” elements (repeated elements are deleted), where $r_0 < r/2$.

For the second part of the next population ($r/2 - r_0$ elements):

1. Choose the first parent from the set of “best” elements of the current population, and the second parent from the set of other elements of the current population.
2. Crossover the two selected parents to obtain a child.
3. Put the child into the next population.
4. If the next (partial) population contains less than $r/2$ members, return to step 1.

For the second half of the next population ($r/2$ elements):

1. Choose an individual from the current population.
2. Mutate the individual by replacing it by another, randomly generated element of the search space.

3. Put the mutated individual in the next population.
4. If the next (partial) population contains less than $r/2$ members, return to step 1.

Such a process of evolution can continue infinitely. Therefore, an important aspect in the algorithm is the stopping criterion, which can be either a given number of generations or convergence of a population in a certain sense.

To get our stopping criteria, we will be using some properties of mutation which is generally understood as changing one element of the search space to another with a certain probability. We denote by $u_{i,j}$ the probability that individual $i \in \Omega$ will mutate into $j \in \Omega$. In this way, we obtain a $l \times l$ matrix $U = [u_{i,j}]_{i,j \in \Omega}$. We will denote by

$$\Pr(q \mid p) = \Pr(\tau(p) = q) \tag{9}$$

the probability of obtaining a population q in the current iteration of the RHS algorithm provided the previous population is p. The probability of generating individual $j \in \Omega$ from population p by successive application of selection, crossover and mutation is equal to (see [25], formula (7))

$$\mathcal{G}(p)_j = \Pr([j] \mid p)_{scm} = \sum_{i=0}^{l-1} u_{i,j} \Pr([i] \mid p)_{sc}, \tag{10}$$

where the symbol $[i]$ means that we generate a single individual i (not a whole population as in (9)), the subscript sc means that we are dealing with the composition of selection and crossover, and the subscript scm indicates the composition of selection, crossover and mutation. However, in our algorithm mutation is applied to the second half of population only, and for the first half it is omitted, which corresponds to the case where $u_{i,i} = 1$ and $u_{i,j} = 0$ for $i \neq j$. Therefore, in our case, formula (10) applies only to the generation of the second half of population (with the crossover c meaning in fact "doing nothing"), while to generate the first half, we should use

$$\mathcal{G}(p)_j = \Pr([j] \mid p)_s \tag{11}$$

for the first r_0 elements, and

$$\mathcal{G}(p)_j = \Pr([j] \mid p)_{sc} \tag{12}$$

for the remaining $r/2 - r_0$ elements.

To get a whole new population, one should draw an r-element sample from the probability distribution $\mathcal{G}(p)$, using one of the formulas (10)–(12) (depending on the position of the generated individual).

3 Stopping criteria for finding all minimal elements of Ω

Let us consider the following multiobjective optimization problem. Suppose that Ω is a finite search space defined in Section 2, and let $f : \Omega \to F$ be a function being minimized, where $F = \{f(\omega) : \omega \in \Omega\}$ and $(F, \preceq)$ is a partially ordered set. An element $x^* \in F$ is called a *minimal element* of $(F, \preceq)$ if there is no $x \in F$ such that $x \prec x^*$, where the relation $\prec$ is defined by

$$(x \prec y) :\Leftrightarrow (x \preceq y \wedge x \neq y).$$

The set of all minimal elements of F is denoted by $\mathrm{Min}(F, \preceq)$. We define the set of optimal solutions in our multiobjective problem as follows:

$$\Omega^* = \mathrm{Min}_f(\Omega, \preceq) := \{\omega \in \Omega : f(\omega) \in \mathrm{Min}(f(\Omega), \preceq)\}\,. \tag{13}$$

In particular, if F is a finite subset of the Euclidean space $\mathbb{R}^p$, and $f = (f_1, ..., f_p)$, where each component of f is being minimized independently, then the relation $\preceq$ in F can be defined by

$$(x \preceq y) :\Leftrightarrow (x_i \leq y_i,\ i = 1, ..., l). \tag{14}$$

In this case, Ω^* is the set of all Pareto-optimal solutions of the respective multiobjective optimization problem. We assume that the goal of RHS is to find all elements of Ω^*. Suppose that Ω^* has the following form:

$$\Omega^* = \{j_1, j_2, ..., j_m\}, \tag{15}$$

where the (possibly unknown) number m of optimal solutions is bounded from above by some known positive integer M. We will say that *all the elements of Ω^* have been found in the first t iterations* if, for each $\gamma \in \{1, ..., m\}$, there exists $s \in \{1, ..., t\}$ such that $\tau^s(\hat{p})_{j_\gamma} > 0$. This means that each minimal solution is a member of some population generated in the first t iterations.

The following theorem is a variant of [25, Thm. 6.1].

Theorem 1. *We consider the model of algorithm described above. Suppose that there exists a number $\beta \in (0, 1)$ satisfying*

$$u_{i,j} \geq \beta, \quad \forall i \in \Omega,\ j \in \Omega^*. \tag{16}$$

Let M and t be two positive integers satisfying the inequality

$$M(1 - \beta)^{rt/2} < 1. \tag{17}$$

Let Ω^* be of the form (15) with $m \leq M$. Then the probability of finding all elements of Ω^* in the first t iterations is at least

$$1 - M(1 - \beta)^{rt/2}. \tag{18}$$

Corollary 1. *We consider the same model of algorithm as in Theorem 1. Suppose that condition (16) holds for some $\beta \in (0, 1)$ and for all $j \in \Omega^*$. Let M be a given upper bound for the cardinality of Ω^*. For any $\delta \in (0, 1)$, we denote by $t^*_{\min}(\delta)$ the smallest number of iterations required to guarantee that all elements of Ω^* have been found with probability δ. Then*

$$t^*_{\min}(\delta) \leq \left\lceil \frac{2(\ln(1 - \delta) - \ln M)}{r \ln(1 - \beta)} \right\rceil, \tag{19}$$

where $\lceil x \rceil$ is the smallest integer greater than or equal to x.

4 Construction of the set of minimal elements

The results described above enable us to formulate a practical method for constructing the set Ω^*. Various elements of this set are members of different populations created by using a genetic algorithm, and cannot be easily identified. To obtain an efficient method of constructing Ω^*, some modifications of the RHS are necessary. Here is an algorithm which is a combination of the RHS and the base VV (Van Veldhuizen) algorithm described in [20, § 3.1].

1) Suppose we have some RHS satisfying the assumptions of Theorem 1, which generates a sequence of populations (8), where all of them are members of Λ_r. For each $p \in \Lambda_r$, we define the set of individuals represented in population p:

$$\operatorname{set}(p) := \{\omega \in \Omega : p_\omega \neq 0\}. \tag{20}$$

2) We create a sequence $\{D_t\}$ of subsets of Ω as follows:

$$D_t := \operatorname{set}(\tau^t(\hat{p})), \quad t = 0, 1, \dots\,, \tag{21}$$

where $\tau^0 :=$ id is the identity mapping.

3) We define another sequence $\{E_t\}$ of sets recursively by

$$E_0 := \operatorname{Min}_f(D_0, \preceq), \tag{22}$$

$$E_{t+1} := \operatorname{Min}_f(E_t \cup D_{t+1}, \preceq), \quad t = 0, 1, \dots\,, \tag{23}$$

where we have used the notation Min_f as in (13). Formulas (22) and (23) define the VV algorithm.

In [20, Prop. 1] it is shown that the sets $f(E_t)$ converge with probability 1 to $\operatorname{Min}(F, \preceq)$ in the sense of some metric. However, according to [20], the size of the sets E_t will grow to the size of the set of minimal elements. Since this size may quite large, this basic algorithm cannot be always used in practice. In fact, procedure 1)–3) described above can have practical value only if the cardinality of Ω^* is relatively small, which is true at least for some multiobjective optimization problems on discrete sets.

Theorem 2. *Let the assumptions of Corollary 1 be satisfied. Then, with probability* δ*, we have*

$$\Omega^* = E_t, \quad \forall t \geq t^*_{\min}(\delta). \tag{24}$$

5 Problem formulation

Let us assume that $f : X \to \mathbb{R}^p$ is a given mapping, where X is a discrete subset of $\mathbb{R}^k$. We consider the following multiobjective optimization problem:

$$\operatorname{Min}\{f(x) : x \in X\}. \tag{25}$$

The solution of problem (25) lies in finding all Pareto-optimal (efficient) points of X, which respect to the partial order relation defined by formula (14). The elements of X may be, for instance, combinatorial objects: permutation, partial permutation, combination and others. Let us define here the combinatorial set of permutations.

Let us assume that we have a pre-assigned multiset $A = \{a_1, a_2, ..., a_n\}$, and $\mathrm{set}(A) := \{e_1, e_2, ..., e_k\}$ is its base, where $e_j \in \mathbb{R}$ for all $j \in \mathbb{N}_k := \{1, ..., k\}$, and the multiplicity of each element e_j is equal to $k(e_j) = r_j$, $j \in \mathbb{N}_k$, where $r_1 + r_2 + ... + r_k = n$.

An *arranged m-sample* from the multiset A shall be a collection, identified as

$$a = (a_{i_1}, a_{i_2}, ..., a_{i_m}), \tag{26}$$

where $a_{i_j} \in A$ for all $i_j \in \mathbb{N}_n$, $j \in \mathbb{N}_m$, $i_s \neq i_t$ if $s \neq t$ $(s, t \in \mathbb{N}_m)$, $m \leq n$.

Definition 1. [4,5,23] *A set $P(A)$ whose elements are n-samples of the form (26) from the multiset A is called a* Euclidean combinatorial set *if, for its arbitrary elements $a' = (a'_1, a'_2, ..., a'_n)$ and $a'' = (a''_1, a''_2, ..., a''_n)$, the condition*

$$(a' \neq a'') \Leftrightarrow (\exists j \in \mathbb{N}_n : a'_j \neq a''_j)$$

is satisfied. In other words, two elements of the set $P(A)$ are different from one another if, regardless of other differences, they have different arrangements of symbols that constitute them.

A set of permutations with repetitions of n appropriate real numbers, among which there are k different ones, is called a common set of permutations *and denoted by $P_{n,k}(A)$.*

Let us examine the elements of the set of permutations with repetitions as points of the arithmetic Euclidean space $\mathbb{R}^n$.

Let $P(A)$ be a Euclidean combinatorial set, and let a vector a of the form (26) (with $m = n$) be an element of $P(A)$. The mapping

$$\varphi : P(A) \to P_\varphi(A) \subset \mathbb{R}^n$$

is called an *immersion* of the set $P(A)$ into the arithmetic Euclidean space if φ places the set $P(A)$ to an unambiguous correspondence with the set $P_\varphi(A) \subset \mathbb{R}^n$ according to the rule:

$$\text{for } a = (a_{i_1}, ..., a_{i_n}) \in P(A),\ \ x = \varphi(a),\ \ x = (x_1, ..., x_n) \in P_\varphi(A),\ \ \text{we have } x_j = a_{i_j} \text{ for all } j \in \mathbb{N}_n.$$

In this case, problem (25) may be formulated as a vector optimization problem on a discrete set of permutations:

$$\mathrm{Min}\{f(x) : x \in P_{n,k}(A)\}. \tag{27}$$

The solution of problem (27) shall be understood as the task of finding the elements of the set of Pareto-optimal (effective) solutions $\Omega^* = P(f, X)$, where $X = P_{n,k}(A)$.

6 The main algorithm

In this section, we describe a genetic algorithm for solving the multicriterial optimization problem (25) on a discrete combinatorial set X. It is a particular case of the algorithm, described in Section 2.

In the algorithm we use three types of crossover. The first type is the classical one-point crossover, while the remaining two types are variants of two-point crossover. The third type may be used whenever permutations with repetitions are not allowed. We will explain them on a simple example. Let us assume that there are two parental permutations (12345), (34521).

1. Randomly determine a crossing point at which both permutations (12|345), (34|521) are divided into two parts, and the final segments are exchanged. As a result, we obtain (12|521), (34|345). It should be noted that we have obtained two permutations with repetitions.
2. We choose – randomly and uniformly – two crossing positions. The first point of discontinuity is situated between the first and the second elements of permutations, while the second one – between the fourth and the fifth elements: (1|234|5), (3|452|1). The permutations exchange the fragments placed between the crossing positions: (1|452|5), (3|234|1). The resulting permutations also have repeating elements.
3. In the same way as in the previous case, we randomly and uniformly choose two crossing positions: (1|234|5), (3|452|1). The first stage: the permutations exchange the fragments placed between the crossing points: $(*|452|*)$, $(*|234|*)$. The second stage: instead of asterisks, the respective elements from the parental permutations, starting with the second element, are being inserted. If the permutation element is repeated, then we take the next element in the parent permutation. In particular, in the first permutation (1|234|5), 3 is such a number, followed by 4, which is present in the new permutation thus being omitted, 5 is also omitted and we move to the start of permutations, select the number 1. As a result, instead of $(*|452|*)$ we receive (14523), in a similar way from (3|452|1), instead of $(*|234|*)$, we receive (52341).

The mutation process is very simple and consists in replacement of a part of the population with another one, which is indiscriminately selected and has the same size. However, the stopping criteria, described in Section 3, are still actual for this algorithm because their proofs use properties of mutation only.

The following algorithm can be used to solve problem (27):

Step 1. We set the population size r, a probability $\delta \in (0,1)$, and the number of algorithm iterations $t^*_{\min}(\delta)$ which is calculated by formula (19), where M is a given upper bound for the cardinality of Ω^*, and $\beta = 1/|\Omega|$ describes the probability of mutation. We also set the initial value $t = 0$.

Step 2. We form a population $P^{(t)}$ of randomly generated permutations $a_i \in X$, $i \in \mathbb{N}_r$.

Step 3. We compute the values for each of p criteria $f_1, ..., f_p$ over the whole population $P^{(t)}$.

Step 4. We determine the set F_t of *nondominated* elements (the first front) of $P^{(t)}$. For this purpose, we can use, for example, the "fast-non-dominated-sort" procedure described in [3].

Step 5. We place the whole set F_t in the next population $P^{(t+1)}$ (repeated permutations are excluded from F_t). Then we complement the population of $r/2$ elements by adding $r/2 - |F_t|$ permutations obtained by crossover of elements from F_t with elements from $\mathrm{set}(P^{(t)}) \backslash F_t$.

Step 6. We finish the formation of population $P^{(t+1)}$: the remaining $r/2$ elements are obtained by generation of random permutations.

Step 7. We construct the set E_t according to (22)–(23) (note that, for $t = 0$, we have $E_0 = F_0$).

Step 8. We increment the value of t by 1. If $t < t^*_{\min}(\delta)$, then we move to step 3. Otherwise, by Theorem 2, the current set E_t is equal to the set of solutions Ω^* with probability δ.

7 Numerical examples

In this section we present the results of computational testing of the algorithm described in Section 6 on two examples. In both examples, we have used the first type o crossover only.

Example 1. Let us define a vector function $f = (f_1, f_2, f_3)$ by

$$f_1(x_1, ..., x_6) = \frac{3x_1 + 2x_2 + 5x_3 + x_4 + 7x_5 + 3x_6}{4x_1 + x_2 + 2x_3 + 3x_4 + 5x_5 + x_6},$$
$$f_2(x_1, ..., x_6) = \frac{5x_1 + x_2 + 7x_3 + 2x_4 + 8x_5 + x_6}{4x_1 + 2x_2 + 2x_3 + 4x_4 + 2x_5 + 3x_6},$$
$$f_3(x_1, ..., x_6) = \frac{7x_1 + 2x_2 + 9x_3 + 2x_4 + 2x_5 + 3x_6}{2x_1 + 2x_2 + x_3 + 7x_4 + x_5 + x_6}.$$

We consider the problem of minimizing f on the combinatorial set of permutations without repetitions with the base $A = \mathrm{set}(A) = \{1, 2, 3, 4, 5, 6\}$, that is, we consider problem (27) with $n = k = 6$.

The cardinality of the set $P_{6,6}(A)$ is equal to $6! = 720$. Therefore, we can take $M = 720$ as an upper bound for the number of Pareto-optimal solutions. Then $\beta = 1/M \approx 0,001389$. The population size is $r = 300$. For the stopping criterion, we accept the probability $\delta = 0,99$. We calculate from formula (19) $t^*_{\min}(\delta) = 54$. After 54 iterations of the algorithm, we obtain a set of permutations E_t, where $t = t^*_{\min}(\delta)$, consisting of 15 elements which are listed in the second column of Table 1.

Example 2. We consider the problem of minimizing the vector function $f = (f_1, f_2)$, where

$$f_1(x_1, x_2) = \frac{3x_1 + 5x_2}{4x_1 + 2x_2}, \quad f_2(x_1, x_2) = \frac{5x_1 + 7x_2}{2x_1 + 3x_2},$$

on the discrete set

$$X = \{(x_1, x_2) : x_1 \in \{0\} \cup \mathbb{N}_4,\ x_2 \in \{0\} \cup \mathbb{N}_5\}.$$

Table 1. Results for Example 1

No.	Element of E_t	Value of f_1	Value of f_2	Value of f_3
1	562431	1,120690	1,278689	1,555556
2	651342	1,129032	1,322581	1,62000
3	215634	1,285714	1,387097	1,516667
4	431562	1,117647	1,451613	0,771739
5	342651	1,109375	1,409836	0,808989
6	451632	1,034483	1,09375	0,806818
7	351642	1,084746	1,177419	0,725275
8	532641	1,030303	1,338462	0,953488
9	513624	1,084746	1,161765	1,010989
10	251634	1,153846	1,000000	0,65625
11	451623	1,037807	0,969231	0,808989
12	431625	1,066074	0,940299	0,762887
13	541623	1,000120	1,000000	0,865169
14	243615	1,239130	0,952381	1,238095
15	234165	1,578947	1,811321	2,656250

This is an example of problem (25), where the cardinality of X is equal to 30. Therefore, we can take $M = 30$ and $\beta = 1/30 \approx 0,03333$. The population size is $r = 25$. For the stopping criterion, we take $\delta = 0,99$. We calculate from formula (19) $t^*_{\min}(\delta) = 19$. After 19 iterations of the algorithm, we obtain a set $E_t \subset X$, where $t = t^*_{\min}(\delta)$, consisting of 5 elements which are listed in the second column of Table 2.

Table 2. Results for Example 2

No.	Element of E_t	Value of f_1	Value of f_2
1	(1,0)	0,75	2,5
2	(1,1)	1,33	2,4
3	(2,0)	0,75	2,5
4	(1,2)	1,625	2,375
5	(3,0)	0,75	2,5

8 Conclusions

We have developed a new method of generating Pareto-optimal solutions of a discrete multiobjective programming problem on some set of combinatorial objects (for example, permutations partial permutations, or combinations). This has been achieved by using a specially designed genetic algorithm which includes some probabilistic stopping criterion. The preliminary results of numerical tests, presented above, show the efectiveness of our method.

References

1. Alharbi, S., Venkat, I.: A genetic algorithm based approach for solving the minimum dominating set of queens problem. Journal of Optimization **Vol. 2017**, Article ID 5650364, 1–8
2. Aytug, H., Koehler, G.J.: Stopping criteria for finite length genetic algorithms. INFORMS Journal on Computing **8**, 183–191 (1996)
3. Deb. K, Pratap, A., Agarwal, S., Meyarivan, T.: A fast and elitist multiobjective genetic algorithm: NSGA-II. IEEE Transactions on Evolutionary Computation **6**(2), 182–197 (2002)
4. Donets, G.A., Kolechkina, L.N.: Method of ordering the values of a linear function on a set of permutations. Cybernetics and Systems Analysis **45**(2), 204–213 (2009)
5. Emelichev, V.A., Kovalev, M.M., Kravtsov, M.K.: Polytopes, Graphs, and Optimisation. Nauka, Moscow (1981)
6. Engau, A., Wiecek, M.M.: Generating ε-efficient solutions in multiobjective programming. European Journal of Operational Research **177**, 1566–1579 (2007)
7. Greenhalgh, D., Marshall, S.: Convergence criteria for genetic algorithms. SIAM Journal on Computing **30**, 269–282 (2000)
8. Kiyoumarsi, F.: Mathematics programming based on genetic algorithms education. Procedia – Social and Behavioral Sciences **192**, 70–76 (2015)
9. Koehler, G.J., Bhattacharya, S., Vose, M.D.: General cardinality genetic algorithms. Evolutionary Computation **5**, 439–459 (1998)
10. Koliechkina, L.N., Dvernaya, O.A., Nagornaya, A.N.: Modified coordinate method to solve multicriteria optimization problems on combinatorial configurations. Cybernetics and Systems Analysis **50**(4), 620–626 (2014)
11. Koliechkina, L.N., Dvirna, O. A.: Solving extremum problems with linear fractional objective functions on the combinatorial configuration of permutations under multicriteriality. Cybernetics and Systems Analysis **53**(4), 590–599 (2017)
12. Lima, A., Vettorazzi, D., Cruz, A., Lima, C., Soares, A.: ATM: a new heuristic algorithm based on genetic algorithm and betting theory. IEEE Latin America Transactions **15**(3), 510–516 (2017)
13. Long, Q., Wu, Ch.: A hybrid method combining genetic algorithm and Hooke-Jeeves method for constrained global optimization. Journal of Industrial and Management Optimization **10**(4), 1279–1296 (2014)
14. Nix A., Vose, M.D.: Modelling genetic algorithms with Markov chains. Annals of Mathematics and Artificial Intelligence **5**, 79–88 (1992)
15. Osman, M.S., Abo-Sinna, M.A., Mousa, A.A.: An effective genetic algorithm approach to multiobjective resource allocation problems (MORAPs). Applied Mathematics and Computation **163**, 755– 768 (2005)
16. Rahmo, E.-D., Studniarski, M.: A new global scalarization method for multiobjective optimization with an arbitrary ordering cone. Applied Mathematics **2017**(8), 154–163
17. Rahmo, E.-D., Studniarski, M.: Generating epsilon-efficient solutions in multiobjective optimization by genetic algorithm. Applied Mathematics **2017**(8), 395–409
18. Rani K., Kumar V.: Solving travelling salesman problem using genetic algorithm based on heuristic crossover and mutation. International Journal of Research in Engineering and Technology **2**(2), 27–34 (2014)

19. Reeves, C.R., Rowe, J.E.: Genetic Algorithms – Principles and Perspectives: A Guide to GA Theory. Kluwer, Boston (2003)
20. Rudolph,G., Agapie, A.: Convergence properties of some multi-objective evolutionary algorithms. In: Zalzala, A. et al. (eds.) Proceedings of the 2000 Congress on Evolutionary Computation (CEC 2000), vol. 2, pp. 1010–1016. IEEE Press, Piscataway (NJ) (2000)
21. Rowe, J.E., Vose, M.D., Wright, A.H.: Structural search spaces and genetic operators. Evolutionary Computation **12**, 461–493 (2004)
22. Salgueiro, R., de Almeida, A., Oliveirac, O.: New genetic algorithm approach for the min-degree constrained minimum spanning tree, European Journal of Operational Research **258**, 877–886 (2017)
23. Stoyan, Yu.G., Yakovlev, S.V.: Mathematical models and optimization methods for geometric design. Naukova Dumka, Kiev (1986)
24. Studniarski, M.: Stopping criteria for genetic algorithms with application to multiobjective optimization. In: R. Schaefer et al. (eds.) Parallel Problem Solving from Nature – PPSN XI, Part I, LNCS, vol. 6238, pp. 697–706. Springer, Berlin (2010)
25. Studniarski, M.: Finding all minimal elements of a finite partially ordered set by genetic algorithm with a prescribed probability. Numerical Algebra, Control and Optimization **1**(3), 389–398 (2011)
26. Tabatabaee, H.: Solving the traveling salesman problem using genetic algorithms with the new evaluation function. Bulletin of Environment, Pharmacology and Life Sciences **4**, 124–131 (2015)
27. Vose, M.D.: The Simple Genetic Algorithm: Foundations and Theory. MIT Press, Cambridge, Massachusetts (1999)

Section 12

Image Analysis

Fast Object Detector based on Convolutional Neural Networks

Karol Piaskowski, and Dominik Belter

Poznan University of Technology, Institute of Control, Robotics and Information Engineering,
Poznan, ul. Piotrowo 3A, Poland;

Abstract. We propose a fast object detector, based on Convolutional Neural Network (CNN). The object detector, which operates on RGB images, is designed for a mobile robot equipped with a robotic manipulator. The proposed detector is designed to quickly and accurately detect objects which are common in small manufactories and workshops. We propose a fully convolutional architecture of neural network which allows the full GPU implementation. We provide results obtained on our custom dataset based on ImageNet and other common datasets, like COCO or PascalVOC. We also compare the proposed method with other *state of the art* object detectors.

The full text will be available in the edited book "Computational Modeling of Objects Presented in Images. Fundamentals, Methods, and Applications", eds. Barneva R.P., Brimkov V.E., Kulczycki P., Tavares J.M.R.S., to be published by Springer in the *Lecture Notes in Computer Science* series soon.

Applying computational geometry to designing an occlusal splint

Dariusz Pojda, Agnieszka Anna Tomaka, Leszek Luchowski, Krzysztof Skabek, and
Michał Tarnawski

Institute of Theoretical and Applied Informatics, Polish Academy of Sciences,
Baltycka 5, Gliwice, Poland;

Abstract. The occlusal splint is one of the methods of treatment of discrepancies between the centric relation and maximal intercuspation (CR/MI), and other temporomandibular joint (TMJ) disorders. It is also a method of reducing the effects of bruxism. Designing an occlusal splint for a given relation between the maxilla and the mandible involves: creating partial surfaces, integrating them, and producing the splint on a 3D printer. The paper presents and compares some techniques used to design splint surfaces under a required therapeutic maxilla-mandible relation.

The full text will be available in the edited book "Computational Modeling of Objects Presented in Images. Fundamentals, Methods, and Applications", eds. Barneva R.P., Brimkov V.E., Kulczycki P., Tavares J.M.R.S., to be published by Springer in the *Lecture Notes in Computer Science* series soon.

Assessment of Patients Emotional Status According To iris Movement

ALHAMZAWI HUSSEIN[1] [0000−0002−9537−6208] and ATTILA FAZEKAS

[1] Department of the Computer Graphics and Image Processing, Faculty of Informatics, University of Debrecen, Debrecen, Hungary
`Aliov.mezher@gmail.com`

[2] Department of the Computer Graphics and Image Processing, Faculty of Informatics, University of Debrecen, Debrecen, Hungary
`fazekas.attila@inf.unideb.hu`

Abstract. The human eye allows vision but also reflects mood, emotional state, mental and physical condition. Eye activity and behavior reflected in pupil size, gaze direction, eyelid motion or eye-opening are affected by states of effect. Investigating literature, it was clear that features extracted from the eye region are included in the most innovative techniques in emotion recognition giving comprehensive, reliable and objective information relating to subjects emotional state. The aims of this Article, it delivers the foundational work required for investigating the role of gaze distribution as an emotional index. Towards this objective, an eye gaze detector is developed and tested analyzing videos of volunteers performing a specific gaze task. The accuracy of the method was checked using different lighting and distance conditions in order to find the best parameters to be used. In short-term (tracking the gaze and plot a medically diagram that will give us information about the Patients situation for example if she/he is angry or may have some stress so we can be postponed giving the medicine for a while and we could wait until her/his situation will be better and then we can give her/him the medicine).

Keywords: Gaze tracking · Biomedical information · Canny edge filter · Emotion recognition .

1 INTRODUCTION

Humans are great at deciphering emotional expressions quickly and efficiently, reflect their significance the success of the social interaction [1] . Inability to respond to the emotional state of others and the exact discrimination is associated with a range of social unrest, from autism to psychopathy [2] ,[3],[4]. Across the cultures, people can be recognize from the face at least six fundamental expression of emotion ,Including surprise , joy , Sadness , Fear , disgust and anger [5],[6].as long facial expression of self sensitive emotion , like An embarrassment or the shame [7],[8] and the pride [9]. The fundamental emotions for the facial expressions are created with characteristic configurations of the movement of the facial muscle, which provide the basic sensory perception of discrimination between a various types of the emotional expressions [10]. For example, The wideness of the eye and the flexing the muscles of the mouth reflect the state the facial expression of fear ,while alternative flexion of the muscle of the mouth and eye restriction reflect the state the facial expression of the joy [10]. Emotional expression have been arisen as efficacious adaptation to advantage the expresser and become only communicative as a minor function through continued the practice and heredity [12]. For example, when people put expressions of fear, The patterns of eye movements indicate the size of the nose To enhance the perception of one environment While the opposite pattern was noted and indicted for the disgusting [13]. For categorization the facial emotion , we need more information that is provided by different regions of the face[14.],[15] And also the identity of the face[16],[17]. many studies and researches indicated to show that they used spread strategy for focus on a more diagnostic area, It is usually indexed by eye movements, a public reflection of attention spread[18]. For example, The rhesus macaque spend a lot of time fixation at the eyes, While watching faces that are threatened compared to other faces like yawn and lip smack, which they are Focused more strongly at the mouth [19] fixation pattern for the human display is an individual difference when viewing the faces, These patterns also varied with one person through different tasks, However, these patterns were surprisingly reliable through examples of a specific participant and task [20]. While it is not clearly always both attentional strategies really progress and improve the performance, for successful emotion recognition in some cases, we need to select a specific area of appearing face. For example, patients with bilateral amygdala damage are comparatively inexact at Fear recognition from the face compared to observation of healthy [21], and a large enroll to this Disability perhaps a lack of attention in the face for the eye region. Uncommonly, when given straightforward instruction to look or move their eyes into the region of the eye of facial expression, amygdala damage patients can recognize the fear [22], Indicating that the basic deficit of the patient is not to identify fear, In itself, but to some extent in selectively looking at the area of the face most diagnostic for successful recognition of the fear. As an example likely to be similar, a typical autistic person looks a lot of time at nondiagnostic relative to characteristic (e.g., mouth , nose, eyes) areas of the face through the emotion recognition, Probably contributes to the inability to recognize emotion[23]. There is other works on a specific nation have been shown that when the patterns of the eye-gaze were restrained, Encoding for the memory was impaired on face identity, depending on a condition where eye gaze allowed to move freely[24]. Deployment Strategy of attention inside the face is driven not just by properties of low-level visual, But also through the attributes and objectives of the observer. Slow eye-movement patterns are displayed through Spider phobics when presenting stimuli [25] Related to fear for controls. People who have a high degree of neuroscience are looking longer in the eye area than fear faces relative to those in low neurotic [26]. Westerners are less likely to fixate on the eye area of the face less than extent compared to Easterners, who are more likely to fixate on the eye area [27]. The effective context in which identical faces were embedding has also been shown to alter emotional perception dramatically.[28]. These results reveal individual and collective differences in eye movements during emotion recognition leading to Target-based biases in cognitive processing. The requirements for addressing emotion recognition seem to stimulate certain patterns of attention across the face. We are here exploring how attention, as illustrated by eye movement patterns, four different classics of the emotional expression were detection during this experiment. We recorded eye movements where participants were neutralizing the emotional expressions of certain emotions. Experiments were done upon a student in University of Debrecen,Hungary and people around the university and in Afak hospital ,Iraq .. The work presented here differs from those identified in the literature for using as input only a low-cost Webcam, low resolution (640x480) and low acquisition speed (15 FPS) and does not use any feature to restrict user movements, or any type of zoom to aid in the identification of the eyes.

2 RELATED WORK

Peng [29] identifies the eyes from the gradient of the grayscale image, which restricts the search region of the eyes very effectively. The use of horizontal and vertical projections of the gradient points allows the desired region to be identified with high precision. The whole process is shown in Figure 1. Once this region is identified (part B of Figure 1), the final step is to identify the exact location of the eyes. For this purpose, a scan with a pre-defined model (part A of Figure 1) is made in the eye region. Until the area where the eyes are in the image is located In each position an evaluation of the image of the eye region with the model is made using equations (1) and (2) below, the region that minimizes equation (2) is considered to be the eyes.

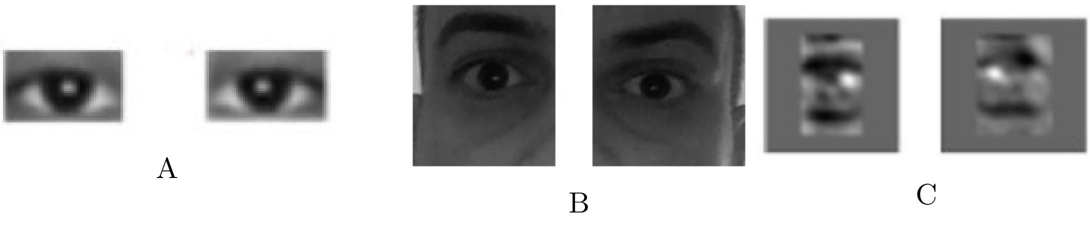

Fig. 1: Search process in the Peng system [29]. [A] Model used for searching, [B] Eye region extracted by gradient ,[C] Difference between the image and the model in the eye region.

$$C_{f,j}[i,j] = \sum_{k=1}^{m} g[k,l] f[k+1,l+j] \tag{1}$$

$$M[i,j] = \frac{C_{f,g}[i,j]}{[\sum_{k=1}^{m} \sum_{l=1}^{n} f^2[k+i]l+j]]^{\frac{1}{2}}} \tag{2}$$

Where g [k, l] represents the intensity of the pixel [k, l] in the image and f [i, j] the intensity of the pixel [i, j] in the model. Equation (1) represents the correlation between the model and the image considering the image from the point [k, l]. Note that the denominator of the second equation is the quadratic mean of the image in the segment being evaluated, the method proposed by Zhang [30] used to adjust the "red-eye" of photographs, identify regions of red color (*) and makes refinements using search masks that are applied to the image in succession.
Li [31] searches the iris from a point, the method searches for a radial sequence of points that are consistent with the iris edges. From there the RANSAC (random sample consensus) algorithm is used to randomly select a group of points and check if the sequence fits the desired model. In this case the model looks for is an ellipse, where size and eccentricity restrictions are added in the search process. Figure (2) shows the procedure used by Li.

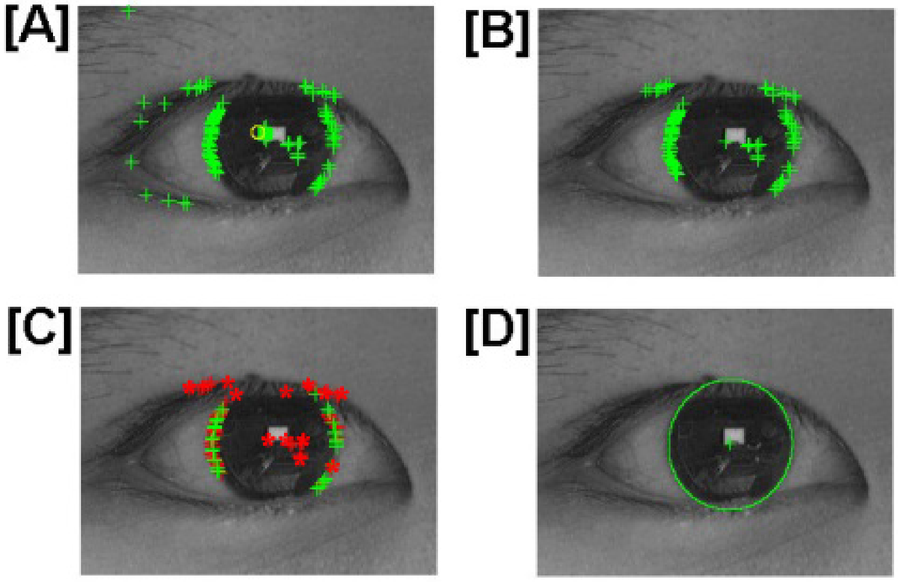

Fig. 2: Procedure proposed by Li [31]. [A] Set of all points found (+) [B] Points remaining after exclusion of points far from average [C] Selected points (+) and deleted (*) [D] Best ellipse using only the selected points.

3 PROPOSED MODEL

The work presented here is part of a color image with the already delimited user face, this step is done as described in [32]. From this result, we look for a set of border points that approach a circumference in the two regions expected for the identification of the eyes. Some restrictions are used in the eye detection process to reduce the number of false positives, as the expected iris diameter in the image and, also, the existence of a striking difference between the tone external and internal points of the region considered.

3.1 Implementation

In the works were presented in [29] a camera with a resolution higher than a "Web Cam" is used, or the face is supported on a holder reducing freedom of movement of the user or even using special lenses to increase the eye region. The system presented here initially uses the procedure described by Candide in [32] to identify the face region, and then the color image generated directly by the "Webcam" is converted to gray scale.
A gradient-type filter is then applied to the grayscale image and a resultant binarization of the image is done. Two points close to the eyes are identified through a procedure similar to that used by Peng [29], as shown in Figure 3. In [A], from the horizontal projection of the image gradient are two points of maximum, one in each half of the image. These points identify the vertical lines that delimit the sides of the face. In [B], in the middle third of the face, bounded by the lateral vertical lines, the maximum point of the vertical projection of the region is identified. This point determines the horizontal line passing through the eyes. And finally in [C], in the same region identified in the previous step, there are two maximum points in the horizontal projections, one in each half of the face. These points, together with the horizontal straight line that passes through the eyes, determine the two points where the search begins and have close proximity to the two eyes.

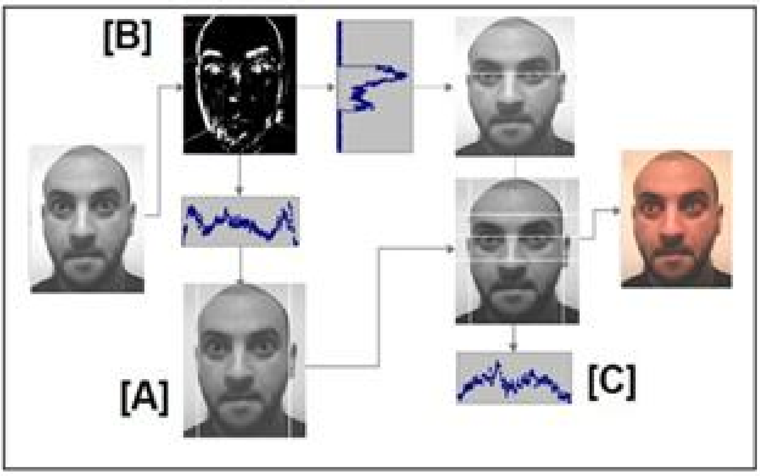

Fig. 3: Model used to identify the eye region in the system.

In each of the steps it is evaluated the possibility of not having maximum points in the expected region with the desired amplitude. In these cases a default value is set. Identification of the lateral borders, for example, is usually impaired in people with long hair, which causes a dispersion of the edge region. In 95% of the cases the initial points found are on the eyes and even in the worst cases, the region delimited by the sides of the face and the lines parallel to the eyes are sufficient for a good initial estimate.

The next step in the process is finding the contours of the irises. To do this, a search for edge points that are closest to a circumference within the region delimited in the previous step is performed.

For the identification of the contours, a canny type filter [33] is applied to the grayscale image. The filter is applied with a distinct set of parameters, depending on the side of the selected face, in order to minimize uneven lighting effects. As shown in [33] the Canny filter uses two parameters that represent a range of intensities. If the intensity of the contour is greater than the largest parameter, the point will be considered as belonging to the contour, if it is lower than the smaller it will be disregarded. Points with intermediate intensity will be considered if they participate in a chain of points that have at least one point with intensity higher than the highest parameter.

The Canny filter parameters are obtained iteratively. Initially, the filter is applied and the proportion of edges in the region of the search mesh is identified. If the number of border points is less than the expected range, the canny filter parameters are decreased in order to identify more points. If the number of border points exceeds the accepted range, the parameters are increased to minimize edge identification.

Figure (4) shows the result of applying the Canny filter to different parameters. In [A] we observe the result of the process after the 1st iteration, and in [B] after the 8th iteration.

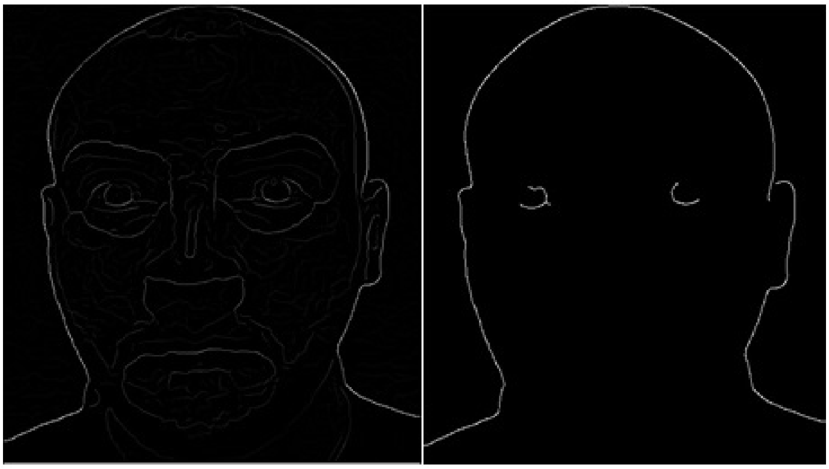

Fig. 4: Images after application of the Canny filter. [A] Image after the first iteration. [B] Image after the 8th iteration.

The search for the iris is made starting from points in an 18x6 mesh with center at the point identified in the previous step that are equally between 0.017 * (Face Width), this constant was inferred as follows: for the images used in the tests, the lowest ratio between the iris diameter and the face width was 0.0425, thus, a 20% margin was used for the accepted minimum radius is 0.034 * (Face Width). For the mesh step, half of this value was considered, ensuring that at least one point of the mesh starts inside the iris. Figure (5) shows the search mesh superimposed on the initial image.

From each point of the mesh, a radial search with a neighborhood 8 is started. If an edge point is identified, a local search is made to identify if this point is part of a larger set, with at least 25 pixels (value identified experimentally). If this does not occur the point is discarded.

This method avoids small blemishes in the eye region. The search continues until a point that meets the constraint is found or the number of attempts is greater than 15. If the number of points found is greater than 3, identifies the circle which best fits the set. Otherwise, the search restarts from the next point in the mesh and this set is discarded. The quality of the fit of the points to the circumference is defined by equation (3).

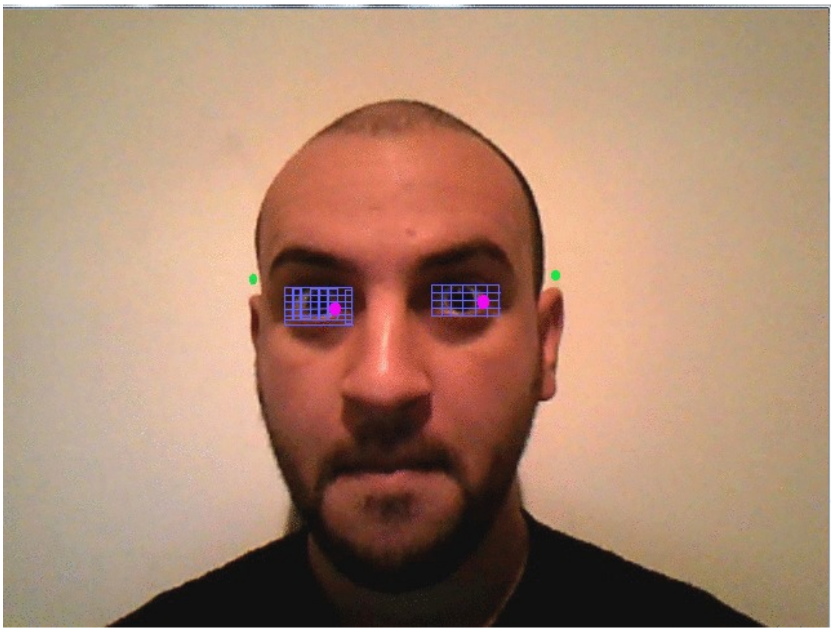

Fig. 5: Overlap of the search grid over the initial image

$$\varepsilon = \frac{\mid \sum_{k=1}^{m} \sqrt{(x_k - x_c) + (y_k - y_c)^2} - R \mid}{M * R} \tag{3}$$

Where R is the radius of the circumference found, Xc and Yc are the coordinates

of the center of the circumference, Xk and Yk are the coordinates of each of the points, and m is the total number of points considered.
Equation (3) determines the error of fitting the points to a circumference. If the error is less than 0.24 a search refinement procedure will be done. In this refinement a local search is made starting from each of the original points in search of other edge points that are close to the contour of the estimated circumference. From this new set of points lies the new circumference that best suits this new set. Sets of points that are not evenly distributed around the circumference are discarded; the criterion used to define this uniformity is the following:

- The circumference is divided into 36 bands of 10 degrees.
- Check the number of points within each track. The more bands have points the better the "uniformity" of the circumference.
- Sets that are not distributed over 140 degrees are discarded.

Figure (6) illustrates the two-condition search refinement process, in 6 [A] one has the search in a point that meets the initial conditions of diameter of the circumference, number of points and error, in 6 [B], after refinement, the set is discarded because the points do not distribute radially within the expected range. In 6 [C] and 6 [D] we observe a group where the refinement meets a set that meets the requirements.

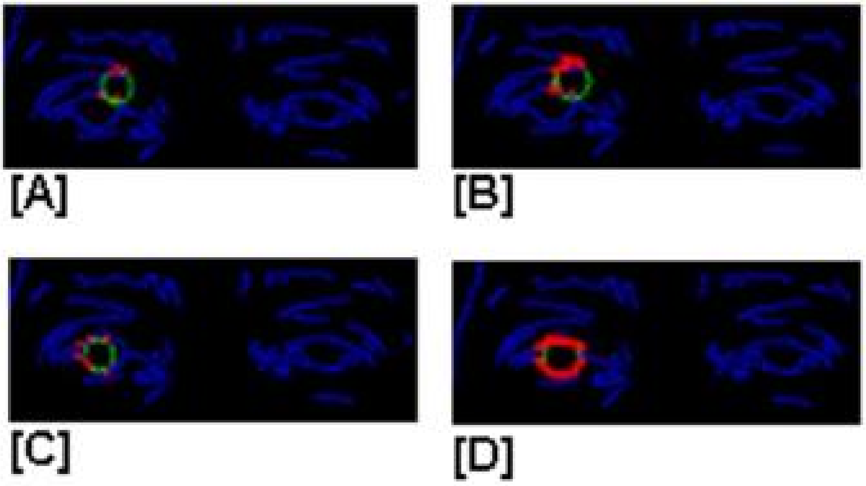

Fig. 6: Refinement of search in two conditions.

The process is repeated for each point of the mesh, the sets of points that meet the constraints (minimum error, circumference diameter, point distribution) are stored. Among the sets of points selected, one that has the greatest difference of intensity between points inside the estimated and immediately external circumference will be considered as the user's iris. The movement of the mouse pointer

will be defined from the deviation of the position of the iris in front of the calculated average in the first ten seconds of execution. If the current position drifts to the right the mouse will move to the right, if the current position deflects to the left the mouse will be moved in this direction and in the same way if it deflects in the vertical direction.
The last step of our project it was used kalman filter as shown in [34] to tracking the mouse that moved through iris movement and drawing diagram for it .

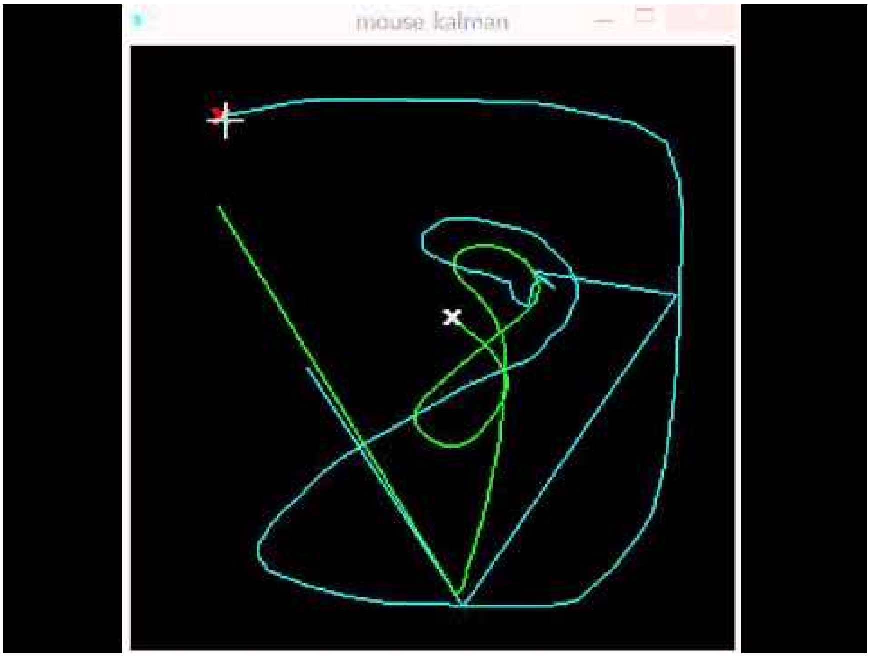

Fig. 7: Drawing daigram for mouse cursor movement using kalman filter.

4 EXPERIMENTS

The experiments were divided into two parts. In the first part, iris identification tests were performed on static images, the second part, tests were performed on images acquired in real time , and the third part is a physiology part to determine the patients situation mood .For the experiments with static images the images of the IMM Face Database group were used. Only colored images were selected, with front faces totaling 60 images. The intention to use a sample already available on the Internet is to enable other works to be compared in a simple and standardized way. Figure (7) illustrates the result of the search for 12 images under different light conditions and facial expression.

Fig. 8: Identification of irises in 12 IMM Face Database images [35].

The first and second faces were selected to illustrate conditions in which the algorithm usually fails, in the first case the person is with the eyes slightly closed and in the second case the difference of illumination between the sides of the face of the individual is much accented.

For the group of images selected, 109 hits were obtained (each eye individually considered as a hit) and 6 false positives. Experiments with the sequences of images presented a new set of difficulties. The images used in the first experiment have resolution of 480x640, the images taken directly from the camera (Creative Webcam Live! Pro), although they have a similar definition and good lighting conditions do not have the same quality as those extracted from a digital camera because even small movements generate slightly blurred images. The time taken to acquire a webcam image used is about 8 times slower compared to a digital camera, Typically on a webcam the acquisition speed is 15FPS (0.067s per image), while digital cameras require only 1 / 125s (0.008s per image). This makes even small movements with the face; generate slightly "blurred" images in the acquisition made by the webcam which impairs the detection of edges. Another factor that influences the result is the positioning of the camera, in this case the distance from the camera to the face is not the main factor, and the main problem is the height of the camera with respect to the eyes. Positioning the camera below the eye line favors the system, while the reverse adversely affects the system. The higher the position of the camera, the more the eyelids overlaps the iris, hampering the search for a circumference.

Figure (8) shows the equipment used and the lighting conditions during the tests.

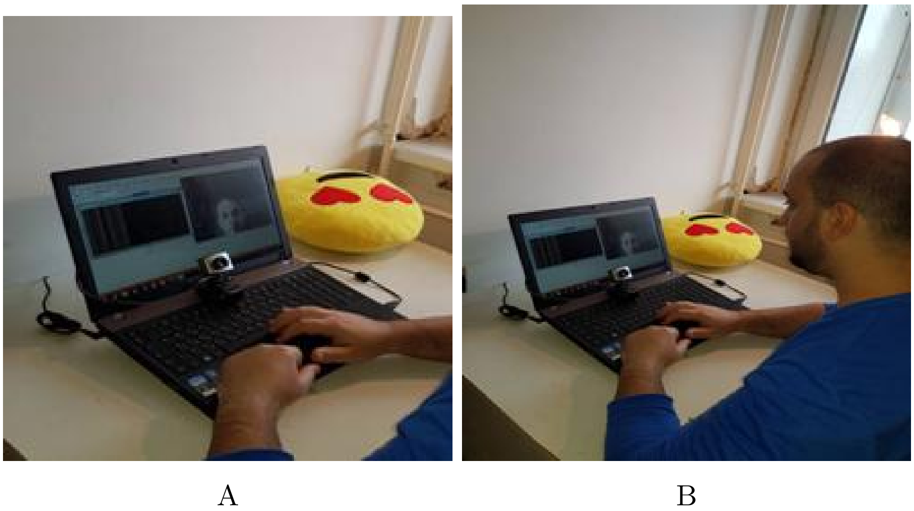
A B

Fig. 9: In [A] the assembly with the Webcam is displayed. In [B] it is observed the quality of the illumination and the typical distance in which the tests were carried out.

The final tests were performed on 4 people with favorable lighting conditions and with the positioning of the camera below the eye line similar to the scheme observed in figure (8) [B]. Images of each of the users were stored as they directed the eyes to each end of the screen, to the medians of the sides and the center of the screen. It was observed that the system often ”lost” the irises as the users changed the direction of the eyes, and then identified them again. As mentioned earlier during the movement the detection of the edges is impaired. The iris identification was successful in 87.5% of cases and 2% of false positives occurred. Eventually the edge detection step captures small spots due to reflections that impair the identification of irises. In Figure 9 [B] we can identify in detail the contours identified for the right eye. One can observe the formation a considerable number of border points inside the iris which causes a system failure.

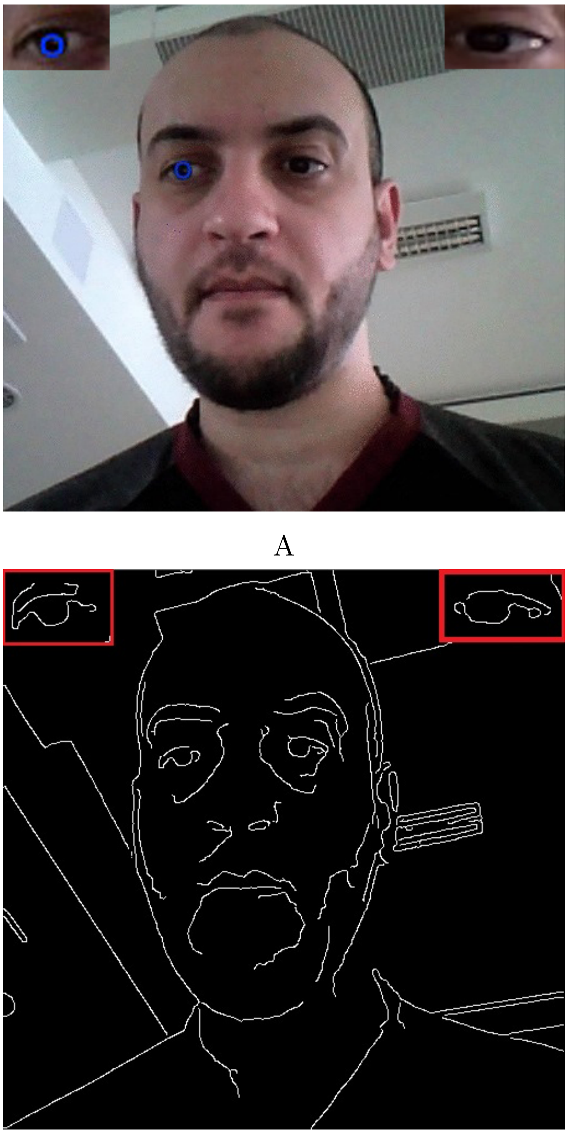

A

B

Fig. 10: In [A] an error occurs in the system. In [B] the image generated by the edge detector is displayed.

After the iris had been detected and tracked and diagram had been plotted it as we explained above, now we discuss the psychological aspect of this experiment in which comparison with the diagram to obtain the exact result for the persons emotional state, in this case we need to divided the screen virtually into four equal part as shown in the figure last one . According to psychological analysis by Robert Phipes [36] :

- Angry person: looking at the middle of the screen (0,0) and soundly jump around it .
- Joy/happens: looking at the upper middle of the screen.
- Sadness: looking at down left side of the screen.

- Scary and afraid :looking at the middle down of the screen .
- Surprise :looking down the screen and jumping right and left at the down edge of the screen

Fig. 11: eyeball movement

5 CONCLUSION AND FUTURE WORKS

In this work, we have focused on the problem of human emotion recognition in the case of naturalistic, rather than acted and extreme, expressions. The main elements of our approach are that we use multiple algorithms for the extraction of the difficult eye movement characteristics in order to make the overall approach more robust to image processing errors, we focus on the dynamics of eye movement reference points rather than on the exact facial deformations they are associated with, thus being able to handle sequences in which the interaction is natural or naturalistic rather than posed or extreme and we follow a multimodal approach where audio and visual modalities are combined, thus enhancing both performance and stability of the system. Our system was made using the cheap equipment under natural light condition. Our future work will be improving speed and quality of our system by trying to use dots summation, in order to determine the person emotional state rather than one diagram method(i.e every

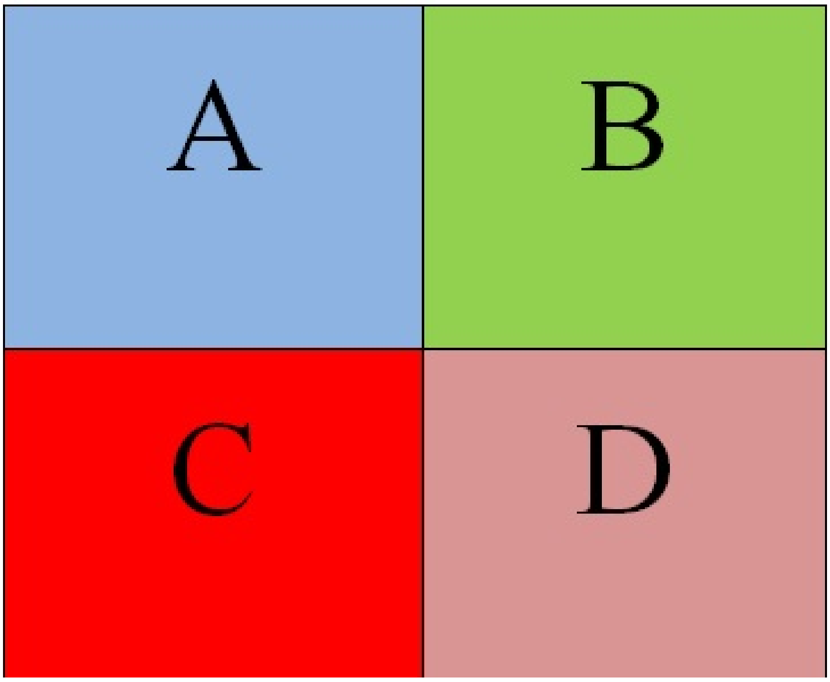

Fig. 12: Screen divide into 4 parts

dot represents the iris focus point per millisecond) . This done by a mathematical method that calculates all dots in every part of the screen as shown in the figure 12.

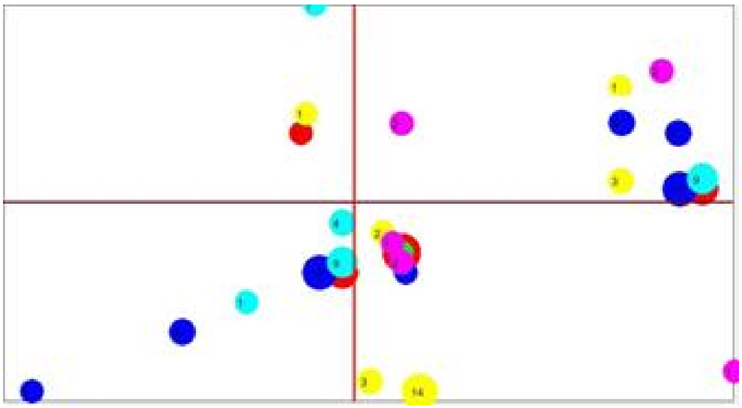

Fig. 13: Iris focus points on the screen per millisecond

References

1. Smith, Fraser W., and Philippe G. Schyns. ”Smile through your fear and sadness: transmitting and identifying facial expression signals over a range of viewing distances.” Psychological Science 20, no. 10 (2009): 1202-1208.
2. Baron-Cohen, Simon, and Sally Wheelwright. ”The empathy quotient: an investigation of adults with Asperger syndrome or high functioning autism, and normal sex differences.” Journal of autism and developmental disorders 34, no. 2 (2004): 163-175.
3. Marsh, Abigail A., Megan N. Kozak, and Nalini Ambady. ”Accurate identification of fear facial expressions predicts prosocial behavior.” Emotion 7, no. 2 (2007): 239.
4. Ben-Sasson, Ayelet, Liat Hen, Ronen Fluss, Sharon A. Cermak, Batya Engel-Yeger, and Eynat Gal. ”A meta-analysis of sensory modulation symptoms in individuals with autism spectrum disorders.” Journal of autism and developmental disorders 39, no. 1 (2009): 1-11.
5. Ekman, Paul, and Wallace V. Friesen. ”Unmasking the face: A guide to recognizing emotions from facial cues.” (1975).
6. Caldara, Roberto, Philippe Schyns, Eugene Mayer, Marie L. Smith, Frdric Gosselin, and Bruno Rossion. ”Does prosopagnosia take the eyes out of face representations? Evidence for a defect in representing diagnostic facial information following brain damage.” Journal of cognitive neuroscience 17, no. 10 (2005): 1652-1666.
7. Hejmadi, Ahalya, Richard J. Davidson, and Paul Rozin. ”Exploring Hindu Indian emotion expressions: Evidence for accurate recognition by Americans and Indians.” Psychological Science 11, no. 3 (2000): 183-187.
8. Keltner, Dacher, Randall C. Young, and Brenda N. Buswell. ”Appeasement in human emotion, social practice, and personality.” Aggressive behavior 23, no. 5 (1997): 359-374.
9. Tracy, Jessica L., and Richard W. Robins. ”” Putting the Self Into Self-Conscious Emotions: A Theoretical Model”.” Psychological Inquiry 15, no. 2 (2004): 103-125.
10. Ekman, Paul, and Wallace V. Friesen. Manual for the facial action coding system. Consulting Psychologists Press, 1978.
11. Fox, N.A. and Davidson, R.J., 1988. Patterns of brain electrical activity during facial signs of emotion in 10-month-old infants. Developmental Psychology, 24(2), p.230.
12. Darwin, Charles. ”The expression of emotion in animals and man.” London, England: Murray (1872).
13. Aviezer, Hillel, Ran R. Hassin, Jennifer Ryan, Cheryl Grady, Josh Susskind, Adam Anderson, Morris Moscovitch, and Shlomo Bentin. ”Angry, disgusted, or afraid? Studies on the malleability of emotion perception.” Psychological science 19, no. 7 (2008): 724-732.
14. Smith, Marie L., Garrison W. Cottrell, FrdAric Gosselin, and Philippe G. Schyns. ”Transmitting and decoding facial expressions.” Psychological science 16, no. 3 (2005): 184-189.
15. Spezio, Michael L., Ralph Adolphs, Robert SE Hurley, and Joseph Piven. ”Abnormal use of facial information in high-functioning autism.” Journal of autism and developmental disorders 37, no. 5 (2007): 929-939.
16. Gosselin, Frdric, and Philippe G. Schyns. ”Bubbles: a technique to reveal the use of information in recognition tasks.” Vision research 41, no. 17 (2001): 2261-2271. Zhao, Wenyi, Rama Chellappa, P. Jonathon Phillips, and Azriel Rosenfeld. ”Face recognition: A literature survey.” ACM computing surveys (CSUR) 35, no. 4 (2003): 399-458.

17. Kowler, Eileen, Eric Anderson, Barbara Dosher, and Erik Blaser. "The role of attention in the programming of saccades." Vision research 35, no. 13 (1995): 1897-1916.
18. Nahm, Frederick KD, Amelie Perret, David G. Amaral, and Thomas D. Albright. "How do monkeys look at faces?." Journal of Cognitive Neuroscience 9, no. 5 (1997): 611-623.
19. Walker-Smith, Gail J., Alastair G. Gale, and John M. Findlay. "Eye movement strategies involved in face perception." Perception 42, no. 11 (2013): 1120-1133.
20. Adolphs, Ralph, Daniel Tranel, Hanna Damasio, and Antonio Damasio. "Impaired recognition of emotion in facial expressions following bilateral damage to the human amygdala." Nature 372, no. 6507 (1994): 669.
21. Adolphs, Ralph, Frederic Gosselin, Tony W. Buchanan, Daniel Tranel, Philippe Schyns, and Antonio R. Damasio. "A mechanism for impaired fear recognition after amygdala damage." Nature 433, no. 7021 (2005): 68.
22. Pelphrey, Kevin A., Noah J. Sasson, J. Steven Reznick, Gregory Paul, Barbara D. Goldman, and Joseph Piven. "Visual scanning of faces in autism." Journal of autism and developmental disorders 32, no. 4 (2002): 249-261.
23. Henderson, John M., Carrick C. Williams, and Richard J. Falk. "Eye movements are functional during face learning." Memory cognition 33, no. 1 (2005): 98-106.
24. Pflugshaupt, Tobias, Urs P. Mosimann, Wolfgang J. Schmitt, Roman von Wartburg, Pascal Wurtz, Mathias Lthi, Thomas Nyffeler, Christian W. Hess, and Ren M. Mri. "To look or not to look at threat?: Scanpath differences within a group of spider phobics." Journal of anxiety disorders 21, no. 3 (2007): 353-366.
25. Perlman, Susan B., James P. Morris, Brent C. Vander Wyk, Steven R. Green, Jaime L. Doyle, and Kevin A. Pelphrey. "Individual differences in personality predict how people look at faces." PloS one 4, no. 6 (2009): e5952.
26. Jack, Rachael E., Caroline Blais, Christoph Scheepers, Philippe G. Schyns, and Roberto Caldara. "Cultural confusions show that facial expressions are not universal." Current Biology 19, no. 18 (2009): 1543-1548.
27. Aviezer, Hillel, Ran R. Hassin, Jennifer Ryan, Cheryl Grady, Josh Susskind, Adam Anderson, Morris Moscovitch, and Shlomo Bentin. "Angry, disgusted, or afraid? Studies on the malleability of emotion perception." Psychological science 19, no. 7 (2008): 724-732.
28. Peng, Kun, Limin Chen, Su Ruan, and Georgy Kukharev. "A robust agorithm for eye detection on gray intensity face without spectacles." Journal of Computer Science Technology 5 (2005)
29. Zhang, Lei, Yanfeng Sun, Mingjing Li, and Hongjiang Zhang. "Automated red-eye detection and correction in digital photographs." In Image Processing, 2004. ICIP'04. 2004 International Conference on, vol. 4, pp. 2363-2366. IEEE, 2004
30. Li, Dongheng, and Ruqin Zhang. "Eye Typing Using A Low-Cost Desktop Eye Tracker." Iowa State University (2005).
31. Cndido, Jorge, and Mauricio Marengoni. "Enhancing face detection using bayesian networks." In IASTED International Conference on Signal and Image Processing-SIP2006, vol. 1, no. 1. 2006.
32. Canny, John. "A computational approach to edge detection." In Readings in Computer Vision, pp. 184-203. 1987.
33. Garg, Pragati, Naveen Aggarwal, and Sanjeev Sofat. "Vision based hand gesture recognition." World Academy of Science, Engineering and Technology 49, no. 1 (2009): 972-977.
34. LNCS Homepage, http://www2.imm.dtu.dk/ aam/ . Last accessed 31 may 2018

35. Phipps, Robert. Body language: it's what you don't say that matters. John Wiley Sons, 2012

Computer-aided diagnosis system for lumbar spinal stenosis detection in MRI based on radiological criteria

Dominik Horwat[1†] and Marek Krośnicki[1‡]

Faculty of Mathematics, Physics and Informatics, Institute of Theoretical Physics
and Astrophysics, University of Gdansk, Wita Stworza 57, 80-309 Gdańsk, Poland
[†]`horwat.dominik@gmail.com`
[‡]`fizmk@univ.gda.pl`

Abstract. Lumbar spinal stenosis (LSS), a narrowing of the spinal canal, is a common cause of lower back pain. Magnetic Resonance imaging (MRI) play an important role in the diagnosis of lumbar abnormalities and is preferred modality for diagnosis of lower back pain. The purpose of this work is to design a semi-automatic computer-aided diagnosis (CAD) system for detecting LSS from Magnetic Resonance images. For sake of this study the STIR sequence of MRI mid-sagittal images of the lumbar spine are used. We present preliminary results of our work on an algorithm for quantification and detection of the spinal stenosis.

Keywords: lumbar spinal stenosis · computer-aided diagnosis · STIR-MRI · region growing segmentation · quantitative evaluation.

1 Introduction

According to the World Health Organization, the worldwide prevalence of low back pain may be as high as 42% [10]. A common cause of low back pain is lumbar spinal stenosis (LSS). Hughes *et al.* [7] define lumbar spinal stenosis as "a pathological condition of the spinal canal with its concentric narrowing and presence of specific clinical syndrome". LSS causing a difficulties especially during walking resulting in patients disability [19][5]. LSS affect millions of middle-aged and elderly patients [5]. It is estimated that more than 200.000 adults are affected by LSS in the United States [20]. LSS is also the most common reason of the spinal surgery for >65 years old patients. Wu *et al.* [20] reports that in the period of time 2002 to 2007, the rate of lumbar stenosis surgery per 100.000 patients is about 135.5–137.5 persons.

Radiological findings are crucial in the diagnosis of lumbar spinal stenosis beside symptoms and clinical signs [17]. Magnetic Resonance imaging (MRI) is commonly used to assess patients with lumbar spinal stenosis [14]. Typically, the sagittal T1-weighted, T2-weighted, STIR, and proton density-weighted, and axial T1- and T2-weighted sequences are used for lumbar spine imaging [18]. The T1- and T2-weighted sequences are most frequently used in spinal stenosis quantitative evaluation [4]. A few quantitative radiological criteria can be found in the literature [17]. The frequently applied criterion is measurement of the mid-sagittal antero-posterior diameter of dural sac (DSAPD).

The increasing number of patients (about 8%) and the growing demand for radiological diagnostics are not correlated with an increase in radiologists (about 1%) [1]. In the result, the demand of a computer-aided diagnosis (CAD) methods has increased in the last few years. Using the CAD methods allow to limit radiologist's time spent on imaging diagnostics. This time saving is necessary to ensure a sufficiently high quality of patient's health care. Moreover, the stenosis diagnosis is commonly based on subjective parameters. The lack of the methodological rigor in the LSS quantitative assesment process results in inter- and intra-radiologists variability [22]. Some studies found that correlation between clinical symptoms and radiology findings are poor [2]. This shows the urgent need for CAD methods to ensure the reproducibility and comparability of the diagnosis results.

Several methods for diagnosis of lumbar spinal stenosis have been developed, but no full CAD system is available to detect and quantify spinal stenosis [14]. Koompairojn *et al.* [10] present a system based on machine learning classification technique to automatically recognize lumbar spine components and LSS diagnose by applying a Multilayer Perceptron. Koh *et al.* [9] developed method based on inter- and intra-context features generation using a two-level classifier for performing the diagnosis. Ruiz *et al.* [14] developed an interesting methodology to classify and quantify spine disease (disc degeneration, herniation and spinal stenosis). In this method a comparison between real and ideal contour was used to set a threshold for a subsequent detection of spinal stenosis. Quantification of the dural sac canal ratio was carried out as the main criteria for calculation of spinal stenosis. All of this researches used T2-weighted MRI images.

In this study preliminary results of the development of a semi-automatic computer-aided diagnosis system for detecting lumbar spinal stenosis from STIR MRI mid-sagittal images are shown. In the presented method the LSS was quantified using the dural sac antero-posterior diameter. Detection was carried out by comparing DSAPD with the mean diameter of the dural sac in each lumbar spine segment.

For this purpose the image was firstly preprocessed to enhance the edge and to reduce the inhomogeneities of the pixels intensity over the dural sac region. Then, the dural sac was segmented using a region growing technique.

2 Method

2.1 Magnetic Resonance imaging

Examinations was performed on 3-T MRI (Philips Medical Systems Achieva). In this study the STIR sequence was used. All images used for testing were obtained using the same image acquisition protocol: 13 slices of 4 mm thickness, pixel spacing of $0.44mm \times 0.44mm$, image resolution of 784×784, repetition time 4100-4500 ms, effective echo time 70 ms.

2.2 Preprocessing

The presented method consist of three steps: image preprocessing, region growing segmentation and lumbar spinal stenosis quantitative evaluation (diagnosis). First, a single mid-sagittal slice was manually selected from a MRI dataset. At the preprocessing step the MRI mid-sagittal image was prepared for segmentation by edge enhancement (image sharpening). The process was carried out as follows:

1. Gaussian smoothing: the image was smoothed by the two-dimensional (2D) Gaussian filter $G(x, y)$ to eliminate the noise while still preserving object boundaries,

$$G(x,y) = \frac{1}{2\pi\sigma^2} exp\Big(- \frac{x^2 + y^2}{2\sigma^2} \Big), \tag{1}$$

where: x, y are image coordinates and σ is a standard deviation of the associated probability distribution. Value of σ was set to 2.5.

2. Range operation: a range operator was applied to the smoothed image. Range is the local texture operator defined with respect to a certain neighborhood Ω which defines the local region over which the calculation is made[16],

$$\Re = \big\{ max(I(x,y)) - min(I(x,y)) \big\}_{\Omega}, \tag{2}$$

where: x, y are image coordinates.

Range operator captures intensity fluctuations between groups of neighboring pixels by calculating the difference between maximum and minimum value over the defined neighborhood. Applying the range operator over 3×3 neighborhood Ω allowed detection of the edge between the dural sac and the vertebral bodies.

3. Binarization: image after applying range operator (range image) was binarized. The threshold was selected empirically as 0.35 of maximum value of range image.

4. Edge extration: the connected-component labeling was performed on binarized image to extract the biggest object which is the edge between the dural sac and the vertebral bodies [6].

5. Edge thinning: the extracted edge was skeletonized using morphological skeletonization algorithm [21].

6. Edge enhancement: the image obtained as a result of previous steps operations was used as a sharpening mask I_{mask}. The original MRI image was filtered using 2D Gaussian filter with $\sigma = 1$. Next, the smoothed image $I_{smoothed}$ was enhanced using a contrast enhancement method called histogram equalization [16]. Finally, a sharpening mask was applied to the resulting image $I_{equalized}$. This operation produced image with emphasized vertebral bodies-dural sac boundary. Figure 1 shows a results of the preprocessing stage.

$$I_{enhanced} = I_{equalized} + I_{mask} \tag{3}$$

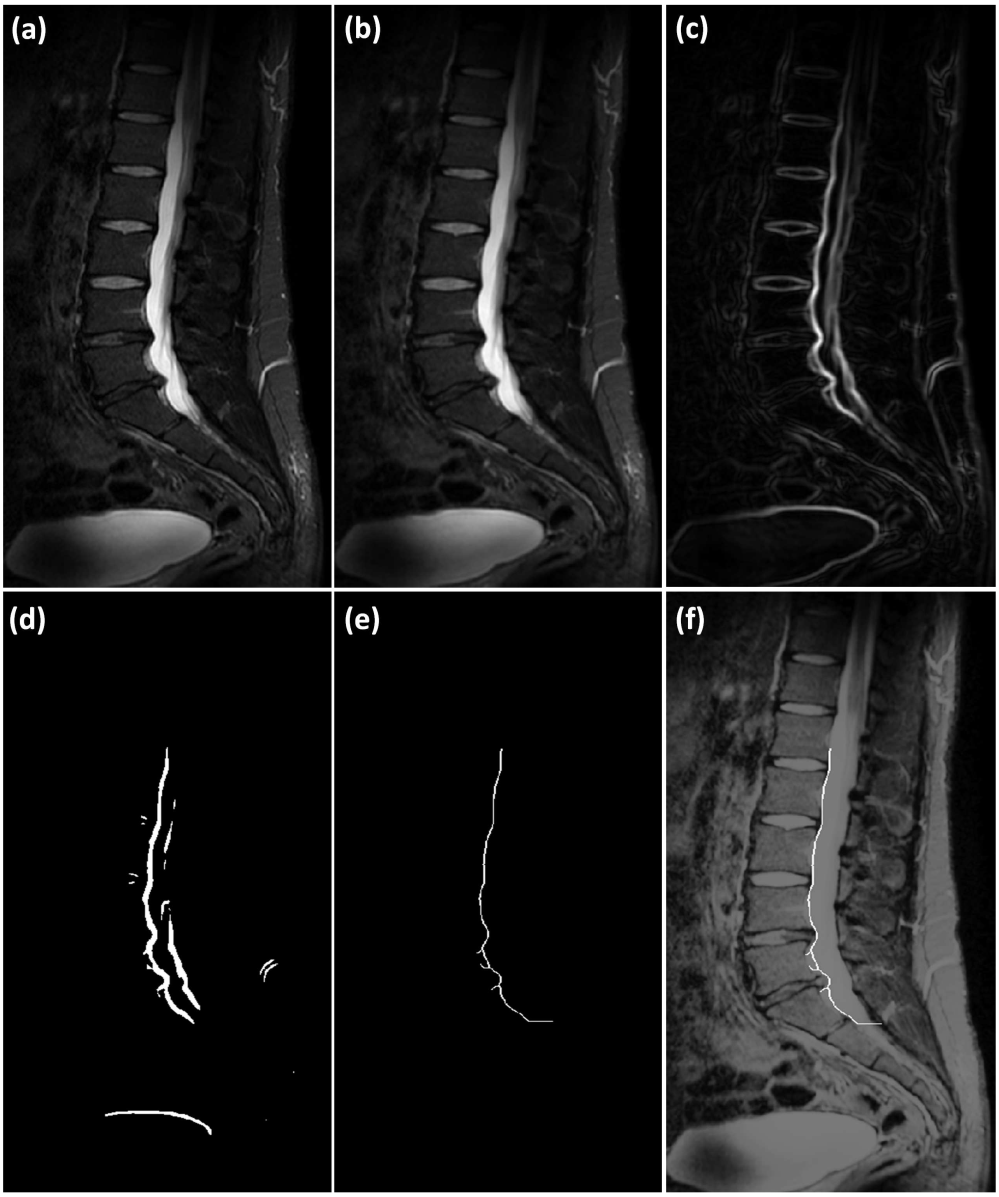

Fig. 1. Preprocessing process: a) Original MRI STIR image. b) Image (a) smoothed using Gaussian filter with $\sigma = 1$. c) Image (b) after applying range operator. d) Binarized image (c). e) The longest edge extracted from (d). e) Mask (d) applied to original image (a).

2.3 Segmentation

In the next step the dural sac region was segmented out from preprocessed image using region growing method. In this technique segmentation algorithm starts from the seed points and append the pixels in the neighborhood to the same region if they satisfy the similarity criteria. At the same time an adjacency spatial relationships between pixels must be considered.

The similarity criterion was defined based on pixels intensity: the intensity value of a candidate pixel must lie within a specified range. The lower threshold of the range was set as a 0.9 value of the running average intensity of the growing region. The upper threshold was determined by the maximum value of original image pixel (without edge enhancement mask). An 8-connected neighborhood for image pixels adjacent relationship was chosen. A single seed point was manually placed in the dural sac region. An initial threshold value was calculate as the mean pixels intensity of the 10×10 window centered on seed point. At each next iteration the running average intensity of the growing region was calculated and then was set as a new lower range threshold. Despite of image preprocessing, in the segmented region holes and discontinuities can appear. Therefore, the morphological closing operator $(A \oplus B) \ominus B$ was used to fill holes and to join a narrow isthmuses (isthmuses occurred as a result of the edge enhancement) within the segmented region. A 4×6 rectangle structuring element B was used [15]. Finally, the segmented dural sac region was obtained.

At the last step, the contour of the segmented region was found using "marching squares" method [12]. The morphological closing ensure producing an enclosed contour. Finally, the region contour was split out into two contours to get two points sets describing anterior and posterior boundary of the dural sac.

2.4 Diagnosis

The diagnosis of lumbar spine stenosis is based on one of the radiological criteria [17][11]. The mid-sagittal antero-posterior diameter of dural sac was chosen as the LSS stenosis descriptor. In the proposed method measurements were carried out perpendicularly to a curvature of the spine. To model the spine curvature a set of landmark points was manually placed in the middle of the posterior margin of the vertebral body (L1, L2, L3, L4, L5, S1). The B-spline curve then was fitted to markers (see figure 2a). Next, the normal to B-spline was traced at the point closest to the anterior contour for all points of this contour (it was assumed that both points satisfies the equation of normal). Next, the intersection points between normals and posterior contour were calculated. This approach allowed to get the set of measurements points.

Finally, quantification of the LSS was performed by calculating the dural sac antero-posterior diameter (see figure 2b). DSAPD was calculated for each pair of points using the Euclidean distance and DICOM Pixel Spacing(0028,0030) attribute (see equation 4). Pixel Spacing atribute holds the physical distance in the patient between the center of each pixel in mm [13],

$$d = Pixel\_spacing_y \cdot \sqrt{(x_1 - x_2)^2 + (y_1 - y_2)^2}, \tag{4}$$

where: $Pixel\_spacing_y$ is the horizontal physical size of pixel, x_1, y_1 is coordinates of the point on anterior contour, x_2, y_2 is coordinates of the point on posterior contour.

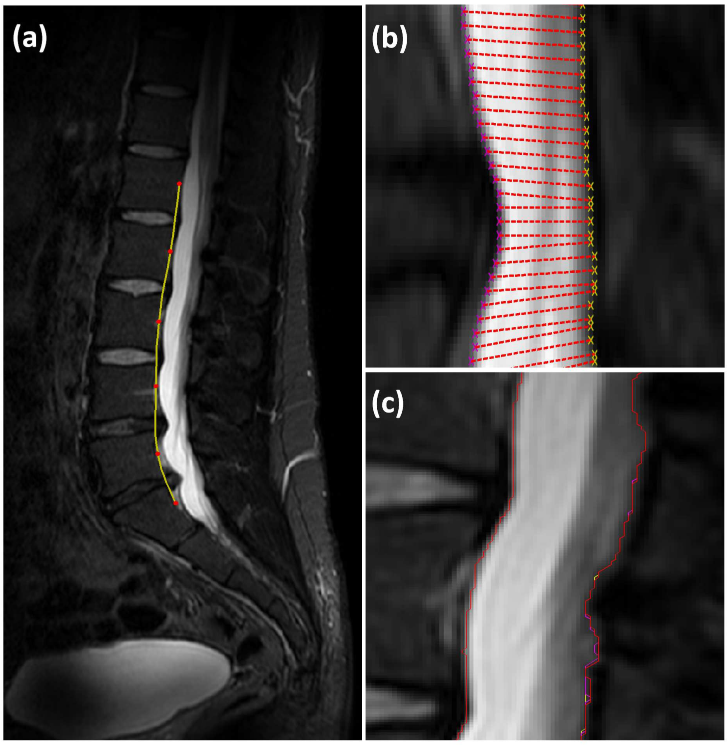

Fig. 2. a) B-spline model of the spine curvature. Yellow line is the B-spline, red points are the landmarks placed at the midpedicular level of the vertebral bodies. b) Set of measurements points. Red lines show the measurements of antero-posterior diameter of the dural sac. c) Comparison of segmentation results for the different position of the seed point. The magenta, yellow and red line correspond to initial point placed in the cerebrospinal fluid, the spinal cord and the boundary of the two regions, respectively.

Detection of spinal stenosis was done by comparing each of the diameter measurement with the mean DSAPD for the corresponding lumbar spine segment. The lumbar spine was divided into segments (L1-L2, L2-L3, L3-L4, L4-L5, L5-S1). The comparison ratio CR was calculated using the following formula:

$$CR = 1 - \frac{DSAPD}{segment\_mean} \cdot 100\%. \tag{5}$$

The comparison ratio was used to establish a cut-off value t for LSS detection. The threshold t was set as a 10% of the CR.

3 Results and Discussion

The method proposed in this study was evaluated in MRI STIR images of $n = 7$ subjects. The test dataset included both normal and stenosed spine images. The result of the segmentation is shown in the figure (see figure 3b,c). The usage of morphological closing ensure obtaining an enclosed region. To present precision of the segmentation, the original MRI image was blended with the contour extracted from the segmented dural sac region. It can be clearly seen that output contour accurately capture the anterior and posterior boundary of the dural sac (see figure 3d).

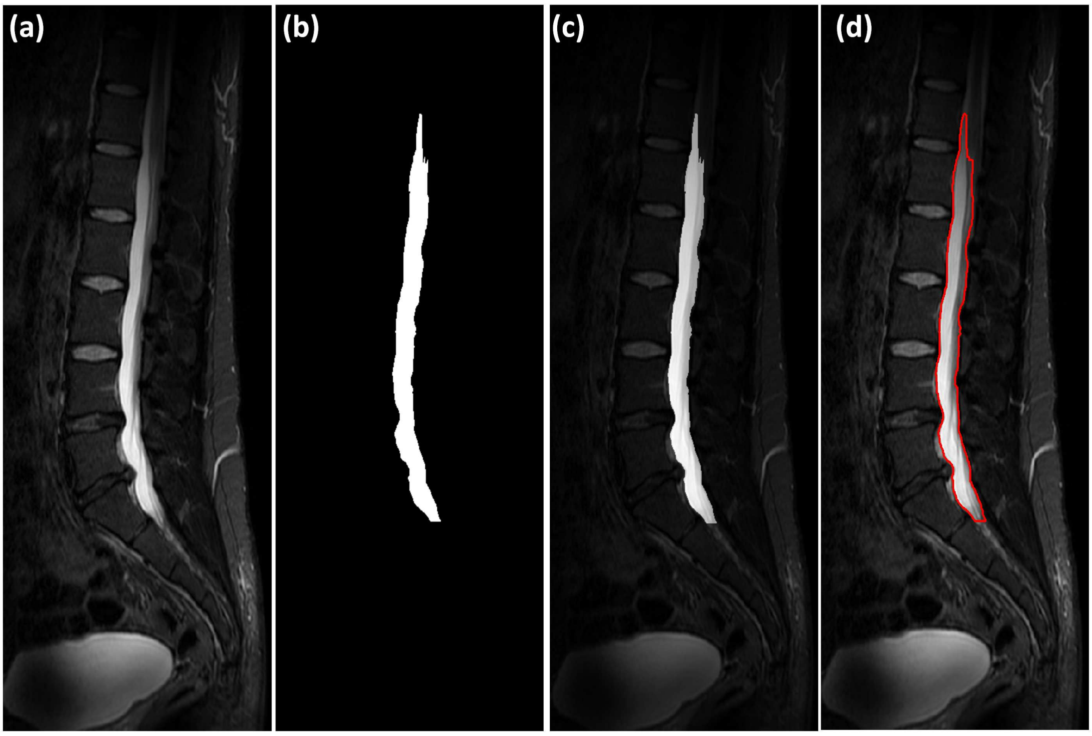

Fig. 3. a) Original MRI STIR image, b) Segmented dural sac region. c) Segmented region (b) superimposed on (a). d) Comparison of the contour of the segmented dural sac region with the original image (a).

Application of a Gaussian filter and histogram equalization eliminates inhomogeneities of the segmented dural sac region associated with the difference in cerebrospinal fluid (CSF) and spinal cord intensity values. Such inhomogeneities can lead to wrong segmentation (see figure 4).

Applying the range operator prevents growing region from spreading out to the vertebral bodies (see figure 5).

To test the independence of the region growing algorithm from the location of the starting point, the seed point was placed in the CSF, the spinal cord and

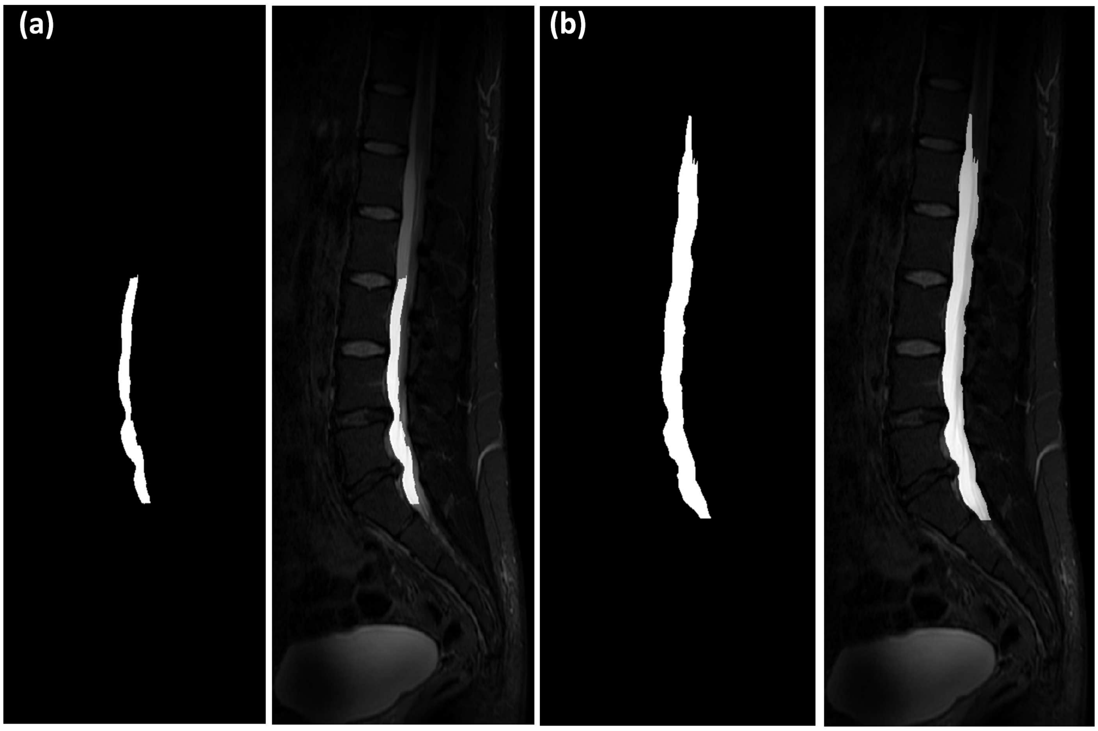

Fig. 4. Segmentation result: a) before histogram equalization. b) after histogram equalization.

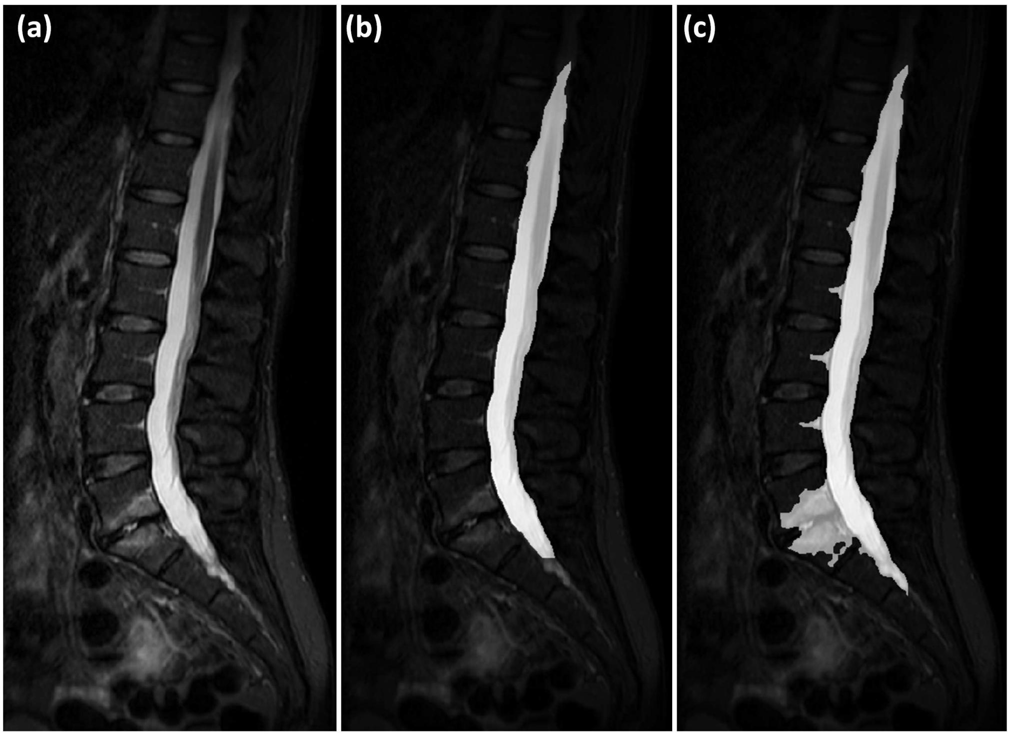

Fig. 5. a) Original image. b) Segmentation result before applying range operator. c) Segmentation result after applying range operator.

the boundary of the two regions. This experiment shown that the location of the seed point does not significantly affect the result of segmentation (see figure 2c).

In the literature two definition (cut-offs) of stenosis are commonly used: ≤ 12 mm or ≤ 10 mm (”relative” or ”absolute” stenosis, respectively) [8] and ≤ 9 mm [3]. These descriptors are somewhat arbitrary and do not take into consideration the inter-individual variability of the dural sac diameter. The method proposed in this work overcomes this problem. Comparison of DSAPD with mean DSAPD in corresponding segment allows for taking into account the anatomical narrowing of the dural sac in its lower part direction in the LSS detection process. The method presented in this study gives possibility to establish the individual LSS detection threshold for each subject.

In the figure 6 the results of the lumbar spinal stenosis detection in a normal case and in two cases classified by radiologist as LSS are shown. It can be seen (see figure 7 and figure 8) that the CAD method found narrowed spinal segments in both pathological cases. In the normal case narrowing was not found by CAD. At this stage of the research, the lack of full and accurate radiological reports did not allow to assess the accuracy of LSS detection. Nevertheless, based on the general diagnosis of the radiologist, it can be concluded that the results of LSS detection are promising.

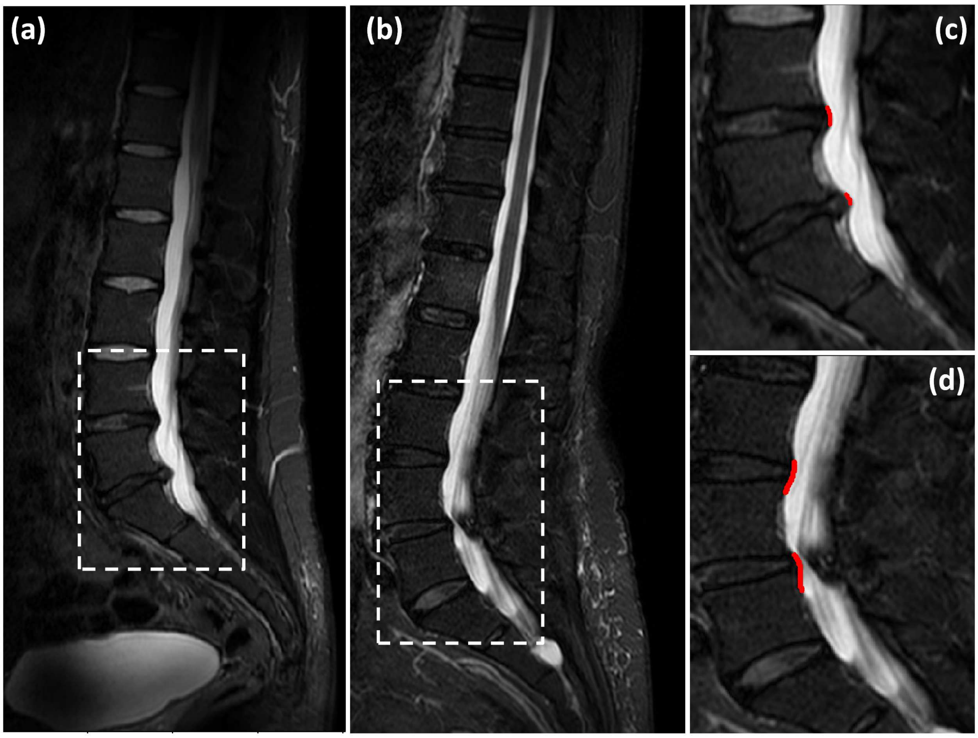

Fig. 6. LSS detection results: a)-b) MRI studies of two subjects classified by radiologist as pathological (the white square show the zoomed region in (c) and (d)). c)-d) Result of LSS detection for cases shown in (a) and (b). Red markers indicate the narrowed segments.

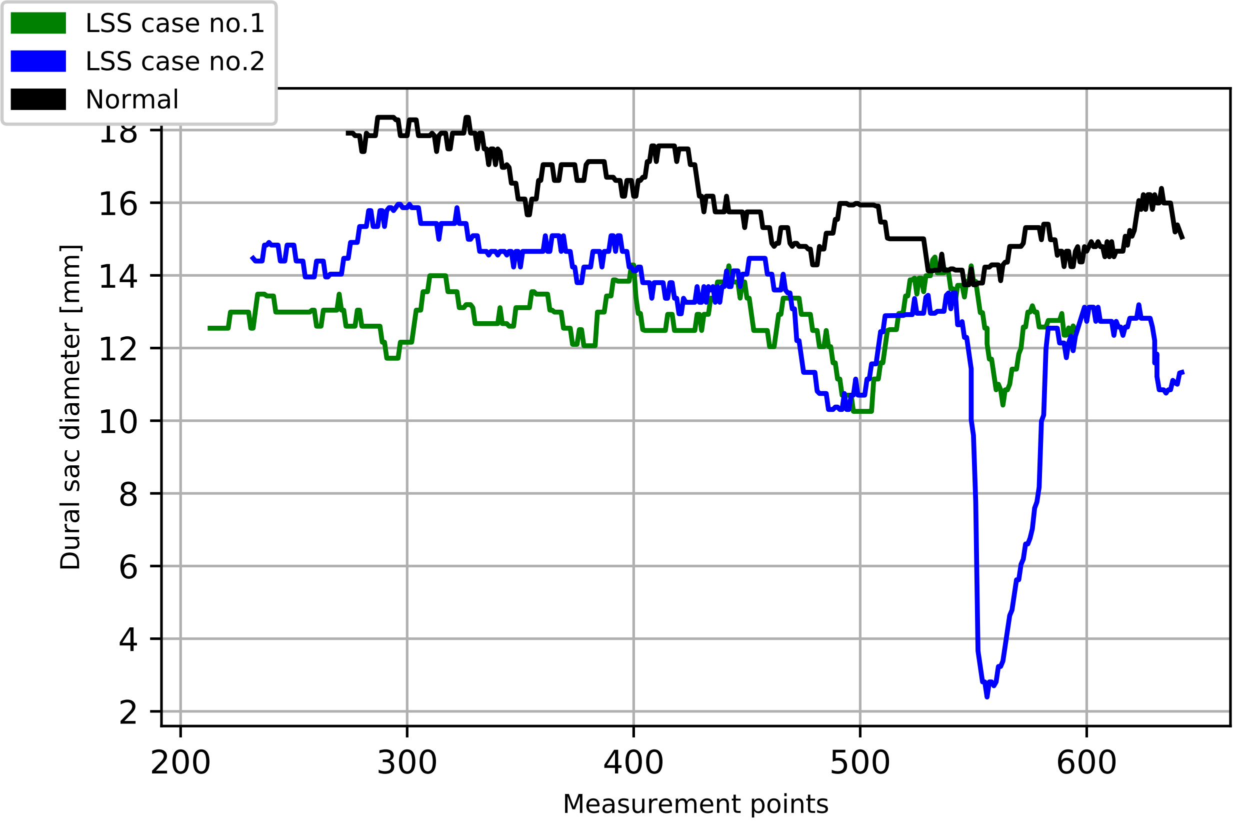

Fig. 7. Dural sac antero-posterior diameter measurements.

4 Conclusions

This work presents preliminary results of the research on the development of a computer-aided diagnosis system for lumbar spinal stenosis detection from Magnetic Resonance images. The system uses STIR mid-sagittal slices as input data. This method enhances the images at the preprocessing stage, segments the dural sac using the region growing technique, quantifies spinal stenosis using the dural sac antero-posterior diameter as a radiological criterion and detects LSS based on comparing the diameter of the dural sac with the dural sac mean diameter values (Comparison Ratio). Preliminary tests with 7 subjects show promising results of lumbar spinal stenosis detection.

As part of further research, the method will be tested on bigger set of subjects to evaluate its diagnostic applicability. The diagnostic accuracy of the method will also be evaluated on the basis of full radiological reports. The quantification process will be verified by comparing the CAD measurements of the dural sac diameter with measurements manually performed by radiologist. The next goal will be to reduce the user's input to the minimum. The mile stones towards the development of fully-automated CAD are automatic selection of the mid-sagittal slice and automatic determination of the curvature of the spine.

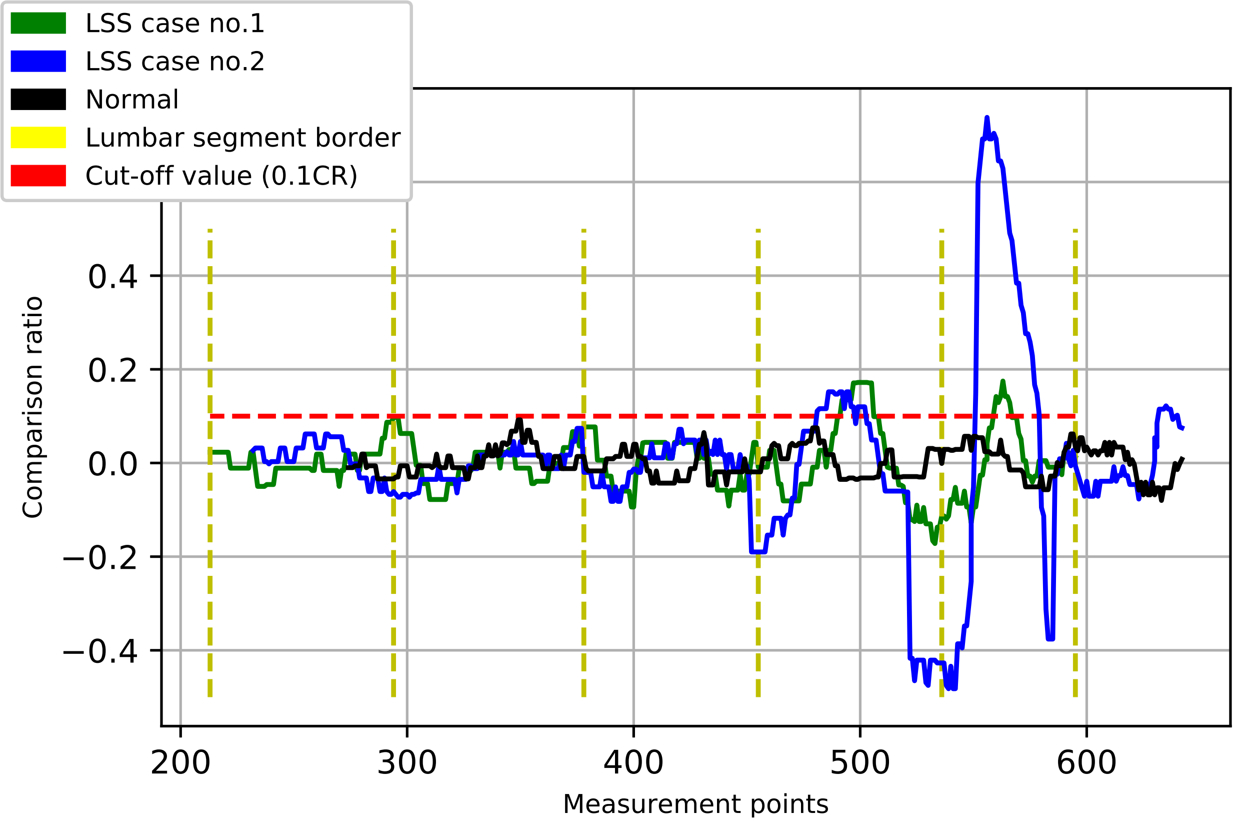

Fig. 8. Lumbar spinal stenosis detection using Comparison Ratio.

5 Conflict of interest statement

All authors declare that they have no conflict of interest to disclose.

References

1. Alomari, R.S., Chaudhary, V., Dhillon, G.: Computer aided diagnosis system for lumbar spine. In: ISABEL (2011)
2. Amundsen, T., Weber, H., Lilleas, F., Nordal, H., Abdelnoor, M., Magnaes, A.: Lumbar spinal stenosis: Clinical and radiologic features. Spine 20(10), 1178–1186 (1995)
3. Chatha, D., Schweitzer, M.E.: Mri criteria of developmental lumbar spinal stenosis revisited. Bulletin of the NYU hospital for joint diseases 69(4), 303–307 (2011)
4. Cheung, J.P.Y., Shigematsu, H., Cheung, K.M.C.: Verification of measurements of lumbar spinal dimensions in t1- and t2-weighted magnetic resonance imaging sequences. The Spine Journal 14(8), 1476–1483 (2014)
5. Ciricillo, S.F., Weinstein, P.R.: Lumbar spinal stenosis. Western Journal of Medicine 158(2), 171–177 (1993)
6. Gonzalez, R., Woods, R.: Digital Image Processing. 3 edn. (2009)
7. Hughes, A., Makirov, S., Osadchiy, V.: Measuring spinal canal size in lumbar spinal stenosis: description of method and preliminary results. International Journal of Spine Surgery 9(3), 1–9 (2015)
8. Kalichman, L., Cole, R., Kim, D.H., Li, L., Guermazi, A., Hunter, D.J.: Spinal stenosis prevalence and association with symptoms: The framingham study. The spine journal: official journal of the North American Spine Society 9(7), 545–550 (2009)
9. Koh, J., Alomari, R.S., Chaudhary, V., Dhillon, G.: Lumbar spinal stenosis cad from clinical mrm and mri based on inter- and intra-context features with a two-level classifier. In: Medical Imaging 2011: Computer-Aided Diagnosis. vol. 7963 (2011)
10. Koompairojn, S., Hua, K., A Hua, K., Srisomboon, J.: Computer-aided diagnosis of lumbar stenosis conditions. In: Proc SPIE. vol. 7624, pp. 7624 – 7624 – 12 (2010)
11. Lee, S.Y., Kim, T.H., Oh, J.K., Lee, S.J., Park, M.S.: Lumbar stenosis: A recent update by review of literature. Asian Spine Journal 9(5), 818–828 (2015)
12. Lorensen, W.E., Cline, H.E.: Marching cubes: A high resolution 3d surface construction algorithm. COMPUTER GRAPHICS 21(4), 163–169 (1987)
13. National Electrical Manufacturers Association: National Electrical Manufacturers Association: Digital Imaging and Communications in Medicine (DICOM) Part 3: Information Object Definitions (2011)
14. Ruiz-España, S., Arana, E., Moratal, D.: Semiautomatic computer–aided classification of degenerative lumbar spine disease in magnetic resonance imaging. Computers in Biology and Medicine 62, 196–205 (2015)
15. Soille, P.: Morphological Image Analysis. Principles and Applications. 2 edn. (2004)
16. Solomon, C., Breckon, T.: Fundamentals of Digital Image Processing (2011)
17. Steurer, J., Roner, S., Gnannt, R., Hodler, J.: Quantitative radiologic criteria for the diagnosis of lumbar spinal stenosis: a systematic literature review. BMC. Musculoskeletal Disorders 12(175), 1–9 (2011)
18. Talekar, K., Cox, M., Smith, E., Flanders, A.: Imaging spinal stenosis. Applied Radiology 46(1), 8–17 (2017)

19. Taylor, V., Deyo, R., Cherkin, D., Kreuer, W.: Low back pain hospitalization: recent us trends and regional variation 19(11), 1207–1212 (1994)
20. Wu, A.M., Zou, F., Cao, Y., Xia, D.D., He, W., Zhu, B., Chen, D., Ni, W.F., Wang, X.Y., Kwan, K.: Lumbar spinal stenosis: an update on the epidemiology, diagnosis and treatment. AME Medical Journal 2(5), 1–14 (2017)
21. Zhang, T.Y., Suen, C.Y.: A fast parallel algorithm for thinning digital patterns. Image Processing and Computer Vision 27(3), 236–239 (1984)
22. Zheng, F., Farmer, J.C., Sandhu, H.S., OLeary, P.F.: A novel method for the quantitative evaluation of lumbar spinal stenosis. HSS Journal 2(2), 136–140 (2006)

Section 13
Intelligent Data Analysis

CREDIBILITY OF FUZZY KNOWLADGE

OLEKSANDR PROVOTAR 0000-0002-6556-3264
Department of Computer Science, University of Rzeszow,
Rzeszow, **Aleja Rejtana 16c, 35-959,** Poland
aprowata1@bigmir.net

Abstract. An approach to finding a credible estimates of fuzzy knowledge in fuzzy inference systems is considered. To investigate a credibility the elements of the theory of probabilities of fuzzy events are used. The examples of application of the proposed approach in expert diagnostic systems and bioinformatics is given.

Key words: fuzzy event, probability, credibility.

1. Introduction

It is known that the fuzzy fuzzy inference systems [3-5, 7-11] are the convenient tool to present knowledge in information systems, which are built on the basis of ideas and methods of inductive mathematics [2].

The fuzzy specification of problem means ordered set of fuzzy instructions. The fuzzy specification of the problem with the algorithm during fulfilling which the approximate (fuzzy) solution of the problem is received will be called as fuzzy inference system.

Let $x_1, \dots, x_n$ are input linguistic variables and y – output linguistic variable [9-11].

The ordered set of fuzzy instructions looks like as following:

$$\begin{array}{l}
\textbf{\textit{if}}\ x_1 \text{ is } A_{11} \wedge \dots \wedge x_n \text{ is } A_{1n}\ \textbf{\textit{then}}\ y \text{ is } B_1 \\
\textbf{\textit{if}}\ x_1 \text{ is } A_{21} \wedge \dots \wedge x_n \text{ is } A_{2n}\ \textbf{\textit{then}}\ y \text{ is } B_2 \\
\dots\dots\dots\dots\dots\dots\dots\dots\dots\dots\dots\dots \\
\textbf{\textit{if}}\ x_1 \text{ is } A_{m1} \wedge \dots \wedge x_n \text{ is } A_{mn}\ \textbf{\textit{then}}\ y \text{ is } B_m
\end{array}$$

where A_{ij} и B_i – fuzzy sets, symbol “$\wedge$” is interpreted as t-norm of fuzzy sets.

The algorithm of calculating the output of such specification under the inputs $A'_1, \dots, A'_n$ consists in performing such steps:

1. Calculate the truth level of the rules:

$$\alpha_i = \min[\max(A_1^{'}(x_1) \wedge A_{i1}(x_1)),\ldots,\max(A_n^{'}(x_n) \wedge A_{in}(x_n)];$$

2. Calculate outputs of each rule:

$$B_i^{'}(y) = \min(\alpha_i, B_i(y));$$

3. Calculate aggregated output:

$$B(y) = \max(B_1^{'}(y),\ldots, B_m^{'}(y)).$$

2. Probability of Fuzzy Events

The proposed approach to solving problems (based on fuzzy models) allows simplifying the methods of solving problems. But, there is a necessity for additional studies of the results reliability.

For determining the probability of the event A in the space of elementary events X, the concept of probability measure P is introduced. The function P is a numerical function which assigns a number $P(A)$ to the elementary event A, and in addition:

$$0 \leq P(A) \leq 1,\ P(\boldsymbol{X}) = 1,\ P(\bigcup_{i=1}^{\infty} A_i) = \sum_{i=1}^{\infty} P(A_i)$$

for each $A_1, A_2, \ldots$ such that $A_i \cap A_j = \varnothing$, if $i \neq j$.

Fuzzy set

$$A = \{(x, \mu_A(x)), x \in \boldsymbol{X}\}$$

in the space $\boldsymbol{X}$ will be called a fuzzy event in space $\boldsymbol{X}$, where $\mu_A: \boldsymbol{X} \to [0,1]$ is a membership function of fuzzy set A.

A probability of fuzzy event A can be calculated according to the formula

$$P(A) = \sum_{\boldsymbol{x} \in \boldsymbol{A}} \mu_A(x) P(x),$$

where $P(x)$ is a function of the probability distribution.

Conditional probability of fuzzy event A given fuzzy event B will be determined with the help of Cartesian product notion. Namely, the distribution function $P_{(A|B)}$ of the conditional probability of fuzzy event A given the fuzzy event B is determined by the distribution function $P_{(A,B)}$ of binary Cartesian product $A \times B$ probability and probability distribution function P_B of fuzzy event B, provided it is not zero, that is for any pair (x,y) of Cartesian product $\boldsymbol{X} \times \boldsymbol{Y}$ performed

$$Q_{(A\times B)}(x,y)=\begin{cases}\dfrac{P_{(A,B)}(x,y)}{P_B(y)}, & P_B(y)\neq 0\\ 1, & P_B(y)=0.\end{cases}$$

$$P_{(A|B)}(x,y)=\begin{cases}\dfrac{Q_{A\times B}(x,y)}{\sum\limits_{x,y}Q_{A\times B}(x,y)}\end{cases}.$$

Given this, we can calculate the conditional probability of any fuzzy events at a given probability measure.

The probability distribution function of binary Cartesian product $A\times B$ will be calculated by the formula

$$P_{(A,B)}(x,y)=\min(P_A(x),P_B(y)).$$

3. Fuzzy Knowledge in Expert Diagnostics Systems

Let $\boldsymbol{X}_1$ = {5, 10, 15, 20}, $\boldsymbol{X}_2$ = {5, 10, 15, 20}, $\boldsymbol{X}_3$ = {35, 36, 37, 38, 39, 40} – spaces for determining the values of linguistic variables:

x_1 = “Coughing” = {“*weak*”, “*moderate*”, “*strong*”},
x_2 = “Running nose” = {“*weak*”, “*moderate*”, “*strong*”},
x_3 = “Temperature” = {“*normal*”, “*raised*”, “*high*”, “*very high*”}

accordingly.

Determine the elements of these sets:

“Coughing”: “*weak*” = 1/5 + 0.5/10; “*moderate*” = 0.5/5 + 0.7/10 + 1/15; “*strong*” = 0.5/10 + 0.7/15 + 1/20.

“Running nose”: “*weak*” = 1/5 + 0.5/10; “*moderate*” = 0.5/10 + 1/15; “*strong*” = 0.7/15 + 1/20.

“Temperature”: “*normal*” = 0.5/35 + 0.8/36 + 0.9/37 + 0.5/38; “*raised*” = 0.5/37 + 1/38; “*high*” = 0.5/38 + 1/39; “*very high*” = 0.8/39 + 1/40.

Let $\boldsymbol{Y}$ = {influenza, sharp respiratory disease, angina, pneumonia} is a space for determining the value of linguistic variable y. Then the dependence of the patient’s disease on his symptoms can be described by the following system of specifications:

if x_1 is “*weak*” $\wedge$ x_2 is “*weak*” $\wedge$ x_3 is “*raised*” ***then*** y is “0.5/influenza +0.5/ОРЗ +0.4/angina + 0.8/pneumonia”;

if x_1 is "*weak*" $\wedge$ x_2 is "*moderate*" $\wedge$ x_3 is "*high*" ***then*** y is "0.8/influenza +0.7/sharp respiratory disease +0.8/angina + 0.3/pneumonia";

if x_1 is "*weak*" $\wedge$ x_2 is "*moderate*" $\wedge$ x_3 is "*very high*" ***then*** y is "0.9/influenza +0.7/sharp respiratory disease +0.8/angina + 0.2/pneumonia".

If to the input x_1 of this algorithm to supply value $A_1^{'} = 1/5 + 0.7/10$, to the input x_2 – value $A_2^{'} = 1/5 + 0.5/10$, to the input x_3 – value $A_3^{'} = 1/36 + 0.9/37$, then in accordance with procedure of fulfilling the algorithm the fuzzy solution of the problem is

B = 0.5/influenza + 0.5/sharp respiratory disease + 0.4/angina + 0.5/ pneumonia.

3. Fuzzy Knowledge in Bioinformatics

It is known [2, 6] that the problem of recognizing the structures of the proteins of different organization levels is rather complicated. To solve it the different methods and approaches, including experimental (based on physics of chemical relations creation), machine teaching (used the data bases of experimentally found secondary structures as learning samples), probabilistic (on the basis of the Bayes procedures and Markov chains) are used.

The method of recognition of the secondary structure of DNA using fuzzy inference systems is proposed. The problem is the following: it is necessary to build the fuzzy inference systems which using random amino acid sequence would define (as a fuzzy set) the secondary structure of central remainder (of the amino acid) of the input sequence.

To solve this problem at first it is necessary to design the fuzzy specification of the problem according to learning samples. One of the methods to build the system of fuzzy instructions according to numerical data consists of the following. Let's the rules base with n inputs and one output is created. There are learning dates (samples) as the sets of pairs for that

$$x_1(i), x_2(i), ..., x_n(i); d(i), i = 1,2, ... , m,$$

where $x_j(i)$ – inputs and $d(i)$ – output, at that $x_j(i) \in \{a_1, a_2, \ldots, a_k\}$, $d(i) \in \{b_1, b_2, \ldots, b_l\}$. It is necessary to build the fuzzy inference systems which would generate the correct output data according to random input values. The algorithm of solving of the provided problem consists in the following sequence of steps:

1. Dividing the space of inputs and outputs for areas (dividing learning data for groups on $m_1, \ldots, m_k$ lines, which means, each input and output is divided for $2N$+1 cuts where N for each input is selected individually. Separate areas (segments) will be called in the following way:

M_N(left N), ... , M_1(left 1), S(medium), D_1(right 1), ... , D_N(right).

Determination membership function for each areas.

2. Building fuzzy sets on the basis of learning samples (for each group m_i learning data

$$\begin{array}{l}
(x_1(1), x_2(1), \dots, x_n(1); d(1)) \\
(x_1(2), x_2(2), \dots, x_n(2); d(2)) \\
\dots\dots\dots\dots\dots\dots\dots \\
(x_1(m_i), x_2(m_i), \dots, x_n(m_i); d(m_i))
\end{array}$$

we build the fuzzy sets of the form:

$$A_1^{(m_i)} = \frac{\left|a_1^{(1)}\right|}{m_i} / a_1 + \dots + \frac{\left|a_k^{(1)}\right|}{m_i} / a_k$$

$$\dots\dots\dots\dots\dots\dots\dots\dots$$

$$A_1^{(m_i)} = \frac{\left|a_1^{(n)}\right|}{m_i} / a_1 + \dots + \frac{\left|a_k^{(n)}\right|}{m_i} / a_k$$

$$B^{m_i} = \frac{\left|b_1\right|}{m_i} / b_1 + \dots + \frac{\left|b_k^{(1)}\right|}{m_i} / b_k$$

where $\left|a_1^{(j)}\right|$ – number of symbols a_1 in column j of the learning data group, $\left|b_1\right|$ – number of symbols b_j in the last column of the learning data group.

3. Building fuzzy rules on the basis of fuzzy sets from the previous step on the following scheme:

$$\left.\begin{array}{l}
(x_1(1), x_2(1), \dots, x_n(1); d(1)) \\
(x_1(2), x_2(2), \dots, x_n(2); d(2)) \\
\dots\dots\dots\dots\dots\dots\dots \\
(x_1(m_i), x_2(m_i), \dots, x_n(m_i); d(m_i))
\end{array}\right. \quad \Rightarrow$$

$$R^{(1)} : \boldsymbol{if}\ x_1 \text{ is } A_1^{(m_1)} \wedge x_2 \text{ is } A_2^{(m_1)} \wedge \dots \wedge x_n \text{ is } A_n^{(m_1)}\ \boldsymbol{then}\ y \text{ is } B^{m_1}$$

4. Elimination of contradictions.

This algorithm puts in accordance to each set of learning data the fuzzy rule of the logical inference.

It will be shown how to use the suggested algorithm of building the fuzzy sets for recognizing the secondary structure of DNA.

It is known [2, 6], that the secondary structure of the pieces of polypeptide sequence is determined mainly the by the interactions of neighbor amino acids within these pieces. To be more exact, the type of secondary structure of the exact remain is determined by its surrounding.

To build the fuzzy inference systems the learning samples from 15 remains of the protein MutS [6] are used which look like the following:

К V S E G G L ***I*** *R E G Y D P D*
e - - - h h h ***h*** *h h h h h h h*
V S E G G L I ***R*** *E G Y D P D L*
- - - h h h h ***h*** *h h h h h h h*
S E G G L I R ***E*** *G Y D P D L D*
- - h h h h h ***h*** *h h h h h h h*
E G G L I R E ***G*** *Y D P D L D A*
- h h h h h h ***h*** *h h h h h h h*
G G L I R E G ***Y*** *D P D L D A L*
h h h h h h h ***h*** *h h h h h h h*

The prediction belongs to the central remain, besides the following denotations are used: *h* – for spiral, *e* – for cylinder, – other

According to the algorithm, the teaching data is divided, for example, for 3 groups:

*КVSEGGL**h**REGYDPD* *SEGGLIR**h**GYDPDLD*
*VSEGGLI**h**EGYDPDL*; *EGGLIRE**h**YDPDLDA*;

*КVSEGGL**h**REGYDPD* *SEGGLIR**h**GYDPDLD*
*VSEGGLI**h**EGYDPDL*; *EGGLIRE**h**YDPDLDA*;

*GGLIREG**h**DPDLDAL*

and compared to each group with according fuzzy sets

$$A_i^{(m_1)}, A_i^{(m_2)}, A_i^{(m_3)}, B^{(m_1)}, B^{(m_2)}, B^{(m_3)}$$

Then fuzzy specification of the recognition problem will look like:

$$R^{(1)}: \textbf{if } x_1 \text{ is } A_1^{(\mathrm{m}_1)} \wedge \mathrm{x}_2 \text{ is } A_2^{(\mathrm{m}_1)} \wedge \ldots \wedge x_{14} \text{ is } A_{14}^{(\mathrm{m}_1)} \textbf{then } y \text{ is } B^{(\mathrm{m}_1)},$$
$$R^{(2)}: \textbf{if } x_1 \text{ is } A_1^{(\mathrm{m}_2)} \wedge x_2 \text{ is } A_2^{(\mathrm{m}_2)} \wedge \ldots \wedge x_{14} \text{ is } A_{14}^{(\mathrm{m}_2)} \textbf{then } y \text{ is } B^{(m_2)},$$
$$R^{(3)}: \textbf{if } x_1 \text{ is } A_1^{(\mathrm{m}_3)} \wedge x_2 \text{ is } A_2^{(\mathrm{m}_3)} \wedge \ldots \wedge x_{14} \text{ is } A_{14}^{(\mathrm{m}_3)} \text{t}\textbf{hen } y \text{ is } B^{(\mathrm{m}_3)},$$

Using the algorithm of solving the specification, we will find the output received system of fuzzy instructions, if to the input the following amino acid sequence is supplied:

*L K V S E G G **L** I R E G Y D P.*

In accordance with the procedure of executing the algorithm we will get that the secondary structure of the remainder ***L*** is *h*.

4. Credibility of Fuzzy Knowledge

Consider an example. Let $\boldsymbol{X}_1$ = {5, 10}, $\boldsymbol{X}_2$ = {5, 10}, $\boldsymbol{X}_3$ = {36, 37, 38, 39, 40} are spaces to determine the values of linguistic variables

x_1 = "Coughing" = { "*weak* (*C*)", "*moderate* (*C*)", "*strong* (*C*)"}
x_2 = "Running nose" = { "*weak* (*R*)", "*moderate* (*R*)", "*strong* (*R*)"}
x_3 = "Temperature" = { "*normal*", "*raised* ", "*high*", "*very high*"}.

Define the elements of these sets:

"Coughing": "*weak* (*C*)" = 1/5; "*moderate* (*C*)" = 0.5/5 + 0.5 / 10; "Strong (*C*)" = 1/10.

"Running nose": "*weak* (*R*) "= 1/5; "*moderate* (*R*)" = 0.5 / 5 + 0.5 / 10; "*strong* (*R*)" = 1/10.

"Temperature": "*normal*" = 1/36 + 0.5/37; "*raised*" = 1/37 +0.5/38; "*high*" = 1/38 + 0.5/39; "*very high*" = 0.5/39 + 1/40.

Let $\boldsymbol{Y}$ = {influenza, sharp respiratory disease, angina, pneumonia} be a space to determine the values of linguistic variable *y*. Then the patient dependent on its symptoms can be described by the following specifications:

if x_1 is "*weak* (*C*)" $\wedge$ x_2 is "*weak* (*R*)" $\wedge$ x_3 is "*raised*" ***then*** *y* is "0.5/influenza + 0.5/sharp respiratory disease + 0.4/angina + 0.8/pneumonia";

if x_1 is "*weak* (*C*)" $\wedge$ x_2 is "*moderate* (*R*)" $\wedge$ x_3 is "*high*" ***then*** *y* is "0.8/influenza + 0.7/sharp respiratory disease + 0.8/angina + 0.3/pneumonia";

if x_1 is "*weak* (*C*)" $\wedge$ x_2 is "*moderate* (*R*)" $\wedge$ x_3 is "*very high*" ***then*** *y* is "0.9/influenza + 0.7/sharp respiratory dis*ease* + 0.8/angina + 0.2/pneumonia".

Let an input x_1 of this algorithm is $A_1^{'} = 1/5 + 0.5/10$, an input x_2 is $A_2^{'} = 1/5 + 0.5/10$ and an input x_3 is $A_3^{'} = 1/38$. Then in accordance with procedure of fulfilling the algorithm of the fuzzy inference system the fuzzy solution of the problem is

B' = 0.5/influenza + 0.5/sharp respiratory disease + 0.5/angina + 0.5/pneumonia.

We need to find the probability of this disease at symptoms A_1', A_2', A_3' accordingly. Also, let the probability distribution in the spaces $\boldsymbol{X}_1$ = {5, 10}, $\boldsymbol{X}_2$ = {5, 10}, $\boldsymbol{X}_3$ = {36, 37, 38, 39, 40}, $\boldsymbol{Y}$ = {influenza, sharp respiratory disease, angina, pneumonia} are

"Coughing": $P_{\boldsymbol{X}_1}(5) = 0.4,\ P_{\boldsymbol{X}_1}(10) = 0.6;$

"Running nose": $P_{\boldsymbol{X}_2}(5) = 0.4,\ P_{\boldsymbol{X}_2}(10) = 0.6;$

"Temperature":

$$P_{\boldsymbol{X}_3}(36) = 0.3,\ P_{\boldsymbol{X}_3}(37) = 0.3,\ P_{\boldsymbol{X}_3}(38) = 0.2,\ P_{\boldsymbol{X}_3}(39) = 0.1,\ P_{\boldsymbol{X}_3}(40) = 0.1;$$

"Disease": P_Y(influenza) = 0.5, P_Y(sharp respiratory disease) = 0.3,
P_Y(angina) = 0.1, P_Y(pneumonia) = 0.1.

First, calculate the probability of hypotheses – fuzzy inference specifications. Transform the first hypothesis

H_1 = ***if*** x_1 is "*weak* (*C*)" $\wedge$ x_2 is "*weak* (*R*)" $\wedge$ x_3 is "*raised*" ***then*** *y* is "0.5/influenza + 0.5/sharp respiratory disease + 0.4/angina + 0.8/pneumonia"

to the expression

H_1 = $\neg$(x_1 is "*weak* (*C*)") $\vee$ $\neg$(x_2 is "*weak* (*R*)") $\vee$ $\neg$(x_3 is "*high*") $\vee$ *y* is "0.5/influenza +0.5/sharp respiratory disease +0.4/angina + 0.8/pneumonia.

Then we find the appropriate additions and obtain fuzzy sets:

$\neg$(x_1 is "*weak* (*C*)") = 1/10;
$\neg$(x_2 is "*weak* (*R*)") = 1/10;
$\neg$(x_3 is "*raised*") = 1/36 + 0.5/38 + 1/39 + 1/40.

Then we calculate the probability of fuzzy events:

P ($\neg$(x_1 ϵ "*weak* (*C*)")) = 0.6·1 = 0.6;
P ($\neg$(x_1 ϵ "*weak* (*R*)")) = 0.6·1 = 0.6;
P ($\neg$(x_3 ϵ "*raised*")) = 0.3 + 0.1 + 0.1 + 0.1 = 0.6;
P("0.5/influenza + 0.5/sharp respiratory disease + 0.4/angina +
+ 0.8/pneumonia") = 0.25 + 0.15 + 0.04 + 0.08 = 0.52.

Then the probability of the first hypothesis is $P(H_1)$ = 0.58.
Similarly we calculate the probability of hypotheses

H_2 = ***if*** x_1 is "*weak* (*C*)" $\wedge$ x_2 is "*moderate* (*R*)" $\wedge$ x_3 is "*high*" ***then*** *y* is "0.8/influenza + 0.7/sharp respiratory disease + 0.8/angina + 0.3/pneumonia"

and

H_3 = ***if*** x_1 is "*weak* (*C*)" $\wedge$ x_2 is "*moderate* (*R*)" $\wedge$ x_3 is "*very high*" ***then*** *y* is "0.9/influenza + 0.7/sharp respiratory disease + 0.8/angina + 0.2/pneumonia".

So, the probability of the hypothesis H_2 is $P(H_2) = 0.5675$ and the probability of the hypothesis H_3 is $P(H_3) = 0.6775$.

At the next step we calculate the conditional probability $P(A/H_1)$, $P(B/H_2)$, $P(B/H_3)$. The calculation algorithm of the conditional probability $P\ (A/H_i)$ consists in performing the following steps:

1. Calculate the distribution function of binary probability $P_{(B,H_i)}$:

$$P_{(B,H_i)}(x_1,\dots,x_n,y) = \min[\max(\ P_{\boldsymbol{X}_1}(x_1)\cdot\mu_{A_1'}(x_1),\ \dots\ ,P_{\boldsymbol{X}_n}(x_n)\cdot\mu_{A_n'}(x_n),\ P_{\boldsymbol{Y}}(y)\cdot\mu_{B'}(y)),$$
$$\max(\ P_{\boldsymbol{X}_1}(x_1)\cdot\mu_{A_{i1}}(x_1),\ \dots\ ,P_{\boldsymbol{X}_n}(x_n)\cdot\mu_{A_{in}}(x_n),\ P_{\boldsymbol{Y}}(y)\cdot\mu_{B_i}(y))].$$

2. Calculate the probability function of Cartesian product:

$$Q_{(B\times H_i)}(x_1,\dots,x_n,y) = \begin{cases} \dfrac{P_{(B,H_i)}(x_1,\dots,x_n,y)}{P_B(y)}, & P_B(y)\neq 0 \\ 1, & P_B(y)=0. \end{cases}$$

3. Calculate the conditional probability distribution function:

$$P_{(B|H_1)}(x_1,\dots,x_n,y) = \begin{cases} \dfrac{Q_{B\times H_1}(x_1,\dots,x_n,y)}{\sum\limits_{x_1,\dots,x_n,y} Q_{B\times H_1}(x_1,\dots,x_n,y)}. \end{cases}$$

Let’s calculate, for example, values

$$P_{(B,H_1)}(5,5,36,\text{influenza})\ ,\ Q_{(B\times H_i)}(5,5,36,\text{influenza})\ \text{ and }$$
$$P_{(B|H_1)}(5,5,36,\text{influenza}).$$

We obtain

$$P_{(B,H_1)}(5,5,36,\text{influenza}) =$$
$$\min[\max(\ P_{X_1}(5)\cdot\mu_{A_1'}(5),\ P_{X_2}(5)\cdot\mu_{A_2'}(5),\ P_{X_3}(36)\cdot\mu_{A_3'}(36),\ P_Y(\text{influenza}))\cdot\mu_{B'}(\text{influenza})),$$
$$\max(P_{X_1}(5)\cdot\mu_{A_{11}}(5),\ P_{X_2}(5)\cdot\mu_{A_{12}}(5), P_{X_3}(36)\cdot\mu_{A_{13}}(36),\ P_Y(\text{influenza})\cdot\mu_{B_1}(\text{influenza}))] =$$
$$= \min[\max(\ 0.4, 0.4, 0, 0.25), \max(\ 0.4, 0.4, 0, 0.25)] = 0.4.$$
$$Q_{(B\times H_1)}(5,5,36,\text{influenza}) = P_{(B,H_1)}(5,5,36,\text{influenza}) \,/\, P_B(y) = 0.8.$$

$$P_{(B/H_1)}(5,5,36,\text{influenza}) =$$

$$Q_{(B\circ H_1)}(5,5,36,\text{influenza}) \Big/ \sum_{x_1,\dots,x_n,y} Q_{B\times H_1}(5,5,36,\text{influenza}) = 0.8/190 = 8/1900.$$

The distribution function of binary probability, probability functions of Cartesian product, and distribution function of conditional probability for other values of arguments are calculated in a similar way.

On the next step, we calculate the Cartesian products $A_1' \times A_2' \times A_3' \times B'$, $A_{11} \times A_{12} \times A_{13} \times B_1$ and their aggregation.

Now we can calculate the conditional probability $P(B/H_1)$. Namely,

$$P(B/H_1) = \frac{131}{1425}.$$

To calculate the probability $P(B/H_2)$ we find Cartesian product $A_{21} \times A_{22} \times A_{23} \times B_2$ and calculate the conditional probability

$$P(B/H_2) = \frac{77}{950}.$$

To calculate the probability $P(B/H_3)$ we find Cartesian product $A_{31} \times A_{32} \times A_{33} \times B_3$ and calculate the conditional probability $P(B/H_3)$. Namely,

$$P(B/H_3) = \frac{122}{950}.$$

Then, using the analogue of law of total probability

$$P(B) = \sum_{i=1}^{n} P(H_i)P(B/H_i),$$

we can calculate the probability of an event B, that is, the probability of output of fuzzy inference system is B'. Therefore, we have

$$P(B) = \sum_{i=1}^{3} P(H_i)P(B/H_i) = 0.58\cdot\frac{131}{1425} + 0.5675\cdot\frac{77}{950} + 0.6775\cdot\frac{122}{950} \approx 0.2.$$

5. Conclusion

The proposed approach based on fuzzy models allows to simplify the methods of solving of above mentioned problems. But, there is a necessity for additional studies of the credibility results.

Very often, there is a necessity in solving so-called inverse problems mentioned above. In this case, to calculate the reliability of the results, we can use Bayes' formula

$$P(A_k / B) = P(B / A_k)P(A_k) / \sum_{i=1}^{n} P(B / A_i)P(A_i)$$

Bayes' theorem offers an approach to the assessment of the reliability of the results and has achieved some success in expert systems in the last 20 years.

Given a probability distribution [1] in the space X Bayes' recognition procedure allows to evaluate the credibility of the fuzzy inference system outputs (inputs) by analogy with [2].

References

1. Buckley JJ. Fuzzy Probabilities. Physica-Verlag, Heidelberg, Germany (2003).
2. Gupal, A.M., Sergienko, I.V.: Optimal Recognition Procedures (in Russian). *Naukova Dumka, Kyiv* (2008).
3. Katerynych, L., Provotar, A.: Neural Networks Diagnostics in Homeopath System. *International Journal Information Theories & Applications*. 15, 89-93 (2008).
4. Konysheva, L.K., Nazarov, D.M.: Foundations of Fuzzy Sets Theory (in Russian). *SPB Piter, Moscow* (2011).
5. Klir GJ, Yuan B, eds. Fuzzy Sets, Fuzzy Logic and Fuzzy Systems: Selected Papers by Lotfi A. Zadeh. World Scientific, Singapore (1996).
6. Lesk, A.: Introduction to Bioinformatics (in Russian). *Labaratoria Znaniy, Moscow* (2009).
7. Leski, J.: Systemy Neuronowo-Rozmyte (in Polish). *Naukowo-Techniczne,Warszawa* (2008).
8. Provotar, A.I., Lapko, A.V., Provotar, A.A.: Fuzzy Inference Systems and Their Applications. *International Scientific Journal Cybernetics and Systems Analysis*. 49, 517-525 (2013).
9. Rutkowska, D., Pilinski, M., Rutkowski, L. Sieci Neuronowe, Algorytmy Genetyczne, Systemy Rozmyte (in Polish). *Wydawnictwo Naukove PWN, Warszava* (1999).
10. Rutkowski, L. Metody i Techniki Sztucznej Inteligencji (in Polish). *Wydawnictwo Naukove PWN, Warszava* (2009).
11. Zadeh, L.A.: Fuzzy Sets as a Basis for a Theory of Possibility. *Fuzzy Sets and Systems*. 1, 3-28 (1978).

RMID: a novel and efficient image descriptor for mammogram mass classification

Sk Md Obaidullah, Sajib Ahmed, Teresa Gonçalves, and Luís Rato
Dept. of Informatics, University of Évora, Portugal

Abstract. For mammogram image analysis, feature extraction is the most crucial step when machine learning techniques are applied. In this paper, we propose RMID (Radon-based Multi-resolution Image Descriptor), a *novel* image descriptor for mammogram mass classification, which perform *efficiently* without any clinical information. For the present experimental framework, we found that, in terms of area under the ROC curve (AUC), the proposed RMID outperforms, upto some extent, previous reported experiments using histogram based hand-crafted methods, namely Histogram of Oriented Gradient (HOG) and Histogram of Gradient Divergence (HGD) and also Convolution Neural Network (CNN). We also found that the highest AUC value (0.986) is obtained when using only the carniocaudal (CC) view compared to when using only the mediolateral oblique (MLO) (0.738) or combining both views (0.838). These results thus proves the effectiveness of CC view over MLO for better mammogram mass classification.

The full text will be available in the edited book "Information Technology, Systems Research and Computational Physics", eds. Kulczycki P., Kacprzyk J., Kóczy L.T., Mesiar R., Wisniewski R., to be published by Springer in the *Advances in Intelligent Systems and Computing* series soon.

Instrumentals/songs separation for background music removal

Himadri Mukherjee[1], Sk Md Obaidullah[2], K.C. Santosh[3], Teresa Gonçalves[2],
Santanu Phadikar[4], and Kaushik Roy[1]

[1] West Bengal State University;
[2] University of Évora;
[3] The University of South Dakota;
[4] Maulana Abul Kalam Azad University of Technology;

Abstract. The music industry has come a long way since its inception. Music producers have also adhered to modern technology to infuse life into their creations. Systems capable of separating sounds based on sources especially vocals from songs have always been a necessity which has gained attention from researchers as well. The challenge of vocal separation elevates even more in the case of the multi-instrument environment. It is essential for a system to be first able to detect that whether a piece of music contains vocals or not prior to attempting source separation. In this paper, such a system is proposed being tested on a database of more than 99 hours of instrumentals and songs. Using line spectral frequency-based features, we have obtained the highest accuracy of 99.78% from among six different classifiers, viz. BayesNet, Support Vector Machine, Multi Layer Perceptron, LibLinear, Simple Logistic and Decision Table.

The full text will be available in the edited book "Information Technology, Systems Research and Computational Physics", eds. Kulczycki P., Kacprzyk J., Kóczy L.T., Mesiar R., Wisniewski R., to be published by Springer in the *Advances in Intelligent Systems and Computing* series soon.

Modern metaheuristics in physical processes optimization

Tomasz Rybotycki
Centre of Statistical Data Analysis,
Systems Research Institute Polish Academy of Science, Warsaw, Poland;

Abstract. The subject of this work is applying the artificial neural network (ANN) taught using two metaheuristics - the firefly algorithm (FA) and properly prepared evolutionary algorithm (EA) - to find the approximate solution of the Wessinger's equation, which is a nonlinear, first order, ordinary differential equation. Both methods were compared as an ANN training tool. Then, the discussion of applying this method in selected physical processes is discussed.

The full text will be available in the edited book "Information Technology, Systems Research and Computational Physics", eds. Kulczycki P., Kacprzyk J., Kóczy L.T., Mesiar R., Wisniewski R., to be published by Springer in the *Advances in Intelligent Systems and Computing* series soon.

Section 14

From Theory to Applications

Effect of left ventricular longitudinal axis variation in Pathological hearts using Deep learning

Yashbir Singh1[1], Deepa2[1], Shi-Yi Wu3[1], João Manuel R. S. Tavares4[3], Michael Friebe5[4] and Weichih Hu6[1]

1 Chung Yuan Christian University, Zhongli, Taiwan
2 Instituto de Ciência e Inovação em Engenharia Mecânicae Engenharia Industrial, Departamento de Engenharia Mecânica, Faculdade de Engenharia, Universidade do Porto, Porto, PORTUGAL
3Otto-von-Guericke-Universität, Magdeburg, Germany
weichihhu@gmail.com,
yashbir143@gmail.com

Abstract. Cardiac disease is a primary cause of death worldwide. Prior studies have indicated that the dynamics of the cardiac left ventricular (LV) during diastolic filling is a major indicator of cardiac viability. Hence, studies have aimed to evaluate cardiac health based on quantitative parameters unfolding LV function. In this research, it is demonstrated that major aspects of the cardiac function, mainly ejection fraction, are due to abnormalities of the left ventricular on longitudinal axis variation. We used Bayesian deep learning algorithms to measure the wall motion of the LV that correlates well with the LV ejection fraction. Our results reveal relations among the wall regions of the LV. The findings of this research can potentially be used as determination value to identify patients with future cardiac disease problems leading to heart failure.

Keywords: Pathological heart, Ejection Fraction, Deep learning, longitudinal axis.

1 Introduction

Death caused by Heart Failure (HF) has remarkably increased in the past few years mainly due to the general aging of the human population. While modern developments in the biomedical field are surely helping in diagnosing and subsequently treating patients whether it is the cost related to the interventional device.

Research, production, distribution and subsequent clinical training is a huge concern that society has to deal with in form of ever-increasing healthcare expenses. Screening of the population that is susceptible to HF, can be helpful to reduce the deaths due to HF [1] and simultaneously reduce healthcare expenses through preventative treatments. By the guidelines of The American College of Cardiology Foundation and American Heart Association (ACCF/AHA), there are two classes of HF that has been categorized in these patients: class A and class B of HF [2]. In class A, patients are more susceptible to HF, but lacking any structural heart disease or symptoms. In class

B, patients are seen with the structural disease, but lacking signs and symptoms of HF. Additional contributors to developing HF are other diseases like hypertension, diabetes mellitus, metabolic syndrome and atherosclerotic [2, 3].

Now, the question is that what else can be done in preventing HF at major scale. We see Bayesian deep learning (DL) research and recent algorithms as possible future tools for screening and diagnosis in order to facilitate the detection of patients prone to HF. DL is a technique that utilizes machine learning algorithms (supervised or unsupervised) that are perfectly dependent on the choice of the data representation used for training the algorithm on various layered models of non-linear operational input [4].

The applications may be multifunctional and involve pattern recognition, statistical classification, convolutional deep neural networks and deep belief networks [5]. Here, we present our work on building a computer aided diagnosis system with the goal to detect wall motion of LV based on DL.

2 Method

In this study, our focus was on the classification portion of the LV; as to the image processing part, the reader can find the details in the referenced papers that address the automatically detection of the interior (endocardial) and exterior (epicardial) borders of the LV [6, 7]. The images were acquired using a computerized tomography scanner SIEMENS_LEOVB30B at the National Institute of Hospital of Yang Ming, National Yang Ming University, Taiwan. The study and the informed consent procedure were approved by the Institutional Review Board of National Yang Ming University Hospital. A number of features were studied to identify the cardiac motion in order to discover cardiac wall motion abnormalities, mainly: velocity, radial strain and circumferential strain, local and global Simpson volume and segmental volume, which are based on the inner (endocardial) contour.

We used Bayesian Networks (BNs) to detect both the interior (endocardial) and exterior (epicardial) borders of the LV [8, 9]. Motion interferences were compensated by using global motion estimation based on robust statistics outside the LV; this is done so that the heart’s motion is only analyzed on the longitudinal axis (Fig. 1). Then, numerical feature vectors, which were calculated using the contours extracted from two consecutive time frames, were tracked through time.

In general, velocity, radial strain and circumferential strain can be calculated in terms of standard deviation or/and mean of five segment’s respective feature values from any one view.

The features used to help in the detection of local and global dysfunction of heart were:

(i) Velocity features used to determine how fast any pair of control points change in the *x* and *y* coordinates per image frame;

(ii) Circumferential strain features to assess how much the contour between any two control points shrinks in the systolic phase;

(iii) Radial strain features also called Thickening of cardiac wall;

(iv) Local and global Simpson Volume to determine the volume as computed by the Simpson rule for each frame of the heart as a whole;

(v) Segmental Volume in order to obtain the volume per segment per frame and the segmental EF values.

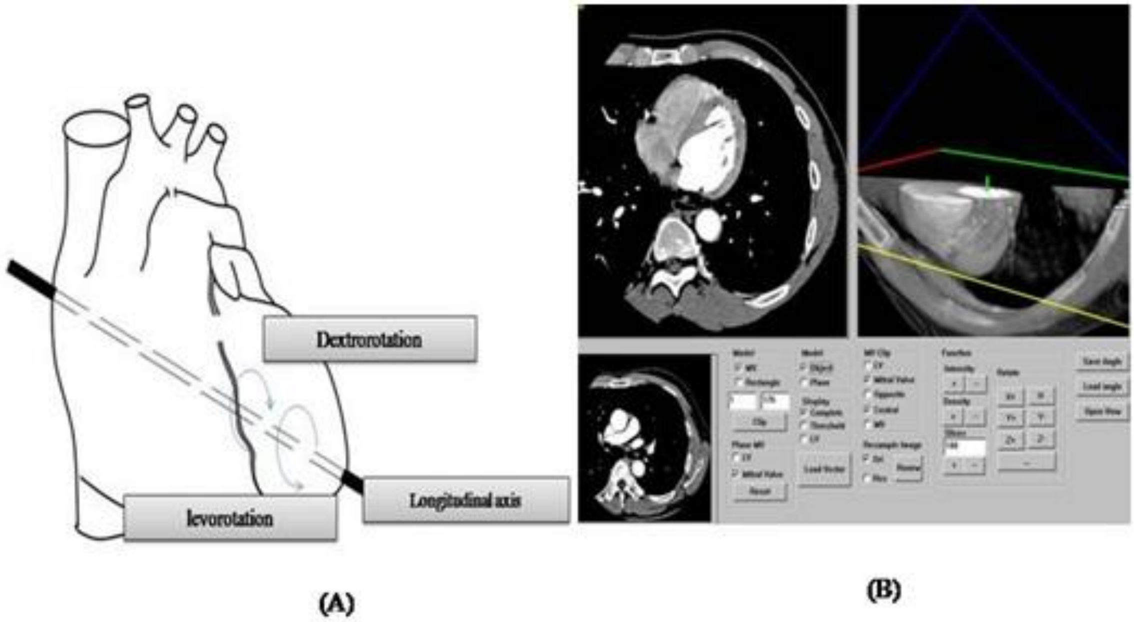

Fig. 1. (A) Longitudinal axis representation of LV; (B) Computer Tomography transverse section on the short axis of LV.

3 Results

Most of the research reported the longitudinal strain as a very sensitive parameter of sub endocardial dysfunction. In addition, evaluation of circumferential, radial strain and local and global Simpson Volume are also significant when assessing compensation patterns of LV function. Though, lack of a normal range of values and associated variation hinder their use for everyday clinical evaluation.

We implemented Bayesian Network to detect wall motion abnormalities of LV and did parameter training using 220 training cases with CT images of size 512 × 512 pixels. Our feature selection resulted in every segment dependent on five features such as Velocity features, Circumferential strain features, Radial strain features, Local and global Simpson Volume, Segmental Volume. Table 1 is showing the Area under the ROC curve for the testing set. The classifier did well every heart segment, and entirely achieved high sensitivity and specificity between 84% and 98%.

Table 1. Area under the ROC curve for the test set.

Segment of LV	Bayesian Network of testing set	Segment of LV	Bayesian Network of testing set
1	0.90873	9	0.9648
2	0.86170	10	0.9176
3	0.97790	11	0.8450

4	0.91673	12	0.9837
5	0.84506	13	0.9715
6	0.9874	14	0.9155
7	0.8643	15	0.9471
8	0.8200	16	0.9450

This study studies the effect of ejection fraction due to LV variation on the longitudinal axis. We have also seen some variation about volume change and performed the simulation study with the actual volume of LV (Fig. 2), which has been done by Weichihhu lab [10]. We got the variation on the longitudinal axis performing a comparative study of actual and simulated LV heart. Variations of 1%, 4%, 7% and 10% were found on various points of LV (Fig. 2, Panel C). This can be seen as an initial step to recognize local and global dysfunction in the heart.

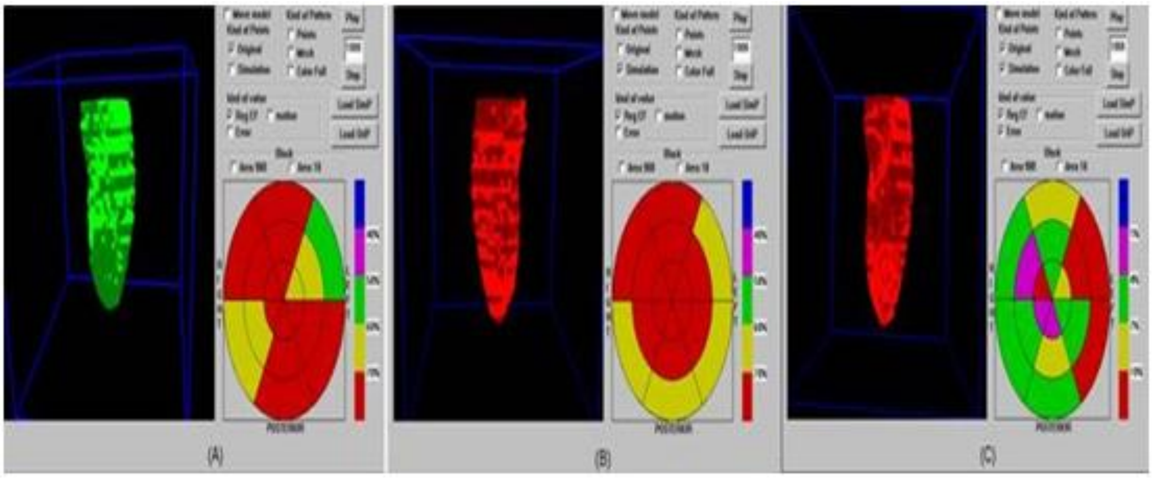

Fig. 2. (A) Actual volume of heart model; (B) Simulated heart model; (C) Difference between the two models (A, B).

4 Conclusion

In this research, we addressed the task of building an objective classification application for ejection fraction analysis and LV wall motion on the longitudinal axis based on extracted features. The simple, but effective feature selection technique used, resulted in a classifier that depends on only a small subset of the calculated features, and their limited number makes it easier to explain the final classifier result to physicians in order to get their feedback. Further research will integrate ejection fraction and LV motion of pathological heart.

Acknowledgement

João Manuel R.S. Tavares gratefully acknowledges the funding of Project NORTE-01-0145-FEDER-000022 - SciTech - Science and Technology for Competitive and Sustainable Industries, co-financed by “Programa Operacional Regional do Norte” (NORTE2020), through “Fundo Europeu de Desenvolvimento Regional” (FEDER).

References

1. Nagueh, S. F., Smiseth, O. A., Dokainish, H., Andersen, O. S., Abudiab et al. Mean Right Atrial Pressure for Estimation of Left Ventricular Filling Pressure in Patients with Normal Left Ventricular Ejection Fraction: Invasive and Noninvasive Validation. Journal of the American Society of Echocardiography (2018).
2. Yancy, C. W., Jessup, M., Bozkurt, B., Butler, J., Casey et al. 2013 ACCF/AHA guideline for the management of heart failure. Circulation, (2013).
3. Chen, I. L., Singh, Y., & Hu, W. Comparative Study of Arterial Compliance Using Invasive and Noninvasive Blood Pressure Waveform. Journal of Biomedical Engineering, 5(1), 25-29 (2017).
4. Singh, Y., Wu, S. Y., Friebe, M., Tavares, J. M. R., & Hu, W. Cardiac Electrophysiology Studies Based on Image and Machine Learning (2018).
5. Angermueller, C., Pärnamaa, T., Parts, L., & Stegle, O. Deep learning for computational biology. Molecular systems biology, 12(7), 878 (2016).
6. Georgescu, B., Zhou, X. S., Comaniciu, D., & Krishnan, S. U.S. Patent No. 7,421,101. Washington, DC: U.S. Patent and Trademark Office (2008).
7. Zheng, Y., Georgescu, B., Scheuering, M., & Comaniciu, D. (2012). U.S. Patent No. 8,150,119. Washington, DC: U.S. Patent and Trademark Office (2012).
8. Fung, G., Qazi, M., Krishnan, S., Bi, J., Rao, B., & Katz, A. Sparse classifiers for automated heartwall motion abnormality detection. In Machine Learning and Applications,. Proceedings. Fourth International Conference on pp. 194-200 (2005).
9. Murphy, K. P., & Russell, S. Dynamic bayesian networks: representation, inference and learning (2002).
10. Deepa, D. , Singh, Y. , Wu, S. Y. , Friebe, M. , Tavares, J. M. , Wei-Chih, H. 'Development of 4D Dynamic Simulation Tool for the Evaluation of Left Ventricular Myocardial Functions'. World Academy of Science, Engineering and Technology, International Science Index, Computer and Information Engineering, 12(5), 2814 (2018).

Finding Graph from Retinal Vascular Network for Image Verification

Nilanjana Dutta Roy[1] and Arindam Biswas[2]

[1] Department of Computer Science and Engineering, Institute of Engineering and Management, Kolkata, India
[2] Department of Information Technology, Indian Institute of Engineering Science and Technology, Shibpur, Howrah, India
`{nilanjanaduttaroy, barindam}@gmail.com`

Abstract. Retina biometrics for secured system is increasingly becoming popular because of its unchangeable nature throughout the life span, robustness against tampering and contact free capture process. In this paper, the authors show the benefits of retina graph representation in image matching for person verification. This paper presents a retinal image verification framework based on the retinal vascular graph matching algorithm (RVGM). Retinal vascular structure is extracted using a family of enhancement, proper illumination distribution, noise removal and morphological operators. Then, unique retinal patterns are defined as formal spatial graphs derived from the retinal vascular structure. A node level graph matching approach, later distinguishes between genuine and fake comparisons. Because of unavailability of multiple datasets, experiments are done on all the images of DRIVE database. A matching score estimation (MSE) method for the genuine and fake score distribution of the database is used to measure performance of the RVGM algorithm. A MSE score 0 to 5 ensures the authenticity of the user whereas above that denies the user. The authors also show that a simple retina graph is used to bring down the verification time by considerable amount compared to other junction point based methods and the cost functions that include location based, point to point node matching.

Keywords: closed polygons, rings, polygon approximation, graph, matching score, retinal vascular network

1 Introduction

Efficient registration and verification process decide the prosperity of any authentication system. The retinal biometry is best-suited for high security applications where the user is cooperative [6]. The vascular structure of eye shares a uniqueness pattern across the human population [6]. It remains unchanged throughout the lifespan of a person and it is claimed to be robust to changes in human physiology. This is not easily accessible as it is located safely under the layer of conjunctiva and this is hard to tamper with the retinal images. The retinal vascular structure can be viewed as a formal graph for image registration also [3]. Using BGM algorithm, extraction of a spatial graph from retina was proposed in [8]. In [2], a classification of the entire vascular tree deciding on the type of intersection point for artery/vein classification has been proposed. In this paper, we present a complete graph-representation of retinal vascular structure. It is used for vascular pattern matching over traditional vascular biometrics of feature-based or image-based template matching.

We present the features of retinal blood vessels into a topological feature-based graph, taken from DRIVE database [1]. We also show how retinal vascular structure influences the prevalent graph features present in retina for faster verification and registration process. While analyzing retinal vasculature, a large number of 'ring' structures are found in it which bears the significance in this research. Rings are the closed polygons, formed by arteriovenous crossings on the retinal vascular structure.

This paper is organized in the following way. Section 2 describes the methodology where image enhancement and segmentation are described. Feature extraction, graph representation from fundus image and image verification are discussed in Section 3. Analyzed experimental results are discussed in Section 4 and Section 5 draws the final conclusion.

2 Methodology

2.1 Image preprocessing and segmentation

Some common image processing steps are applied here over the fundus images to make the image ready for further processing. Grayscale conversion, sharpening using multiple passes of illumination distribution by CLAHE, followed by Otsu thresholding [9] helped us to give the image a good shape at its initial stage. The grayscaled image is then passed through 2-D median filtering for de-noising and finally, a smooth textured image in binary platform is hence presented. Figure 1 shows the process for segmentation.

2.2 Feature extraction

The task of feature extraction transforms rich content of images into usable content features. In this work, the closed polygons called 'rings', present in the fundus images, formed by many arterio-vascular crossings bear significance in feature selection. To accomplish this work, width [5] of every vessel has been calculated to eliminate the tiny and disconnected ones from the segmented image. It further results in a binary image (I_t), shown in Figure 2 (b), with all thick and major vessels present in it. Then, morphological image analysis [10] is applied to extract the skeleton of the vessels. To detect the terminal points, t_p, a 9 pixel (3×3) mask is passed through the skeleton image (I_p). If the central pixel with value 1 has exactly one neighbor with the same value, it is then defined as terminal point, t_p. The objects are identified by connected component

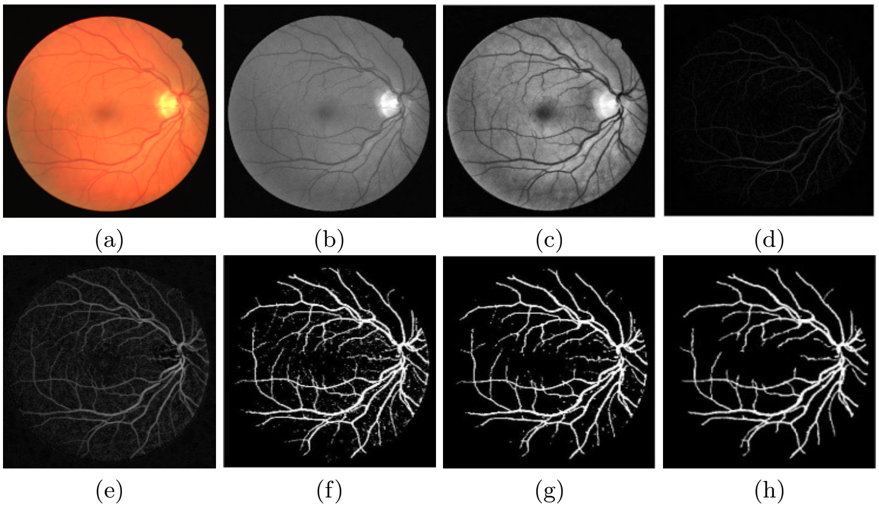

Fig. 1. (a) original RGB image (b) green channelled image (c) CLAHE filtered image (d) image after bottom hat (e) contrast enhanced image (f) extracted blood vessels by Otsu thresholding (g) median filtered image (h) segmented image after noise removal

labelling [4] and then for each object, the above mentioned method is applied to distinguish between two closely related terminal points.
Removal of single threaded vessels from I_p starts by scanning each t_p with a 9 pixel (3×3) mask again and sets a new value to it as 0 which results in I_{new}. Histograms of the images I_p and I_{new} are compared at this stage. Histogram error ($diff$) between them ensures the scope for further removal of single threaded vessels from t_p. Removal stops at every crossing, a center pixel of value 1 with its four or more neighbors with same value in a 9 pixel mask. The process continues every iteration till $diff$ becomes 0. $diff = 0$ indicates similarity between both the images. Features which we wanted to focus on, is finally extracted where all the bounded polygonal regions are found. The retina graph would be generated next based on the extracted feature made up of rings.

3 Graph representation

The primary reason behind graphical representation of retinal structure is to accelerate the image verification stage. It simplifies a complicated retinal vascular structure into a more logical and understandable graphical format which would further be worthwhile in graph matching. More detailing of this stage has been explained below.

3.1 Disjoint Region Identification

From I_{final}, which is now an image with only bounded polygonal structures, distinct regions have been identified by connected component labelling method [4] with a user defined masking window of size 3×3. It is shown by different colors in Figure 3 (b).

3.2 Polygonal approximation of each disjoint region by modified split and merge method

To accomplish the goal, we have identified each disjoint polygon with specified region code for every member of the ring. For outer boundary approximation of the polygons, split and merge method is used with little modification in it as per our requirement. Any two random points $P1$ and $P2$ are chosen on any part of the polygon boundary C and a straight line is drawn between $(P1, P2)$ following the formula

$$y = mx + b \tag{1}$$

where m is defined as $\frac{\triangle y}{\triangle x}$.
Now, on the n number of segments on the straight line, stored in $sg_p[i]$, perpendicular lines are drawn which intersect C at certain intersection points stored in $intersect_p[i]$. The similarity on of slopes with a little tolerance in both $P1$ and $P2$ concludes the final segment of C as $(P1, P2)$. On the other hand, maximum distance, δ ($\delta \geq 0.006$), between $sg_p[i]$ and $intersect_p[i]$ breaks C into two more segments, $(P1, temp)$ and $(temp, P2)$ where $temp$ is the maximum distant point between $(P1, P2)$ and C. The process continues till all the segments on the curve C are covered. Boundary approximation drives us to calculate the unique region codes for each member of the. At the end of approximation stage, the closed polygon receives multiple number of line segments over the boundary of it. Linear distance between each segment on the boundary adds value in forming a parameter for region code generation. At each segment, the direction of the current side is noted by placing a reference frame for $8-$ connected region (Figure 5) on it, clockwise. These generated features further act as notable parameters in forming the region code. Hence, the formation of region code is done as a sequence of l_i and d_i from any point where l_i is the distance of line segment and d_i is the direction of the current side with reference frame and i is the no. of segments where $1 \leq i \leq n$. Following the above mentioned method, unique region codes are generated for the images from DRIVE database. The region code for Image 4 from DRIVE has been calculated on total 19 contour points (Figure 4).

3.3 Graph from vascular network

A graphical representation from any complicated retinal vascular network is the most indispensable phase of the proposed method and plotting the graph is also

a challenging task.
The biometric template here is defined as a spatial graph extracted from the retinal vascular structure. The retina graph is defined as $G = \{V, E\}$, where V is the set of vertices formed from rings and E is the corresponding edges between them. Figure 6 shows that any two polygons on rings, sharing a common edge between them, seem to be directly connected with each other. A spatial graph representation, made from vascular structure of retina by following the steps is defined in Figure 2.
In the Figure 6 (a), there are common polygonal sides exist between node 1 and node 3 and also node 2 and node 3 which resembles the connected edges between the nodes. But, no edge has been formed between node 1 and node 2 as they don't share a common polygonal side between them as per Figure 6 (b). Following the same process, a corresponding graphical representation, shown in Figure 2 (f), has successfully been plotted from the whole retinal vascular network.

4 Experimental evaluation

4.1 Materials

The proposed method was evaluated on the images collected from DRIVE [1] database. The images of DRIVE were captured by Canon CR5 non-mydriatic 3 CCD cameras with a 45 degree FOV for medical imaging. The collected RGB images are passed through the different stages of preprocessing to make the images ready for the experiment.

4.2 Results

The purpose of the proposed approach is to represent a retinal vascular structure into its equivalent graph. To accomplish the work, stable features are extracted from retinal vasculature and they are identified as distinct closed polygons, rings. Outer boundaries of the polygons are measured by approximation and their corresponding region codes are generated. The code is formed as a sequence of (l_i and d_i) where l_i is the length of a side of polygon between two consecutive contours and d_i is the direction of the present side according to the reference frame, shown in Figure 5. Table 1 shows the formed region codes against each polygon of the image no. 4 (04_manual1) from DRIVE database. Approximated boundaries and corresponding contour points of the same image are shown in Table 2. To wrap up with the above mentioned experiments, this is the final stage of node matching process by using Levenshtein string matching algorithm [7]. Levenshtein distance (LD) is a string metric for measuring the difference between two sequences, which we will refer to as the source string (s) and the target string (t). Matching scores between individual nodes are shown in Table 5 using Levenshtein distance algorithm.

Table 1. Unique region codes have been generated against each graphical node

Node no.	**Unique region code**
Node1	10024532462320776,343771513065252884
Node2	57210813003661897896476744413231413
Node3	173291682392240257781014973042483552963
Node4	9411244202230772570271900546417626425356125356664854
Node5	29241215722028197331340206425456865696273
Node6	232213422200492221352201202801300147 2201017246375276205356 575224205254136674
Node7	4021932644624613627026111312073063753966371097265384255414
Node8	9332093762662300256307145765722461703864531303

4.3 Performance measures

It is a common practice to measure the performance of any algorithm based on its accuracy calculation. Accuracy here is defined by

$$Accuracy = \frac{(Correct\ detection * 100)}{No.\ of\ nodes}\% \tag{2}$$

which is comparable to other point to point matching algorithms described in [3], [8], [2]. Average accuracy of all the images of DRIVE is 92.88% which is shown in Table 3.

In most of the existing works, the graph features that they have used as nodes are mostly the branch points and terminal points which are again dependent on accurate segmentation process and proper image capturing method. Changes in resolution, improper illumination distribution and any transformation further affect the node selection process for the approaches mentioned in the Table 5. More number of nodes need more comparison also for point-to-point template matching of any two graphs. Whereas in the proposed method, focus is given on the closed regions formed by artery-vascular structures on thick vessels which are robust against poor segmentation, improper illumination distribution and little transformation. Moreover, minimum number of nodes of graph reduces the complexity of graph matching over point-to-point template matching approaches.

5 Conclusion

An approach towards retinal image verification system is proposed here based on retinal graph matching. The segmented binary image has been generated from the original fundus image and then the unattached, tiny blood vessels were removed from the terminal points. A spatial graph is finally formulated upon the existing, closed polygonal structures of the binary image where each polygon is considered as individual node of the graph. Against each node, a generated

Table 2. Polygon approximation on each node and its contour points

Nodes	Approximated Polygons with contour points, $\delta \geq 0.006$	Nodes	Approximated Polygons with contour points, $\delta \geq 0.006$
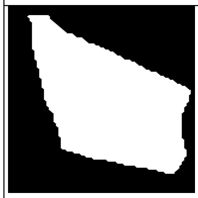	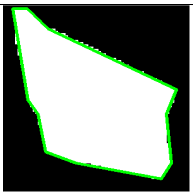 contour points=10	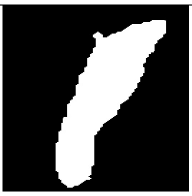	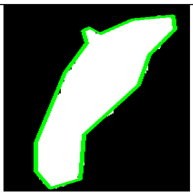 contour points=14
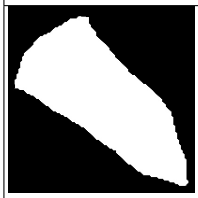	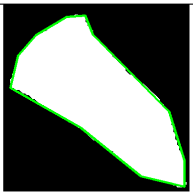 contour points=10		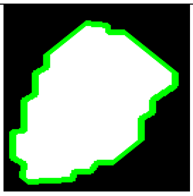 contour points=25
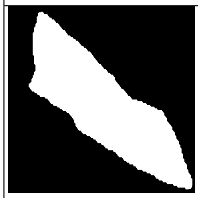	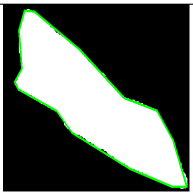 contour points=12		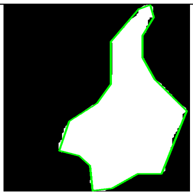 contour points=19
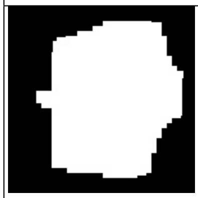	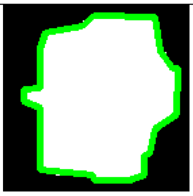 contour points=17		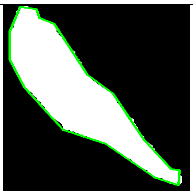 contour points=14

Table 3. Result and analysis

Samples	No. of nodes (Manual)	Correct detection	False detection	Failure Rate	Accuracy (%)
Image 1	12	11	1	1	91.6
Image 2	13	13	2	0	100
Image 3	9	8	0	1	88.88
Image 4	10	8	0	2	80
Image 5	10	9	0	1	90
Average performance on all the images from DRIVE dataset					92.88

Table 4. Matching score between each node using the Levenshtein distance string matching

	Node 1	Node 2	Node 3	Node 4	Node 5	Node 6	Node 7	Node 8
Node 1	0	30	28	37	31	57	38	32
Node 2	30	0	26	37	32	59	42	32
Node 3	28	26	0	38	29	58	42	31
Node 4	37	37	38	0	33	52	42	37
Node 5	31	32	29	33	0	55	40	36
Node 6	57	59	58	52	55	0	49	54
Node 7	38	42	42	42	40	49	0	41
Node 8	32	32	31	37	36	54	41	0

unique region code is the major strength of this proposal which identifies a polygon uniquely. The best part of the approach is that, the code sequence of the regions always shows the robustness (proves the same polygon) even for the distorted and sheared images. Each node of a new retinal graph is compared with every other nodes of the existing retinal graph in database and hence, authentic source is identified. The approach also shows that a simple retina graph is used to bring down the verification time by 60% compared to other junction point based methods and the cost functions that include location based, point to point node matching. Focus on the rings, which are bounded polygonal structures, reduces the chances of getting false positive values. The future of this work will include improving the algorithm for poor quality images and making it more robust against any transformation during image capturing and graph creation. Also, to strengthen the verification stage in less time, additional stage for verification will be added with the existing one. This work also seeks to test the image matching algorithm on multiple samples of larger retina databases when it is available.

References

1. The DRIVE database, Image sciences institute, university medical center utrecht, The Netherlands. http://www.isi.uu.nl /Research/Databases/DRIVE/, last ac-

Table 5. Comparison with other methods

Authors	Features used as graph nodes	No. of nodes (Average)	Graph matching
[3]	Vascular bifurcation point and vessel segment end point	169	point-to-point template matching based on stable and unstable structure
[2]	Connecting point, meeting point, bifurcation point, crossing point and end point	120	NA
[8]	Terminal point, a central pixel with value 1 has exactly 3 neighbours with value 1, and if a central pixel is a feature point and has two or more neighbours which are feature points and on different sides of central pixel	100	Maximum common subgraph (MCS), which will be the intersection of two compared graphs based on finding minimum graph edit distance
RVGM (proposed method)	Closed polygons formed by arterio-vascular structures on thick vessels and their region codes	12	Node level region code matching

cessed on 7th July, 2007

2. Dashtbozorg B., Mendonca A. M., Campilho A., An automatic graph based approach for artery-vein classification in retinal images. IEEE Transactions on Image Processing 23, 10731083, 2014

3. Deng K., Tian J., Zheng J., Zhang X., Dai X., Xu M., Retinal fundus image registration via vascular structure graph matching. International Journal of Biomedical Imaging, 2010

4. Gonzalez R. C., Woods R. E., Eddins S. L., Digital Image Processing using Matlab. 3rd ed., Prentice-Hall, Upper Saddle River, NJ, USA, 2006

5. Goswami S., Goswami S., De S., Automatic Measurement and Analysis of Vessel Width in Retinal Fundus Image, Proceedings of the First International Conference on Intelligent Computing and Communication, pp.451-458, 2016

6. Hill R., Biometrics: Personal Identification in Networked Society. Springer-Verlag, New York, NY, USA, 1999

7. Ho T., Oh S., Kim H., A parallel approximate string matching under Levenshtein distance on graphics processing units using warp-shuffle operations, Plos one journal, 2017

8. Jiang X., Mojon D., Adaptive local thresholding by verification based multithreshold probing with application to vessel detection in retinal images. IEEE Trans. Pattern Anal. Mach. Intell. 25, 131137, 2003

9. Otsu N., A threshold selection method from gray-level histogram, IEEE Transactions on System Man Cybernetics, Vol. SMC-9, No. 1: 62-66, 1979

10. Sofka C.V., Stewart M., Retinal vessel centerline extraction using multiscale matched filters, confidence and edge measures. IEEE Trans. Med. Imag. 25, 15311546, 2006

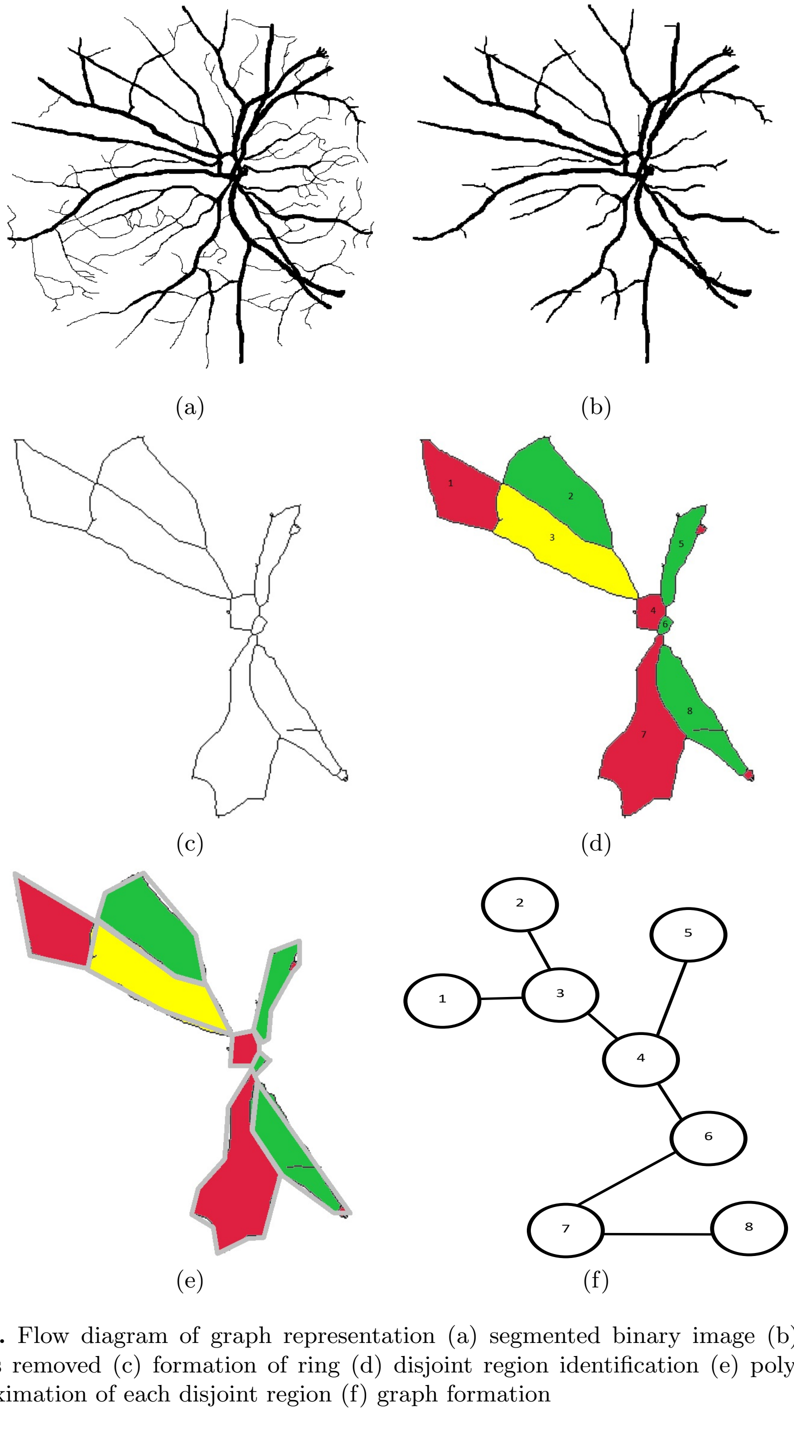

(a) (b) (c) (d) (e) (f)

Fig. 2. Flow diagram of graph representation (a) segmented binary image (b) thin vessels removed (c) formation of ring (d) disjoint region identification (e) polygonal approximation of each disjoint region (f) graph formation

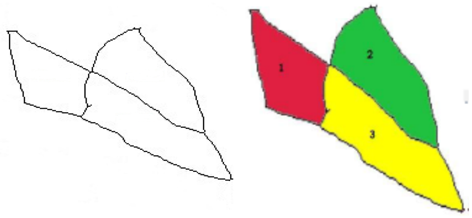

(a) (b)

Fig. 3. Region identification by CCN (a) possible polygons (b) identified regions shown by different colors

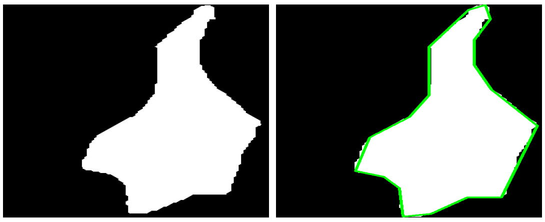

Fig. 4. Boundary approximation with 19 contour points and region code 4021932644624613627026111312073063753966371097265384255414

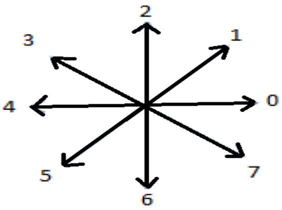

Fig. 5. Reference frame for directional encoding

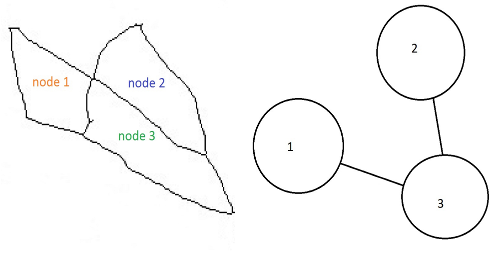

(a) (b)

Fig. 6. Graph plotting (a) disjoint polygons (b) edges exist between $1-3$ and $2-3$ as their corresponding polygons share common side between them

Pure Hexagonal Context-Free Grammars Generating Hexagonal Patterns

Pawan Kumar Patnaik[1], Venkata Padmavati Metta[1], Jyoti Singh[2], and D.G. Thomas[3]

[1] Department of Computer Science and Engineering,
Bhilai Institute of Technology, Durg, India;
[2] Chhattisgarh Professional Examination Board, Raipur, India;
[3] Department of Mathematics, Madras Christian College, Chennai, India;

Abstract. A new syntactic model, called pure hexagonal context free grammar is introduced based on the notion of pure two-dimensional context-free grammar. These grammars generate hexagonal picture arrays on triangular grids. We also examine certain closure properties of pure hexagonal context free languages.

The full text will be available in the edited book "Computational Modeling of Objects Presented in Images. Fundamentals, Methods, and Applications", eds. Barneva R.P., Brimkov V.E., Kulczycki P., Tavares J.M.R.S., to be published by Springer in the *Lecture Notes in Computer Science* series soon.

Design of a haptic exoskeleton for the hand with Internet of Things

Juan Camilo Calvera Duran[1], Octavio José Salcedo Parra[1,2] and
Carlos Enrique Montenegro Marín[2]

[1] Faculty of Engineering, Universidad Nacional de Colombia, Bogotá, Colombia;
[2] Faculty of Engineering, Universidad Distrital "Francisco José de Caldas", Bogotá, Colombia;

Abstract. This paper focuses on the design of a functional haptic hand exoskeleton with the purpose of offering physical rehabilitation of the hand. Moreover, some existing studies of such type of exoskeleton are analyzed which are later used to design our own exoskeleton. Finally, the conclusions regarding the design are presented, including some evaluations and possible improvements in the exoskeleton for future work.

The full text will be available in the edited book “Computational Modeling of Objects Presented in Images. Fundamentals, Methods, and Applications”, eds. Barneva R.P., Brimkov V.E., Kulczycki P., Tavares J.M.R.S., to be published by Springer in the *Lecture Notes in Computer Science* series soon.

Section 15
Early Stage Researchers

Crisp vs Fuzzy Decision Support Systems for the Forex Market

Przemysław Juszczuk[1] and Lech Kruś[2]

[1] Faculty of Informatics and Communication, Department of Knowledge Engineering,
University of Economics, 1 Maja 50, 40-287 Katowice, Poland;

[2] Systems Research Institute, Polish Academy of Sciences, Newelska 6, 01-447 Warsaw, Poland;

Abstract. A new concept of the multicriteria fuzzy trading system using the technical analysis is proposed. The existing trading systems use different indicators of the technical analysis and generate buy or sell signal only when assumed conditions for a given indicator are satisfied. The information presented to the trader – decision maker is binary. The decision maker obtains a signal or no. In comparison to the existing traditional systems called as crisp, the proposed system treats all considered indicators jointly using the multicriteria approach and the binary information is extended with the use of the fuzzy approach. Currency pairs are considered as variants in the multicriteria space in which criteria refer to different technical indicators. The introduced domination relation allows generating the most efficient, non-dominated (Pareto optimal) variants in the space. An algorithm generated these non-dominated variants is proposed. It is implemented in a computer-based system assuring sovereignty of the decision maker.

We compare the proposed system with the traditional crisp trading system. It is made experimentally on different sets of real-world data for three different types of trading: short-term, medium and long-term trading. The achieved results show the computational efficiency of the proposed system. The proposed approach is more robust and flexible than the traditional crisp approach. The set of variants derived for the decision maker in the case of the proposed approach includes only non-dominated variants, what is not possible in the case of the traditional crisp approach.

The full text will be available in the edited book "Information Technology, Systems Research and Computational Physics", eds. Kulczycki P., Kacprzyk J., Kóczy L.T., Mesiar R., Wisniewski R., to be published by Springer in the *Advances in Intelligent Systems and Computing* series soon.

Neural network and dynamic programming for R&D sector development in Poland

Jacek Chmielewski[1]

[1] System Research Institute, Polish Academy of Sciences
[2] ul. Newelska 6, 01-447 Warszawa, Poland
jchmiel@ibspan.waw.pl

Abstract. The paper summarizes the methods of systematic approach for R&D sector development in Poland. System maps R&D sector through neural network. Neural network becomes object for dynamic programming task in searching of better solution.
.

Keywords: R & D sector, neural networks, dynamic programming, the task of searching for a better solution.

1 Introduction

In recent years, there are more and more documents and reports that introduce long-term forecasts of state development scenarios. Development scenarios pointed to threats that could significantly affect the slowdown in economic growth. Sustainable development of the country in the times of globalization requires a systematic approach to development planning. The removal of threats should start as soon as possible, and the research and development (R & D) sector can play an important role in solving problems. The potential of the R & D sector should be used for proper identification of developmental threats and issuing recommendations in a timely manner and well in advance.

The system approach is needed to solve problems, because due to the complexity of the problems, their intuitive solutions will not return acceptable results. One of the possible system solutions is the economic model of the R & D sector, which is mapped to the neural network. The neural network allows you to build an object for dynamic programming. Dynamic programming can further improve the results of the system approach. An important role in improving the country's economic performance should be played by the development of the R & D sector, which in the world of the global economy has a big impact on the country's development results.

The situation of the R & D sector depends on many factors is also included in the economic situation of the country, strongly depends on the innovative approach of politicians and businessmen. An important part of the development of the R & D sector is the proper use of resources allocated to this sector.

In the article, I would like to present the assumptions of a systemic approach, which enables long-term analysis of the development of the R & D sector. The system will support decision-making processes to obtain the best results in planning R & D sector development. A model of the research and development sector will be created using the neural network, and in the next step I will search for a better solution using dynamic programming. Dynamic programming is used to search decision data that can improve the results achieved by the B + R sector.

2 The system solution description

Greater chances of success in terms of economic development, scientific and social development of the country exist when we implement the implementation of the strategy for the R & D sector as soon as possible. Considering the scale of the project, it is important to implement the system better than in comparison to the intuitive approach. Below I present the elements of the system, which in my opinion should be considered for the governmental, academic and business organizations involved in the implementation of the strategy.

Documents that are published, such as: "Poland 2030. The Third Wave of Modernity" [2], "Poland 2030. Threats to development" [3], "Foresight 2020 Poland" [17] and the OECD report [13] is an important step in Strategic thinking about the country's development with the R & D sector. However, the documents are only a starting point from which we can start a systematic approach leading to the implementation of a long-term strategy.

Appropriate organizational link between scientific research subjects, to ensure adequate financing of the necessary conditions for success, which in the long term will be a reversal of the GDP trend in Poland presented in the OECD report [13].

The implementation of the development strategy must consider a part of the R & D sector, which can significantly change the negative tendency and development in advance to develop risk mitigation methods. If there is a limitation of human resources that can actively develop a national method of product elimination, there is a risk of increasing the productivity of resources that create GDP.

The significant development of research and development infrastructure fosters the emergence of innovative solutions. R & D infrastructure is a complex structure that should be adapted to the financial and organizational capacity of the state. R & D infrastructure consists of:

- Polish Academy of Sciences
- R & D unit
- Higher education institutions operating in the field of research and development
- Parks of knowledge and technology
- Innovative enterprises

The system approach to long-term development of the R & D sector should strive to find the most sensitive points of the system, whose change at the current moment will help to reverse the negative trend in the long-term scale. System presented in this article is focused on improving the performance of R&D sector in Poland, so that by means of a strategy supporting the of the country development.

It seems a reasonable approach to the challenges facing the system in implementing the strategy; this can increase the likelihood of successful implementation.

The implementation of long-term strategies and development can take place in an environment that is difficult to predict in a dozen or so years. The system approach eliminates errors that may appear in the definition of resources and the financial capacity needed to properly implement the strategy.

The proposed system supporting decisions in long-term periods for the R & D sector is based on three pillars. The first pillar of the system is the model of the research and development sector in Poland created using a neural network. The second pillar is dynamic programming in which the data provided by the first pillar is used to provide the possibility of analyzing the impact of decision variables on system results. The third pillar is built on the knowledge of an expert or analyst who chooses boundary conditions based on his own experience.

3 Neural network as model of R&D sector

In browsing the bibliography, I was unable to find examples of models for the R & D sector. Interesting solutions for the country's macroeconomic model were based on scientific descriptions of dr. Paweł Rośczak from the Łódź University. This page roszczak.com presents EMIL [26] and Makrosim [35] applications based on neural networks. Makrosim is a project carried out at the University of Lodz, whose aim was to build a computer system that, based on the introduced macroeconomic data, allows to stimulate economic growth. EMIL is an econometric model of the Swedish economy; the creators are prof. Jan B. Gajda from the University of Lodz and prof. Claes-Hakan Gustafson from the University of Orebro (Sweden) [9].

The R & D sector model is a very important element of the proposed decision support system. Without this model, it is difficult to find elements that need to be modified to achieve the expected goal. There are different approaches to creating a model of the R & D sector in Poland. In my opinion, an interesting approach to modeling the R & D sector in Poland, apart from the mathematical model or statistical solution, is a model based on a neural network.

Data for the R & D sector are available on the websites of statistical agencies, including the Central Statistical Office, Poland and Eurostat, as well as in sector reports and studies. To build a research and development sector model using a neural network, the Neuroph Studio application developed by Zoran Sevarac and the University of Belgrade team in Serbia [28] is used. The Neuroph Studio application helps in creating a neural network by sharing Java Neural Network Tools libraries and a graphical user interface that allows creating, learning, testing and writing a structured neural network. Neuroph Studio supports most of the known neural network architectures.

3.1 Neural network data selection, testing, learning and verification

Data for R&D sector in Poland has been selected based on sector structure then it was defined input values and decision-making variables. The statistical data to be used for learning neural network. Data should be verified by the following tests [16]:

- Chi-square test of independence
- Correlation ratio
- Coefficient of convergence Czuprowa
- Evaluation of independence and correlation

This is an important element in design of the system as inappropriately selected data will impact the accuracy of the model of R&D sector in Poland. At the end, it might have decreased the quality of the outcome results.

Neural network learning takes place through the upload input to Neuroph Studio application. Data is prepared in the form of tables with input and output data. Data is entered to the MLP (Multi-Layer Propagation) neural network with three hidden layers (16, 8, and 4).

Network learning takes place with available data in the proportions 60/40 learning and testing data. The learning process ends when it reached the stop criteria as Max error = 0.01 and Learning Rate = 0.02

Neural network verification will be performed by comparing generated neural network forecasts with the empirical values [35] as following measures:

$$\mathrm{MPE} = \frac{1}{T}\sum_{\mathrm{t}=1}^{\mathrm{T}} \frac{(\tilde{\mathrm{y}}_{\mathrm{t}} - \mathrm{y}_{\mathrm{t}})}{\mathrm{y}_{\mathrm{t}}} 100 \tag{1}$$

Where:

MPE - mean percentage error

$\tilde{\mathrm{y}}_{\mathrm{t}}$ - Forecast value

y_{t} - Empirical value

$$\mathrm{MAPE} = \frac{1}{T}\sum_{t=1}^{T} \left|\frac{(\tilde{\mathrm{y}}_{\mathrm{t}} - \mathrm{y}_{\mathrm{t}})}{\mathrm{y}_{\mathrm{t}}}\right| 100 \tag{2}$$

Where:

MAPE - mean absolute percentage error

$\tilde{\mathrm{y}}_{\mathrm{t}}$ - Forecast value

y_{t} - Empirical value

$$\mathrm{RMSPE} = \sqrt{\frac{1}{T}\sum_{t=1}^{T} (\tilde{y}_t - y_y)^2} \tag{3}$$

Where:

RMSPE - root mean square percentage error

$\tilde{y}_t$ - Forecast value
y_t - Empirical value

3.2 Conversion of neural network in the form of an explicit

At this stage, we implement the connection of the output from the neural network subsystem to the input of the dynamic programming subsystem. The data from the neural network outputs is transferred to the dynamic programming input in the form of a matrix of weighing and transformation functions. Dynamic programming allows system experts or analysts to evaluate and modify decision data.

In the next step, the programming system will evaluate the best solution with the desired range of decision variables.

Dynamic programming uses the explicit form of a neural network in the form of a matrix. In the case of a unidirectional three-layer neural network, the outputs from each layer go to the next layer of neurons.

Hereafter is a schema of the multilayer one-way network:

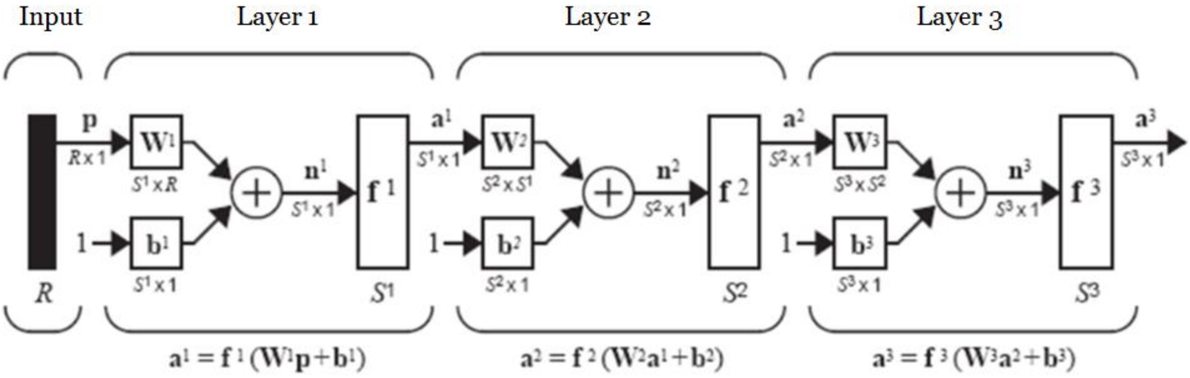

Fig.1. Three-layer one-way neural network schema using MATLAB symbols [8]

Where:

R - Number of inputs
S^w- Number of neurons in the first layer, the second and third
f^w - Activation function of the neuron layer
p – Input data
W^w - Weight matrix layer
b^w- Value of the bias layer
a^w- Output layer

The dimensions of the matrix for the layer neurons are as follows [8]:

$$p = \begin{bmatrix} p_1 \\ p_2 \\ \vdots \\ p_R \end{bmatrix} \quad W = \begin{bmatrix} w_{1,1} & w_{2,2} & \cdots & w_{1,R} \\ w_{2,1} & w_{2,2} & \ldots & w_{2,R} \\ \vdots & \vdots & \vdots & \vdots \\ w_{S,1} & w_{S,2} & \cdots & w_{S,R} \end{bmatrix} \quad b = \begin{bmatrix} b_1 \\ b_2 \\ \vdots \\ b_S \end{bmatrix} \quad a = \begin{bmatrix} a_1 \\ a_2 \\ \vdots \\ a_S \end{bmatrix} \tag{4}$$

Where:

p - Input data matrix
W - Weight matrix layer
b- Matrix biases, output data matrix
R- Number of inputs
S- Number of neurons in layer

The explicit form of the equation of neural network with three layers of hidden has the form:

$$a^3 = f^3(W^3 f^2(W^2 f^1(W^1 p + b^1) + b^2) + b^3) \qquad (5)$$

Where:

a^3- Output of the third layer
f^w - Activation function of the neuron layer
W^w - Weight matrices layers
p - Input data matrix
b^w- Matrix of bias layer

We have defined how we can connect between neural network subsystems and dynamic programming. The range of decision values is determined by experts who can determine the scope of, for example, investment in an element of the sector. This will allow you to choose better to use your existing financial resources.

4 Dynamic programming package

The problem of dynamic programming has been defined as the search for the best solution for decision variables introduced by an expert or analyst who studies the influence of input variables on output parameters.

An expert or analyst may simulate the preservation of the preferred strategy for the development of the R & D sector in the period under consideration. An expert or analyst may use different strategies, observing how the system reacts to changing the parameters of decision variables.

The problem of dynamic programming is defined as searching for better solutions for output parameters at intervals defined by input parameters within the range defined by an expert or analyst.

As a dynamic programming platform, the DP2PNSolver package developed by Lew A. and Mauch H. [20] can be used. The package allows you to solve problems in dynamic programming. The DP2PNSolver tool contains modules on two levels: the first level contains an input to introduce the specification of a discrete DP problem.

The specification of the problem that is being processed is in the temporary Petri network (PN) representing the Bellman network (BN). The transient level problem is normalized to the problem of mathematical modeling. The optimal solution to the problem is the second layer called the code output (Java or Excel spreadsheet).

I am using the DP2PNSolver package [24], which is available in a computer application with the installed Java SDK 1.4.2 package with the "javac" compiler.

4.1 Dynamic programming data verification

The R & D sector model built on the neural network provides input data to the problem defined in dynamic programming. It is very important to check whether the problem we have defined meets Markov's property [11].

This means that when deciding d_1, d_2, ..., d_k in subsequent k stages the stage s_{n+1} at the end of the stage n, that depend entirely on the stage of s_{k+1} after decision d_{k+1},, d_{k+2}, ..., d_n.

If the problem has properties you can apply dynamic programming method for Markov and Markov property follows the principle of Bellman optimality:

"The optimal Strategy has the property that, regardless of what was the initial state, and what were the initial decisions, the remaining decisions must create optimum strategy due to the condition being the result of these initial decisions."

Dynamic programming task is defined as the search for the better solutions for output parameters at intervals defined by the input of an expert or analyst.

$$a_5^3 = \max_{p_1,p_2,p_3,p_4} f^3(W^3 f^2(W^2 f^1(W^1 p + b^1) + b^2) + b^3) \quad (6)$$

Where:

$\boldsymbol{a^3}$- Matrix output
a_1^3 - Investment in fundamental research
a_2^3 - Investment in R & D sector
a_3^3 - Investments in innovative enterprises
a_4^3 - Investment in science and technology parks
a_5^3 - Transfer the results to the economy
f^n - Activation functions of neurons in each layer neural network,
W^n- Weight matrices of neurons in each layer neural network,
b^n - Bias in the individual layers of the neural
$\boldsymbol{p_n}$- Decision-making matrix input
p_1 - Expenditures on R & D sector,
p_2 - Business expenditures on R & D sector
p_3 - Expenditures on education system,
p_4 - Expenditures for the support system
p_1, p_2, p_3, p_4 - belong to a range of expert decision-making data

Neural network maps impact goes to exit through a system of weights of neurons that are explicit.

The weight shall be transferred to the dynamic programming system, so we have a system reproduces the behavior of the R&D sector-development on the input parameters, which will be introduced by an expert or analyst. From this stage, dynamic programming system is ready for analysis and presentation of results for the search for a better solution.

4.2 Better solution approach

The concept of better solution approach might be a matter of expert's discussions who can present different preferences of the R&D sector development. My approach of better solution is the direction the development of the sector R&D, which allows maximizing the transfer of research results to economy and business.

Better solution is based on the following decision-making variables:

- Expenditures on R & D sector,
- Business sector expenditures on R & D sector
- Expenditures on education system
- Expenditures for the support system

Decision-making variables in range preferred by expert or analyst give data output on relocation resources where transfer of R&D sector research results to economy is set up as goal for maximizing allocation:

- Investment in fundamental research
- Investment in R & D sector
- Investments in innovative enterprises
- Investment in science and technology parks

I have defined goal for the system to get better results on transferring R&D outcomes to economy what might positively influence on economy development.

The transfer of R&D sector research results to economy [23] is to my understanding a key element that can prevent long-term slowdown of GDP growth, what determined my own definition of better solution.

Better solutions approach is implemented in dynamic programming problem as following steps:

- For each input range is the maximum value of dynamic programming task decision transfers the results of research to the economy and business.
- Dynamic programming task is performed in four steps separately for any given decision.
- In each step, only one decision is a test range, the remaining data is fixed. The value of a decision giving the greatest value of transfers in the next step, for the next decision is the value of a constant.
- The result is a collection of four decision-making parameters that give the value of the maximum transfer of the results of R&D sector to business and the economy.

5 Conclusion

Forecasts with a very small increase in gross domestic product by 1% in 2030-2060, according to the OECD report, should lead to actions that can counteract the long-term slowdown of Poland's development.
Proper investments in the development of the R & D sector can help the economy develop above a somewhat pessimistic development forecast. The R & D sector has the necessary intellectual capital to solve non-trivial development problems.

Finding the right factor blocking the development of the country requires a systemic approach with a strong commitment to the R & D sector, which can increase the effectiveness of eliminating factors affecting the slowdown in GDP growth

My proposition of a system solution is based on the methodology of neural network and dynamic programming, to first create a model R & D sector, then find the most sensitive parameters and propose realistic solutions that will reduce the risk of GDP slowdown in the period 2030-2060.

References

1. Bartosz J. , Dorocki S. , *Wpływ wielkości nakładów inwestycyjnych w sektorze B+R na regionalne zróżnicowanie tempa rozwoju Francji,* Zakład Przedsiębiorczości i Gospodarki Przestrzennej, Instytut Geografii, Instytut Pedagogiczny im. KEN w Krakowie, 2009
2. Boni M. , *Raport Polska 2030 - Trzecia fala nowoczesności*, Ministerstwo Administracji i Cyfryzacji, 2011
3. Boni M. , *Raport Polska 2030. Wyzwania rozwojowe*, Ministerstwo Administracji i Cyfryzacji, 2009
4. Chmielewski J. , Konieczność inteligentnego programowania dynamicznego dla rozwoju sektora B+R , Techniki Informacyjne Teoria i Zastosowania – wybrane problemy tom 4 (16) , 2014
5. Chmielewski J., Transfer wiedzy i innowacji w zakresie zastosowań informatyki i cybernetyki jako sposób zwiększenia kapitału intelektulanego dla Polski i Regionów, Technologie Informacyjno – Komunikacyjne, możliwości, zagrożenia, wyzwania, 2009
6. Chmielewski J. , Zastosowanie programowania dynamicznego i sieci neuronowych dla sektora badań naukowych i rozwoju, Seria: Studia i materiały Polskiego Stowarzyszenia Zarządzania Wiedzą, 2008
7. Duval, R., de la Maisonneuve C. , *Long-Run GDP Growth Framework and Scenarios for the World Economy*, OECD Working Papers No 663 , 2009
8. Duzinkiewicz K., Grochowski M. , *Metody sztucznej inteligencji*, Politechnika Gdańska, Wydział Elektrotechniki i Automatyki, Katedra Inżynierii Systemów Sterowania, Metody sztucznej inteligencji, Zajęcia laboratoryjne , (brak daty)
9. Gajda J. , Gustafson C. , *EMIL - An Econometric Macro Model of Sweden,* Ö. U. Department of Economics, 1999
10. Główny Urząd Statystyczny, *Działalność badawczo - rozwojowa (B+R) w Polsce*, Urząd Statystyczny w Szczecinie, 2013

11. Jakowska-Suwalska K. , *Programowanie dynamiczne - przykłady i zadania,* Politechnika Śląska w Gliwicach Wydział Organizacji i Zarządzania , 2013
12. Johansson Å. , *Long-Term Growth Scenarios*, OECD Economics Department Working Papers, No. 1000, OECD Publishing, 2013
13. Johansson Å. , *Looking to 2060: Long-Term Global Growth Prospects: A Going for Growth Report,* OECD Economic Policy Papers, No. 3 - OECD Publishing - ISSN 2226583X, 2012
14. Kacprzyk J. , *Studies in Computational Intelligence,* Springer Berlin/Heidelberg, 1860-949X, Volume 38/2007, 2007
15. Kacprzyk J. , Towards Perception-Based Fuzzy Modeling: An Extended Multistage Fuzzy Control Model and Its Use in Sustainable Regional Development Planning. ISBN 981-238-751-X, pages: 321-337, 2006
16. Kaszubski K., Kuczewski M., Rośczak P. , Gra ekonomiczna symulująca sterowanie gospodarką narodową implementowana za pomocą systemu komputerowego wykorzystującego sztuczną sieć neuronową, Uniwersytet Łódzki Wydział Ekonomiczno - Socjologiczny Kierunek Informatyka i Ekonometria, Łódź, 2002
17. Kleiber M. , Praca Zbiorowa - Wyniki Narodowego Programu Foresight Polska 2020, 2009
18. Klimczak D. , Strojny M. , Żagun K. , Czy warto inwestować w innowacje. Analiza sektora badawczo-rozwojowego w Polsce, Raport KPGM, 2009
19. Leśniewski Ł. , *Sektor badawczo - rozwojowy w Polsce*, Polska Agencja Informacji i Inwestycji Zagranicznych S.A. , Wydział Informacji, Departament Informacji Gospodarczej, 2010
20. Lew A. , Mauch H , *Dynamic Programming, a Computational Tool,* ISBN-10 3-540-37013-7, Springer Berlin Heidelberg New York, 2006
21. Matusiak K. , *Ośrodki innowacji i przedsiębiorczości w Polsce,* Polska Agencja Rozwoju Przedsiębiorczości, *2010*
22. Matusiak K. ,Rekomendacja zmian w polskim systemie transferu technologii i komercjalizacji wiedzy, Polska Agencja Rozwoju Przedsiębiorczości, 2010
23. Matusiak K. , System transferu technologii i komercjalizacji wiedzy w Polsce - siły motoryczne i bariery, Polska Agencja Rozwoju Przedsiębiorczości, 2010
24. Mauch H. , *DP2PN2Solver: a flexible dynamic programming solver software tool,* Control and Cybernetics, 2006, Vol.: 35, Part 3, pages 687-702, Polish Academy of Science , 2006
25. Mosionek-Schweda M. , *Finansowanie działalności badawczo-rozwojowej przedsiębiorstw w Polsce*, Wyższa Szkoła Bankowa w Toruniu, Oeconomia Copernicana, 2011
26. Rośczak P. , *Model gospodarki Szwecji EMIL w postaci sieci neuronowych*. http://www.rosczak.com/index.php/pl/oprogramowanie/emil, 2003
27. Santarek K. , Bagiński J. , Buczacki A. , Sobczak D. , Szerenos A. , Transfer technologii z uczelni do biznesu. Tworzenie mechanizmów transferu technologii, 2008
28. Severac Z. , Koprivica M. , *Getting started with Neuroph,* Neuroph Studio framework version 2.3 , 2012
29. Straszak A. , Lokalny Transfer Wiedzy i Innowacji w Internetowych Lokalno-Globalnych Społeczeństwach i Gospodarkach opartych na wiedzy, Unia Europejska – Transfer wiedzy i innowacji w warunkach lokalnych, tom 4 , 2008
30. Straszak A. , Przyspieszenie kreatywności i innowacyjności w regionach wiedzy poprzez zwiększenie zastosowań automatyki, informatyki i cybernetyki, Technologie Informacyjno - Komunikacyjne, możliwości, zagrożenia, wyzwania, 2009
31. Straszak A., Kruszewski T. , *Long-term global stability in the world in the years 1960 - 2060.* Artykuł na Konferencję w Kosowie, 2013

32. Straszak A. , Studzinski J. , Bogdan , L. , *Poland 21st Century Infrastructure for „Global Great Transition"(Eco – Info – Communalism),* Scenarios Looking for Future System Research Solutions, 2005
33. The Organization for Economic Co-operation and Development #1, *Medium and Long-term Scenarios for Global Growth and Imbalances,* OECD Economic Outlook - Volume 2012 Issue 1 - OECD Publishing, 2012
34. The Organization for Economic Co-operation and Development #2, *OECD Economic Outlook,* Vol. 2012/2 OECD Publishing, 2012
35. Zieliński S. , Rośczak P. , Gra ekonomiczna symulująca sterowanie gospodarką narodową implementowana za pomocą systemu komputerowego wykorzystującego sztuczną sieć neurnową, Uniwersytet Łódzki Wydział Ekonomiczno-Socjologiczny Kierunek Informatyka i Ekonometria, 2002

Recurrent Neural Networks with grid data quantization for modeling LHC superconducting magnets behavior

Maciej Wielgosz[1] and Andrzej Skoczeń[2]
[1] Faculty of Computer Science, Electronics and Telecommunications,
AGH University of Science and Technology, Krakow, Poland;
[2] Faculty of Physics and Applied Computer Science,
AGH University of Science and Technology, Krakow, Poland;

Abstract. This paper presents a model based on RNN architecture, in particular LSTM, for modeling the behavior of LHC superconducting magnets.High resolution data available in PM database was used to train a set of models and compare their performance with respect to various hyper-parameters such as input data quantization and number of cells.A novel approach to signal level quantization allowed to reduce a size of the model, simplify tuning of the magnet monitoring system and make the process scalable. The paper shows that RNNs such as LSTM or GRU may be used for modeling high resolution signals with an accuracy over 0.95 and as small number of the parameters ranging from 800 to 1200. This makes the solution suitable for hardware implementation essential in the case of monitoring performance critical and high speed signal of LHC superconducting magnets.

The full text will be available in the edited book "Information Technology, Systems Research and Computational Physics", eds. Kulczycki P., Kacprzyk J., Kóczy L.T., Mesiar R., Wisniewski R., to be published by Springer in the *Advances in Intelligent Systems and Computing* series soon.

Author Index

Świebocka-Więk
  Joanna 56
Łukasik
  Szymon 54, 55, 74
Čerňanová
  Viera 78
Šeliga
  Adam 93
Ždímalová
  Mária 112

Ahmed
  Sajib 143, 203

Błażewicz
  Marta 3
Bacigál
  Tomáš 92
Balázs
  Péter 71, 72
Ballová
  Dominika 94
Belter
  Dominik 158
Bielski
  Adam 10
Binaghi
  Elisabetta 11
Biswas
  Arindam 213
Bodyanskiy
  Yevgeniy 76
Bohumel
  Tomáš 112
Bracci
  Fabio 142
Brunner
  Szilvia 8
Buruzs
  Adrienn 140
Charytanowicz
  Małgorzata 54, 55, 74
Chmielewski
  Jacek 229
Coufal
  David 91

Długoń
  Elżbieta 3
Deepa 208
Deja
  Kamil 2
Dragan
  Łukasz 22
Dużyja
  Maria 3
Duran
  Juan Camilo Calvera 226
Dvernaya
  Elena 144

El Falougy
  Hisham 112

Földesi
  Peter 75, 140
Fazekas
  Attila 160
Fogarasi
  Gergő 140
Friebe
  Michael 208

Giebułtowski
  Marek 23
Glinka
  Michał 46
Gołaszewski
  Grzegorz 68
Gonçalves
  Teresa 9, 143, 203, 204

Graczykowski
  Łukasz 2, 46, 113

Halvoník
  Jaroslav 79
Harmati
  István Á 139
Hideghéty
  Katalin 8
Horwat
  Dominik 177
Hu
  Weichih 208
Hudec
  Miroslav 21
Hussein
  Alhamzawi 160

Janc
  Krzysztof 124
Javorszky
  Karl 95
Jayatilake
  Mohan 9
Juszczuk
  Przemysław 228

Kóczy
  László T. 75, 138–140
Kalická
  Jana 79
Kamiński
  Jakub 124
Kardos
  Péter 107
Katona
  Melinda 8
Kołaczek
  Damian 5
Kołodziej
  Anna 3
Kołodziejczyk
  Andrzej 23
Koliechkina
  Liudmila 144
Kollmannsberger
  Stefan 108
Komorník
  Jozef 92
Komorníková
  Magdaléna 92
Kossyk
  Ingo 142
Kowalik
  Marcin 23
Kowalski
  Piotr 54, 55, 74
Kozdrowski
  Stanisław 14
Krośnicki
  Marek 177
Kruś
  Lech 228
Kudela
  László 108
Kulczycki
  Piotr 54, 55, 74
Kulinowski
  Karol 4

Lékó
  Gábor 71
Lalik
  Konrad 55
Li
  Mo 142
Lilik
  Ferenc 138
Luchowski
  Leszek 159

Maździarz
  Artur 47
Majtánová
  Lucia 79
Marín
  Carlos Enrique Montenegro 226
Martinelli
  Samuele 11
Marton
  Zoltan-Csaba 142
Metta
  Venkata Padmavati 225
Minárová
  Mária 79
Moskal
  Paulina 3

Mukherjee
  Himadri 204
Myrcha
  Julian 113

Németh
  Gábor 106
Nánásiová
  Oľga 78
Nagy
  Szilvia 138
Nikolaiev
  Sergii 125
Nowakowski
  Piotr 113
Nyúl
  László G. 8

Obaidullah
  Sk Md 143, 203, 204

Palágyi
  Kálmán 106, 107
Parra
  Octavio José Salcedo 226
Patnaik
  Pawan Kumar 225
Phadikar
  Santanu 204
Piaskowski
  Karol 158
Piesik
  Emilian 31
  Jan 31
Plachá-Gregorovská
  Katarína 112
Pojda
  Dariusz 159
Polanek
  Róbert 8
Provotar
  Oleksandr 192

Rakovská
  Eva 21
Rank
  Ernst 108
Rato
  Luís 9, 203
Rokita
  Przemysław 113
Roy
  Kaushik 204
  Nilanjana Dutta 213
Rybotycki
  Tomasz 205

Sacharz
  Julia 3
Santosh
  K.C. 204
Sarna
  Piotr 55
Sikora
  Grzegorz 80
Singh
  Jyoti 225
  Yashbir 208
Skabek
  Krzysztof 159
Skoczeń
  Andrzej 240
Slapal
  Josef 109
Solecki
  Levente 138
Spisak
  Bartłomiej J. 4, 5
Stodolak-Zych
  Ewa 3
Studniarski
  Marcin 144
Sujecki
  Sławomir 14, 48
Szűcs
  Judit 72
Szabó
  Emília Rita 8
  Imre Zoltán 8
Sziová
  Brigita 138

Túű-Szabó
  Boldizsár 75
Tőkés
  Tüde 8
Tarasiuk
  Jacek 124

Tarnawski
    Michał 159
Tautkute
    Ivona 10
Tavares
    João Manuel R. S. 208
Telenyk
    Sergii 125
Thomas
    D.G. 225
Tokarz
    Wlademar 23
Tomaka
    Agnieszka Anna 159
Trzciński
    Tomasz 2, 10, 46, 113
Tymoshenko
    Yury 125
Tyshchenko
    Oleksii 76

Vörösk𝑜̋i
    Kata 140
Valášková
    Ľubica 78
Varga
    László 70
Vergani
    Alberto Arturo 11

Weismann
    Peter 112
Wesełucha-Birczyńska
    Aleksandra 3
Wielgosz
    Maciej 240
Wit
    Adrian 124
Wołoszyn
    Maciej 4, 5
Woch
    Wiesław 23
Wróblewska
    Anna 22
Wu
    Shi-Yi 208

Zalecki
    Ryszard 23